Some Aspects of

Hypersonic Flow Instrumentations

S.M.C. Ngan

A thesis submitted for the degree of Master of Science

October 1977

The contents of this thesis, except otherwise mentioned in the references, are entirely my own work.

(STANISLAUS MAN CHIU NGAN)

ABSTRACT

A shock speed timing system based on thermocouple transducers is developed. The calibration of a contoured nozzle is carried out using pitot pressure and free-stream density measurements. A system using calorimeter gauges to measure heat transfer rates is described. Finally heat transfer rate measurements on a cylindrical model is compared with theory.

ACKNOWLEDGEMENTS

I would like to express my thanks to my Supervisors, Prof. R.J. Stalker for initiating this project, and Dr H. Hornung for his continual support and advice, without whose help this project would be almost impossible to complete. I would also like to thank Mr R. French, Mr V. Adams for operating T3, Mr D. King, Mr L. Batt for help with manufacturing the printed circuit boards and supplying some of the components used in this project, Mr K. Smith for his photographic prints and Mr M. Daffey for the supply of design information on the contoured nozzle. Finally my special thanks to my sister, Letitia, for typing this thesis.

TABLE OF CONTENTS

LIST OF TABLES

Table No.

LIST OF ILLUSTRATIONS

Figure No.

Figure No.

Figure No.

Figure No.

CHAPTER 1: INTRODUCTION

This project has as its main aim the improvement of some of the experimental facilities offered by the shock tube laboratory in ANU. It is intended to upgrade the following areas, namely, shock speed measurements, heat transfer rate measurements and shock tunnel gas flows, so that reliable and good quality experiments can be obtained as a matter of routine. These three areas of interest are chosen because of their fundamental nature in shock tube applications. The general approach adopted is to examine the existing experimental set-up, determine whether they can be improved and if otherwise design alternative arrangements.

In the area of shock speed measurement, thermocouples are developed. In heat transfer rate measurements, calorimeter gauges are chosen as suitable for routine uses. A contoured nozzle was used to generate parallel test flows. This project is responsible only for the calibration of the contoured nozzle flow, as its design was carried out elsewhere (Daffy).

This project is divided into four sections, as shown in Fig. 1.1. Section 1 covers the development of a new shock

speed measurement system based on thermocouples. Section 2 covers the calibration of the contoured nozzle. Section 3 covers the development of calorimeter gauges in heat transfer rate measurements. Section 4 covers actual heat transfer rate measurements on a chosen model. The main concern of the project is to improve the facility on the shock tunnel known as T3 (Stalker, 1972, Stalker, 1970, Hornung PF 5), but the results can be applied to other shock tubes easily.

CHAPTER 2: SHOCK SPEED MEASUREMENT SYSTEM

2.1 INTRODUCTION

There is a variety of transducers capable of recording the passage of shock waves (Bradley, Gaydon et al). They can be categorised into four groups, operations depend on the various effects caused by the passage of the shock front. Figure 2.1 illustrates the implementation of some of the more common methods and Table 2.1 summarises their characteristics and drawbacks. The main transducers employed in the shock tube laboratory at ANU had been pressure transducers, ionisation gauges and photodiodes. It was the experience of the author that they perform satisfactorily only under a limited set of operating conditions. Changing the operating conditions often necessitates a considerable amount of time and frustration in reestablishing the correct set-up for another set of transducers that can operate reliably under the new environment. Clearly one has need for a transducer that can cope with all the conditions likely to be encountered in the operation of the shock tubes. It has to be reliable, yet rugged, simple to manufacture and low cost. It should depend on the primary properties of a shock wave, namely, pressure, temperature or density rise. This ruled out transducers such as photodiodes and ionisation gauges. The final

choice was settled on thermocouples. Thermocouples are extremely simple, robust and practically maintenance free for a long period of time.

Its disadvantage lies in the low signal output compared to other gauges, thus necessitating large amplifications. There has been practically no reported literature on its systematic use in shock speed measurements, thus necessitating tests to prove its feasibility. Furler's preliminary work covered only a narrow range in nitrogen as test gas.

2.2 THERMOCOUPLES AS SHOCK SPEED MEASUREMENT DEVICES

2.2.1 Operating Principles

When two dissimilar metals are joined together, and their junctions maintained at different temperatures, a voltage is developed between the two junctions. This voltage has an output E.M.F. of

$$E = A + Bt + Ct^2 \qquad (2.1)$$

where

A, B and C are constants, depending on particular metals and t is the temperature difference.

When one junction of a thermocouple is exposed to a gas flow with positive heat transfer, the voltage output will rise with time, the rate depends on the thermal, physical and electrical properties of the junction and the heat transfer rate. One desires a small thermal capacity so that the thermocouple will have a maximum rate of temperature rise. One technique is to vacuum deposit an extremely thin layer of metal on another metal to form the junction. One can achieve a time constant of less than one microsecond in this way (Moeller). However this method necessitates special techniques and the end product is almost certainly too fragile to withstand the harsh environment in a shock tube repeatedly. The method adopted in constructing the thermocouples used in this project is as follows: 2 wires (chromel and alumel) are

separated by a thin mylar sheet and then set in araldite. Afterwards, the exposed metal surfaces are then filed gently so that a junction is formed between the two metals.

The physical size of the thermocouple is minimised to increase the resolution in detecting the shock front, bearing in mind that with a shock speed of 2 km/second, it takes one microsecond to travel 2 mm. The typical thermocouple element has a width of less than 1 mm, thus introducing only a small error in the shock speed to all intents and purposes, if one takes care in aligning the thermocouples.

One should ideally choose a combination of metals that gives the highest output for the same heat transfer rate, bearing in mind their thermal capacities. However, in this project, only chromel and alumel wires were used because they were readily available, and they exhibit a favourable thermal E.M.F. compared to other common thermocouple materials (Benedict et al).

2.2.2 Feasibility Study of Thermocouples

In order to establish the performance of the thermocouple under various shock tube conditions, it was compared side by side with a reference thin film gauge, the set-up is shown in Fig. 2.2. The operating principle of the thin film gauge will be dealt with in Chapter 4, but briefly, a very

thin metallic film, a few hundred angstrom thick, senses the surface temperature of an insulating substrate subjected to shock heated gas flow. Its rise time is determined by the width of the gauge (Bradley), and since it is about 1 mm for the gauges used in this project, it constitutes a good reference to compare the response time of the thermocouples. This test was also aimed at estimating the outputs of the thermocouples under various conditions. Some direct measurements were made, but the majority was obtained by interpolations from thin-film signals, since only a rough estimate is required for the design of a suitable preamplifier for thermocouples. A series of such comparisons were done on a shock tube T1 (Stalker, 1965). The thin-film gauge was driven by a constant current source capable of supplying 9 to 50 milliamperes, as shown in Fig. 2.3. Its output went to the lower beam of a Tektronix type 565 dual beam oscilloscope. The thermocouple output went to a differential amplifier (Dobkin, Fairchild) shown in Fig. 2.4, having a measured rise time of about 500 nanoseconds at a gain of 200, before going to the upper beam of the 565 oscilloscope. The gain of the amplifier is given by (1 + 2R3/VR1). This differential amplifier was later replaced by a pulse transformer feeding into an inverting amplifier before going into the 565 oscilloscope, as in Fig. 2.5, in order to obtain much higher gain at a lower noise level. The shock speed range covered from 1 km/sec to 5.2 km/sec. The initial shock tube pressure covered from 5.0 torr to 760 torr. The test gases used were air, nitrogen, carbon dioxide, argon and helium. The heat transfer rates ranged

from a few hundred watts/sq cm to a few kW/sq cm. Fig. 2.6a shows one example of the outputs of the thermocouples directly, and Fig. 2.6b output via the amplifier shown in Fig. 2.5. Table 2.2 summarises the minimum sensitivity of a thermocouple preamplifier required to guarantee proper shock timing. Notice that with helium as test gas the system is much less sensitive than for other gases.

This preliminary test was encouraging, and yielded information on the following aspects concerning thermocouples.

1. They were extremely robust, compared to thin-film gauges. In this series, about 300 shots were fired. At least 3 thin-film gauges were destroyed mainly during high performance shots, but essentially the same thermocouple was used throughout the test with no apparent degradation.

2. They appear to be able to cope with all the common gases used in shock tubes in this laboratory.

3. During some shots, charge pick-ups from the ionised gas caused a reversal of the polarity of the rising edge of the signal, as in Fig. 2.6c. This implied that a detector capable of responding to either polarity automatically has to be used to process the signal output from such devices. This actually applied to all other transducers working in an ionised gas environment also.

2.2.3 Design Consideration of Shock Speed Measurement System

Having proven the concept, design work was carried out to build a complete system. The aim is to provide an accurate, easy to operate, economical, compact, reliable and versatile shock speed measurement system. This implied having digital readouts built into the system, rather than relying on external counters being hooked up. These in-built readouts simplify greatly noise problems likely to be encountered otherwise, in addition to being much more economical, since counters available on the market contain features not required for the present set-up. In addition, the use of individual external counters will needlessly duplicate a substantial amount of circuitry common to them, such as power supply and time base generator. To be versatile, this system should be able to accept other transducers with minimum additional circuitry, to cover situations where thermocouples are inadequate, such as in very low enthalpy conditions. The design should be modular so that minimum modifications are required to obtain different configurations for applications not requiring a complete system. Modularity also simplifies servicing and assembly. However, a certain amount of duplication of circuitry is necessary in order to satisfy all of the above criteria.

The final set-up, incorporating modifications done up to date, will now be described. This description is partly intended as a manual of the system for future users and its style is therefore a little like that of operating instructions.

2.3 DESCRIPTION OF SHOCK SPEED MEASURLMENT SYSTEM

2.3.1 Introduction

The system is housed in four sections: the mainframe, the power supply and the displays, which are housed in separate boxes mounted on a 19" rack, and the preamplifiers, which are each mounted physically as near to a transducer as possible. The different sections are interconnected by cables. The system was built to accommodate a varying number of transducers by plugging in additional control channels in the form of printed circuit boards, up to a maximum of 7 transducers to produce a maximum of 6 readings indicating the time elapsed between the passage of the shock front between two consecutive transducers. A block diagram illustrating the set-up is shown in Fig. 2.7a, and a photograph of the system is shown in Fig. 2.7b.

2.3.2 Mainframe Unit

2.3.2.1 Operating Instructions for Mainframe Unit

The mainframe unit houses the control channels, the system-check circuitries, the calibration circuitries, the time base generator, the gating circuitries and the interconnections between the different sections of the system. Fig. 2.8 shows its front panel layout. It was built using an Elco

type Varipack II card frame, housing 1 gating board, 2 clock pulse generating boards and a maximum of 7 control boards, all of which are plugged into 22-pins Elco edge connectors. An extension card is provided so that adjustments can be made to the boards while the system is operating. The back panel houses sockets for connection to preamplifiers, 14-pins Amphenol microribbon connectors to display units and 8-pins Jones connectors to the power supply unit. The front panel has various control switches, potentiometer, light-emitting-diodes as control channel status indicators, a BNC socket for external frequency input,and 7 sets of BNC sockets, providing outputs of the control channels at TTL levels, of both polarities to control external devices such as oscilloscopes.

Switch SW1 selects the system operating mode, i.e. run, system-check and calibration. In the run mode, the system is used for shock timing. In the system-check mode, it is used in conjunction with SW2 to checkout the whole system, excluding the preamplifiers. Pressing SW2 while in system-check mode will result in the displays displaying a reading of 100.0. In the calibration mode, it is used in conjunction with SW6 and VR3 to set the trigger level of the control channels to the same pulse amplitude. The calibration scale of VR3 is relative only, it is not directly in volts. The calibration procedure will be described in 2.3.2.7. SW3 enables selection of either the internal time

base or an external time base, input through CNR15. The external frequency, usually 10 MHz, must have a minimum peak amplitude of 200 mV and a maximum of 10 V peak at 10 MHz, but at mains frequency it is protected up to 300 V RMS. SW4 resets the whole system, lighting up LED 1-1 to LED 1-7, indicating system was reset, ready to receive input. To check internal frequency, set SW1 in either run or system-check mode, connect an accurate standard frequency to the external frequency input socket CNR 15, then press SW5 long enough until both display 1 and 2 stop changing. The internal frequency is then adjusted via VC 1, the system reset, and SW5 pressed again. This process is repeated until the displays read the frequency of the standard. Clearly, it also serves to calibrate an unknown external frequency. LED 1-1 to LED 1-7 indicate the status of the control channels, ON meaning reset. CNR 1 to CNR 7 provide buffered positive going pulses and CNR 8 to CNR 14 buffered negative going pulses from the control channels, being approximately 15 microseconds duration at TTL levels. LED 1-1 to LED 1-7 and CNR 1 to CNR 14 function only as long as their appropriate control channels are plugged in. Fig. 2.9 gives the functional block diagram of the mainframe control unit. It can be divided into six major parts: the inputs selector, the control channels, the gating circuitries, the time base generator, the system-check pulse generator and the calibration pulse generator.

2.3.2.2 Inputs Selector

The inputs selector SW 1 is a 3 positions 7 poles rotary switch which connects the appropriate set of inputs to the control channels. The sets of inputs are:

a. pulses from the timing transducer preamplifiers;

b. pulses from the system-check pulse generator;

c. pulses from the calibration pulse generator.

SW 1 is located on the front panel. In the run mode, it selects the input set a, and this is the mode the system is normally in. In the system-check mode, input set b is selected. In the calibration mode, input set c is selected. Fig. 2.10 gives its wiring diagram.

2.3.2.3 Control Channels

The function of the control channels is to process the signals from the input selector , provide output pulses to external devices via CNR 1 to CNR 14, control the status lights LED 1-1 to LED 1-7 and to provide pulses to control the gating circuitries. Fig. 2.11 shows the circuit of one control channel.

Input from the inputs selector goes to the input overload protection network consisting of C 1, R 1, D 1 and D 2. R 2 serves as bias return for IC 1 and IC 2. IC 1, IC 2, R 3, R 4, R 5, R 6, R 7, R 8, VR 1, VR 2, R 17, R 18,

C 2, C 3, ZD 1 and ZD 2 serve as a window comparator, ie, as a dual-polarity pulse detector. It will detect pulses that are above a threshold voltage as set by VR 1 and VR 2. The threshold can be adjusted from 0 to 440 mV for either polarity. IC 1 is responsible for detecting the positive going pulses and IC 2 for the negative going pulses. The presence of this dual-polarity detector enables signals of whatever polarity to be accepted, thus eliminating need to keep track of polarities of different types of transducers. In some instances, some transducers exhibit reversal of output signal polarity at the rising edge due to interferences superimposed on the desired signal. This condition is solved by this detector. The OR-gate, consisting of IC 3a, IC 3b and IC 3c feeds the output from the comparator to IC 4, which generates a 3 microsecond pulse into a latch consisting of IC 5 and IC 3d. The latch functions to allow just one pulse to pass through until reset via SW 4, functioning similarly to the single shot mode in oscilloscopes. TR 1, R 16, and LED 1 form the status indicator of their particular control channel, LED 1 lighting up when channel is reset and extinguishing when channel has been triggered once. The output pulse from IC 5 goes to the gating board and also to another monostable IC 6. IC 6 together with R 11, C 5, R 12, R 13, R 19, TR 2, R 14, R 15, R 20, and TR 3 provide buffered output pulses of both polarities at TTL level to the front panel connectors, with a duration of 15 microseconds. Fig. 2.12 shows the outputs from one channel. C 6 and C 7, located

physically near to the integrated circuits, are for power line by-passing. C8 is located near the card edge. One control channel occupies one printed circuit board.

2.3.2.4 Gating Circuitries

The function of the gating circuitries is to start and stop the appropriate counters when the control channels are triggered, by routing the time base generator pulses appropriately. They eliminate external interconnecting cables, thus reducing noise, improving signal response time and allowing a much more compact system. Fig. 2.13 shows the circuit.

Inputs coming from control channels #1 and #2 are fed into IC 7a and IC 7b, before going to the gates assembly. The inputs from control channels #3 to #7 go directly to the gates assembly. IC 7a, IC7b, IC 15b, IC 17a, IC 17b, IC 16b, SW 5a, IC 10d, IC 18a and IC 18b form the frequency-check circuitry. When SW 5a is pressed, IC 15b allows 2 pulses separated by 1 second interval, as generated by the dual J-K flip-flop IC 17a and IC 17b, to pass through to the latches IC 8a, IC 10a and IC 8b, IC 10b. It also enables IC 18a so that displays #1 and #2 are combined to provide 8 digits resolution in reading the external frequency. IC 18b can be used to provide 12 digit resolution when needed. However, this facility is not really necessary, it was there because of a spare IC 18b being present otherwise. Another part of the frequency check circuitry is with the time base generator.

When control channel 1 is triggered, IC 7a, IC 8a and IC 10a act to enable the 10 MHz pulses from the time base generator, via the buffer IC 10c, to pass through IC 9a to display board # 1. When control channel # 2 is subsequently triggered, IC 9a is disabled, thus stopping any more 10 MHz pulses from going to display board # 1. This action also enables IC 9b via IC 7b, IC 8b and IC 10b, allowing 10 MHz pulses to go to display board # 2. This action goes on as each control channel is triggered in turn.

SW 4 and R 21 provide the reset function for the whole system, available on a master clear line. R 22 loads a logic '1' into all the 'D' inputs of the dual-D flip-flops and into the 'J' input of one of the J-K flip-flop, IC 17b.

C 8, C 9 and C 10, C 11 provide the power line by-passing and are located physically near to the integrated circuits. C 12 is also for power supply decoupling.

The whole gating circuitry is contained in one printed circuit board, with SW 4, and R 21 mounted on front panel.

2.3.2.5 Time-Base Generator

This generates internally a 10 MHz signal, at TTL level, and also conditions an external signal input for

checking the internal frequency or as a substitute. Fig. 2.14 gives its circuit.

IC 19a, IC 19b, R 24, R 25, C 13, C 14, C 15, VC 1 and XTAL form a 10 MHz oscillator (Lane). IC 23 is a high speed comparator that converts an external signal, usually 10 MHz frequency, of suitable amplitude (see 2.3.2.1) into TTL levels. IC 21b selects either the internal or the external frequency source to be fed to the gating circuitries and to the decade divider chains formed by IC 24 to IC 30. IC 21a, in conjunction with IC 19c, IC 19d, IC 20a, IC 20b, IC 19e, IC 22a and IC 22b, routes the internally generated frequency to the decade divider chains, and the external standard frequency to IC 10c of the gating board. The position of SW 1 does not matter, provided it is not in the calibration mode. The 10 KHz output is fed to pin-12 of IC 20c of the system-check generator, and the 1 Hz output is fed to pin-9 of IC 16b on the gating board for purpose of checking the internal frequency, and also to the calibration pulse generator. IC 21a and IC 21b are used to defeat contact bounce of switches SW 3 and SW 5b. C 17 to C 23 are for power supply by-passing.

2.3.2.6 System-check Generator

This generator outputs 7 pulses, each separated by 100.0 microseconds, to trigger the 7 control channels sequentially. In this way, all the circuitries of the timing system

with the exception of the transducer preamplifiers, are checked in one go. This is intended to detect catastrophic failures each time before the shock tube is fired. Fig. 2.15 gives the circuit diagram.

When SW 2 is pressed, IC 20c is enabled by IC 32a, and 10 Khz pulses are fed to pin-8 of IC 31, a serial to parallel shift register, allowing 7 output pulses separated by 100.0 microseconds to be obtained. The output Q_1 (pin-3 of IC 31) is not used, in order to eliminate partial pulses getting through. When in system-check mode, the outputs from the CNR's can be used to calibrate the time base of oscilloscopes, providing marker pulses at 100.0 microseconds interval.

2.3.2.7 Calibration Pulse Generator

In order to ensure that all control channels have the same triggering sensitivities (which is important in obtaining uniform and thus accurate timing for some types of transducers), a calibration pulse generator is incorporated into the system. Fig. 2.16 gives the circuit diagram.

IC 20d accepts 1 Hz signals from the time-base generator, then differentiates them with C 25 and R 32 and feeds them to the two transistor switches TR 4 and TR 5 clamped at 2 volts output maximum. SW 6 selects the polarity and VR 3

adjusts the amplitude before sending it to the input selector switch SW 1.

To set the trigger levels, SW 1 is set to the calibration mode. VR 1 and VR 2 of all the control channels available are then set so that +400 mV is present on pin-3 of IC 1 and -400 mV is present on pin-2 of IC 2. Then SW 6 is switched to give positive-going pulses. SW 4 is pressed to reset the system. VR 3 is then adjusted so that channel # 1 just triggers. Keeping VR 3 untouched, switch SW 6 to give negative-going pulses. Again reset system and adjust VR 2 so that channel # 1 again just triggers. Again keeping VR 3 untouched, VR 1 and VR 2 of channel # 2 is adjusted in turn so that it just triggers. The procedure is repeated for all the other channels available. In this manner, one can keep the trigger level of all the control channels within ± 5 mV.

The time-base generator, the system-check generator and the calibration-check generator are contained in two printed circuit boards labelled clock pulse board # 1, and clock pulse board # 2.

2.3.3 Counter and Display Units

Counter and display units form the readout to give the shock timings in tenths of microseconds if the time-base frequency used is 10 MHz. A maximum of 6 such units are allowed, with 2 units mounted on one box on a 19" rack.

On display box # 1, a switch SW 8 is present which enables blanking of the displays, reducing the power consumption significantly for the +5 V supply, especially when all 6 displays are used. The readings on the displays will not be affected by this display blanking. It is important to blank the displays after each shot, as the +5 V regulator dissipates a substantial amount of power.

At the back of each display box, a 2-pins Jones type connector allows +5 V to be supplied from the power supply box. Also a 14-pins microribbon connector enables connection to be made to the mainframe control unit, the interconnection is made via a double shielded cable, with the outer shield grounded using the grounding terminals on the power supply box.

Fig. 2.17 shows the functional diagram and Fig. 2.18 shows the circuit of display unit # 1. IC 33 to IC 36 form a 4 decades Binary-coded-decimal (BCD) divider chain, the outputs of which are decoded by IC 37 to IC 40 to drive 7-segment light emitting diodes DISP 1 to DISP 4. R 36 to R 63 limit the segment currents of the displays to prevent damage. R 35 supplies a logic '1' to pin-2 of IC 33 to IC 36. C 30 by-passes the master clear line to prevent interference picked up via the external interconnecting cable from resetting the displays. C 26 to C 31 are for supply decoupling.

2.3.4 Power Supply Unit

Fig. 2.19 is the circuit diagram of the power supply. The system requires 4 supply voltages.

1. +5 V at 5A. This supplies all the TTL logic circuitry and the 7-segment displays. It is provided by transformer T1, fuse F2, bridge rectifier BR 1, filter capacitors C 32, C 33, C 34, R 64 and LED 2, rectifier D 13 and voltage regulator IC 41. D 13 is present to prevent damage to IC 41 should the input-side voltage go lower than the output-side voltage. IC 41 should be a type MIVR 42050 when the maximum configuration for the system is used, but at time of writing, a LM 323k is used instead as the load is much smaller.

2. -5 V at 1A. This supplies some of the comparators and comprises T 2, F 3, BR 2, C 35 to C 37, R 65, LED 3, D 13 and IC 42.

3. +15 V at 1A. This supplies the operational amplifiers and some of the comparators, and comprises T 3a, F 4, BR 3, C 38 to C 40, R 66, LED 4, D 15 and IC 43.

4. -15 V at 1A. This supplies the operational amplifiers and some of the comparators, and comprises T 3b, F 5, BR 4, C 41 to C 43, R 67, LED 5, D 16 and IC 44.

The mains supply is switched by SW 8 and protected by a fuse F 1. It is filtered by a Corcom Powerline filter

before going to T 1, T 2 and T 3. There is provision for a 5th auxiliary supply.

2.3.5 Preamplifiers

The function of the preamplifiers is to act as an interface between transducers and the control channels. The system was conceived to be capable of accepting transducers other than thermocouples by changing the preamplifiers. Only preamplifiers suitable for thermocouples will be described in here. Fig. 2.20 shows its circuit diagram.

The signal from the thermocouple is amplified first by a pulse transformer T 4, then by another non-inverting amplifier IC 45. The signal is then differentiated by C 45 and R 72 and fed to a dual-polarity signal detector. The output from the detector goes to TR 6 acting as a line driver to feed the signal to the mainframe via an external cable. Duplicating the dual-polarity signal detector in the thermocouple preamplifiers is necessary to avoid excessive preamplifications or sending millivolt signals down a long cable, leading to frequent spurious triggering of the control channels. C 46 to C 51 provide supply decoupling.

The pulse transformer T 4 was shielded in a mumetal box and the whole preamplifier is housed in a metal box. It is important that the preamplifiers must not be connected to

the metal structure of the shock tube, because from experience, they are very noisy electrically. Another point to note is to mount the preamplifiers so that mechanical vibrations, such as shock tube recoil, are not picked up by the preamplifiers. This susceptibility to large amplitude mechanical shock comes because of the very large amplification of the amplifier. The design of the amplifier emphasises unconditional stability, leading to some degradation in response time.

Note that all resistors used in the preamplifiers should be of 5% or better tolerance, except R 77, R 78 and R 79. The thermocouple transducer is recommended to be a 5-element one connected in series.

2.4 TESTING OF SHOCK TIMING SYSTEM

2.4.1 Introduction

The testing of the system was carried out using three different methods, namely, bench tests, comparision with thin-film gauge on T 1, and comparision with ionisation gauges on T 3. These tests attempt to pin-point any area where the design goal has not been reached, and to obtain data on the performance of the system with regard to the accuracy of the shock speed timings. The tests were done using thermocouples and their associated preamplifiers feeding into the mainframe unit.

2.4.2 Bench Testing of Shock Timing System

The set-up is shown in Fig. 2.21. The preamplifier receives a signal simulating the expected signal waveform and magnitude from a thermocouple transducer in the low performance region of a shock tube. In this way, realistic results will be obtained, and enables one to place an upper bound on the error of the shock timing.

The pulse generator outputs a fast rising edge square pulse of width 50 microseconds which is integrated by the RC combination having a time constant of 100 microseconds. This signal is fed to a voltage dropping resistor before feeding into the primary of the pulse transformer T 4 of the thermocouple preamplifier. A signal from the pulse generator

is used to start a counter and another signal from the control channel output of the mainframe unit is used to stop the counter. The reading on the counter will give the system delay between the application of an input pulse from the pulse generator to the output of a pulse from the timing system. Table 2.3 gives the measured system delays of four channels, in relation to different input signal slew rates. Fig. 2.22 shows a plot of the system delays versus input signal slew rate to one preamplifier. Fig. 2.23 shows oscilloscope traces of the system delay for one channel.

From Table 2.2, the worst case thermocouple output is that of 760 torr Helium in shock tube at 2.18 km/second, giving an output of about 8 microvolt/microsecond per thermocouple. Thus even with this case, using a 5-element thermocouple transducer, the system delay one expects to be no worse than 3 microseconds. At normal operating conditions, say 20 torr air in shock tube at 4.3 km/second, the system delay will be around 2 microseconds. Table 2.4 gives the estimated system delays under various shock tube conditions. With the same input to all the preamplifiers, the maximum variation in system delay will be no more than $\pm$0.2 microsecond mainly due to the preamplifiers. The accuracy of the timings will depend only on the variation in thermocouple sensitivities and preamplifier trigger levels. The former is estimated to be (worst case) $\pm$10%, generating about another $\pm$0.3 microsecond variation. The combined timing accuracy will thus be better than $\pm$0.5 microsecond.

2.4.3 Comparison with Thin-Film Gauge on T1

The set-up is the same as shown in Fig. 2.2. One difficulty with interpreting the signal from the thin-film gauges is to determine when the shock front actually arrives. Frequently they tend to pick up charges produced by precursors. Fig. 2.24 shows a good example. One can observe at the beginning a period (about 4 microseconds) when the polarity reverses. There are two possibilities.

1. The thin-film gauge is cooled by the arrival of the shock front, which is very unlikely.
2. The thin-film gauge picks up charges, either due to ionisation behind the shock front, or to precursor effects.

Some shots have been taken before under the same condition in T1(but with test gas N_2 instead of air), which monitors the charge picked up by an ionisation gauge. It shows that the ionisation lasts well over 50 microseconds.

Under the above condition, 50 torr air in the shock tube, shock speed 3.1 km/second, driver gas compression ratio 20, one expects a test time of about 70 microseconds, using the formula $\frac{T}{L} = \frac{1}{U} \frac{1}{\rho_{21} - 1}$

where

T = test time, L = distance from diaphragm,

U = shock speed, ρ_{21} = density ratio across shock.

The formula is based on Lacey. Another estimate comes from heat transfer measurements done in Chapter 4. A shot under similar condition (shock speed 2.4 km/second, 760 torr air, driver gas compression ratio 20) gives the test time of about 100 microseconds, as shown in Fig. 2.25.

Thus one concludes that the effect is due to precursors. However one also frequently comes across cases in which positive ions are picked up instead of electrons, as in Fig. 2.26. The evidence supporting this comes from another ionisation gauge trace, shown in Fig. 2.27a and Fig. 2.27b, done under 100 torr N_2 with about the same shock speed. The top trace in Fig. 2.27b is the pulse output of a trigger unit set to trigger on a negative slope, with its input signal from the ionisation gauge. It is seen from Fig. 2.27a that preceding the arrival of the shock front (as evidenced by the violent swing), there is a period of about 5 microseconds when a positive charge is being picked up. Fig. 2.27b shows clearly the response of the thin-film gauge. It picks up the precursor signal before the main heat transfer signal rise due to arrival of the shock front, at which time the output of the ionisation gauge also goes negative, the normal polarity.

For a discussion of precursor effects, see Kamimoto et al, Gaydon et al (p 210), Bradley (p 156, 243), and McClenahan, particularly Gaydon (p210) which also mentions presence of similar effect on thin-film gauges in low temperature shocks (3000° K).

The thermocouples suffer less from this effect because of the common mode signal rejection ability of the preamplifier.

Table 2.5 summarises the measured system delays with thermocouple transducer compared to the signal from thin-film gauges for those cases with well defined shock fronts. Note that the transducer used is a 5-element thermocouple (5 chromel-alumel thermocouples joined in series). The conclusion drawn is that the measured and estimated delay agree roughly and one can expect a delay of no more than 3 microseconds. Under normal operating conditions, the system delay will be around 1.5 microseconds. Even when the precursor signal is included, the maximum delay measured is less than 5.5 microseconds.

2.4.4 Comparison with Ionisation Gauges on T3

This series of tests is also aimed at observing the performance of the whole timing system as it is being operated over a long period of time. This period of service showed up some inadequacies in the various sections of the system and modifications have been or will be incorporated into the system.

This test is based on the assumption that if a timing transducer is operating normally, i.e., near its maximum sensitivity region, then the recorded shock speed timings will

reflect only normal shot to shot variations due to the shock tube itself. However, when the transducer is operating outside its effective region, another component will become prominent, namely, the variations due to the uncertainties in the trigger level of whatever electronics is used to process the signal coming out of that transducer. Fig. 2.28 illustrates this assumption. Suppose the signal from a transducer varies by a certain percentage due to variation in shock tube conditions. The variations in shock timing will be t_1 and t_2 respectively. It is obvious that $t_2 > t_1$, depending on the particular region. This component will be noticeable when its effect is comparable to that due to variation in shock tube operating conditions. This assumption is valid for transducers such as thermocouples and ionisation gauges which have ramp-like signal outputs rather than step-like, in the time that one is interested in, say a few micro-seconds.

A series of tests is done in which all the transducers used are ionisation gauges to provide a reference. Another series of tests is done in which the first three transducers used are thermocouples but the last two are ionisation gauges. The transducers are numbered consecutively, starting from the diaphragm end, each separated by 91.5 cm. Using the variations of the timings from the last two transducers in both cases (both being ionisation gauges) to

normalise respectively the variations of the timings from the first three transducers (one case being thermocouples, the other ionisation gauges), one can obtain a comparison between the fluctuations of the timings in both series. Choosing a condition in which the performance of ionisation gauges has been proven, one can deduce the performance of the thermocouples if the fluctuations are similar in both series.

Table 2.6 shows the results of such tests. The last column normalises the standard deviation so that one can compare the result from series A and B, to eliminate the difference in shot-to-shot variations of the shock tube between the two series. The samples taken for the reference series are 4 in the case of air, and 3 in CO_2. The samples taken for the test series are 25 in the case of air and 16 in the case of CO_2. Although the samples taken for the reference series are not large enough for accurate predictions, one can at least safely conclude from Table 2.6 that the variation in the test series is comparable to that of the reference series.

Two more B series of air shots are available, 2" Hg and 6" Hg initial test gas pressure, with 9 and 29 samples respectively. They yield the normalised standard deviations of 1.6, 1.2, 1 and 1.7, 1.4, 1 which are also similar to the 4" Hg cases.

Thus one concludes that provided the ionisation gauges are accurate in themselves, the thermocouples provide a similar if not better performance in air and carbon dioxide shots. No comparisons have been made in other gases such as helium because it is well outside the normal operating regions of the ionisation gauges.

2.5 CONCLUSIONS

After the initial trial period of operation of the timing system, it was observed that the failure modes fall into 3 categories:

1. pretriggering by interference pick-up before shock tube is fired;
2. displays picking up interferences after recording the shock timings, resetting the most significient digit, causing an erroneous reading;
3. thermocouples failing catastrophically.

Categories 1 and 2 have been solved and modifications incorporated into the system. As to category 3, only 3 such failures have been observed during at least three hundred shots. Two failed because of a damaged junction and one developed an electrical leakage to the shock tube wall. As a routine practice, it is recommended that a set of thermocouples be replaced when any of them exhibits total resistance of more than 2 ohms for a 5-element thermocouple transducer.

The following improvements are suggested as a follow up:

1. Improvement of the response time of the thermocouple preamplifiers by redesigning the circuit. The response time can be cut to half of the present value without major work involved.

2. Thermocouple construction techniques should be improved to obtain better and more uniform junction characteristics, such as described by Zanstra and Vipond.

3. Preamplifiers for other sensors such as pressure transducers, ionisation gauges and photodiodes should be developed to cater for special conditions.

4. Some of the printed circuit boards should be redesigned to accommodate modifications properly.

CHAPTER 3: CALIBRATION OF CONTOURED NOZZLE

3.1 INTRODUCTION

It is desirable to obtain a nozzle flow that is as free from divergence as possible. One can then increase the size of the model in the test section without incurring unacceptable errors due to flow divergence. A contoured nozzle, consisting of an initial conical expansion section, followed by a contoured section in which the gas flow is processed so that the streamlines become parallel, was designed by Daffey. The principles behind the design will be described briefly in here.

3.2 CONTOURED NOZZLE DESIGN

If one makes the expansion section of a contoured nozzle conical, one can simplify the design of the following contoured section by assuming the gas thus expanded to behave as a perfect gas. The reason is that above a certain area ratio, the chemical composition of a test gas will freeze. If one assumes irrotationality of the flow, then this will enable one to reduce the equations of the non-equilibrium method of characteristics (Sedney et al) to one of a perfect gas method of characteristics system, considerably simplifying the problem.

A conical section with a given length and cone angle is first chosen. At an area ratio A_o, less than that of the cone exit, a value of the ratio of specific heats of the test gas, γ , is chosen which will describe the quasi-one-dimensional chemically frozen flow downstream of this point. The flow can be described quasi-one-dimensionally provided that the expansion angle is not too large. γ cannot be calculated by assuming a diatomic and monatomic gas mixture, because of the presence of chemical relaxations. Instead, it is chosen so that it will enable correct predictions of nozzle exit Mach number, by comparing it with calculations based on a quasi-one-dimensional computer program, Nenzf (for Non-Equilibrium Nozzle Flow)(Lordi et al).

Once the conical portion of the nozzle is chosen, a characteristic is then drawn, in small steps, from the wall at the conical section exit to the axis of the nozzle, intersecting it at, say, point P. The Mach number at this point P is selected as the design exit number M_F of the nozzle. Using a perfect gas method-of-characteristics design method (Shields), a wall contour is constructed which results in parallel flow of constant Mach number downstream of the characteristic from P. A trial and error selection of cone angle and length is necessary to achieve a desired exit Mach number or area ratio.

The present contoured nozzle design is based on a 0.5" throat diameter, an exit diameter of 10.5", and a stagnation enthalpy of 36 MJ/kg, with air as test gas, for use on the shock tunnel T3, operating in the reflected mode. Fig. 3.1 shows the contoured nozzle.

This part of the project is to determine how well the contoured nozzle constructed by the above method performs in actual tests on T3, under both in-design and off-design stagnation enthalpy conditions. The tests done were density and pitot pressure measurements of the flow from the nozzle. The tests were mainly done with air as test gas, though some preliminary result was obtained with carbon dioxide. No serious attempts have been made to correlate the various theoretical aspects of nozzle flow

processes with experimental measurements, as it is beyond the scope of this thesis. However, a simple check is made using the program Nenzf.

3.3 FREE-STREAM DENSITY MEASUREMENTS

3.3.1 Introduction

This part of the test is designed to measure the free-stream densities, using interferometry. The set-up is shown in Fig. 3.2. The model used was a pair of wedges separated by 2", with wedge face angles of 30°, 20°, 20°, and 35° for face 1, 2, 3 and 4 respectively. By moving the wedges vertically, one can obtain the radial density distribution across the flow. It is, however, not possible to obtain any meaningful axial density distribution with this set-up. The principle of free-stream density measurement is illustrated in Fig. 3.3. See also Liepmann and Roshko, Alpher and White.

The wedge angles are small so that the shock on them is straight. In the analysis of the data, only two of the wedge faces, faces 2 and 3, are used, because the fringes of face 1 and 4 show a slight tilting after the shock, making determination of fringe shift subject to a larger error than otherwise. The two 20° wedge-faces would still provide the information required.

No boundary-layer correction (Stalker, et al 73) is applied to the measurement of shock angles on the wedges because one is interested only in determining the uniformity

of the test core. Since the effect of the boundary-layer will be similar on the two wedge faces, this error will be small in the present case.

To obtain the value of the Gladstone-Dale constant for the gas mixture, the various free-stream species concentrations of the mixture as calculated by the program Nenzf are used. This will correct for the slight change of the Gladstone-Dale constant with gas composition. The Gladstone-Dale constants of the various species at standard condition are obtained from Wright, Liepmann & Roshko (pp 38, 39), Wettlaufer and Alpher & White.

Fig. 3.4 is a photograph of an interferogram taken in this test. The absolute values of the density measurements involved have an estimated accuracy of $\pm$12%.

3.3.2 Time History of Free-Stream Density Variation

This test is to determine the period for which one has a relatively constant density test core. This is achieved by taking interferograms at various times while the gas flows over the model, by varying the delay time between the arrival of the shock front at the last timing station on the shock tube to the time the light source is activated. Ideally one should use a light source with a

short duration to freeze the density change occurring. However at the time of test, this was not available. Instead an exploding wire was used as light source, with an effective duration of about 50 microseconds, which is acceptable in this circumstance.

As the free-stream density measured will be affected by changes in shock tube variations from shot to shot, one needs to correlate the densities with these changes to eliminate this effect, so that measurements of a series of shots at the same condition can be combined and compared.

To choose a normalisation parameter, it must satisfy the criterion that after its application, the scatter of the combined data from several shots should be comparable to the scatter present in each individual shot. Based on this, the normalised density is found to be

$$\rho_{\infty_N} = \frac{\rho_\infty P_o}{U_s} \quad - (3.1)$$

where

ρ_∞ is the unnormalised free-stream density

P_o is the stagnation pressure

U_s is the shock speed

Fig. 3.11 shows the effect of the normalisation process.

Fig. 3.5 and 3.6 show the result of the case of air shots with 6" Hg initial pressure, compression ratio of 60, shock speed of 4.35$\pm$0.08 km/sec and stagnation enthalpy

of about 18 MJ/KGM. It can be seen that one has a period of about 200 microseconds in which the density remains constant to within ±10%.

Fig. 3.7 shows the result of the case of air shots with 4" Hg initial pressure, compression ratio of 30, shock speed of 4.39±0.09 km/sec and stagnation enthalpy of about 20 MJ/KGM. One can see that because of the lowering of the compression ratio, the period of constant density increases to at least 250 microseconds.

As air is the test gas of interest here, only a brief test is taken of carbon dioxide. Fig. 3.8 shows the result for 4" Hg CO_2 initial pressure, compression ratio of 30 and stagnation enthalpy of 7 MJ/KGM. This test was carried out to obtain information for work outside this project but included in here to observe the performance of the contoured nozzle with CO_2. It is obvious that a more detailed survey is required before any valid conclusion can be reached.

3.3.3 Radial Free-Stream Density Distributions

Since the model consists of two wedges separated by 2", by moving the model vertically, it is possible to obtain a limited vertical scan of the test core. Fig. 3.9 and Fig. 3.10 present the radial density distribution of

the test core. It shows that one has a test core with density constant to within ±5% and with diameter of at least 5 inches. This is for the case of 6" Hg initial pressure in shock tube for air.

3.4 PITOT PRESSURE MEASUREMENTS

3.4.1 Introduction

The pitot pressure survey is done in two parts, a radial pitot pressure survey and an axial pitot pressure survey. In the radial pitot pressure survey, a rake carrying four Kistler type 6031 pressure transducers, separated by distances of 2", 2" and 3" vertically, are used. In the longitudinal pitot pressure survey, only a single Kistler type 6031 pressure transducer carried on a probe is used. The Kistler gauges are mounted inside a small cavity and protected from the hot gas by a small heat exchanger (Stalker, et al, 1973). This arrangement introduces some delay in response time but is not of significance in the present case.

In normal practice, the pitot pressure measurements are normalised to that of the reservoir pressure for that particular shot to compensate for shot to shot variations. However, it is found that for this series of experiments, this normalisation introduces larger error into the pitot pressure measurements than exhibited by the unnormalised data. The probable reason for this is that the stagnation pressure records (used as the reservoir pressure) reflect changes that affect the pitot pressures as well as changes that do not. If the latter dominates, then the advantage

of normalising the pitot pressures to the stagnation pressures will be lost.

This observation is reached after studying pitot pressure measurements taken in repeat shots, i.e. shots under the same condition, but repeated because of one reason or another, such as loss of some of the pitot pressure traces because of equipment malfunction. Under these circumstances, the stagnation pressures and the pitot pressures are compared between the repeat shots, to enable one to see if the pitot pressure changes follow the stagnation pressure changes. The pitot pressure trace is chosen from one that is clear of any boundary layer influences. To provide a valid comparison, the pitot pressures and the stagnation pressures are read at the same time for the two repeat shots (800 microseconds from start of trace for the pitot pressures and 400 microseconds from start of trace for the stagnation pressures). Table 3.1 summarises the results that cover both air and CO_2 shots. The method is to calculate the change in each quantity between the two repeat shots and expresses it as a percentage. It is seen from Table 3.1 that the pitot pressure changes do not follow the stagnation pressure changes nor the shock speed changes, and is, in general, smaller compared to stagnation pressure fluctuations but larger compared to shock speed fluctuations. Hence, in subsequent analysis, the pitot pressure is not normalised to the measured stagnation pressures.

The error estimated for the pitot pressure measurements is ±10%. Fig. 3.19 shows some of the pitot traces.

Table 3.2 gives the sensitivities of the Kistler pressure transducers used for pitot pressure measurements and stagnation pressure measurements.

3.4.2 Radial Pitot Pressure Survey

Fig. 3.12 shows the radial pitot pressure profile for air shots, at 2" inside nozzle exit plane, Fig. 3.13 at nozzle exit plane, Fig. 3.14 at 2" outside nozzle exit plane, and Fig. 3.15 at 4" outside nozzle exit plane. Note that the distance from nozzle exit plane is measured before shock tube recoil, which is about $1\frac{3}{8}$ inches. Only a detailed survey was done in the case of Fig. 3.12, the rest was taken as confirmation tests only. From these surveys one can draw the conclusion that there is a uniform test core (to within ±15%) of at least 6" diameter. This increases to at least 8" in diameter for the lower enthalpy cases. One can also see the decreasing boundary layer thickness (witnessed by the increase of pitot pressures at the points near to the nozzle wall) as the stagnation enthalpy decreases. This series of surveys covers stagnation enthalpies below, at and above the designed enthalpies.

A brief survey is also carried out with carbon dioxide as test gas, and is presented in Fig. 3.16. The performance is similar to the series with air as test gas. The boundary layer thickness, however, is less than that for air, probably due to the smaller viscoscity of carbon dioxide compared to air and the lower stagnation enthalpies.

It is seen that Fig. 3.12 shows a larger scatter of data than the others, due to the fact that data from more than one shot has been combined to produce it.

3.4.3 Axial Pitot Survey

Fig. 3.17 plots the pitot pressure axial survey with probe at a position of ½" below axis for air, with 4" Hg initial pressure and compression ratio of 30. It is clear that one has a uniform region (within ±6%) extending from 10" inside the nozzle exit to 10" outside the nozzle exit.

Fig. 3.18 plots a similar survey for CO_2, at 4" Hg initial pressure and compression ratio of 30. Again the result is similar, although in this case, one has a uniform region (within ±9%) extending from 17" inside the nozzle exit to 10" outside the nozzle exit.

3.4.4 Conclusions

From the results presented in the previous sections, it is seen that the contoured nozzle performs according to expectation, giving a uniform test core radially to within ±1.5% within a diameter of 6" and ±6% longitudinally, within ±10 inches from nozzle exit for air.

Although the program Nenzf is quasi-one-dimensional, it will be interesting to see how they agree with each other. Table 3.3 below tabulates the 3 cases: below design, at design and above design stagnation enthalpies for air. The calculated pitot pressure is approximated by $\rho_\infty U_\infty^2$.

It is seen that the experimental values and Nenzf values agree, within experimental errors.

It is felt that the accuracies in the measurements of pitot pressures should be improved. It is in the author's opinion that the heat exchanger used in preventing the pressure transducers from being affected by the hot gas flow is contributing a significant error. The heat exchanger used in this series of experiments was simply a thin layer of vacuum grease on the transducers' inlet face. Very often, excessive application of the grease causes a severe drop of signal output. It is clear that the effect of this type of heat exchanger will be too uncertain to predict.

Further investigations should be carried out on the stagnation pressure records for two reasons: (1) the upper and lower stagnation pressures do not, as a rule, agree with each other (with differences of $\pm 8\%$); (2) the pitot pressure changes do not follow stagnation pressure changes, with the latter having a larger fluctuation.

CHAPTER 4 DEVELOPMENT OF CALORIMETER HEAT-TRANSFER GAUGES

4.1 INTRODUCTION

The most common device for measuring heat transfer rates in shock tube laboratories has been thin film heat transfer gauges (Schultz et al, Hartunian et al). To describe it in simple terms, it is a device where a thin metallic film, a few hundred Angstrom thick, is deposited on a suitable insulating substrate. A constant current is passed through the gauge to monitor its electrical resistance. When exposed to a gas flow, heat is transferred to the substrate, changing its surface temperature. Since the film is very thin, it follows the surface temperature of the substrate, causing a change in its electrical resistance. However, this type of heat transfer gauge is not suitable for use in situations where there is a high heat transfer rate. This is because of the very high temperature rise of the substrate (about $70^{o}C$ rise per kW/cm^2 of heat transferred for 100 microseconds), leading to a highly non-linear behaviour of the gauge. This may be corrected by various means (Walenta, Cook, Willeke et al), but will make this type of gauge much less simple to use. However, the most serious drawback is its inability to withstand the environment of a shock tunnel for long. A typical gauge will last a few

shots in moderately high enthalpy conditions, necessitating frequent replacement and re-calibration. It was frequently found that the resistance of a gauge changed noticeably after one shot, indicating damage to the thin film.

To overcome these drawbacks, calorimeter gauges were developed by Rose. In contrast to thin film gauges, a thick metallic foil is used to retain essentially all of the heat transferred within itself during the test time considered. This means that the foil thickness has to be chosen with regard to the characteristic heat diffusion depth in that material. The overall temperature rise of the foil will be much smaller than in the case of the thin film gauge, reducing the problem of non-linearity of the thin-film and substrate considerably. The thick metal foil (usually in the sub-millimetre ranges, depending on material, test time, heat transfer rate and heat loss to substrate tolerated) will clearly stand a much better chance of survival in the shock tube environment than the thin-film gauge. Another advantage of calorimeter gauges is that properties of the gauge materials can be taken as their bulk values (which are tabulated in standard handbooks) to good accuracies (within $\pm$5% for pure materials), obviating the necessity of calibrating each new gauge, as is the case for thin-film gauges. The main drawback is that the sensitivity of calorimeter gauges is much lower, which may be a disadvantage when low heat transfer rates are being measured. However,

since the calorimeter gauges are primarily intended for high heat transfer rate measurements, this is not usually a severe problem.

There are several varieties of calorimeter gauges, depending on the method of monitoring the temperature change. Thermocouples, either on the surface or behind the calorimeter, can be used. Alternatively, the total resistance of the calorimeter can be monitored, and is the best scheme because it has the highest frequency response (Schultz et al). This project is based on calorimeters of this type.

4.2 THEORY OF OPERATION OF HEAT TRANSFER GAUGES

Schultz et al showed that both thin film gauges and calorimeter gauges can be analysed in terms of one-dimensional heat conduction. A brief summary of their treatment will be presented here for the sake of completeness.

Fig. 4.1 shows a slab of material (that of the gauge) mounted on a semi-infinite material (that of the substrate). The equations governing the flow of heat in the two media are

$$\frac{\partial^2 T_1}{\partial x^2} = \frac{1}{\alpha_1} \frac{\partial T_1}{\partial t} \tag{4.1}$$

$$\frac{\partial^2 T_2}{\partial x^2} = \frac{1}{\alpha_2} \frac{\partial T_2}{\partial t} \tag{4.2}$$

Where the subscript 1 refers to the slab, and
the subscript 2 refers to substrate,
T refers to temperature, above ambient
x refers to distance from the surface,
t refers to time,
α refers to thermal diffusivity, given by

$$\alpha = \frac{K}{\rho c} \tag{4.3}$$

where K = thermal conductivity,
ρ = density,
c = specific heat.

If the surface heat transfer rate is $\dot{q}_s(t)$, then, from definition,

$$-K_1 \frac{\partial T_1}{\partial x} = \dot{q}_s \quad \text{at } x = o \tag{4.4}$$

and, at the interface $x = \ell$,

$$K_1 \frac{\partial T_1}{\partial x} = K_2 \frac{\partial T_2}{\partial x}, \quad T_1 = T_2 \tag{4.5}$$

$$\text{also} \qquad T_2 = 0 \text{ at } x = \infty . \tag{4.6}$$

By taking the Laplace Transforms of Eq. 4.1 and 4.2, and incorporating the boundary conditions Eqs 4.4 to 4.6, one obtains

$$\bar{\bar{T}}_1 = \frac{\bar{\bar{q}}_s \sqrt{\alpha_1} \left[(1+a) e^{-(x-\ell)\sqrt{\frac{p}{\alpha_1}}} + (1-a) e^{(x-\ell)\sqrt{\frac{p}{\alpha_1}}} \right]}{K_1 \sqrt{p} \left[(1+a) e^{\ell \sqrt{\frac{p}{\alpha_1}}} - (1-a) e^{-\ell \sqrt{\frac{p}{\alpha_1}}} \right]} \tag{4.7}$$

$$\bar{\bar{T}}_2 = \frac{2 \bar{\bar{q}}_s \sqrt{\alpha_1} \, e^{(\ell-x)\sqrt{\frac{p}{\alpha_2}}}}{K_1 \sqrt{p} \left[(1+a) e^{\ell \sqrt{\frac{p}{\alpha_1}}} - (1-a) e^{-\ell \sqrt{\frac{p}{\alpha_1}}} \right]} \tag{4.8}$$

where $$a = \sqrt{\frac{\rho_2 c_2 k_2}{\rho_1 c_1 k_1}} \tag{4.9}$$

and $$\frac{\partial \bar{\bar{T}}}{\partial t} = p \bar{\bar{T}} \tag{4.10}$$

Eqs. 4.7 to 4.10 will be used to analyse thin-film gauges (Section 4.6.2) and to derive design equations for calorimeter gauges.

4.3 THEORY OF OPERATION OF CALORIMETER GAUGES

Basically, a calorimeter gauge functions by measuring the time rate of change of the thermal energy of a metallic foil laid on an insulating substrate. The change of thermal energy can be detected by monitoring the temperature of the foil. The rate of change of this temperature will give the heat flux into the surface of the foil.

Referring to Fig. 4.1, one can write the heat balance of the metal slab as

$$\dot{q}_s = \dot{q}(o, t) = \dot{q}(\ell, t) + \frac{d}{dt}\left[\rho c \ell\, \bar{T}(t)\right] \qquad (4.11)$$

where

$\dot{q}_s$ = heat transfer rate to the surface

$\dot{q}(x, t)$ = heat transfer rate at point x from surface at time t

ρ, c = density and specific heat of the metal slab

$\bar{T}(t)$ = mean slab temperature

By choosing the slab thickness such that, in the test time concerned, most of the heat entering the foil will remain there, i.e., $\dot{q}(\ell,t)$ is negligible or is a small but estimable quantity, one can simplify Eq. 4.11 into

$$\dot{q}_s = \frac{d}{dt}\left[\rho c \ell\, \bar{T}(t)\right] \qquad (4.12)$$

To choose the proper gauge thickness, it is necessary to estimate the likely heat loss to the substrate for a given foil thickness. Based on Eq. 4.7 to 4.10, and assuming a constant surface heat transfer rate, Schultz et al estimated the heat loss to the substrate as

$$\frac{\dot{q}(l,t)}{\dot{q}(o,t)} = \frac{2}{\sqrt{\pi}} \; a\left[\frac{\alpha_1 t}{\ell^2} - 0.167\right]^{\frac{1}{2}} - a^2\left[\frac{\alpha_1 t}{\ell^2} - 0.167\right] \qquad (4.13)$$

where

$$a = \sqrt{\frac{\rho_2 c_2 k_2}{\rho_1 c_1 k_1}} \qquad (4.9)$$

α is the thermal diffusivity, as given in Eq. 4.3. Eq. 4.13 will thus enable one to choose a gauge thickness with an upper limit to the likely heat loss. Note that Eq. 4.13 yields an upper limit only, because the presence of even a very thin layer of air between the foil and the substrate will lower this error very considerably (a one-micron thick layer of air would reduce the heat loss by several orders of magnitude).

Having the thickness ℓ of the foil, one needs to obtain $\bar{T}(t)$ to complete Eq. 4.12. The values of ρ and C will be known from tables or from calibrations. $\bar{T}(t)$ can be most conveniently measured by monitoring the resistance change of the metal foil when its temperature changes.

Consider a foil divided into a number of thin layers, of thickness Δx, so that one can assign a temperature to each of these layers. These layers will thus represent resistances in parallel. Referring to Fig. 4.2, the equivalent resistance of the foil will be, when subjected to a heat transfer,

$$R = R_o \left\{ 1 + \alpha_R \overline{T} - \alpha_R^2 \left[(\overline{T^2}) - (\overline{T})^2 + \ldots \right] \right\} \qquad (4.14)$$

where

R_o = resistance of foil at temp 0^oC

α_R = temperature coefficient of resistance of foil

$\overline{T}$ = mean temperature of foil

In Eq. 4.14, the second and higher order terms represent the non-linear temperature distribution which peak in the first few microseconds, after which they become negligible (less than 1%). Hence one can rewrite Eq. 4.14 to retain only the first order term:

$$R = R_o \ (1 + \alpha_R \overline{T}) \qquad (4.15)$$

The resistance of the foil is monitored by passing a constant current I through it, so that

$$IR = IR_o \ (1 + \alpha_R \overline{T}) \qquad (4.16)$$

The change in voltage across the foil, V_{out} is thus

$$V_{out} = V_o \alpha_R \bar{T} \tag{4.17}$$

Differentiating Eq. 4.17 yields

$$\frac{dV_{out}}{dt} = V_o \alpha_R \frac{d\bar{T}}{dt} \tag{4.18}$$

or re-arranging,

$$\frac{d\bar{T}}{dt} = \frac{1}{V_o \alpha_R} \frac{dV_{out}}{dt} \tag{4.19}$$

Eq. 4.12 can be rewritten as

$$\dot{q} = \rho c \ell \frac{d\bar{T}}{dt} \tag{4.20}$$

provided ρ, c and ℓ are constant (which is a reasonable assumption, provided the gauge temperature is not raised too high).

Combining Eqs. 4.19 and 4.20, one thus arrives at

$$\dot{q}_s = \frac{\rho c \ell}{V_o \alpha_R} \frac{dV_{out}}{dt} \tag{4.21}$$

Equation 4.21 forms the basis of operation of a calorimeter gauge. Note that V_o is referred to the 0^o C condition. It may be more convenient to refer it to another temperature, T_E, say V_E, by using the relation

$$V_E = V_o(1 + \alpha_R T_E) \tag{4.22}$$

thus Eq. 4.21 becomes

$$\dot{q}_s = \frac{\rho c \ell}{\alpha_R} \cdot \frac{1 + \alpha_R T_E}{V_E} \cdot \frac{dV_{out}}{dt} \qquad (4.23)$$

and Eq. 4.18 becomes

$$\frac{dV_{out}}{dt} = \frac{V_o \alpha_R}{1+\alpha_R T_E} \cdot \frac{d\bar{T}}{dt} \qquad (4.24)$$

T_E being the equilibrium temperature reached by the gauge with a particular constant current flowing through it.

4.4 DESIGN CONSIDERATIONS OF CALORIMETER GAUGES

4.4.1 Selection of Foil Material and Thickness

A desirable property of a calorimeter gauge is maximum sensitivity, in order to have a high signal-to-noise ratio. To choose the best foil material, the following are assumed: substrate material, heat loss to substrate, test time, dimensions, heat transfer rate and current, for the contending candidates. The procedure is to choose the thickness ℓ bearing in mind the maximum allowable heat loss to substrate over the test time. Then the rate of rise of temperature of the foil is calculated from Eq. 4.20 by assuming a certain heat transfer rate. By assuming a certain dimension for the gauge, one can calculate V_o (since ρ_R for the metals are known from handbook values). Equation 4.24 can then be used to estimate the output one can expect. Table 4.1 summarises the estimated sensitivities of the more common metals. It is seen that stainless steel (AISI 430), lead and iron have the best sensitivities. Lead may be used in low heat transfer situations when its low melting point is acceptable, but it is ruled out in cases of high heat transfer rates. Although stainless steel has a higher sensitivity than iron, it has the drawback that this sensitivity comes from its high resistivity, 5 times higher than iron, while its temperature coefficient of resistance is only 0.2 times that of iron. The lower the resistivity, the lower

the self-heating effect for a given current passed through the gauge, the less non-linearities in the physical properties of the metal due to the self-heating temperature rise. This meant that iron will be a much better material to use than stainless steel from this point of view. One possible problem with the use of iron foil is oxidation of the surface, resulting in changed gauge characteristics. This, however, does not seem to be a problem in actual use. Iron in high purity form also offers the advantage over stainless steel in that its physical properties are known more accurately, not being dependent on the wide tolerances of compositions of stainless steel.

It is necessary to restrict the calorimeter gauge temperature rise when subjected to a heat transfer rate so that its resistance change is not more than 25%, in order to reduce non-linearities in the gauge properties (Rose). This can be done by choosing the correct gauge thickness.

4.4.2 Selection of Substrate Materials

The desirable property of a substrate is that it should not interfere with the workings of the metallic foil by conducting heat away from the back of the foil. It should have a reasonable mechanical strength to withstand impact force generated in the test flow. It should be easy to machine, be readily available, and at low cost.

To choose a suitable substrate, Eq. 4.13 can be used to estimate the maximum heat loss to the substrate:

$$\frac{\dot{q}\ \text{substrate}}{\dot{q}\ \text{surface}} = \frac{2a}{\sqrt{\pi}}\left[\frac{\alpha_1 t}{\ell^2} - 0.167\right]^{\frac{1}{2}} - a^2\left[\frac{\alpha_1 t}{\ell^2} - 0.167\right] \quad (4.13)$$

where

$$a = \sqrt{\frac{\alpha_2 c_2 k_2}{\alpha_1 c_1 k_1}} \quad (4.9)$$

Since $a \ll 1$, and $\left[\frac{\alpha_1 t}{\ell^2} - 0.167\right] < 1$, for the situation under consideration, the term $\frac{2a}{\sqrt{\pi}}\left[\frac{\alpha_1 t}{\ell^2} - 0.167\right]^{\frac{1}{2}}$ will dominate, and thus to a good approximation, one can assume that the smaller the value of a, or the smaller the thermal product $\sqrt{\alpha_2 c_2 k_2}$, the lower the heat loss to the substrate. Table 4.2 tabulates the thermal products of the various materials.

It is clear from Table 4.2 that plastics have a better performance than glass, and are easier to work with. Araldite and such epoxy type polymers have the advantage that they can be cast , thus obviating the need for accurate machining to obtain a contour fit for the metal foil laid on top. For low heat transfer situations, araldite can be used, while for high heat transfer situations, silicones can be used.

Fig. 4.3 plots the estimated heat loss to an epoxy substrate for the various materials, based on Eq. 4.13.

4.5 CONSTANT CURRENT SUPPLY FOR CALORIMETER GAUGES

4.5.1 Introduction

A constant current supply source for the calorimeter gauge is necessary to ensure its proper operation. The basic requirements for the constant current supply are:

1. it should be capable of supplying an adjustable constant current up to 10 amperes;

2. it should be capable of supplying up to six calorimeter gauges simultaneously;

3. its equivalent output impedance should be much higher than the gauge impedance. Rose recommended a ratio of 10^3, in order to swamp any effect of gauge resistance change on the current.

Condition 2 is necessary because it is required in Section 5 of this project for the measurement of local heat transfer rates at several locations on a model. It is preferable to obtain all the data in as few shots as possible, so as to minimise the effect of shot-to-shot variations on the measurements. Connecting the gauges in series is not permitted because failure of a single gauge will corrupt the signals from all the other gauges. It will also lead to undesirable interactions between the gauges.

Condition 1 is necessary to enable the optimum current level to be chosen, bearing in mind the effect of self-heating of the gauge and the acceptable signal-to-noise ratio. The expected signal output is a few millivolts with a current of 10 amperes, depending on the heat transfer rates.

Rose recommended the circuit shown in Fig. 4.4. With a typical gauge resistance of about 10 mΩ, the value of R needs to be 10Ω. At maximum current of 10A, one needs a 100 V supply capable of supplying 1 KW per gauge, most of which is wasted in the resistors R. Operation with the gauges in series will compound the problem. The problem may be alleviated to some extent by relaxing the requirement of $R > 1000\ R_o$. The circuit is very inefficient and will be expensive to implement if multiple gauges are to be used. Another drawback from the safety point of view is the use of high voltages in such set-up because the gauges are not insulated at the front surfaces.

A solution is proposed here that overcomes all of the problems associated with the circuit used by Rose. It uses a low voltage supply (6 V), thus reducing waste of power drastically. The constant current regulation is better than in the circuit of Rose. The current level can be adjusted from milliamperes to 10 amperes by a single dial. The gauges are isolated from each other from the signal point of view, eliminating interactions.

The basic principle of the constant current supply is illustrated in Fig. 4.5. The voltage amplifier has gain typically in the region of 80 to 100 dB, enabling one to make the assumption of $V_+ = V_-$. Another assumption is that $I = I_E$, which is justified when the current amplifier has a high current gain. Under this condition, $V_{control} = V_+ = V_- = I \cdot R_{ref}$,

$$\therefore \quad I = \frac{V_{control}}{R_{ref}} \tag{4.25}$$

Thus current can be controlled directly by varying $V_{control}$ if one keeps R_{ref} constant. Clearly, the regulation of the current level will depend on how well regulated $V_{control}$ and how constant R_{ref} are. In practice, they can be made reasonably constant by using a well-regulated voltage reference for $V_{control}$ and using a resistor having very low temperature coefficient of resistance and operated so that the temperature rise is small, by using manganin wires bolted to large heat sinks. The equivalent output impedance of this circuit is approximately the open-loop voltage gain of the amplifier times R_{ref}, which is very much larger than the expected gauge resistance.

4.5.2 Design of Constant Current Supply Generator

4.5.2.1 Introduction

The constant current supply generator is built to be simple to operate and flexible. Fig. 4.6 gives its main functions. The generator is assembled from four separate modules: Module 1 - houses the constant current generator control circuitries, meter monitoring circuitries and the thermal shut down circuitries. Module 2 - houses the power supplies for the whole generator, the power supply for the meter circuitries, the current amplifiers and the cooling fans. Module 3 - houses the two 6 V 75 A-h lead-acid batteries for the constant current supplies. Module 4 - for calibration and testing of the generator. It consists of various connectors and terminals.

All the modules are housed in a 19" rack. Fig. 4.7 is a photograph of the complete generator.

4.5.2.2 Operating Instructions of Constant Current Generator

Before powering up the system, the mode switch (SW7) of the control unit is switched to 'stand-by', the meter selector switch (SW10) to 'off', and the channel status switches (SW1 to SW6) to 'disabled'. The gauges are then connected either

to the calibration module or directly, via the power cable to the supply module (module #2) and the signal cable to the control unit (module #1). The system is then powered up by switching on the mains switch (SW13) on the supply module. The desired output current is then dialled on the current output potentiometer (VR19). SW10 is set to 'current' position, the meter range switch (SW11) set to the appropriate range, and the meter channel select switch (SW9) set to say channel #1, and the channel status switch SW1 'enabled'. SW7 is then set to 'operate' mode, switching on the cooling fans automatically, and outputting a constant current which is read on the meter. VR19 is adjusted until the desired output current is indicated on the meter. At output current above 1 A, the dial on VR17 sets the current accurate to within $\pm$ 1%. For output current below 1 A, the dial is only accurate to within $\pm$ 2% or worse. If the system has been calibrated correctly, this current setting should also hold for other channels, to within $\pm$ 1%.

The voltage developed across the gauges can be checked by switching SW10 to the voltage position. The meter range is designed so that for the typical gauges used, the current and voltage share the same range.

The meter zero (VR25) and meter full-scale-deflection (VR26) adjustment potentiometers normally do not need attention except at system calibration, as covered in 4.5.2.7.

The thermal overload light-emitting diode is normally off except when the temperature inside module 2 reaches about 38° C. It then flashes at about 2 Hz, indicating that the system is locked out and no output current is available until the temperature drops below about 34° C.

The external voltmeter terminals allow connection of an external voltmeter to the input of the meter amplifier, for calibration purpose. Refer to 4.5.2.7.

The switch (SW 12) that is unmarked on the photograph (between SW 9 and SW 10) is a momentary contact switch. Pressing it will allow checking of the voltage of the 6-V lead-acid batteries. This functions even when the system is off.

4.5.2.3 Constant Current Generator Control Circuitry

This is responsible for converting the control voltage $V_{control}$ of Fig. 4.5 into a constant current I. Fig. 4.8 shows the circuit of the control circuitries.

SW 7 selects the mode of the system, either 'stand-by' or 'operate'. In the 'stand-by' mode, everything except the driver of the constant current generators is activated. A trickle charge (200 ma) is passed to the lead-acid batteries while in 'stand-by' mode. When SW 7 is switched to 'operate'

mode, + 15V is applied to R19 and VR19. VR19 is a 10 turn potentiometer on the front panel which sets the output current of all the six channels of the generator. The control voltage for each channel thus derived is then fed to the assembly R1, VR1 and SW1 for channel 1; R2, VR2 and SW2 for channel 2, etc. VR1 to VR6 allow one to compensate for the different tolerances of the component values within each channel, so that the same output current can be set by VR19. SW1 to SW6 are used to disable their respective channels in situations when only some of the channels are being used. They are mounted on the front panel, labelled channel status selectors.

The control voltage from VR1 is fed to the non-inverting input of IC1, which is an operational amplifier acting as a high gain voltage amplifier, then to the current amplifier consisting of TR1, TR7, TR13, TR19 and TR25, via R7 and D1. A signal, proportional to the output current, is developed across R13, and fed back to the inverting input of IC1. To explain briefly, any increase in current will cause an increase of voltage at pin-4 of IC1. Since voltage at pin-5 is fixed, the output (pin-10) will decrease, causing a decrease in drive to the current amplifier until the voltage at the inverting-input is again equal to that at the non-inverting input (within a few microvolts).

VR13 is to adjust the input offset voltage of IC1 to prevent it from outputting current even when SW1 is set at disabled position. R7 is to limit the drive current to the current amplifier, and D1 to prevent it from being reverse-biased, thus causing breakdown of the base-emitter junctions of the transistors. C1 (a low-leakage capacitor) is to provide local negative feedback to prevent oscillations due to the high frequency response of TR1. TR1 and TR7 are connected as a super-Darlington pair in order to obtain enough drive for TR13, TR19 and TR25. This could be simplified by using a transistor with the necessary gain and power dissipation to replace TR1 and TR7. However, component availability leads to the present configuration. TR13, TR19 and TR25 are paralleled in order to lower the dissipation of each individual transistor for two reasons: (1) to increase the safety margin and, (2) to enable a higher voltage than 6 V to be used to accommodate a higher load resistances for some applications. All the transistors in the current amplifiers are selected devices with low leakage currents, especially the drivers TR7 to TR12. The calorimeter gauge is connected across the collectors of the current amplifier transistors and the 6 V batteries, via the fuse F1.

The supply source for the current amplifier consists of two 6 V lead acid batteries connected in parallel. This arrangement has the advantage of a zero ripple source, in addition to eliminating a very expensive high current, well

regulated supply derived from the mains. The batteries are normally trickle charged by the system but can be boost charged externally. SW8 switches in the external charger. Note that D7 also functions to protect the internal + 15 V supply should the external charger voltage be higher than + 15 V.

SW7, when in 'operate' mode, also switches on the cooling fans via R17 and RL3. The centre wiper of VR19 also goes to RL2 of the thermal overload shutdown sensor which disables all the channels when the current amplifiers' temperature is excessive.

The voltages across the calorimeter gauges are monitored via SW9. The output currents are also monitored by the voltage drops across R13 and VR7 for channel 1, R14 and VR8 for channel 2, etc. VR7 is for compensating the component tolerances of the different channels to enable a single calibration of the meter amplifier. R13 consists of two 1 cm lengths of 0.315 mm diameter manganin wires connected in parallel and bolted at each end to a large heat sink. The temperature rise at maximum current output is estimated to be no more than 10^{o} C. Since the temperature coefficient of resistance of manganin is 10^{-5}, the error contributed by this reference will be negligible.

C7 to C10 are for supply de-coupling.

4.5.2.4 Meter Amplifier

It is necessary to monitor the resistance of the gauge to calculate the heat transfer rate from Eq. 4.23. In order to reduce the overall experimental error, this measurement of resistance should be as accurate as possible, say around 2%. This necessitates either the use of an accurate Kelvin bridge or a digital resistance meter. The use of a Kelvin bridge is impractical in the present set-up. As to the choice of a digital resistance meter capable of reading milliohms, its cost cannot be justified. The design described in here is the most cost effective for the present application. It measures the voltage drop across and also the current through the gauge, thus enabling one to calculate its resistance. Fig. 4.9 gives its circuit. The accuracy of the circuit is limited primarily by the readout device, the basic amplifier has a linearity of better than $\pm$ 0.3%. Table 4.3 tabulates the linearity of the circuit. It is seen that the non-linearity comes from the meter movement, around $\pm$ 1%, if range switching is utilised to obtain best accuracy.

SW9 switches the two sets (voltage and current) of inputs from the six channels and feed them to SW10 to enable either voltage across the selected gauge or current through the gauge to be measured. The selected input is fed to the range division resistors network comprising R21 to R28 and VR20 to VR24. Although 1% resistors are used for R21 to R26,

it is found that it is still necessary to provide a small degree of trimming to equalise the sensitivities of the ranges.

The meter ranges are from 0.1A/1mV to 50A/500mV to cover all possible situations for use with calorimeter gauges. The selected input is also available on the front panel for calibrating the meter circuitry.

R29 and R30 provide bias current returns for IC7 to ground. Since for the lower voltage ranges, it is necessary to measure microvolts riding on a common-mode voltage of 6 V, the common-mode rejection ability of the amplifier has to approach 80 db in order to eliminate significant errors. This places a stringent demand on the meter amplifier circuitry. To effect this, the following steps are taken:

1. use of an amplifier having a high common-mode rejection ability such as LM321 (National Semi-conductors) having a guaranteed value of 110 db;

2. separation of the meter amplifier ground with the system ground to further increase the rejection;

3. close-matching of R29 and R30 to better than 1%.

The integrated circuit chosen for IC7 (LM321) is a precision preamplifier designed as front ends to industry

standard operational amplifiers, offering considerable improvements in bias current, offset voltage drift, common-mode and power supply rejection. Its bias current can be programmed and in the present design, minimised to reduce error due to this source. Its output is amplified by IC8, converting the differential outputs to single ended output. R34 and R35 provide increased supply rejection. C12 and C13 are for attenuating the high frequency response of the amplifier to decrease noise, as essentially only a D.C. amplifier is needed. The output of IC8 is clamped by D8, D9 to protect the readout meter movement. R36, D10 and RL1 are to protect the meter movement from large and opposite excursions produced by the amplifier on switch off of power. It functions by releasing the contacts when power is removed, thus isolating the meter movement. VR26 provides gain adjustment of the amplifier. SW12 and R37 enable the meter movement to function as a battery voltage indicator.

The calibration of the whole system is covered in 4.5.2.7.

The readout device used is a moving coil meter with nominal 100 microampere full-scale deflection. If higher accuracy is desired, a digital panel meter should be substituted.

4.5.2.5 Thermal Overload Shutdown Sensor

At maximum output, the current amplifiers will be dissipating in excess of four hundred watts total. The

temperature rise of the power transistors of the current amplifiers is kept low by the two cooling fans. However, in the event of failure of the fans or some other malfunctions that cause the temperature rise to be excessive, it is necessary to shut down the system until the temperature drops to a safe level. Fig. 4.10 gives its circuit.

The temperature sensing is done by a thermistor located in the vicinity of the current amplifiers. Rising temperature will lower its resistance, causing the voltage at pin-4 to be lower than the voltage at pin-5. IC9 is connected as a comparator and the output will thus swing towards the positive supply rail. This switches on TR31 via R43 and D11, feeding power to IC10, a LM555 oscillator connected in the astable mode, and with its output driving an LED to act as a visual warning of over-temperature. Its flashing rate is about 2 per second. IC9 also switches TR32 on, energising RL2, removing any drive to the constant current control circuitries, thus effectively shutting down the current amplifiers. D13 is to remove inductive spikes generated by the switching off of the actuating coil of RL2 from damaging TR32.

RL2 is not released until the temperature drops to a safe level.

R40 and R41 are to provide hysteresis in the temperature switching point. VR27 provides a small adjustment range

of the tripping point. The circuit is adjusted to trip when temperature reaches 38.5° C and to release when temperature drops back to 34.5° C.

4.5.2.6 Power Supplies

Two isolated sets of power supplies are required. One set, providing +15 V and -15 V, is to power the meter circuitry. The other set, also providing +15 V and -15 V, is to power the rest of the system. The common point of the supply for the meter amplifier circuitry must not be grounded to the system. Fig. 4.11 gives its circuit.

The mains supply is fed to T1 and T2 via fuse F7 and switch SW13 and indicated by neon light NE1. BR1 rectifies the secondary of T1 and the output is filtered by C27 and C28 before going to the 3-terminal voltage regulator IC11 to provide the +15 V supply. Similarly, BR2, C30, C31, IC12 and C32 provide the -15 V supply.

The secondary of T2 is rectified by BR3, and filtered by C35 and C36 before going to a dual-supply voltage regulator IC13. C37 to C40 provide further filtering to decrease the output impedance. The functions of D15 to D18 are to prevent damage to the voltage regulators should the input power be interrupted, causing them to be reverse-biased.

SW14 enables the cooling fans to be switched on when the system is in stand-by mode. C26 is to suppress the switching transients of fans 1 and 2 from affecting the sensitive meter amplifier circuitry. NE2 indicates when the power to the fans is applied. RL3 is to switch on the fans automatically when system is in operate mode, via SW7.

4.5.2.7 Calibration of Constant Current Supply Generator

The following calibrations are needed before the system will function properly.

1. Set SW7 to 'stand-by', VR19 dial to 0.0, SW1 to SW6 to 'disabled', SW10 to 'off', SW11 to highest range, then power up the system via SW13.

2. Let the system warm up for half an hour, then set SW11 to the 1 mV range and adjust VR25 (meter zero) to zero the meter.

3. Connect a precision voltage reference, adjustable from 1 mV to 500 mV to the HI-LO terminals on the front panel of module # 1. This voltage reference can be built as follows:

For the 1 mV and 10 mV ranges, 3 precision resistors (0.1%) are connected in series, the centre one being 1 ohm and the two outer ones 500 ohms. A well regulated

adjustable voltage supply (up to 15 volt maximum) is then connected across the string of resistors. The output is taken across the 1 ohm resistor. Thus one obtains 1 mV output per volt input. The input voltage is monitored by a 3½ digits digital multimeter.

For the 50 mV and 100 mV ranges, the 1 ohm resistor is substituted by a 10 ohm resistor, with the conversion factor of 100 mV output per 10.1 volt input. For the range 500 mV, the voltage supply is connected directly to the HI-LO terminal. With this set-up, the meter amplifier will be calibrated to within $\pm$ 0.3%.

With SW11 in the 1 mV range, and a 1 mV input at the HI-LO terminals, VR26 is adjusted until the meter movement reads full-scale. Then SW11 is switched to the 5 mV range and a 5 mV input applied, and VR20 adjusted until the meter movement reads full-scale. Similarly all the other ranges are calibrated.

4. Next the offset voltages of IC1 to IC6 are adjusted. With SW1 in the disabled position, connect a voltmeter across pin-10 of IC1 and ground, and adjust VR13 until pin-10 just swings to the negative supply rail. Repeat this for the other channels. This adjustment is necessary to ensure that the offset voltage will not cause a small current to be output even when the channel is disabled.

5. Connect the power cable between module # 2 and module # 4 and the signal cable between module # 1 and module # 4. Connect an accurate ammeter that can read 5 amperes (better than 1%) across the channel 1 current output terminals. Set VR19 (current output dial on front panel of module # 1) to 5.00, SW9 to channel 1, SW10 to 'current' position, SW11 to 5A range, VR1 and VR7 to minimum position. SW1 is set to 'enabled' position and SW7 to 'operate'. VR1 is adjusted until 5 amperes flow across the external ammeter. VR7 is then adjusted until the meter movement reads full-scale.

Reset SW7 to 'stand-by', SW1 to 'disabled', and connect the external ammeter to channel 2 output terminals (on module # 4). Switch SW9 to channel 2,'enable' SW2 and switch SW7 to 'operate'. Adjust VR2 until the external ammeter reads 5 amperes. Then adjust VR8 until the meter movement reads full-scale.

This procedure is repeated for all the other channels.

6. Connect a voltmeter across VR27 and adjust VR27 so that the voltmeter reads 0.95 V. With the type of thermistor used, this will trip the thermal shutdown sensor when the temperature reaches 38.5^{o} C and will release when temperature drops below 34.5^{o} C.

Once the above calibrations have been performed, there is no need to touch any of the preset controls except during a major system check.

4.6 COMPARISON OF CALORIMETER GAUGES WITH THIN-FILM GAUGES ON T1

4.6.1 Introduction

It is felt that the calorimeter gauges should be compared with another type of heat transfer gauge under identical conditions to gain confidence in their use. The results from these two types of gauges should confirm each other. Thin-film gauge is chosen because its operation is well understood and documented and it is available. The two types of gauges are used to measure the heat transfer rate to the side wall of the shock tube T1, side-by-side. The thin-film gauge is platinum on pyrex.

4.6.2 Operating Principle of Thin-Film Gauges

From Eq. 4.8, putting $\ell = 0$ and $x = 0$ gives the substrate surface temperature:

$$\bar{\bar{T}}_s = \frac{1}{\sqrt{\rho ck}} \frac{\bar{\bar{\dot{q}}}_s}{\sqrt{P}} \tag{4.26}$$

after inverting the transform and then integrating, Eq. 4.26 becomes

$$\dot{q}_s = \sqrt{\frac{\rho ck}{\pi}} \left[\frac{T(t)}{\sqrt{t}} + \int_o^t \frac{T(t) - T(\tau)}{(t - \tau)^{3/2}} \, d\tau \right] \tag{4.27}$$

However, if $\dot{q}_s$ is constant, Eq. 4.27 simplifies to

$$T_s = \frac{2\dot{q}_s}{\sqrt{\pi}} \sqrt{\frac{t}{\rho ck}} \tag{4.28}$$

i.e., the surface temperature is parabolic in time.

The surface temperature is monitored by the resistance of a thin metallic film of a few hundred Angstrom thickness, deposited on the substrate surface.

There are a few observations about the use of thin-film gauges.

1. The presence of a thin-film on the substrate will introduce errors to its surface temperature (Schultz, Vidal, Maulard). The thin-film gauge used in the present test was manufactured by painting techniques with estimated thickness of 0.5 micron, so that approximately 100 microseconds is required before the accuracy in the deduced heat transfer rate reaches 5% (Schultz). This implies that comparisons should preferably be taken after that period to be accurate.

2. The substrate should be thick enough for the previous analysis to be valid. Schultz gave an approximate rule of thumb of $0.3\sqrt{t}$ sec, around 0.1 mm for a run time of 1 millisecond. Actually the thickness is determined largely by mechanical strength consideration in the actual

operating environment. In the present case the substrate is a rod 1 cm long, thus no error need be considered from this source.

3. The substrate properties will change as temperature rises, leading to a variation of the thermal product $\sqrt{\rho ck}$. If substrate temperature rises above 150° C, heat transfer measurements will be in error of about 10%. Corrections can be applied either numerically (Cook, Hartunian et al) or by use of electronic circuits to compensate for the variable properties (Walenta), or by use of substrates with small variations of the thermal product, such as beryllia. The error correction as proposed by the various workers contain quite large discrepancies. In the present test, the temperature rise is kept low to minimise this error.

4.6.3 Analogue Circuit For Thin-Film Gauge

In general, the heat transfer rate under the situation to be considered will not assume the simplified form as given by Eq. 4.28 because the heat transfer rate is not constant. Eq. 4.27 has thus to be evaluated using numerical techniques (Cook et al, Maulard, Vidal). However it is more convenient to display the result side-by-side on a photograph with that from the calorimeter gauges, using an analogue circuit to convert the temperature signal from the gauge to heat transfer rates.

The analogue circuit simulates the flow of heat into the semi-infinite substrate using an R-C transmission line. It consists of blocks of R-C lumped together, the lump size depends on the rise time desired and the number of blocks depends on the run duration. The principle of operation and design criteria are covered in Meyer and Schultz et al, and will not be presented here except the analogue circuit equation

$$\dot{q}_s = \sqrt{\rho ck}\sqrt{\frac{r'}{c'}}\ \frac{1}{\alpha_R V_o}\ \frac{V_{out}}{R_1} \qquad (4.29)$$

where

r' and c' are the resistance and capacitance per unit length of the R-C transmission line.

Fig. 4.12a shows such an electrical analogue.

To obtain the value of $\sqrt{\frac{r'}{c'}}$, a gain measurement with frequency is done on the circuit so that

$$\frac{V_{out}}{V_{in}} = \frac{R_1 I_{in}}{V_{in}} = R_1\sqrt{\frac{c'}{r'}}\sqrt{\omega} = R_1\sqrt{\frac{c'}{r'}}\ \sqrt{2\pi f} \qquad (4.30)$$

where

ω is in radians/sec, f is in Hz.

Fig. 4.12b shows an analogue circuit proposed by Meyer having arithmetically increasing lumps in order to reduce the number of stages. Fig. 4.13 is the circuit of the actual

analogue circuit constructed for this project, designed with a run time of 400 microseconds and an RC value of 5 microseconds.

The input from the gauge is coupled to a x 20 non-inverting amplifier IC1 via C10 and R10, before going to the analogue networks. The output voltage is developed across R1 and buffered by the unity gain follower IC2.

A frequency sweep is made of the circuit gain to observe experimentally the run time of the analogue circuit and also to obtain the value of $\sqrt{\frac{r'}{c'}}$. Fig. 4.14 plots the gain versus frequency. It is seen that the operating range covers the region from 50 Hz to 100 KHz. Taking the gain at 10 KHz, Eq. 4.29 for this analogue becomes

$$\dot{q}_s = 40.1 \sqrt{\rho ck} \cdot \frac{V_{out}}{V_o \alpha_R} \tag{4.31}$$

$$\text{or} \quad \dot{q}_s = 40.1 \sqrt{\rho ck} \; \frac{V_{out}}{V_E \alpha_R} (1+\alpha_R T_E) \tag{4.32}$$

if the reference temperature is chosen as the equilibrium temperature T_E of gauge at the operating current, with V_E developed across gauge.

4.6.4 Differentiator For Calorimeter Gauge Signal

Eq. 4.23 of Section 4.3 gives the heat transfer rate as

$$\dot{q}_s = \frac{\rho c \ell}{\alpha_R} \cdot \frac{1 + \alpha_R T_E}{V_E} \cdot \frac{dV_{out}}{dt} \qquad (4.23)$$

Hence by differentiating electrically the temperature signal, one can obtain a direct indication of the heat transfer rate. A simple R-C differentiator is used. The output from a R-C differentiator is $V_{output} = RC \frac{dV_{input}}{dt}$ (4.33)

($RC \ll$ period of input signal).

Combining Eqs. 4.23 and 4.33 yields

$$\dot{q}_s = \frac{\rho c \ell}{V_E \alpha_R} \cdot (1 + \alpha_R T_E) \frac{V_{out}}{RC} \qquad (4.34)$$

where

V_{out} is now the output from the differentiator.

Fig. 4.15 shows the responses of two differentiators to a ramp signal (constant $\frac{dV}{dt}$), for calibrating the time constants of the differentiators. Two time constants are used, with 19.8 ± 0.2 microseconds and 1.91 ± 0.03 microseconds.

4.6.5 Comparison on Tl

The set-up is shown in Fig. 4.16. A thin-film gauge (platinum on pyrex) was compared side-by-side with a calorimeter gauge, measuring the heat transfer rate to the side wall of a shock tube. Fig. 4.17 shows a heat transfer record. The thin-film gauge was driven by the constant current supply shown in Fig. 2.3.

In order to minimise any possibility of non-linear behaviours of the thin-film gauge, the heat transfer rate was chosen to be as low as possible, consistent with a tolerable signal-to-noise ratio. An iron calorimeter gauge was used, with thickness of 0.0075 cm, on an epoxy substrate, with an estimated maximum heat loss to substrate of 5% at 400 microseconds test time.

Fig. 4.18 plots on the same graph the heat transfer rates as obtained from the calorimeter gauge and the thin-film gauge. It is seen that the agreement between the two gauges is, in general, within experimental tolerances, estimated to be about 12% (worst case) for both gauges.

To obtain comparison under large heat-loss-to-substrate condition, a platinum calorimeter gauge was constructed. Its thickness was 0.0020 cm, on an epoxy substrate, and

the maximum heat loss to substrate was estimated at 20% at 400 microseconds test time. Fig. 4.19 plots the comparison. It is seen that the agreement at the early period of the test time is within experimental errors, but at later time, the calorimeter gauge heat transfer rate drops below that of the thin-film gauge. That is to be expected. As the test time increases, the platinum foil is not thick enough to retain all of the heat transferred to it, causing a drop in gauge temperature as heat is transferred to the substrate. However the conclusion is qualitative only, as the estimated heat loss is an upper bound only.

Comparisons were done also at high heat transfer rates. Fig. 4.20a compares an iron calorimeter gauge with a thin-film gauge, and Fig. 4.20b compares a stainless steel calorimeter gauge with the thin-film gauge. The iron calorimeter gauge was the same one used previously, while the stainless steel gauge has a thickness of 0.0125 cm, on an epoxy substrate with an estimated maximum heat loss of less than 1% at 400 microseconds test time. Here the heat transfer rates as deduced from both calorimeter gauges are about 1.5 to 1.9 times larger than those deduced from the thin-film gauge. The explanation lies in the high heat transfer rate. Under this circumstance , the thin-film gauge substrate surface temperature rises to a maximum of more than 300^{o} C, while that of the calorimeter gauge temperature rises to less than 50^{o} C. One expects a considerable change in substrate

properties at 300° C, in addition to change in the electrical properties of the thin-film. In fact, the thermal product $\sqrt{pck}$ increases 1.8 times at 300° C compared to that at 40° C (extrapolated from Table 6 of Schultz et al). Thus it demonstrates the superiority of calorimeter gauges at high heat transfer rates.

4.7 CONCLUSIONS

The theory of operation of calorimeter gauges and thin-film gauges was reviewed and the procedure for choosing the best foil and substrate materials was outlined. For this shock tube laboratory, an iron foil on an araldite substrate was chosen as the best combination.

A constant current supply for calorimeter gauges was constructed and performed as expected. It is simple to operate, much more efficient than the arrangement suggested by Rose, and offers a better performance. Its measured output impedance for each channel is about 20 ohms, and with a typical calorimeter gauge resistance of less than 10 milliohms, the current regulation is better than 0.1 %. In the construction of the supply, a single point ground and shielding of appropriate signal and power lines were found necessary to ensure the correct functioning of the meter amplifier circuit. It is suggested that to get more accurate gauge resistance calibrations, a 3½ digits digital panel meter be substituted for the analog meter movement installed.

Comparison of calorimeter gauges with thin-film gauges was carried out. Under circumstances of low heat transfer rates (less than 1 kW/CM^2), both types of gauges yield the same result, within experimental errors. Under high heat transfer situations, calorimeter gauges are superior to thin-film gauges.

CHAPTER 5: HEAT TRANSFER MEASUREMENTS ON A MODEL IN T3

5.1 INTRODUCTION

In order to observe the performance of calorimeter gauges under actual operating conditions in a shock tunnel, six calorimeter gauges, with iron foils on epoxy substrates, were mounted on a steel cylinder.

The measurements were performed in two parts. The first part dealt with the stagnation point heat transfer under various shock tunnel conditions, and the second part dealt with the heat transfer profile on the cylinder at a particular tunnel condition.

5.2 THEORY OF HYPERSONIC HEAT TRANSFER

The theoretical calculations of heat transfer rates in hypersonic dissociating gas flows have been covered by numerous authors (Fay, Fay & Riddell, Fay & Kemp, Hayes & Probstein 1959, Dorrance, Dewey & Gross, Scala and others). Their treatment will not be repeated here in detail. It is intended to provide here a summary of the theory, for comparison with experimental results.

The boundary layer equations for the flow are :

1. Continuity

$$\rho u \frac{\partial m_i}{\partial x} + \rho v \frac{\partial m_i}{\partial y} = \frac{\partial}{\partial y} \left(\rho D_{12} \frac{\partial m_i}{\partial y} \right) + W_i \qquad (5.1)$$

2. Momentum

$$\rho u \frac{\partial u}{\partial x} + \rho v \frac{\partial u}{\partial y} = - \frac{\partial p}{\partial x} + \frac{\partial}{\partial y} \left(\mu \frac{\partial u}{\partial y} \right) \qquad (5.2)$$

3. State

$$p = \rho \sum m_i R_i T \qquad (5.3)$$

4. Energy

$$\rho u \frac{\partial H}{\partial x} + \rho v \frac{\partial H}{\partial y} = \frac{\partial}{\partial y} \left(\frac{\mu}{Pr} \frac{\partial H}{\partial y} \right) + \frac{\partial}{\partial y} \left[\mu \left(1 - \frac{1}{Pr} \right) \frac{\partial}{\partial y} \left(\frac{u^2}{2} \right) \right]$$

$$+ \frac{\partial}{\partial y} \left[\rho D_{12} \left(1 - \frac{1}{L} \right) \sum \left(h_i - h_i^0 \right) \frac{\partial m_i}{\partial y} \right] \qquad (5.4)$$

The following assumptions have been made for the above equations :

1. the boundary layer is very thin compared to the body radius of curvature, and is laminar;
2. the body is either two dimensional or axisymmetric;
3. the gas in the boundary layer is regarded as a binary mixture of atoms of one species and molecules of another species;
4. thermal and pressure diffusions are neglected;
5. each component of the fluid behaves as a perfect gas in contributing to the total pressure,

and p = pressure

u, v = velocity components in the x and y directions, where x is along the body surface, y is normal to the body surface

m_i = mass fraction of the i-th component of the gas mixture

W_i = mass rate of formation of the i-th species

D_{12} = binary diffusion coefficient

ρ = density

μ = viscoscity

R_i = gas constant for the i-th component

T = temperature

H = total enthalpy

h_i = enthalpy of the i-th component

h_i^o = heat of formation of the i-th component

Pr = Prandtl number = $\frac{C_p \mu}{k}$

C_p = mean specific heat of mixture at constant pressure

k = thermal conductivity of mixture

L = Lewis number = $\frac{\rho D_{12} C_p}{k}$

The equations 5.1 to 5.4 are partial differential equations which cannot be solved for blunt-body flows unless they can be reduced to ordinary differential equations, i.e., if similar solutions can be found for them. For stagnation points, such similar solutions exist.

Define $$X(x) = \int_o \rho_w \mu_w u_e r_b^{2j} \, dx \tag{5.5}$$

$$E(x,y) = \frac{u_e r_b^{\,j}}{\sqrt{2X}} \int_o \rho \, dy \tag{5.6}$$

$$f = \int_o \frac{u}{u_e} \, dE \tag{5.7}$$

$$\frac{\partial f}{\partial E} = \frac{u}{u_e} \tag{5.8}$$

$$g = \frac{H}{H_e} \tag{5.9}$$

$$z_i = \frac{m_i}{m_{ie}} \tag{5.10}$$

where r_b = cylindrical radius of body

j = 0 for two dimensional flow

1 for axisymmetric flow

subscript e refers to edge of boundary layer

w refers to body surface (wall)

Using equations 5.5 to 5.10, together with the fact that near a stagnation point of an inviscid flow all fluid properties except velocity are approximately constant, the momentum and energy equations are transformed to

$$(Nf'')' + ff'' + (1+j)^{-1}(\frac{\rho_e}{\rho} - f'^2) = 0 \qquad (5.11)$$

$$\text{and } (\frac{N}{Pr} g')' + fg' + \left[N(L-1)Pr^{-1} \sum (h_i - h_i^o) \frac{dm_i}{dh} g' \right]' = 0 \qquad (5.12)$$

$$\text{where } N = \frac{\rho\mu}{\rho_w \mu_w}$$

and the primes denote differentiation with respect to E.

Together with the heat conduction equation at the wall,

$$\dot{q}_s(0) = -(\frac{k}{c_p} \frac{\partial h}{\partial y})_w \qquad (5.13)$$

the numerical solution of these equations yields various correlation formulae for stagnation point heat transfers. Two of the correlation formulae are:

1. Fay & Riddell Formula :

$$\dot{q}_s(0) = -0.763\ Pr^{-0.6} (\rho_e \mu_e)_s^{0.5} (\frac{du_e}{dx})_s^{0.5} (\frac{\rho_w \mu_w}{\rho_e \mu_e})_s^{0.1} (H_e - h_w)_s$$
$$\left[1 + (L^t - 1) h_a^o (\alpha_e - \alpha_w)_s \right] \qquad (5.14)$$

where $t = 0.63$ and 0.52 for a frozen and equilibrium boundary layer respectively,

α = dissociation fraction,

$\left(\frac{du_e}{ds} \right)_s$ = velocity gradient at stagnation point

$$= \frac{1}{R}\left[\sqrt{\frac{2P_e}{\rho_e}}\right]_s \quad , \qquad (5.15)$$

eq. 5.15 assumes a Newtonian pressure distribution,

R = blunt body nose radius,

Pr = 0.67 and L = 1.4 for dissociated air,

and subscript s refers to stagnation region.

2. Scala Formula:

Scala arrived at a correlation formula based on the enthalpy difference across the boundary layer, the stagnation pressure and the ambient molecular weight of the free stream gas,

$$\dot{q}_s(0) = \frac{1.61 + 0.116\,\bar{M}_\infty}{\sqrt{R}} \sqrt{\rho_\infty} U_\infty^3 \quad w/cm^2 \qquad (5.16)$$

where $\bar{M}_\infty$ = molecular weight of mixture,

R = nose radius of body in cm,

ρ_∞ = free-stream density in gm/cm^3,

U_∞ = free-stream velocity in cm/sec.

Equation 5.14 requires an inviscid flow calculation to determine the stagnation temperature (for viscoscity calculations), density, pressure and dissociation fractions. Equation 5.16 requires only $\bar{M}_\infty$, ρ_∞ and U_∞ which are readily available from the program Nenzf (Lordi et al). Note that in equation 5.16, the stagnation pressure is approximated by $\rho_\infty U_\infty^2$, which is accurate enough for the present application. Another disadvantage of equation 5.14 is that it is based on dissociated air, making its use on other gases such as carbon dioxide uncertain. Equation 5.16 applies also to the calculations with other gases. Hence it is used in the present calculation.

In regions away from the stagnation point, the heat transfer can be approximated by applying the concept of local similarity. This concept patches together local solution in which the history of the flow is involved only in the X dependence of the definition of E in equation 5.6. This is justified on the ground that the external and body flow properties vary only slowly with X. Using this concept, the heat transfer rate at any point (with angle θ to the axis) on a cylinder is

$$\frac{\dot{q}_s(\theta)}{\dot{q}_s(0)} = \frac{\rho_w \mu_w u_e}{\sqrt{2X\rho_{w_s}\mu_{w_s}\left(\frac{du_e}{dx}\right)_s}} \qquad (5.17)$$

Making the approximations:

$$\rho_w \mu_w = \rho_{w_s} \mu_{w_s} \cos^2\theta \qquad (5.18)$$

$$u_e = x \left(\frac{du_e}{dx} \right)_s \qquad (5.19)$$

equation 5.17 becomes

$$\frac{\dot{q}_s(\theta)}{\dot{q}_s(0)} = \frac{\sqrt{2}\,\theta \cos^2\theta}{\sqrt{\theta^2 + \theta \sin 2\theta + \frac{1}{2}\cos 2\theta - \frac{1}{2}}} \qquad (5.20)$$

where θ is in radians.

5.3 MEASUREMENT OF HEAT TRANSFER RATES

A steel cylinder of diameter 3" and length 6" is chosen as the model. The cylinder is assembled from two parts, with one part (2" long) fixed and the other part (4" long) that can be rotated with respect to the fixed part. Six calorimeter gauges are installed on the model, two on the stagnation region of the fixed part and four on the rotatable part, as shown in fig 5.1. The two gauges on the fixed part serve as references to monitor the shot to shot variations so that results from a series of shots can be compared more accurately.

The foil material is iron, and the thickness used in this series of experiment is 0.075 mm. The substrate is araldite. The estimated maximum heat loss to substrate is 7 % in a run time of one millisecond. Thicker foil material was not available during the experiment. The calorimeter gauges are mounted so that they are flush with the surface of the model. The gauges are supplied by the constant current generator described in chapter 4. During this series of experiments, the gauges increase their resistances by an average of 0.2 % per shot over 50 shots, and none of them needs replacement. Thin film gauges, under similar conditions, need to be replaced every few shots because of the damages to the film. Thus it clearly demonstrates the robust nature of the calorimeter gauges in shock tunnel measurements. Fig. 5.2 shows the experimental set-up.

It is found that the signals from the calorimeter gauges need to be filtered properly to remove noise components due to the ionisation of impurities during the flow, and mechanical resonance of the model. It is also found necessary to clean the model and gauges before each shot to remove deposits from the previous shot. Fig. 5.3 shows clearly the effect of the deposits on the noise level of the signal. It is recommended that for future experiments, attention be paid to eliminating the problem of microphonics in the cables inside the shock tunnel, and to making the model from materials that will not generate mechanical resonances within the bandwidth of the desired heat transfer signal.

In the present series of experiments, the signals from the calorimeter gauges are not generally differentiated because of the noise problems outlined above. Analyses of the experimental results rely on manual measurements of the slope of the signal to give heat transfer rates. Lack of time prevents the proper solution of the noise problem. Fig. 5.4 shows an example of a relatively good heat transfer record. Fig. 5.5 shows a noisy shot in which differentiation of the signal is not useful. Fig. 5.6 shows a record in which the shock tunnel flow is known to be of good quality. The RC differentiators used have time constants of approximately 100 microseconds.

In this series of experiments, the calorimeter gauge signals are filtered before going to the oscilloscopes. Two of

the low-pass filters are Barr & Stroud variable filter unit, type EF2, and the others are 6-th order active filters, with the circuitry shown in fig 5.7. The design of the filters is discussed in Al-Nasser. The filter frequencies are set to 7.5 kHz. The heat transfer rate measurement errors are estimated to be ± 20 %, with a substantial contribution from the dv/dt measurements on the oscilloscope traces.

The calculation of the experimental heat transfer rates is based on equation 4.23, while the theoretical rates for the stagnation points are from equation 5.16, and the radial distribution profile is from equation 5.20.

Fig. 5.8 shows the stagnation point heat transfers under various shock tunnel conditions. One can draw two conclusions. The first conclusion is that the experimental results and the theoretical results agree with each other, within experimental error. The second conclusion is that the longitudinal stagnation heat transfer profile is approximately constant. However, the first gauge returns much higher heat transfer rates than the rest, probably due to a combination of effects due to the contoured nozzle boundary layers and three dimensional flow on the model unaccounted for by the theory. It is not clear though, why the 6-th gauge is not affected similarly.

Fig. 5.7 shows the radial distribution of heat trans-

fer rates on the cylindrical model. Since the data has been accumulated over a number of shots, a simple correction for shot to shot variations is applied to $\dot{q}_s(\theta)/\dot{q}_s(0)$ by monitoring the measured values of gauge 2, which remains on the stagnation point all the time. It is assumed that the shot to shot variations affect all the gauges approximately equally. Some of the values have been omitted from the graph because these signals are grossly distorted by noise. In general, fig. 5.7 shows a fair agreement between experimental data and theoretical calculations, except at large values of θ. The reason is not clear, but is most probably due to the simplified assumptions used in the derivation of equation 5.20.

5.4 CONCLUSIONS

The following is recommended if heat transfer rates are to be measured in a shock tunnel:

1. The cables, both power and signal, should be shielded and should be made of non-microphonic type of materials. This is necessary to avoid charge pick-ups from the ionised gas in the tunnel flow.

2. The mechanical mounting of the model should either be very stiff or very resilient, so that any noise generated by this source falls outside the signal bandwidth and can be filtered.

3. The model and the gauge surfaces are to be cleaned prior to each shot to remove deposits of impurities from the previous shot.

4. The signals should be differentiated to give $\dot{q}_s$ directly, using an active operational amplifier differentiator. This differentiation will decrease the overall error of the measurements.

5. The calorimeter gauges should be stamped from a die to hold their dimensions repeatable and within close tolerances.

The measurements of heat transfer rates obtained in this series of experiments agree within experimental error with the values expected on the basis of existing theories. This provides good confirmation of the enthalpy levels in these nozzle flows, which have previously only been calculated numerically from the measured reservoir conditions. Stagnation heat transfer measurements, if performed with care, can yield good estimation of free-stream velocities according to equation 5.16.

References

Alpher, R.A. and White, D.R., "Optical Refractivity of High-Temperature Gases" Part I - Effects Resulting from Dissociation of Diatomic Gases. Physics of Fluids, March 1959, Vol. 2, No. 2, pp. 153-161.

Benedict, R.P. and Ashby, H.F., "Improved Reference Tables for Thermocouples", Temperature; Its Measurement and Control in Science and Industry, Reinhold, 1962, pp. 56-64.

Bradley, J.N., Shock Waves in Chemistry and Physics, Methuen, 1962, pp. 151-163, 243.

Chapman, A.J., Heat Transfer, 3rd Ed., McMillan, 1964, pp. 36-51.

Chung, P.M. and Anderson, A.D., "Heat Transfer Around Blunt Bodies with Non-Equilibrium Boundary Layers", Proceedings of the 1960 Heat Transfer and Fluid Mechanics Institute, Stanford University Press, 1960.

Clark, J.B., New Physical and Mathematical Tables, Oliver & Boyd, 1970, p. 56.

Cook, W.J., "Determination of Heat-Transfer Rates from Transient Surface Temperature Measurements", AIAA, Vol. 8, No. 7, pp. 1366-1368.

Cook, W.J. and Felderman, E.J., "Reduction of Data from Thin-Film Heat Transfer Gauges: A Concise Numerical Technique", AIAA Journal, March 1966, Vol. 4, No. 3, pp. 561-562.

Daffey, M., (Private communication).

Dannenberg, R.E. and Humphry, D.E., "Microsecond Response System for Measuring Shock Arrival by Changes in Stream Electrical Impedance in a Shock Tube", Rev. Sci. Instr., November 1968, Vol. 39, No. 11, pp. 1692-1696.

Dewey, C.F. and Gross, J.F., "Exact Similar Solutions of the Laminar Boundary Layer Equations", Advances in Heat Transfer, Academic Press, 1967, pp. 317-446.

Dobkin, R.C., "Instrumentation Amplifier", National Semiconductor Linear Applications, 1973, Vol. I, LB1-1.

Dorrance, W., Viscous Hypersonic Flow - Theory of Reacting and Hypersonic Boundary Layers, McGraw Hill, 1962.

Fairchild Linear Integrated Circuit Data Book, Fairchild Semiconductors, 1972.

Fay, J.A., "Hypersonic Heat Transfer in the Air Laminar Boundary Layer", High Temperature Aspects of Hypersonic Flow, Pergamon Press, 1962, Ch. 30, pp. 583-604.

Fay, J.A. and Kemp, N.H., "Theory of Stagnation - Point Heat Transfer in a Partially Ionized Diatomic Gas", AIAA Journal, December 1963, Vol. 1, No. 12, pp. 2741-2751.

Fay, J.A. and Riddell, F.R., "Theory of Stagnation Point Heat Transfer in Dissociated Air", J. Aeronautical Sciences, February 1958, pp. 73-85.

Furler, S., "The Use of Thermocouple Heat Transfer Gauges as Shock Timing Devices", Physics Department internal report.

Gaydon, A.G. and Hurle, I.R., The Shock Tube in High-Temperature Chemical Physics, Chapman and Hall, 1963, pp. 108-132, 210.

Hartunian, R.A. and Varwig, R.L., "On Thin-Film Heat-Transfer Measurements in Shock Tubes and Shock Tunnels", Phy. of Fluids, February 1962, Vol. 5, No. 2, pp. 169-174.

Hayes, W.D. and Probstein, R.F., Hypersonic Flow Theory, Vol. I, Inviscid Flows, Academic Press, 1966, p. 462.

Hornung, H.G., "Non-Equilibrium Dissociating Nitrogen Flow over spheres and circular cylinders", J. Fluid Mech., 1972, Vol. 53, Part 1, pp. 149-176.

Kamimoto, G. and Teshima, K., "Study on Precursor Phenomena Ahead of Ionising Shock Waves", Current Paper 31, Department of Aeronautical Engineering, Kyoto University.

Kaye, G.W.C. and Laby, T.H., Tables of Physical and Chemical Constants, 13th Ed., Longmans, p. 187.

Kemp, N.H., Rose, P.H. and Detra, R.W., "Laminar Heat Transfer Around Blunt Bodies in Dissociated Air", J. Aerospace Sciences, July 1959, pp. 421-430.

Knight, H.T. and Duff, R.E., Rev. Sci. Instr., 1955, Vol. 26, p. 257.

Lacey, J.J., "Experimental Shock Tube Test Time - Turbulent Regime", AEDC - TR - 69 - 131, p. 5.

Lane, M.F., "Crystal Oscillator Design Employing Digital Integrated Circuits as the Active Element", Report No. 6949, Telecon Australia Research Laboratories.

Liepmann, H.W. and Roshko, A., Elements of Gas Dynamics, John Wiley & Sons, pp. 38-39, 87.

Lordi, J.A., Mates, R.E. and Moselle, J.R., "Computer Program for the Numerical Solution of Non-Equilibrium Expansions of Reacting Gas Mixtures", NASA-CR-472.

McClenahan, J.O., "Optimal Use of Double Pin Ionisation Gauges for Shock Wave Detection", Rev. Sci. Instr., February 1973, Vol. 44, No. 2, pp. 212-215.

Meir, R.F., "A Heat-Fluxmeter for Use with Thin-Film Surface Thermometers", National Research Council of Canada Aeronautical Report LR 279.

Moeller, C.E., "Thermocouples for the Measurement of Transient Surface Temperatures", Temperature, Its Measurement and Control in Science and Industry, Reinhold, 1962, Vol. 3, pp. 617.

Mulac, A.J. and Guzman, J.A., "Contact shock-wave detector", Rev. Sci. Instr., August 1975, Vol. 46, No. 8, pp. 1117-1118.

National Semiconductor Linear Integrated Circuit Handbook, 1974.

Rose, P.H., "Development of the Calorimeter Heat Transfer Gauge for Use in Shock Tubes", Rev. Sci. Instr., July 1958, Vol. 29, No. 7, pp. 557-564.

Rose P.H., and Stankevics, J.O., "Stagnation Point Heat Transfer Measurements in Partially Ionized Air", AIAA Journal, December 1963, Vol. 1, No. 12, pp. 2752-2763.

Rose, P.H. and Stark, W.I., "Stagnation Point Heat Transfer Measurements in Dissociated Air", J. Aeronautical Sciences, February 1958, pp. 86-97.

Sandeman, R.J. and Allen, G.H., "A Double Diaphragm Shock Tube for the 10 - 20 kilometer per second range", Proceedings of the Eighth International Shock Tube Symposium, 1971.

Scala, S.M., "Hypersonic Heat Transfer", Developments in Heat Transfer, Edward Arnold, 1964, Ch. 17.

Schultz, D.L. and Jones, T.V., "Heat-Transfer Measurements in Short-Durations Hypersonic Facilities", Agardograph 165, 1973.

Sedney, R., South, J.C. and Gerber, N., "Characteristics Calculation of Non-Equilibrium Flows", The High Temperature Aspects of Hypersonic Flows, Pergamon Press, 1962, Ch. 5.

Shields, I., Nozzle Design Using Method of Characteristics, (unpublished).

Stalker, R.J., "Characteristics of the Free Piston Shock Tube", Proceedings of the Fifth International Shock Tube Symposium, April 1965, pp. 339-350.

_____, "Development of a Hypervelocity Wind Tunnel", Aero. Journal, June 1972, Vol. 76, No. 738, pp. 374-384.

_____, "Hypervelocity Aerodynamics Instrumentation", Proceedings of the IREE, April 1974, pp. 90-95.

_____, "Shock Tube Developments at the Australian National University", The Australian Physicist, July 1970, Vol. 7, No. 7, pp. 99-102.

Stalker, R.J. and Hornung, H.G., "The ANU Free Piston Shock Tunnel T3", Physics Department Laboratory Report PF-5.

Stalker, R.J. and McIntosh, M.K., "Hypersonic Nozzle Flow of Air with high initial dissociation levels", J. Fluid Mech., Part 4, 1973, Vol. 58, pp. 749-761.

Touloukian, Y.S., ed., Thermophysical Properties of High Temperature Solid Materials, Vol. 4, Thermophy. Prop. Res. Centre (TRPC), New York, MacMillan, 1967.

Vidal, R.J., "Model Instrumentation Techniques for Heat Transfer and Force Measurements in a Hypersonic Shock Tunnel", C.A.L. Report AD-917-A-1, 1956.

Vipond, R., "Cold Pressure welded copper-constantan thermo-couples", J. Phy. E., Vol. 8, 1975, pp. 262-263.

Walenta, Z.A., "Analogue Networks for High Heat Transfer Rate Measurements", UTIAS Tech., No. 84, 1964.

Wettlaufer, D.E., "An Interferometric Determination of the Specific Refractivities of the Nitrogen and Oxygen Atoms", UTIAS Technical Note No. 175.

Willeke, K. and Bershader, D., "An Improved Thin-Film Gauge for Shock-Tube Thermal Studies", Rev Sci. Instr., January 1973, Vol. 44, No. 1, pp. 22-25.

Wright, J.K., Shock Tubes, Methuen, 1961, p. 41.

Zanstra, P.E., "Welding Uniform Sized Thermocouple Junctions from Thin Wires", J. Phy. E., Vol. 9, 1976, pp. 526-528.

Al-Nasser, F., "Tables Shorten Design Time for Active Filters", Electronics, October 1972, pp. 113-118.

Hayes, W.D., Hypersonic Flow Theory, Academic Press, 1959, Chapter VII.

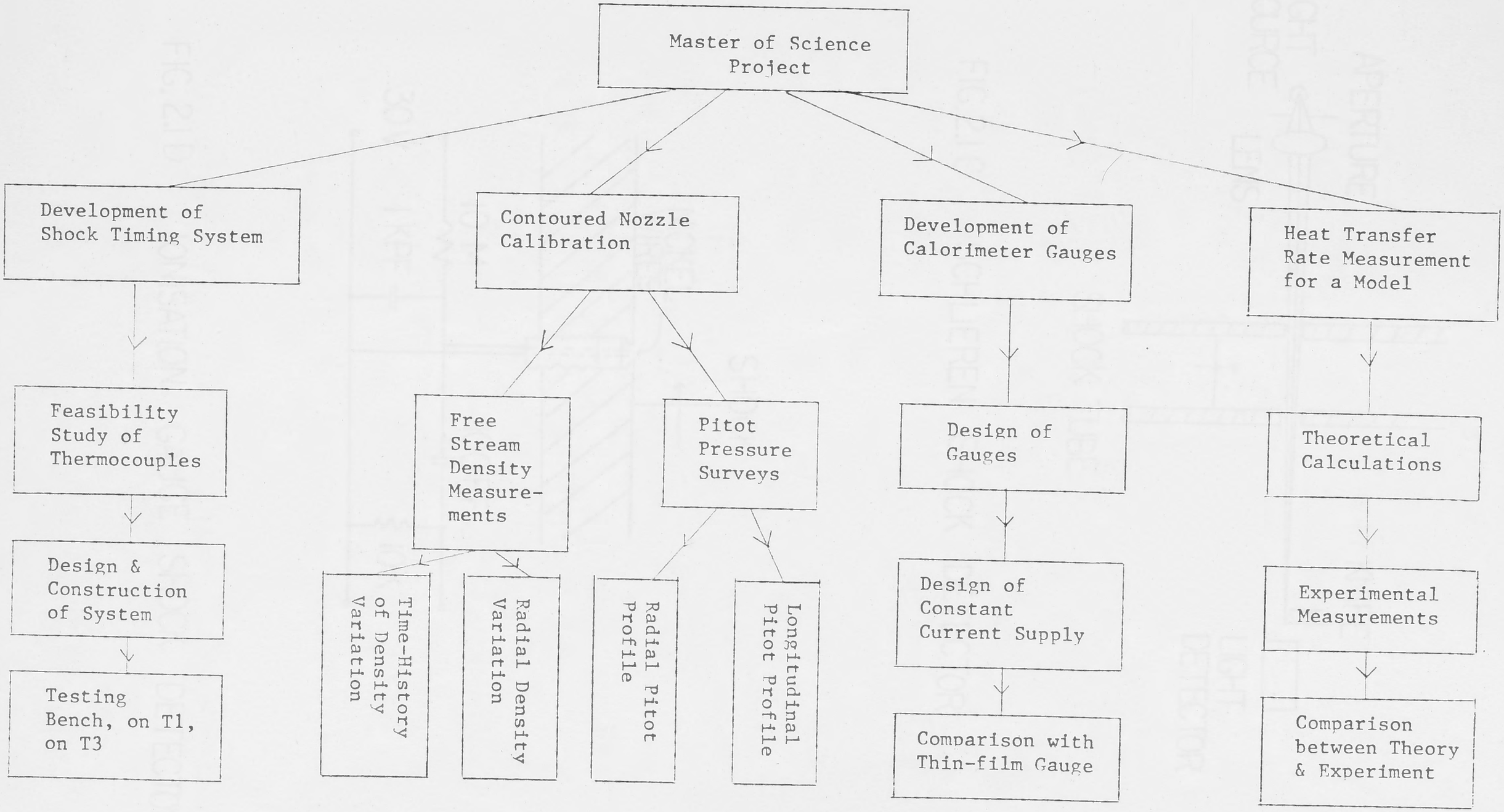

Fig. 1: Summary of Project

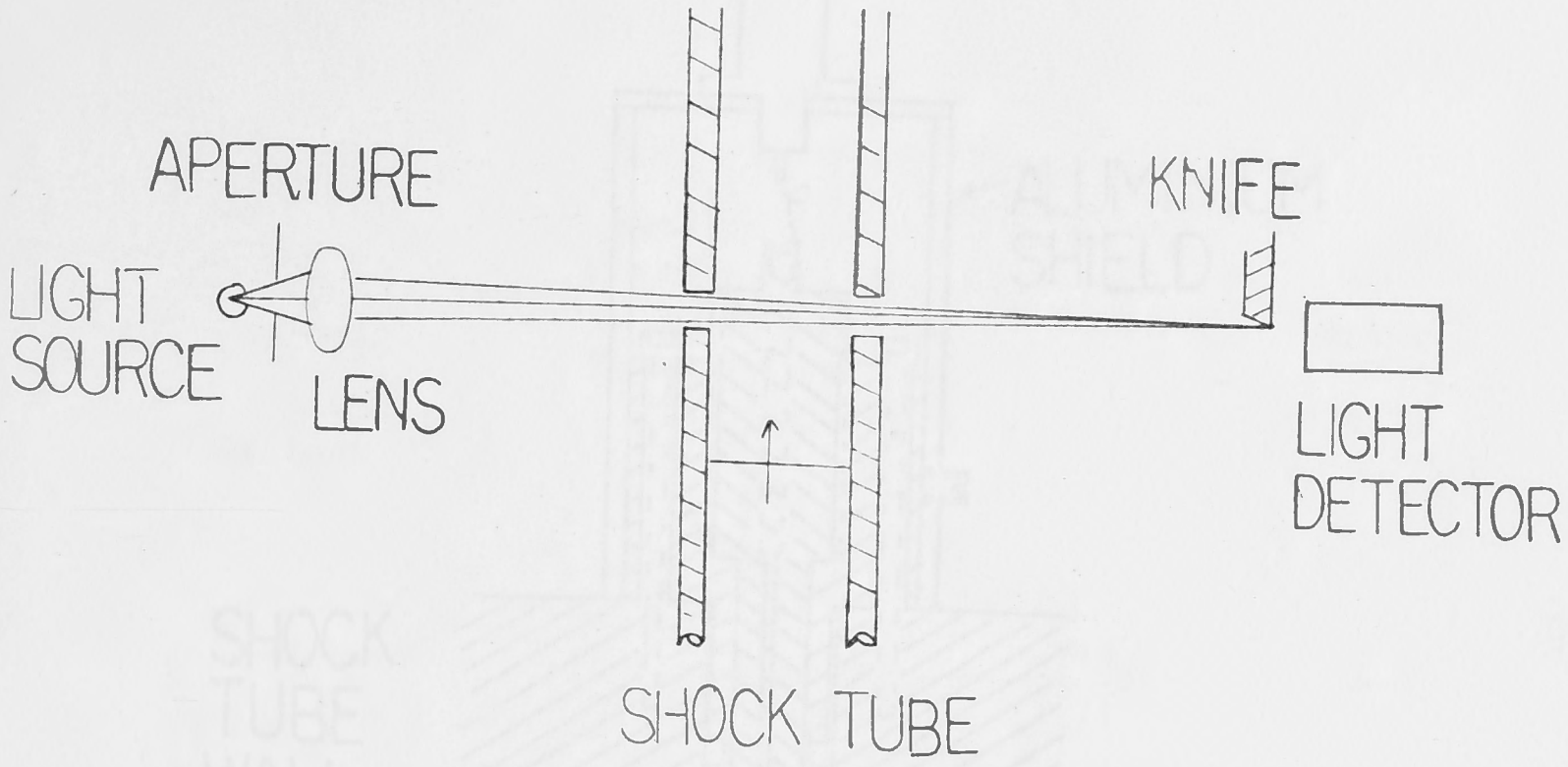

FIG. 2.1 C SCHLIEREN SHOCK DETECTOR

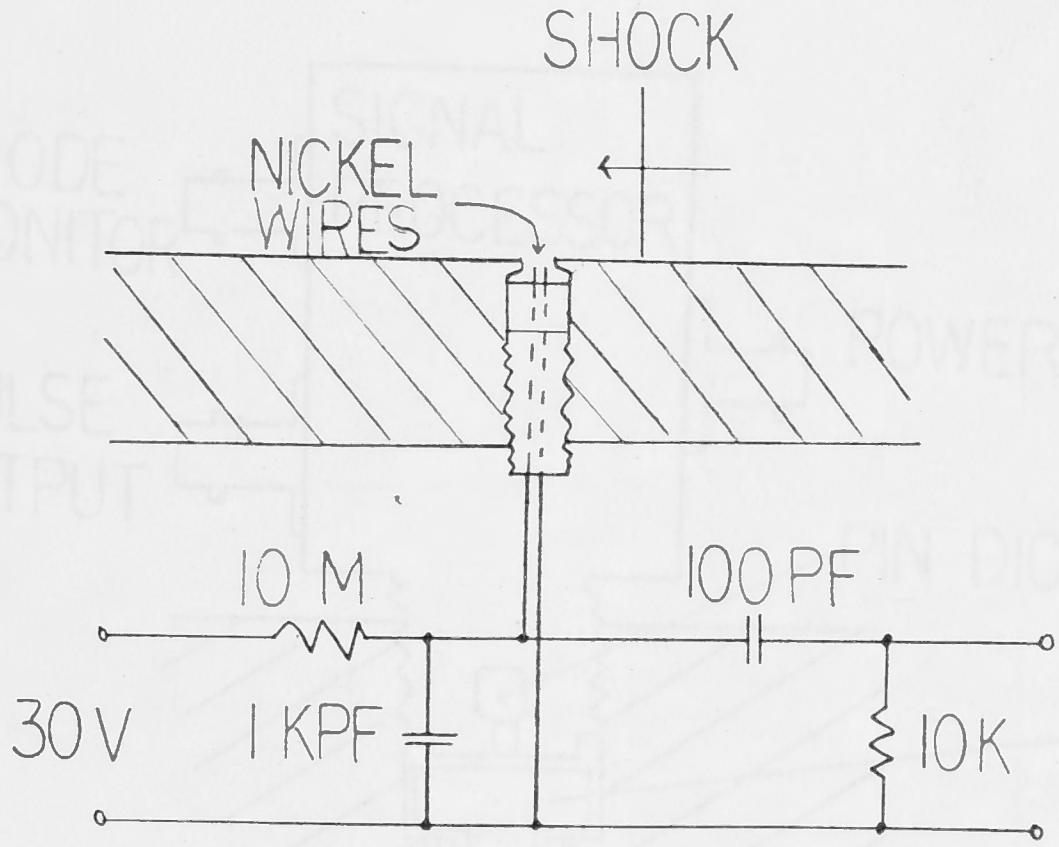

FIG. 2.1 D IONISATION GAUGE SHOCK DETECTOR

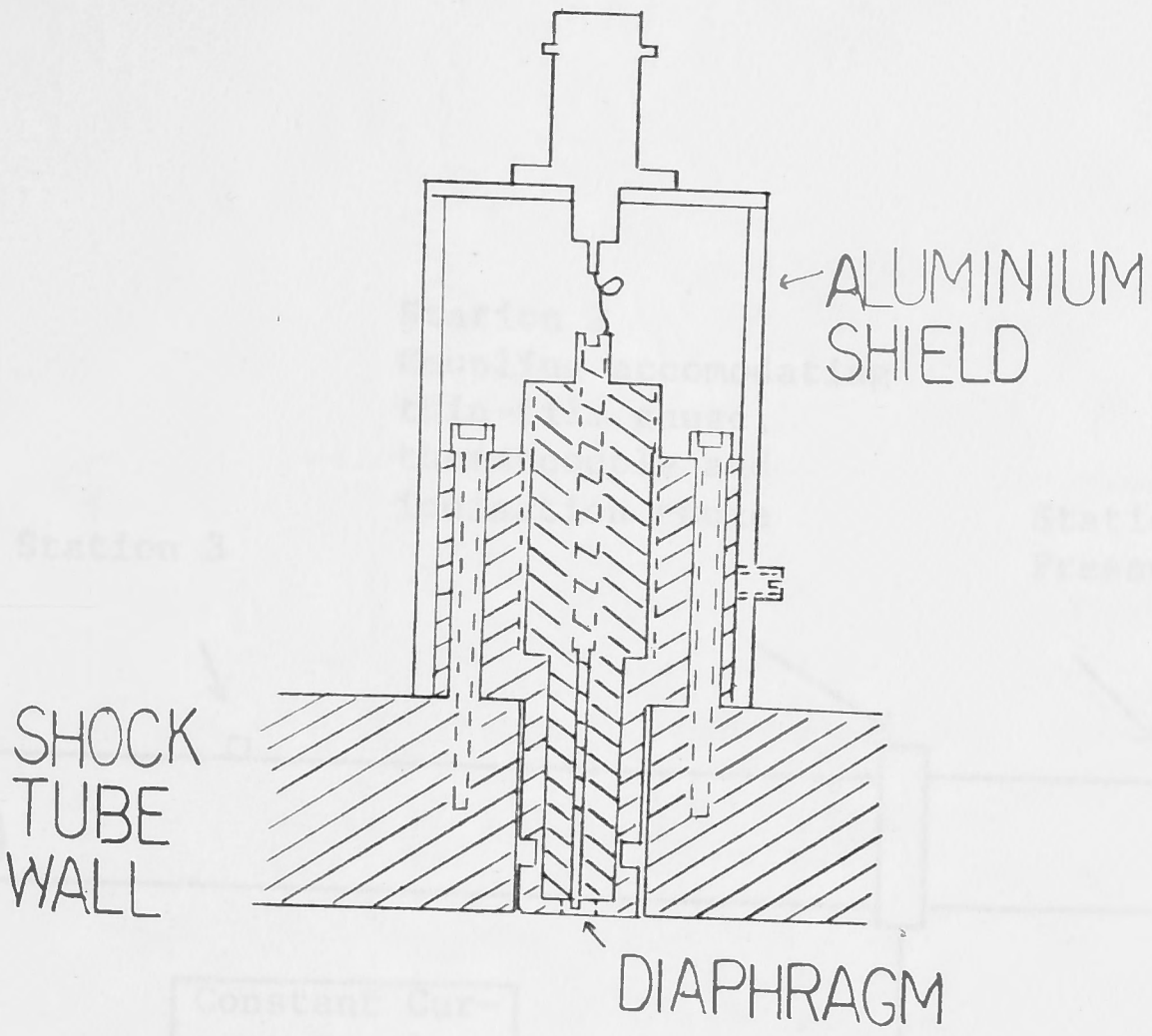

FIG.2.1A CONTACT SHOCK WAVE DETECTOR

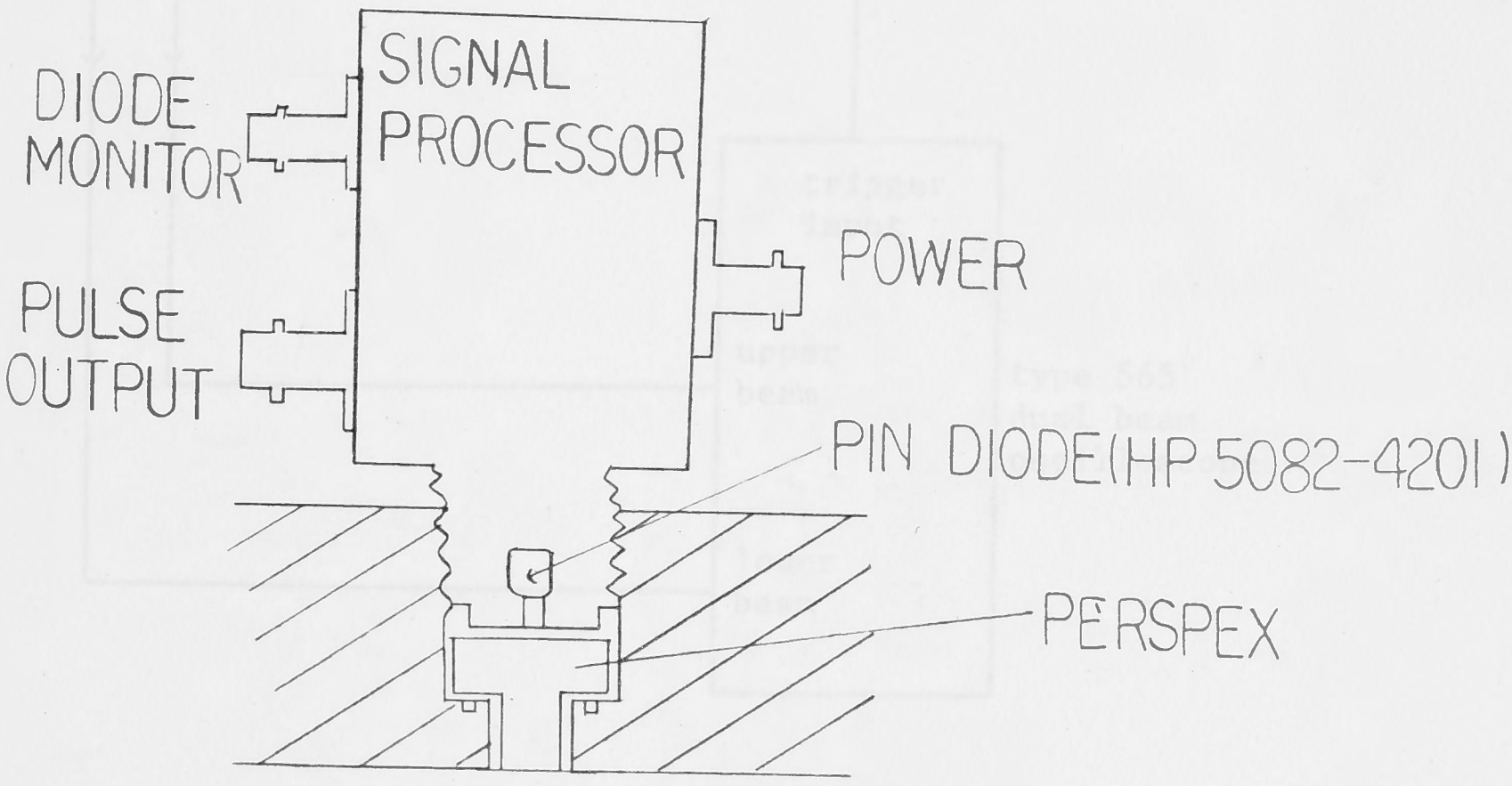

FIG 2.1B PHOTODIODE SHOCK DETECTOR BASED ON SET-UP ON D.D.T.

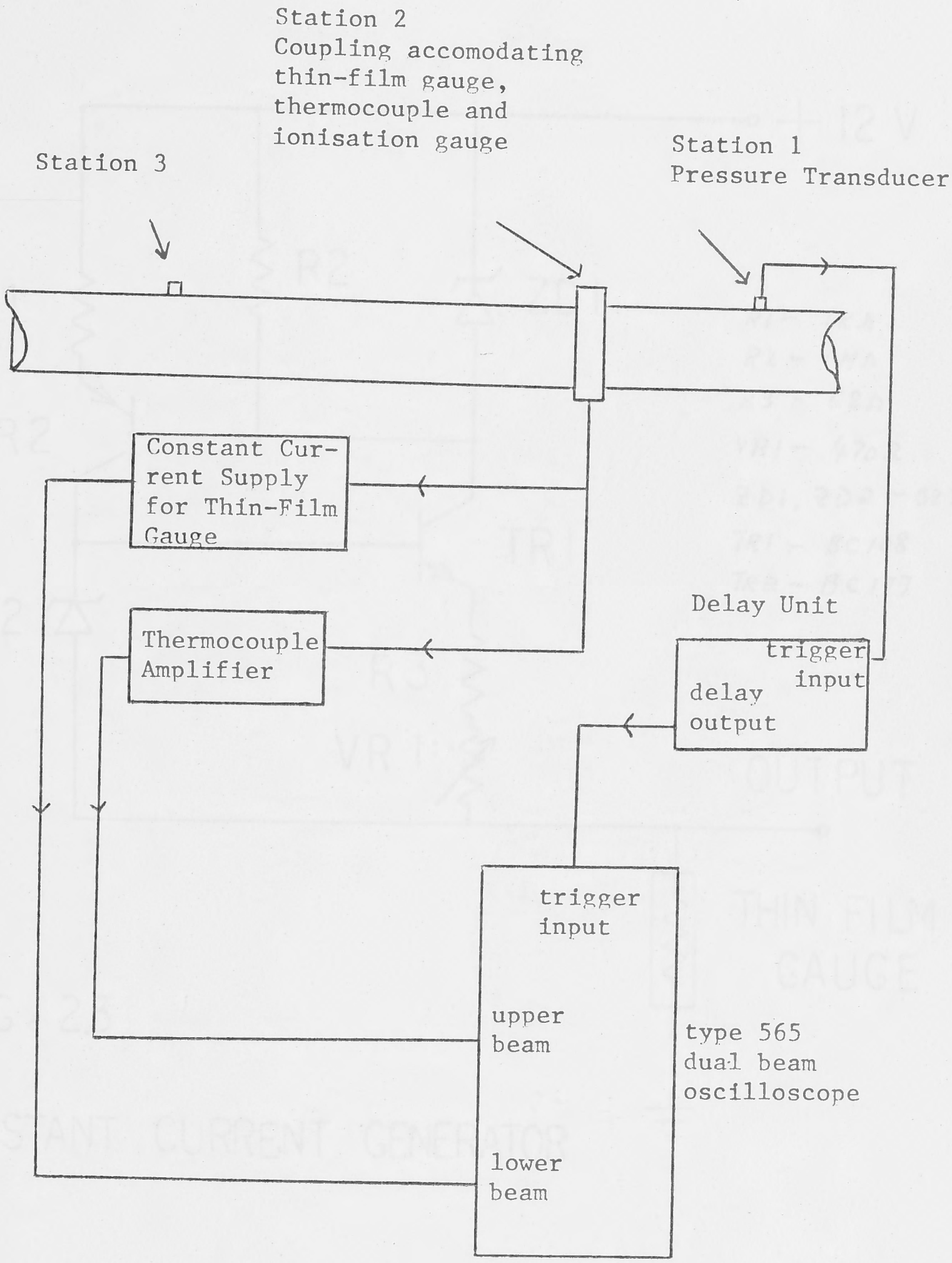

Fig. 2.2: Comparision of thermocouple with thin-film gauge on T1

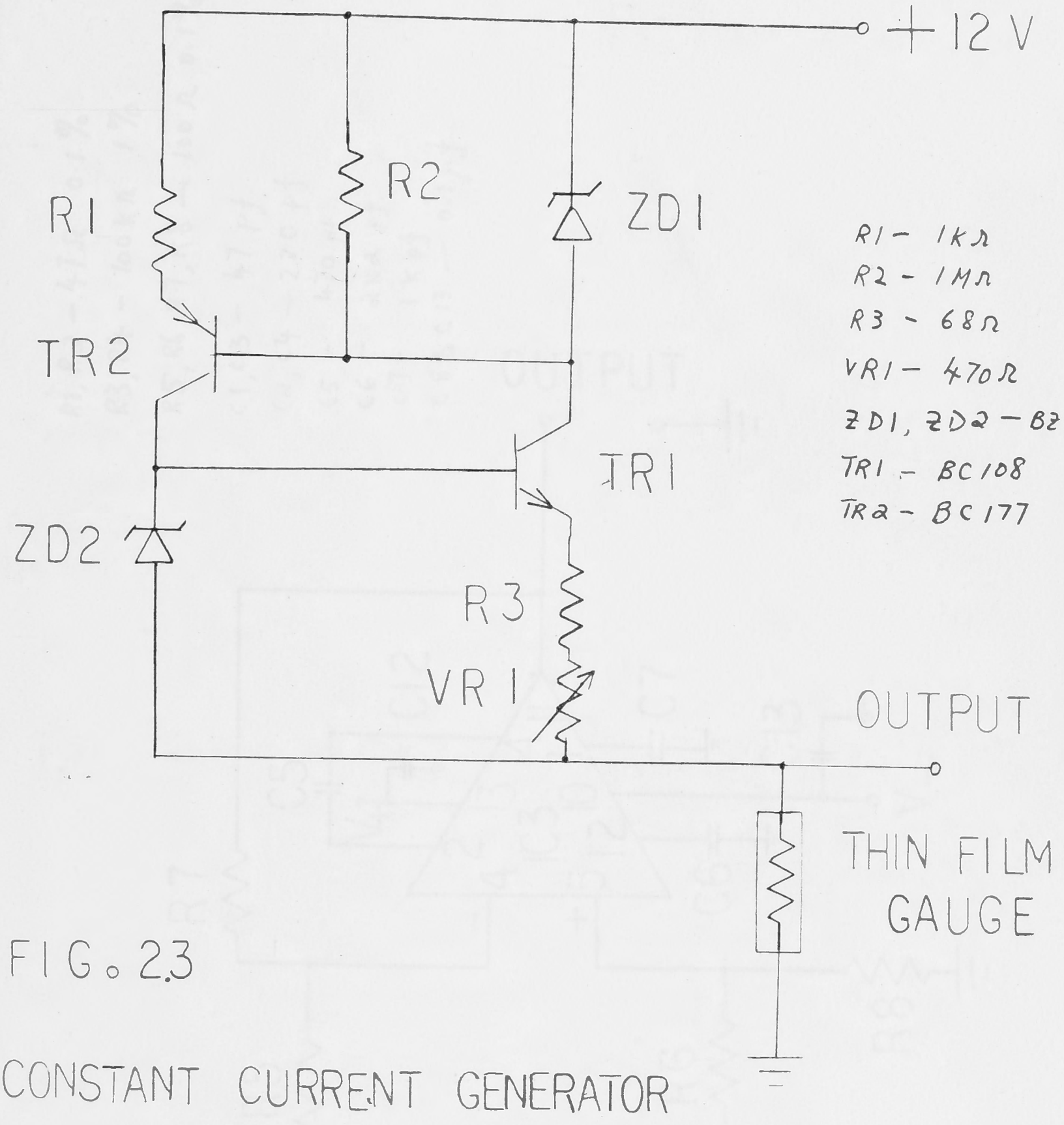

R1 - 1KΩ
R2 - 1MΩ
R3 - 68Ω
VR1 - 470Ω
ZD1, ZD2 - BZY88 C3V9
TR1 - BC108
TR2 - BC177

FIG. 2.3

CONSTANT CURRENT GENERATOR

R1, R2 – 47Ω 0.1%
R3, R4 – 100kΩ 1%
R5, R6, R7, R8 – 100Ω 0.1%

C1, C3 – 47 pf
C2, C4 – 220 pf
C5 – 470 pf
C6 – 2k2 pf
C7 – 1k pf
C8 to C13 – 0.1μf

IC1 to IC3 – μA715DC

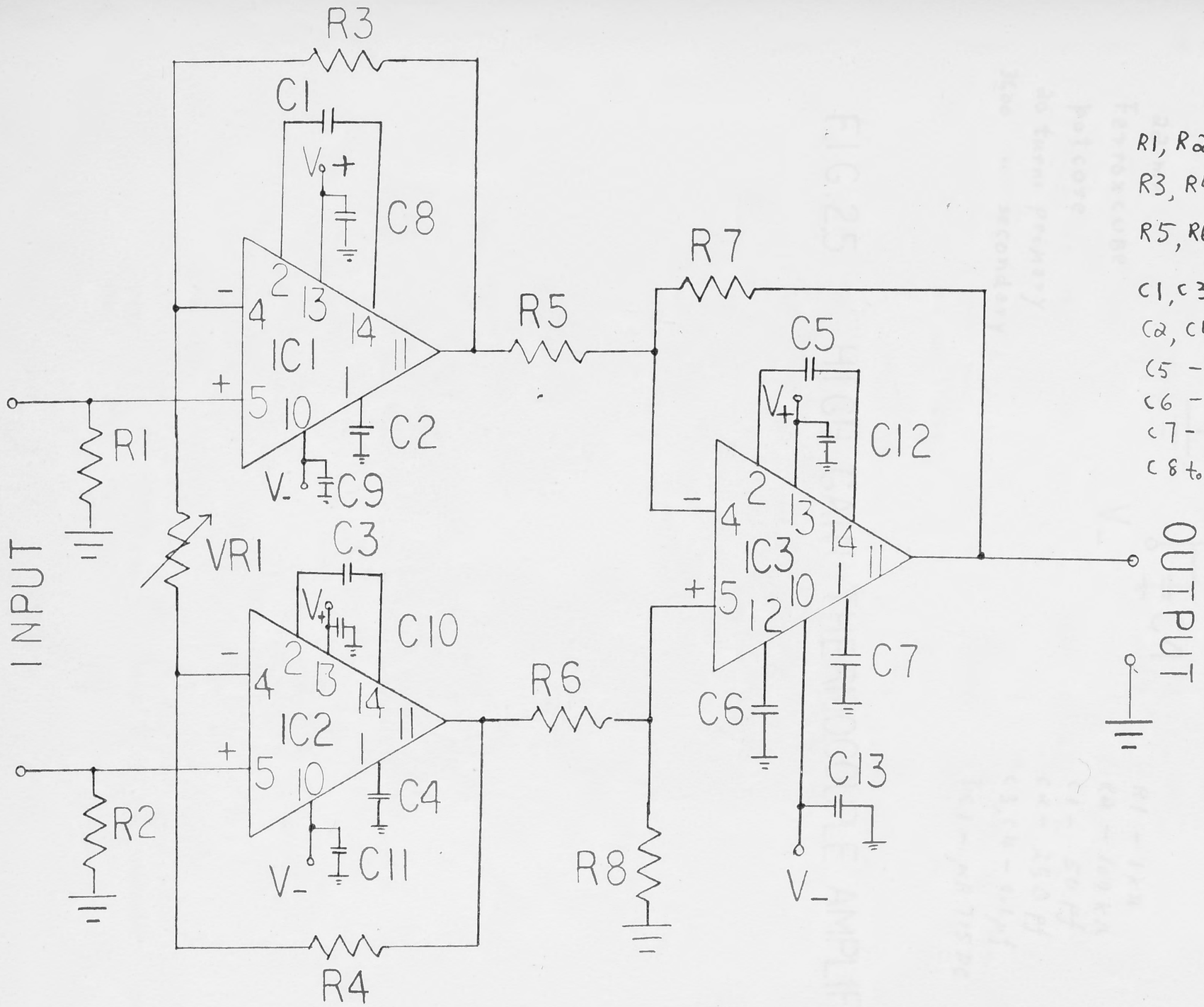

FIG.24 DIFFERENTIAL AMPLIFIER FOR THERMOCOUPLES

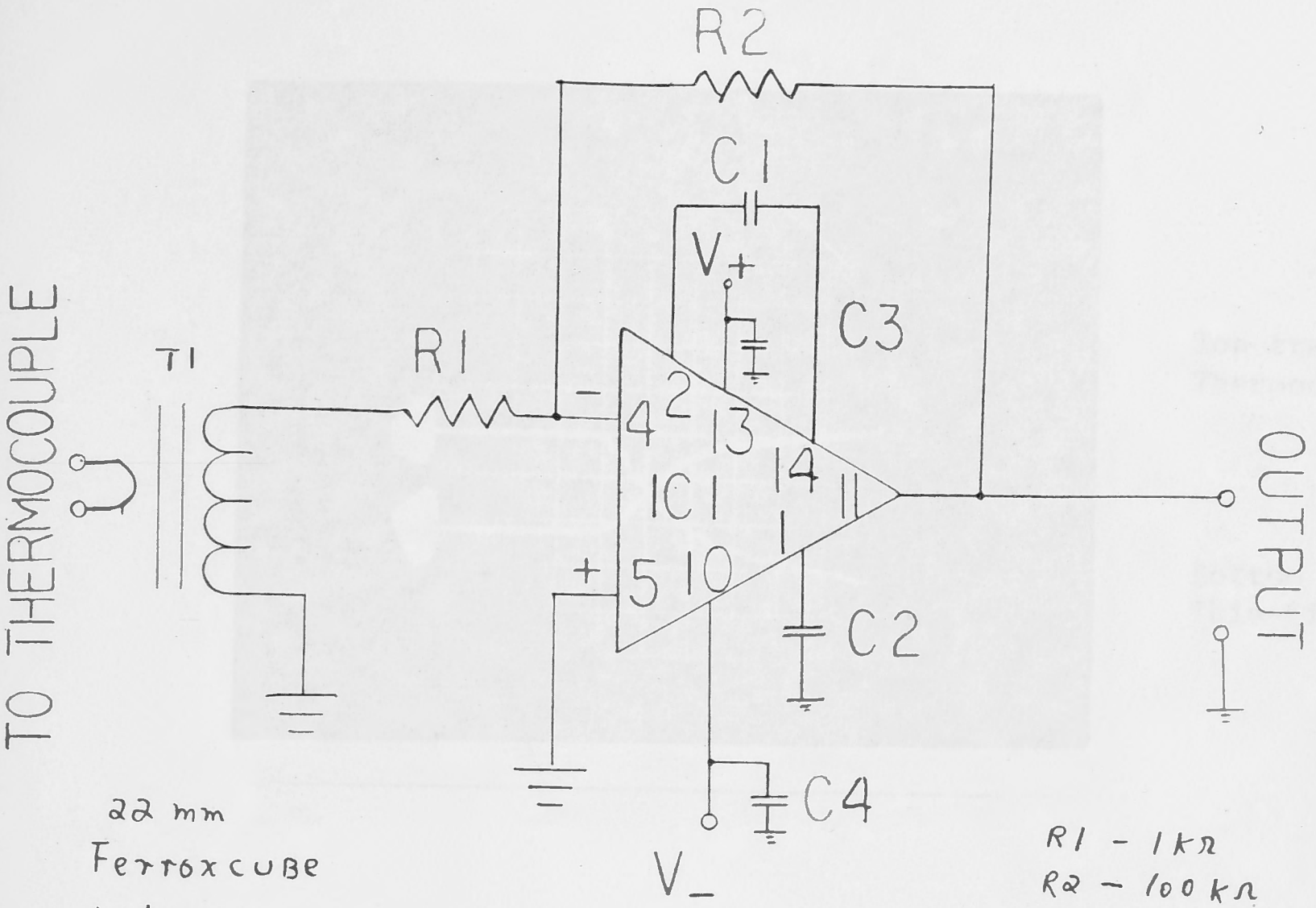

FIG. 2.5 HIGH GAIN THERMOCOUPLE AMPLIFIER

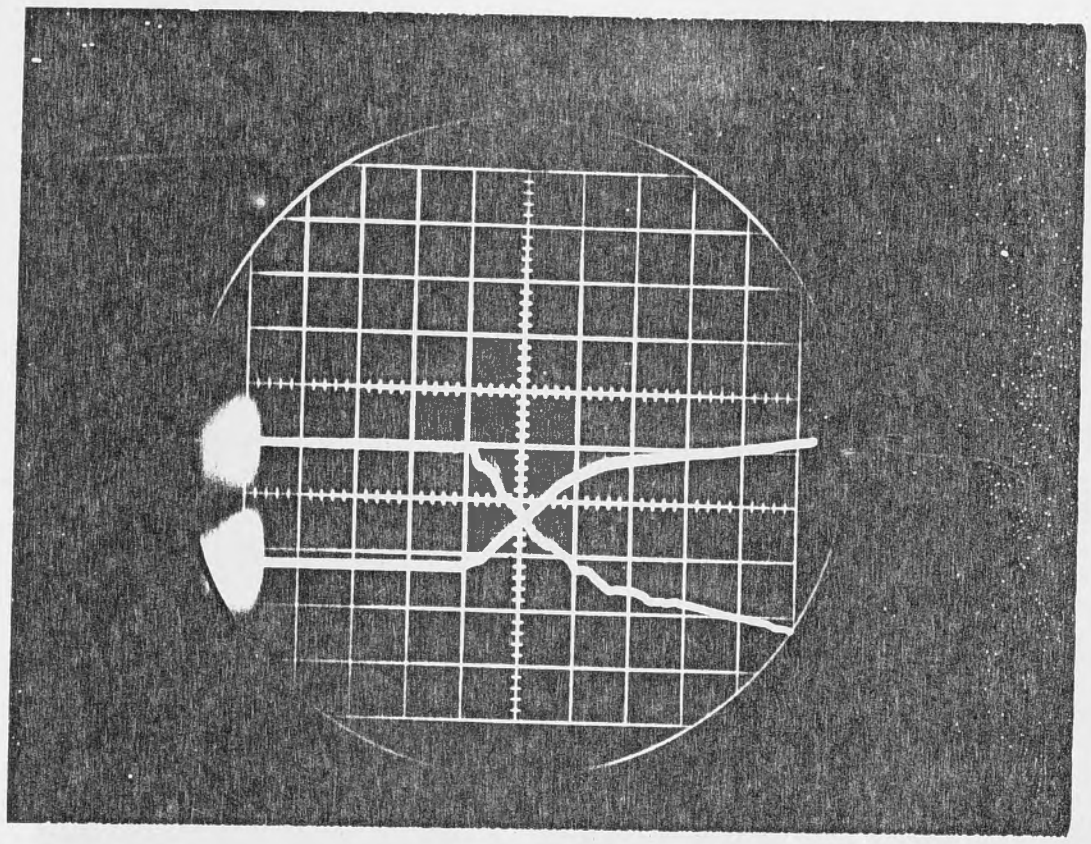

Top trace:
Thermocouple

Bottom trace:
Thin-film gauge

Fig. 2.6a: Direct output of a 5-element thermocouple

test gas = air; shock speed = 1.2 km/s;
initial pressure = 760 torr; delay = 202 microseconds;
upper vert = 1 mV/div; lower vert = 10 mV/div;
horizontal = 20 microsecond/div.

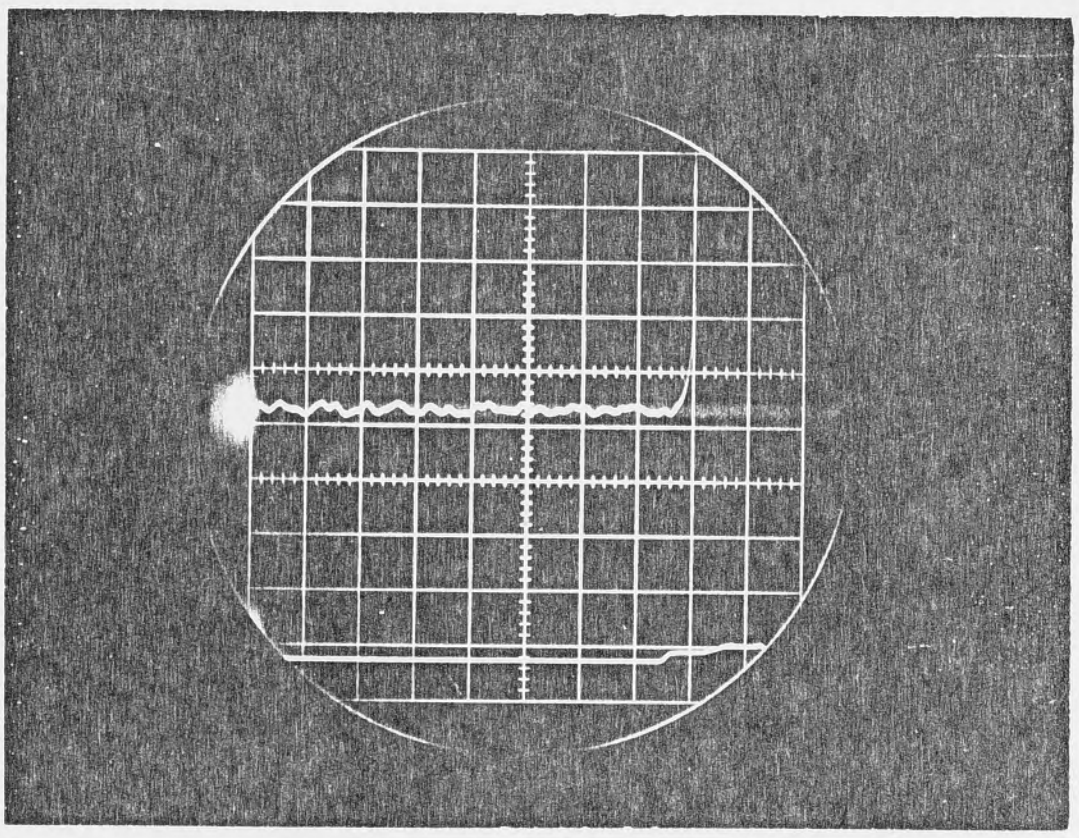

Top trace:
Thermocouple
+ amplifier

Bottom trace:
Thin-film gauge

Fig. 2.6b: Output of thermocouple via amplifier (Fig. 2.5)

test gas = nitrogen; shock speed = 2.2 km/s;
initial pressure = 20 torr; upper vert = 200 mV/div;
lower vert = 10 mV/div; horizontal = 5 microsecond/div;
delay = 110 microseconds.

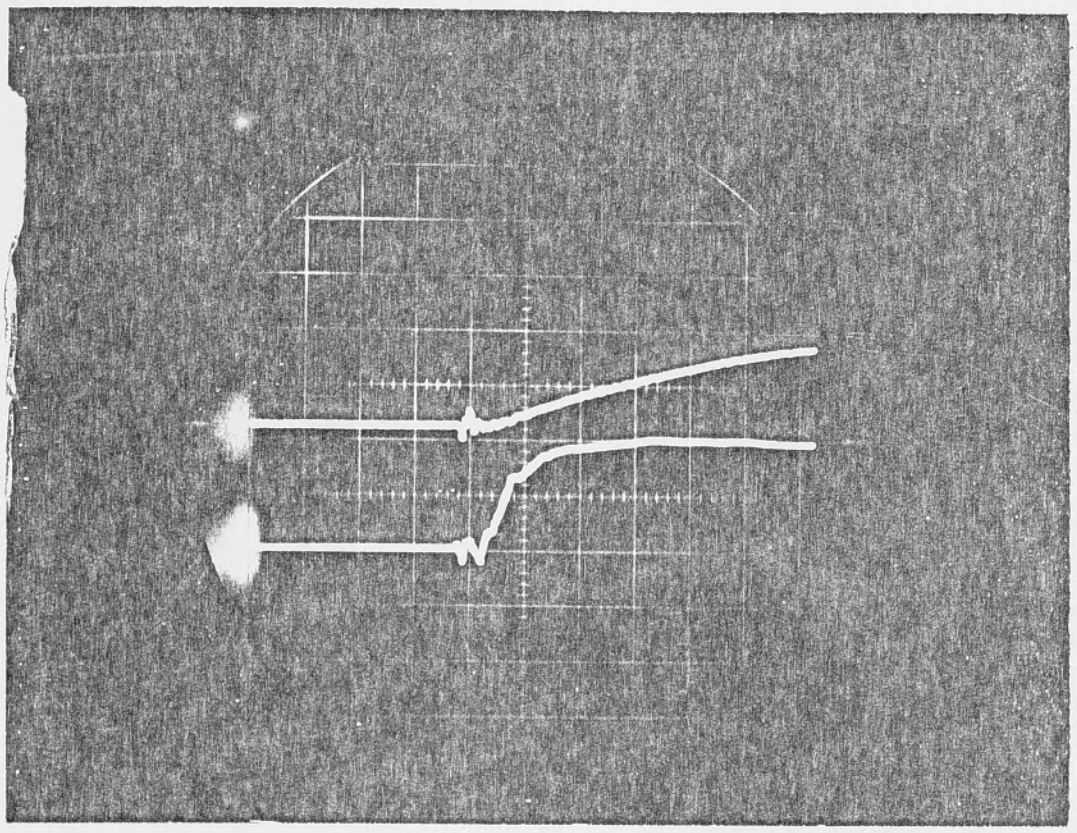

Top trace:
Output from thermocouple via amplifier
(Fig. 2.4)

Bottom trace:
Output from thin-film gauge

Fig. 2.6c: Charge pick-ups by the thermocouple and thin-film gauge cause the initial edge to rise in reverse polarity.

upper vert = 0.5 V/div; lower vert = 0.1 V/div;
horizontal = 50 microseconds/div;
shock speed = 1.8 km/sec; test gas = argon;
initial pressure = 760 torr.

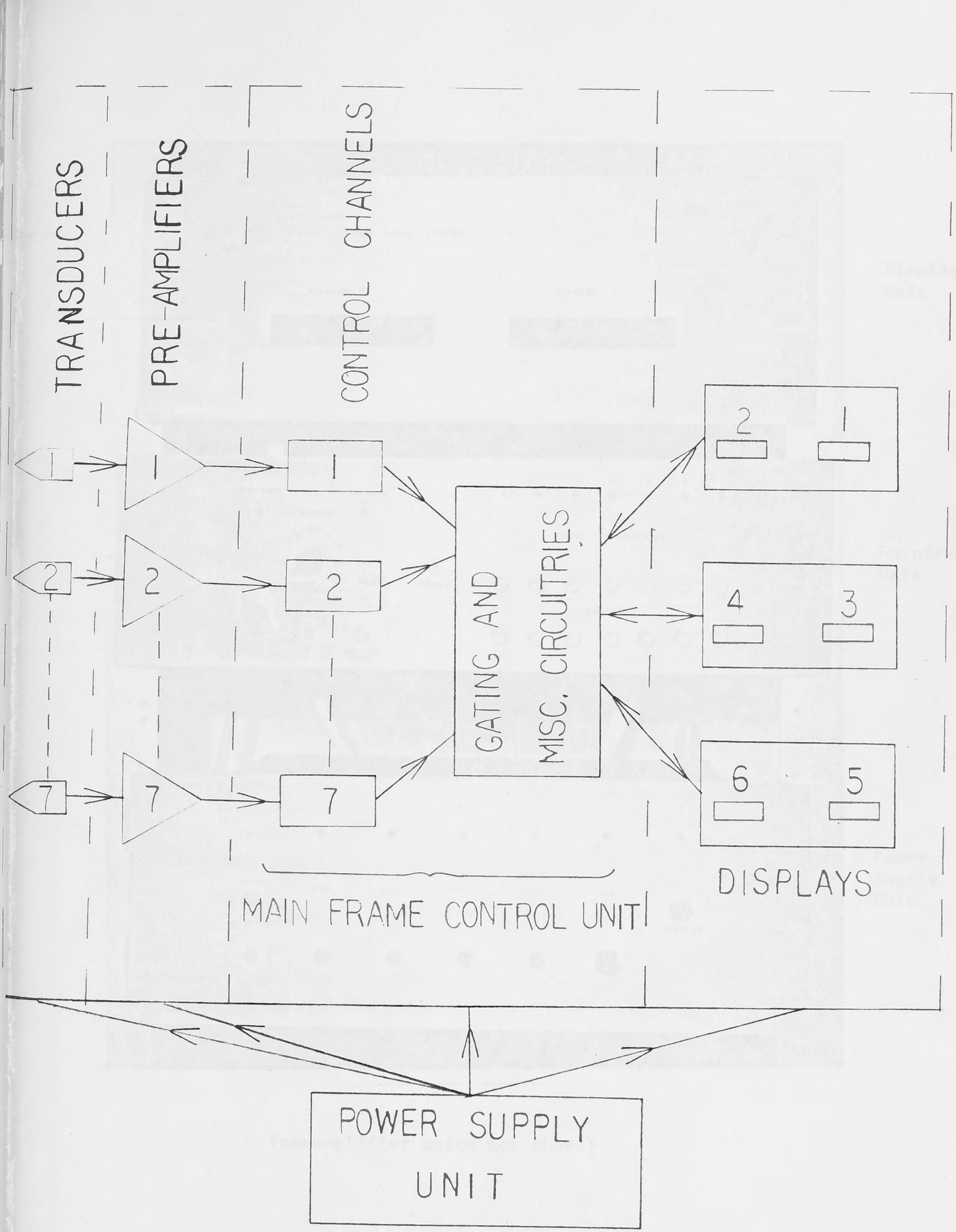

FIG. 2.7A FUNCTIONAL BLOCK DIAGRAM OF SHOCK SPEED MEASUREMENT SYSTEM

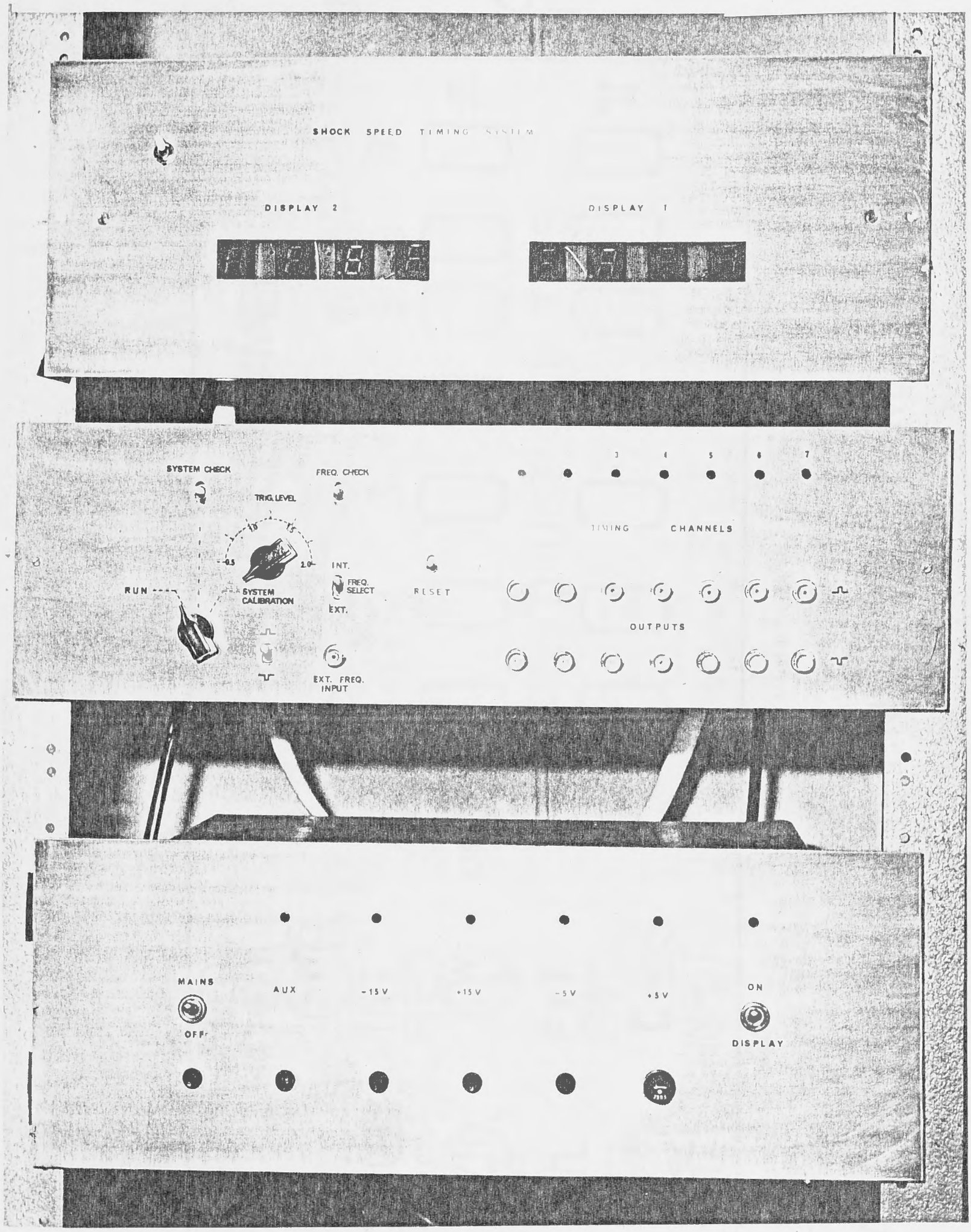

Display Unit

Mainframe Unit

Power Supply Unit

(preamplifier units not shown)

Fig. 2.7b Photograph of Shock Speed Timing System.

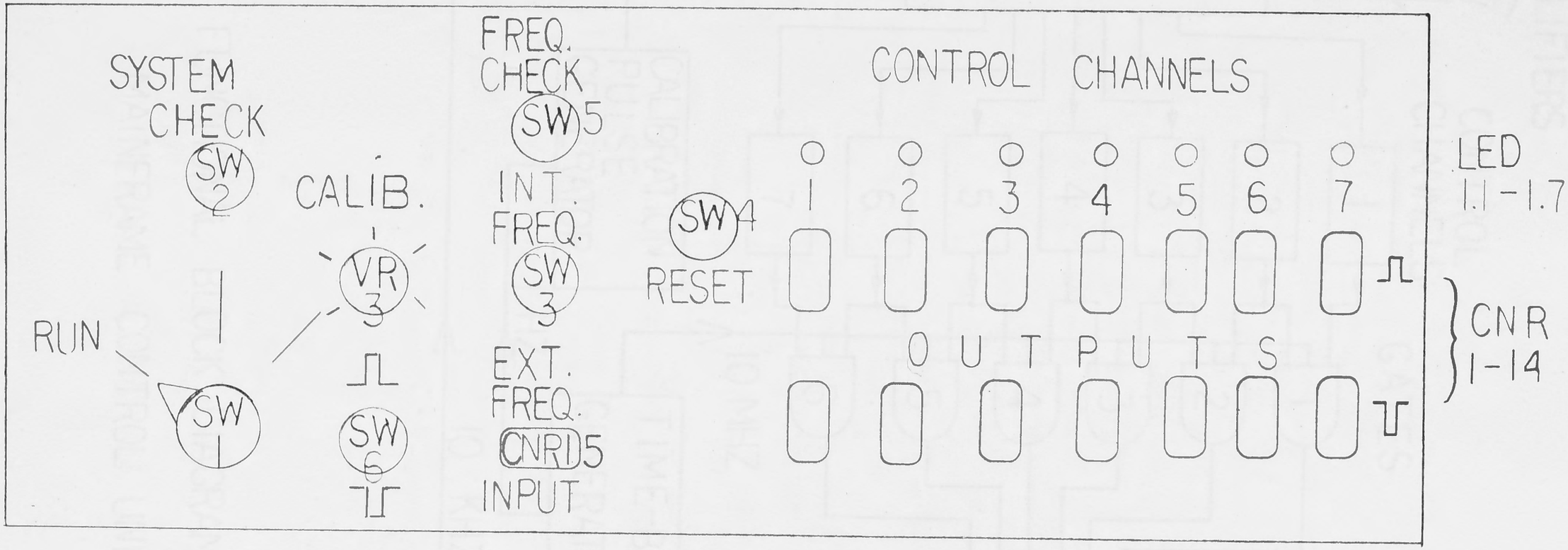

FIG. 2.8 MAINFRAME CONTROL UNIT FRONT PANEL LAYOUT

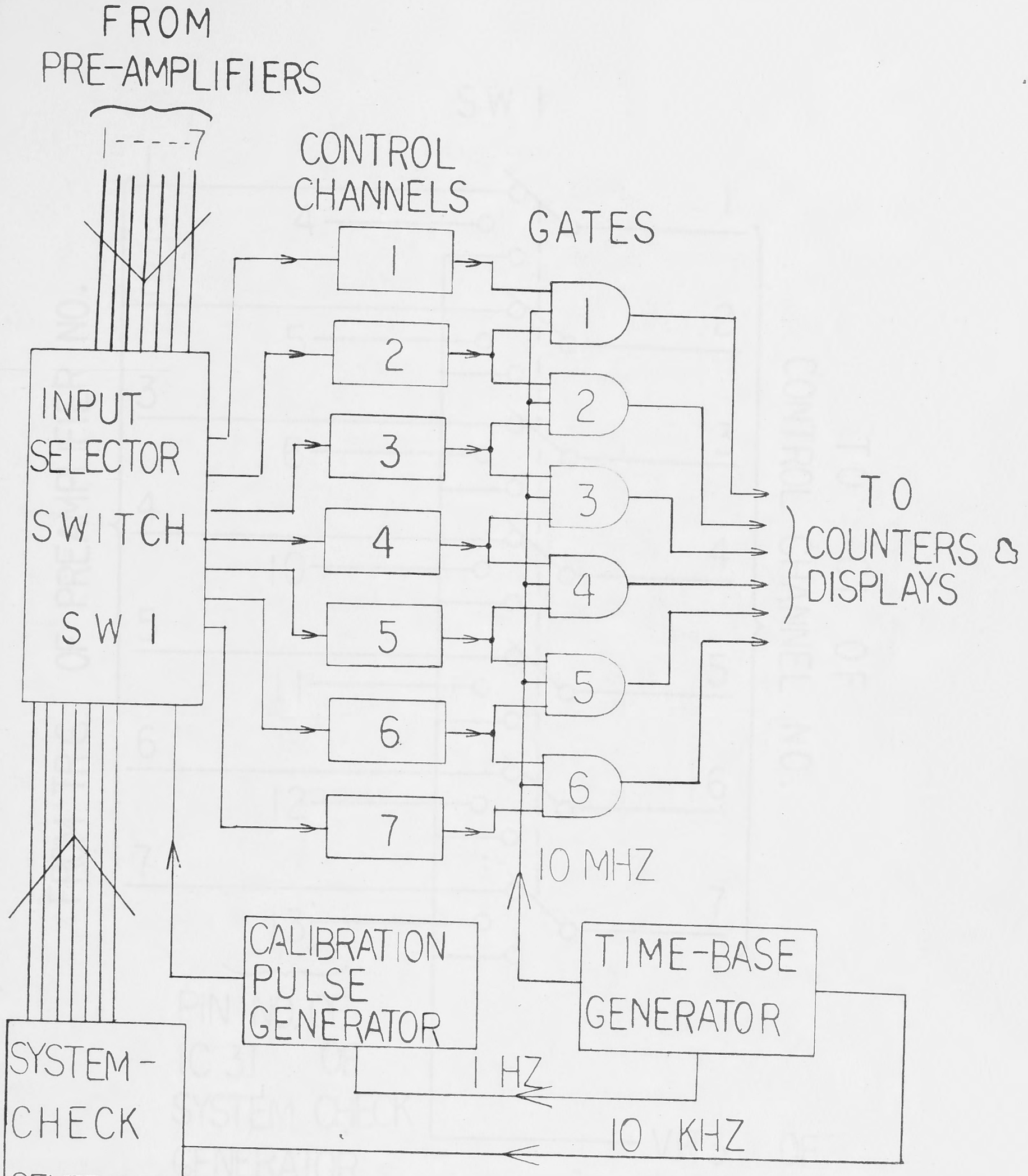

FIG. 2.9 FUNCTIONAL BLOCK DIAGRAM OF MAINFRAME CONTROL UNIT

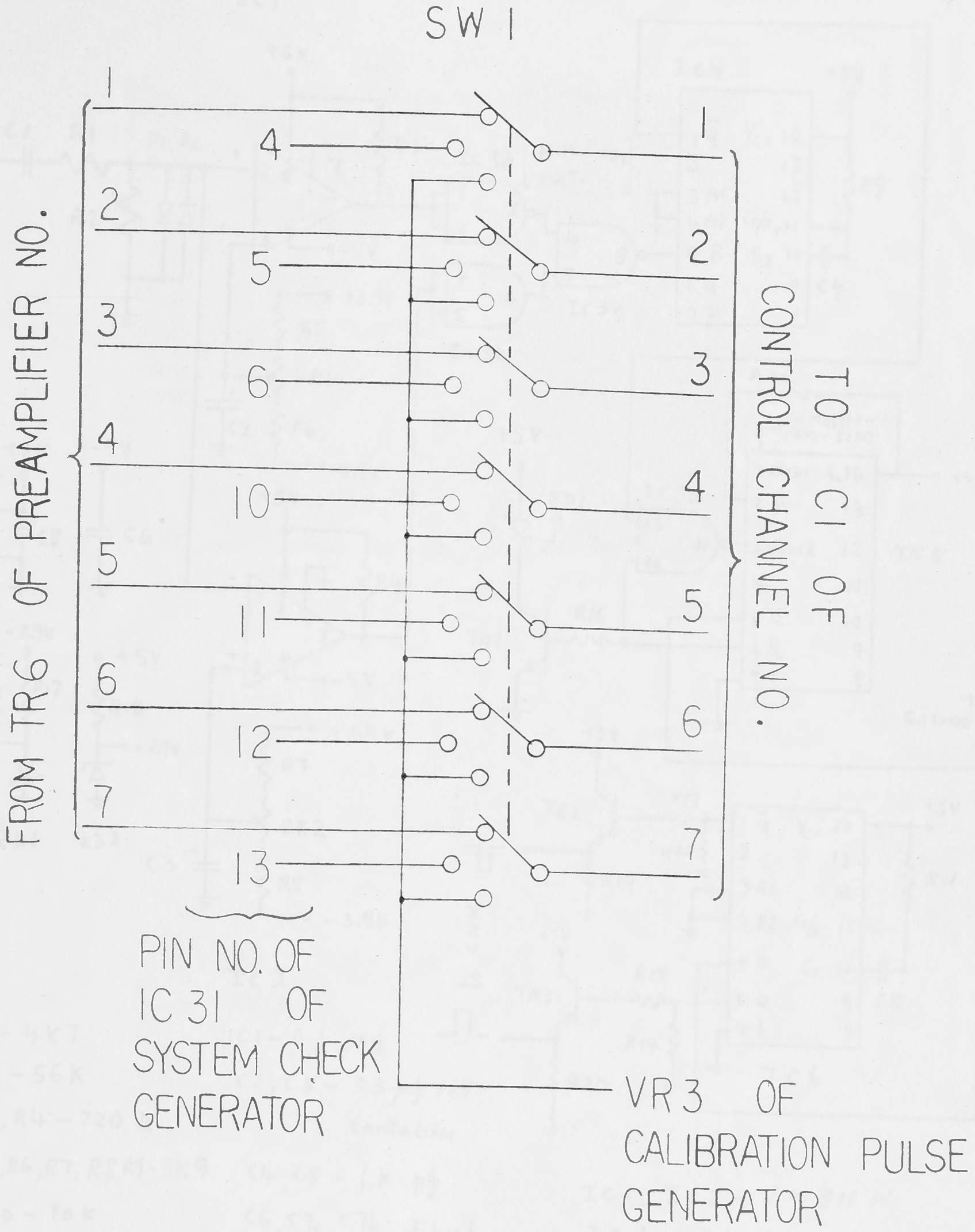

FIG.2.10 WIRING DIAGRAM OF SW I
SWITCH SHOWN IN RUN POSITION

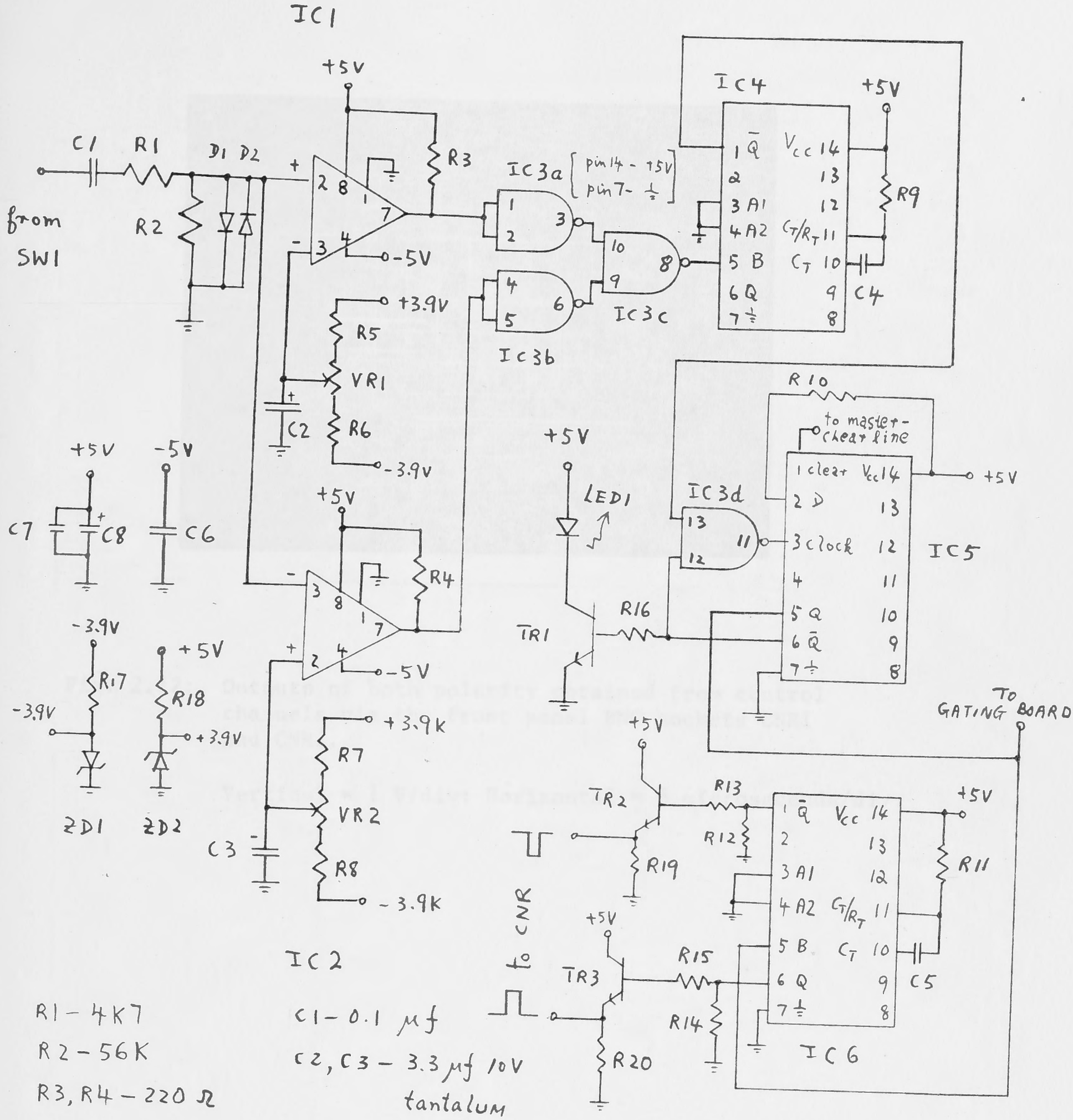

R1 – 4K7

R2 – 56K

R3, R4 – 220 Ω

R5, R6, R7, R8, R9 – 3K9

R10 – 10k

R11 – 22k

R12, R14 – 10k

R13, R15 – 1k

R16 – 12k

R17, R18, R19, R20 – 47Ω

VR1, VR2 – 1kΩ

C1 – 0.1 μf

C2, C3 – 3.3 μf 10V tantalum

C4, C5 – 1k pf

C6, C7a, C7b – 0.1 μf

C8 – 100 μf

D1, D2 – IN914

ZD1, ZD2 – BZY88 C3V9

LED1 – red light-emitting diode

TR1, TR2, TR3 – BC108

IC1, IC2 – LM311H

IC3 – 7400

IC4, IC6 – 74121

IC5 – 7474

FIG.2.11 CIRCUIT OF CONTROL CHANNEL

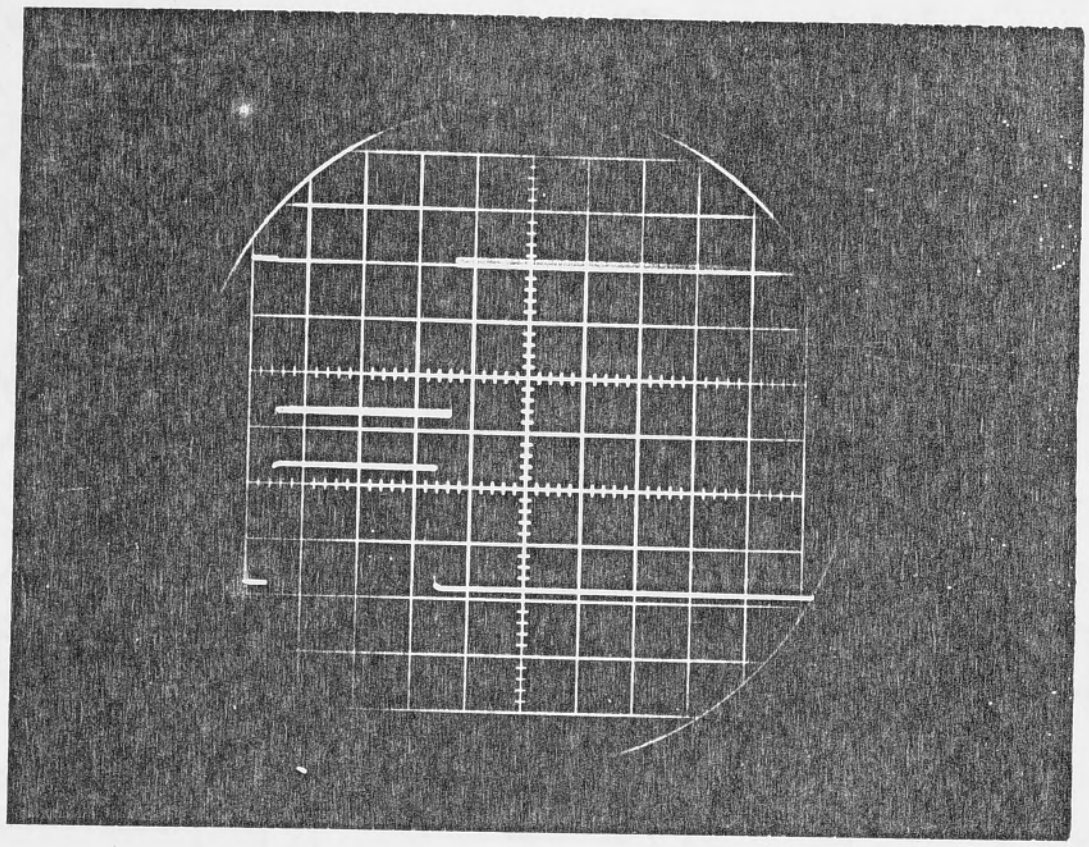

Fig. 2.12: Outputs of both polarity obtained from control channels via the front panel BNC sockets CNR1 and CNR2.

Vertical = 1 V/div; Horizontal = 5 microseconds/div.

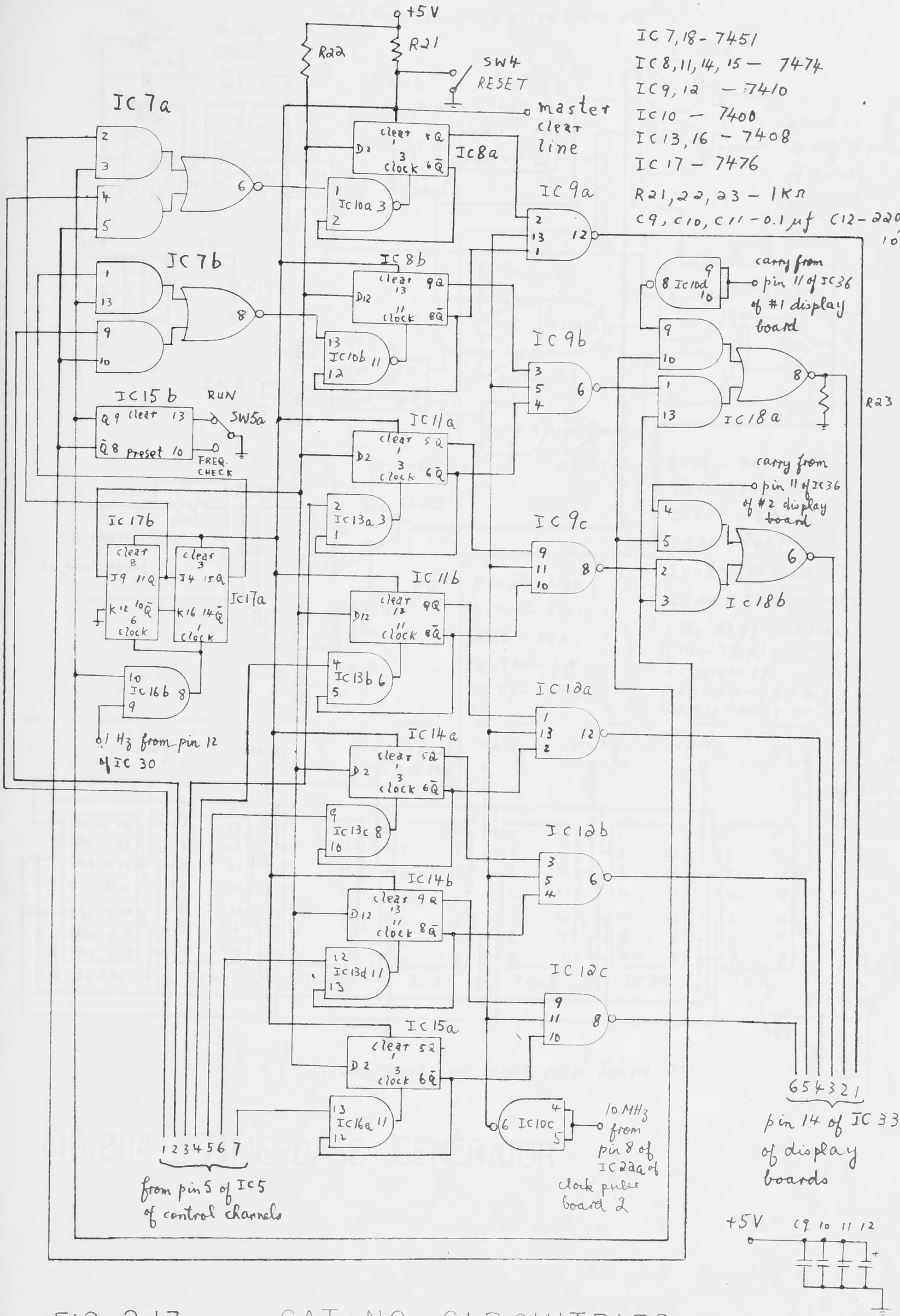

FIG. 2.13 GATING CIRCUITRIES

Top part on clock pulse board #2

VC1
C13
10 MHz XTAL
R24
R25
IC19a
C14
IC19b
C15
SW5b
run
freq. check
IC21a
clear 1
preset 4
IC22a
10 MHz to pins 4,5 of IC 10c
+5V
-5V
C16, 17, 18
C19
IC19c
IC20a
IC19d
IC22b
ext.
int.
SW3
IC21b
clear 13
preset 10
IC20b
IC19e
C20
R26
D3, D4
R27
to CNR15 on front panel
IC23
+5V
-5V
R28
R29
C21
R24,25 - 470Ω
R26,27 - 220K
R28 - 47K
R29,30 - 1K
D3, D4 - IN914
IC19 - 7404
IC20 - 7400
IC21 - 7474
IC22 - 7451
IC23 - LM360H
IC24 to IC30 - 7490
C13 - 33 pf ceramic
C14 - 470 pf "
C15,20 - 100 pf "
C16 to C24 - 0.1 μf
C18, C22 - 220μf 10V

1 MHz
100 KHz
10 KHz to pin12 of IC 20c
1 KHz
100 Hz
10 Hz
1 Hz to pin 9,10 of IC 20 d
R30
IC24
IC25
IC26
IC27
IC28
IC29
IC30
C22,23,24
+5V
+5V

lower part on clock pulse board #1

FIG. 2.14 TIME-BASE GENERATOR

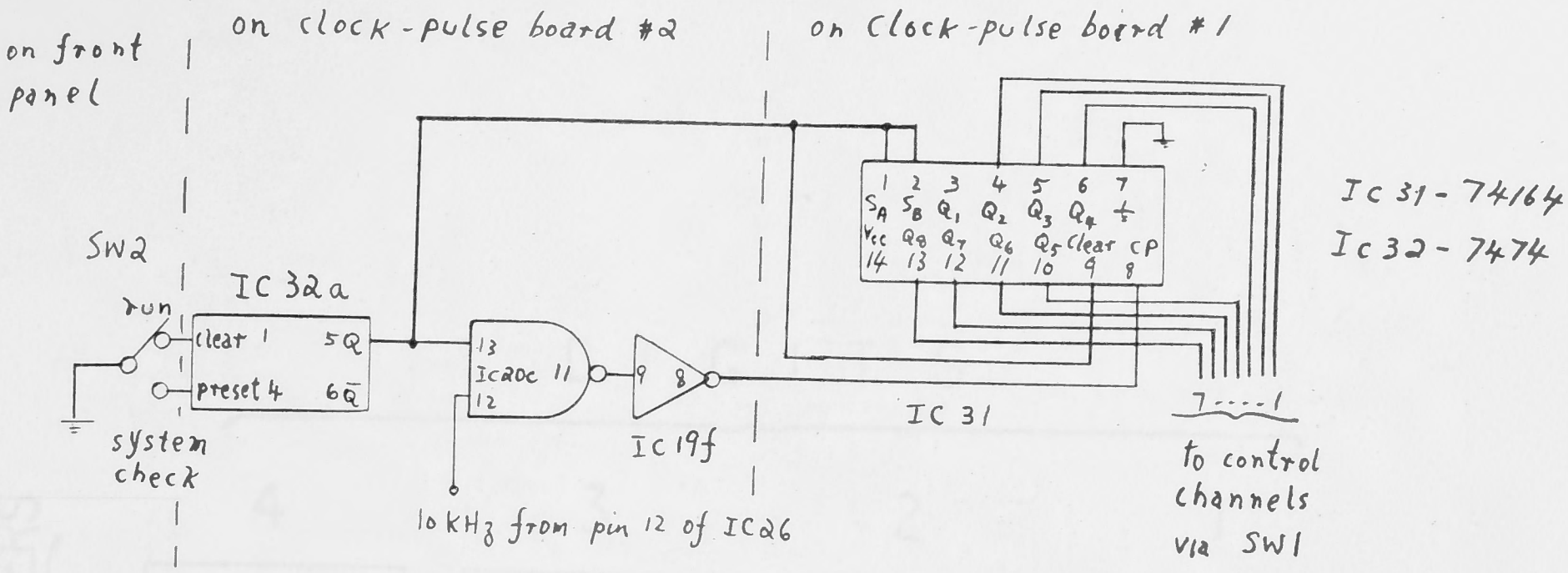

FIG.2.15 SYSTEM-CHECK GENERATOR

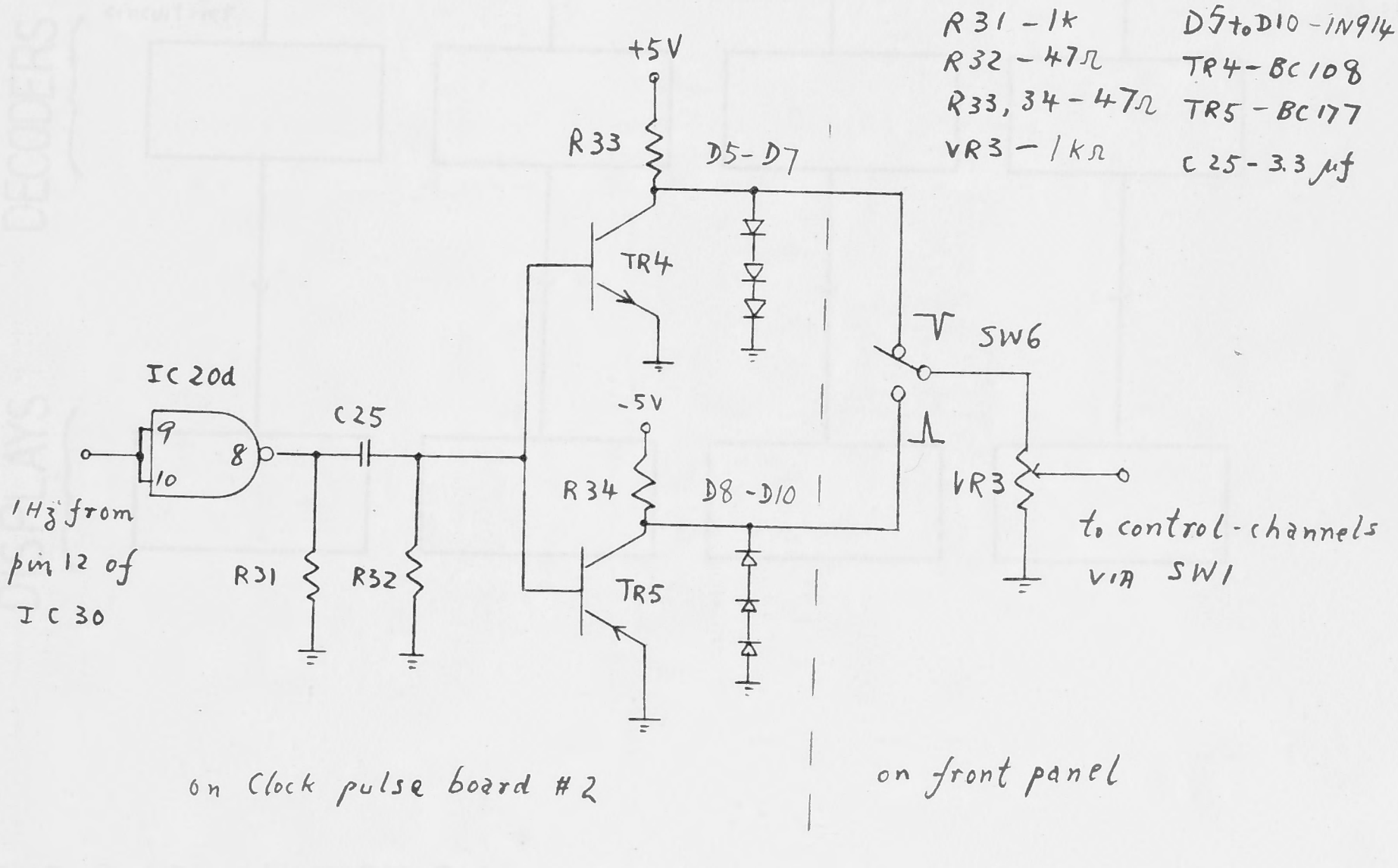

FIG. 2·16 CALIBRATION PULSE GENERATOR

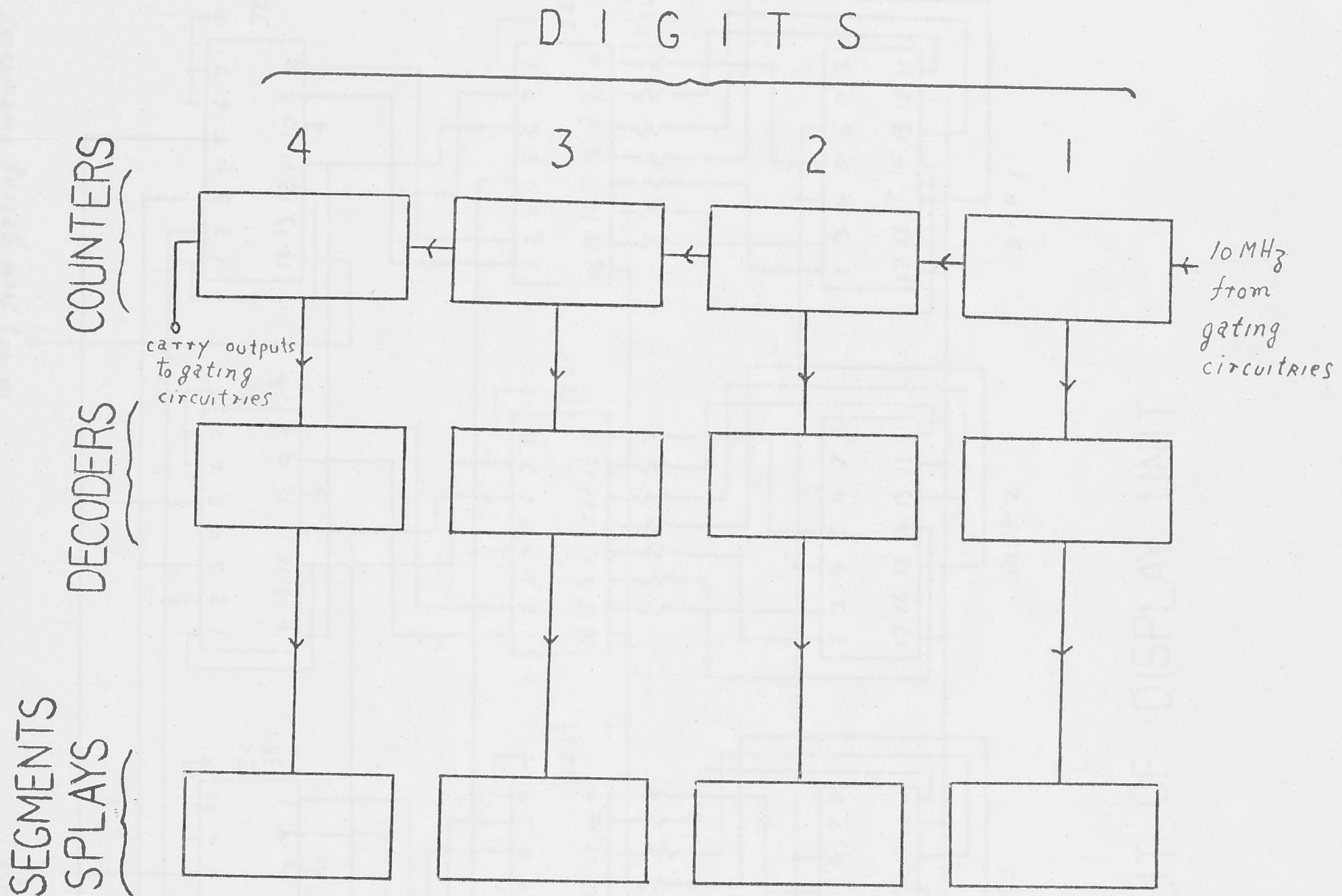

FIG.2·17 FUNCTIONAL BLOCK DIAGRAM OF DISPLAY UNIT

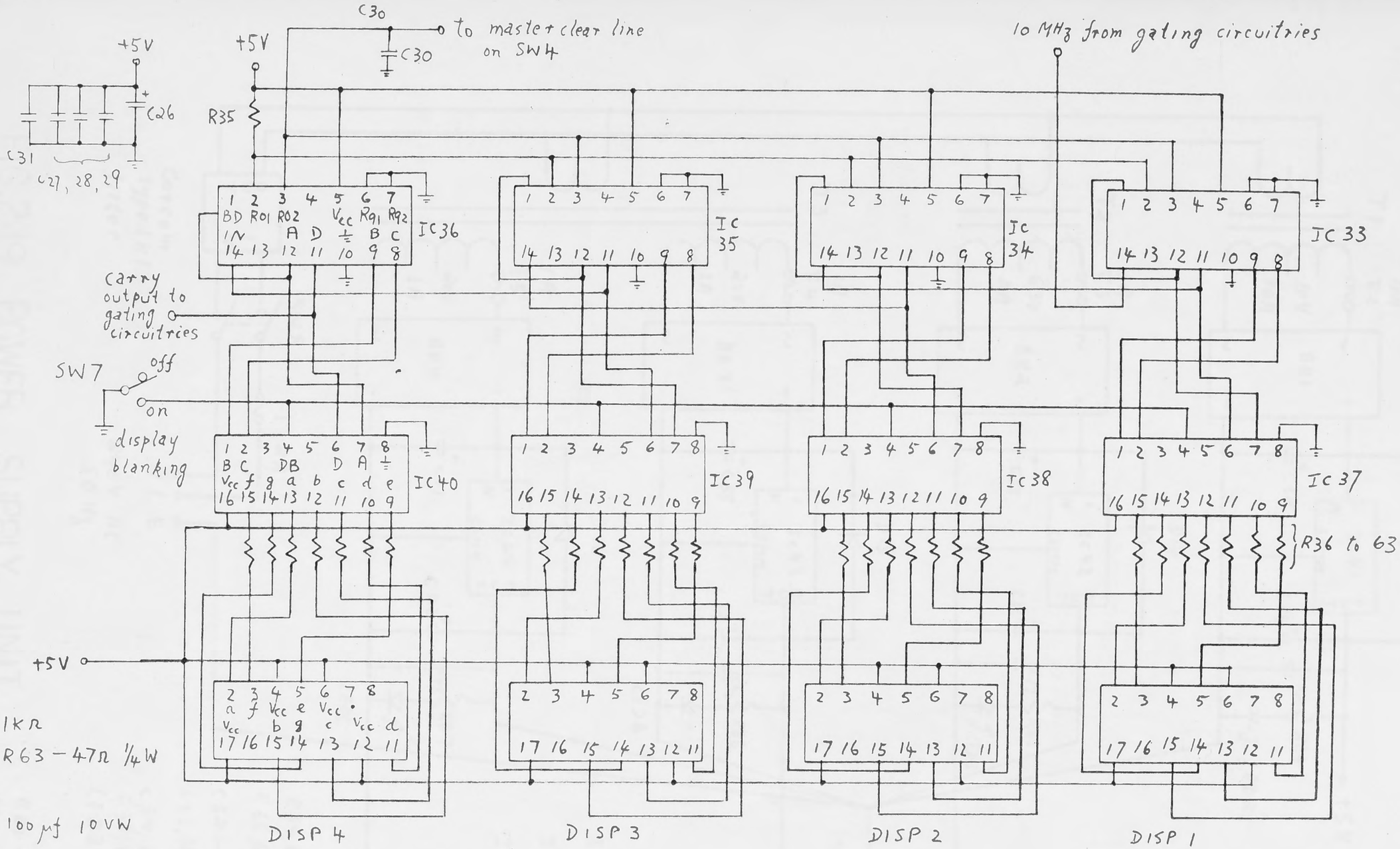

FIG. 2.18 CIRCUIT OF DISPLAY UNIT

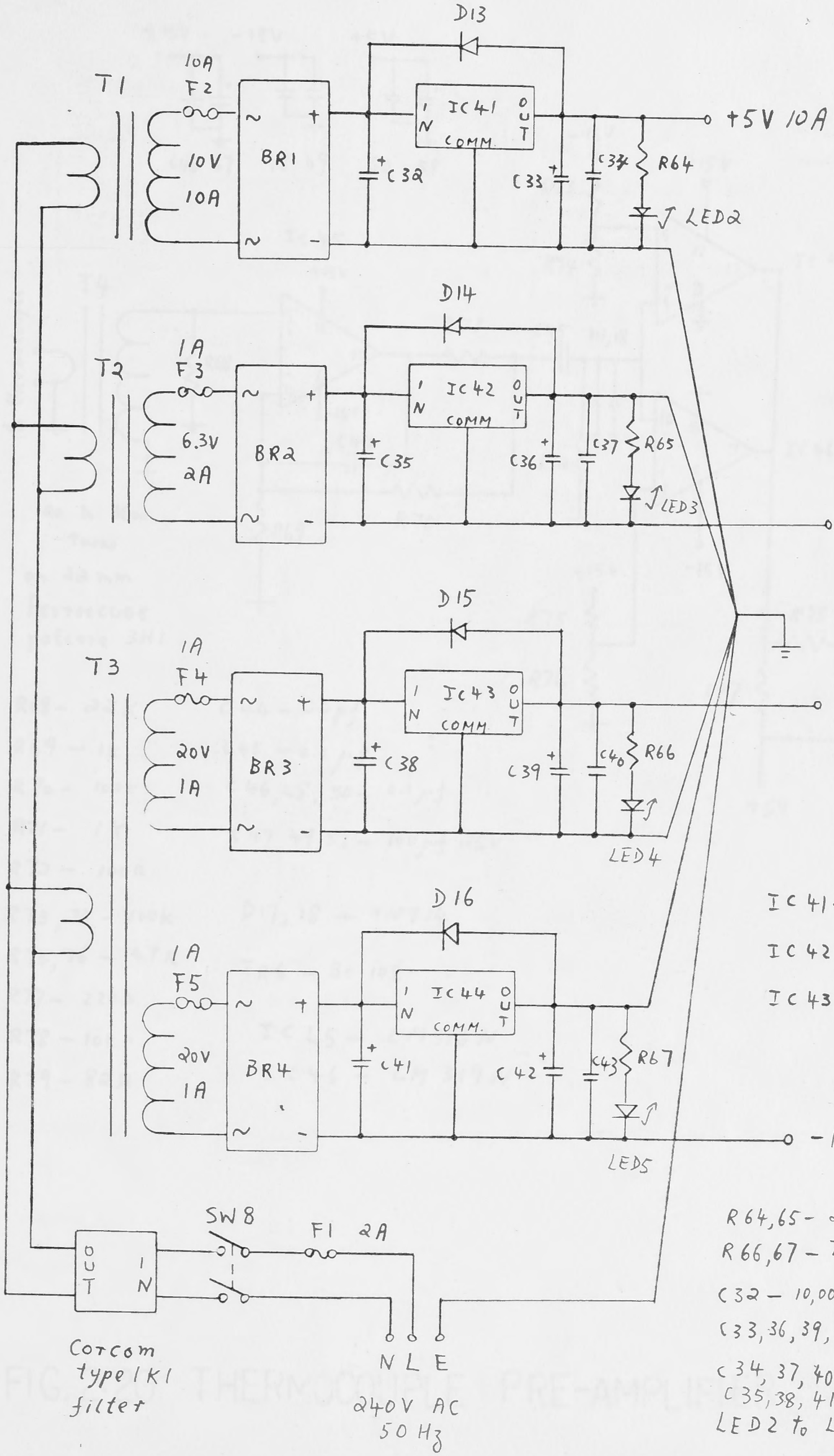

IC 41 – MIVR 42050

IC 42 – LM 309 K

IC 43, 44 – μA 7815

R 64, 65 – 220Ω

R 66, 67 – 750Ω

C 32 – 10,000 μf 16V

C 33, 36, 39, 42 – 100 μf 25V

C 34, 37, 40, 43 – 0.1 μf

C 35, 38, 41 – 2500 μf 25V

LED 2 to LED 5 – HP 5082/4850 red light emitting diodes

BR 1 –

BR 2 to BR 4 – VM 68

D 13 – IN 4719

D 14 to D 16 – IN 4001

FIG. 2·19 POWER SUPPLY UNIT

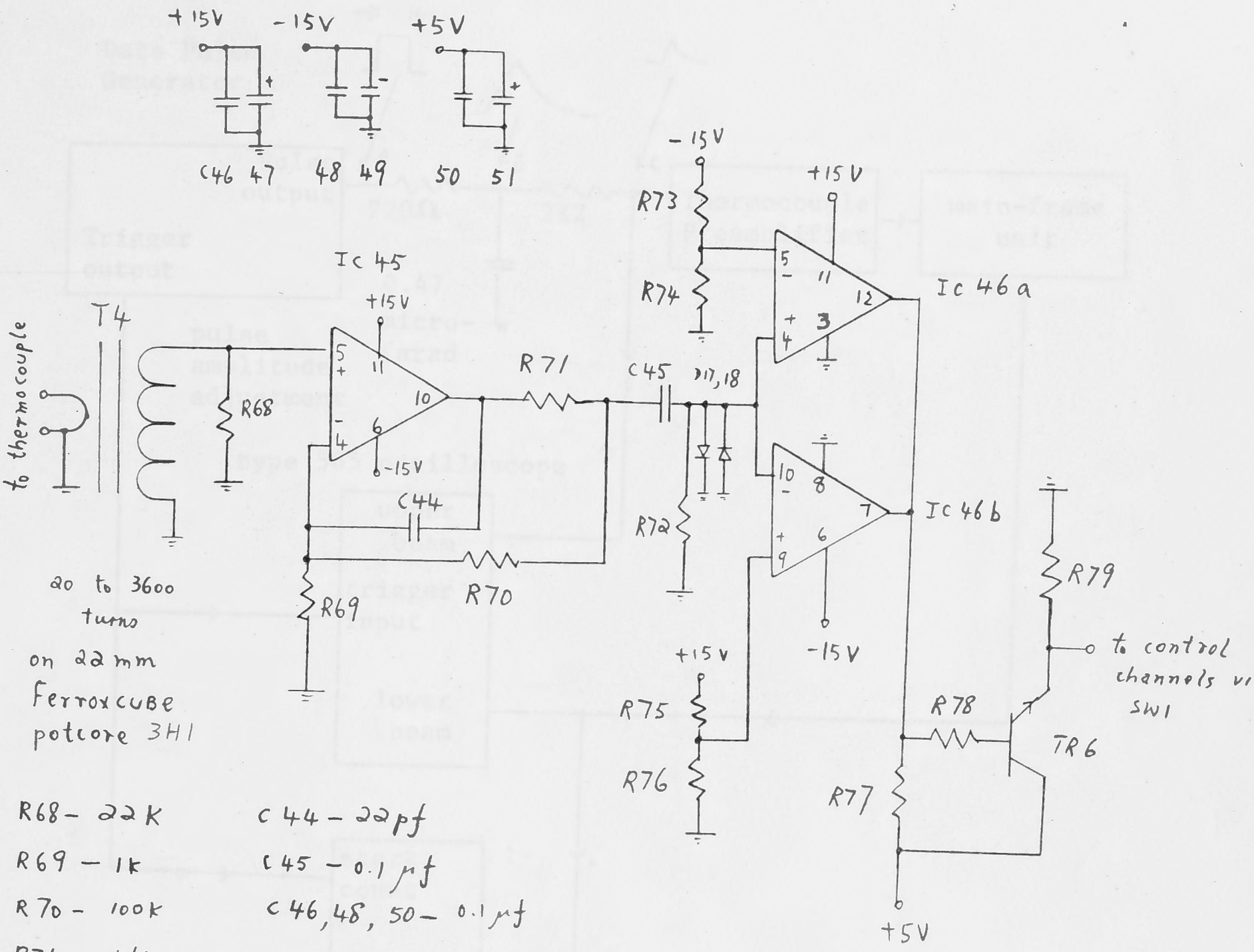

20 to 3600 turns on 22 mm Ferroxcube potcore 3H1

R68 – 22K
R69 – 1k
R70 – 100k
R71 – 1K
R72 – 100Ω
R73, 75 – 100k
R74, 76 – 47Ω
R77 – 220Ω
R78 – 10kΩ
R79 – 82Ω

C44 – 22pf
C45 – 0.1 μf
C46, 48, 50 – 0.1 μf
C47, 49, 51 – 100 μf 25V

D17, 18 – IN914

TR6 – Bc 108

IC 45 – LM318N
IC 46 – LM 319N

FIG. 2·20 THERMOCOUPLE PRE-AMPLIFIER

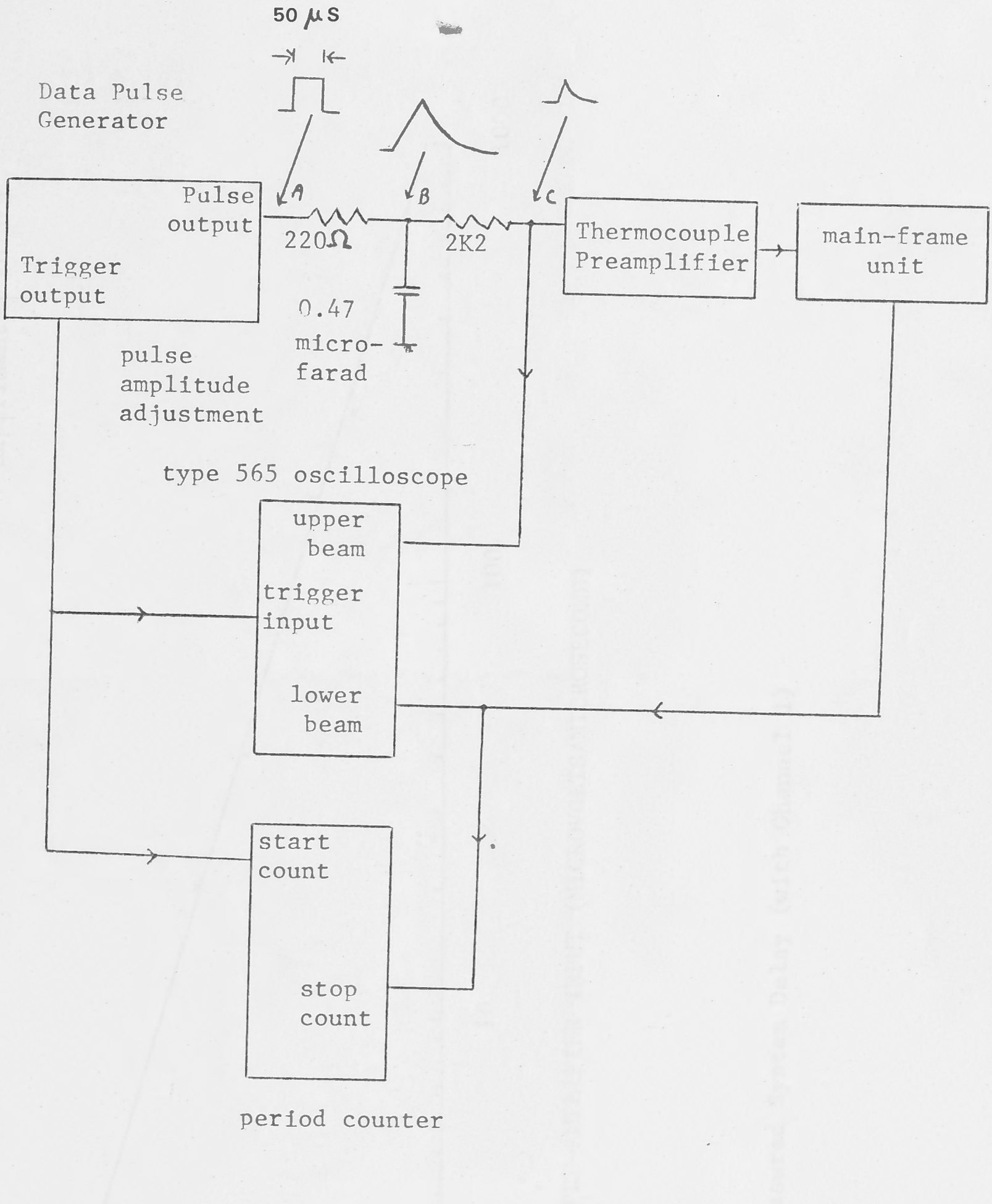

Fig. 2.21: Bench test of system delay for various input slew rates.

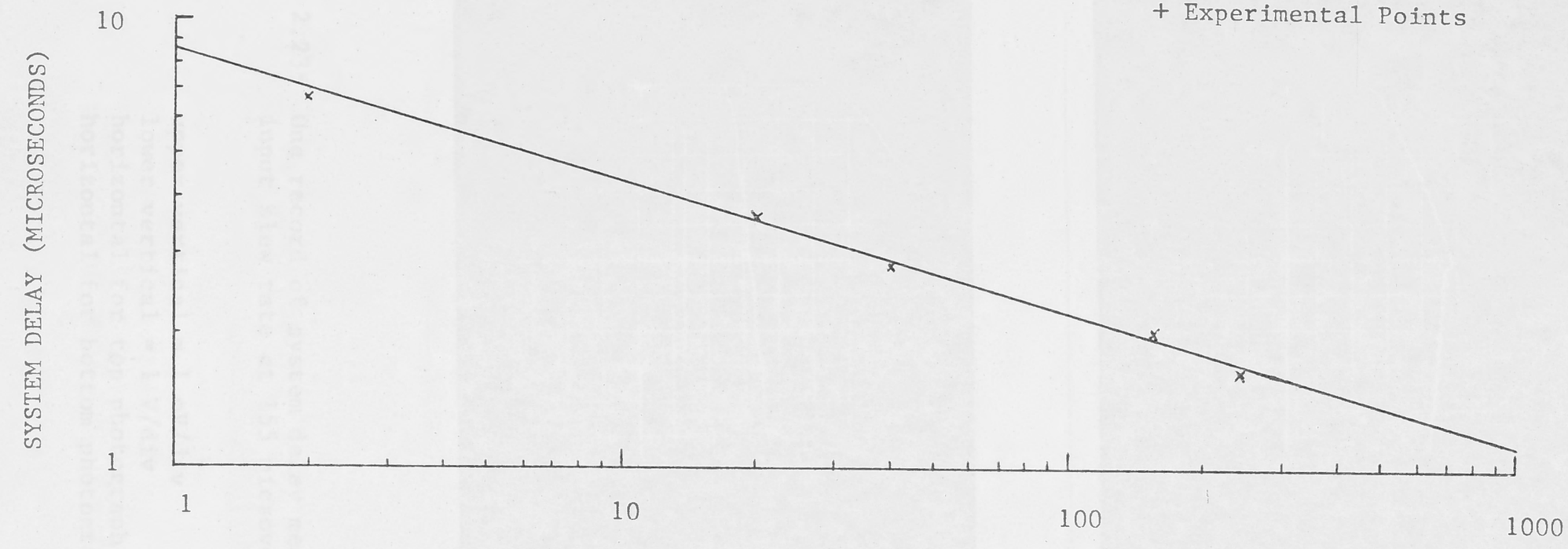

Fig. 2.22: Measured System Delay (with Channel 1)

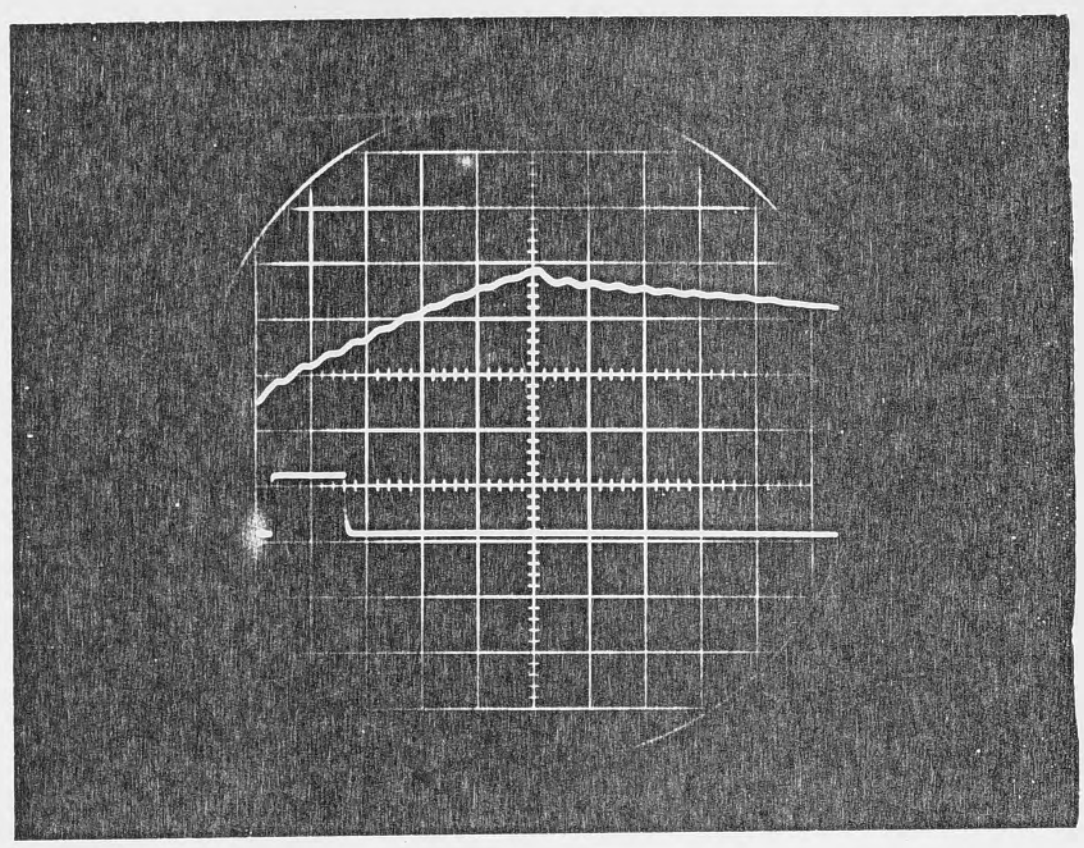

Top trace:
Signal at point C
of Fig. 2.21

Bottom trace:
Output from main
frame

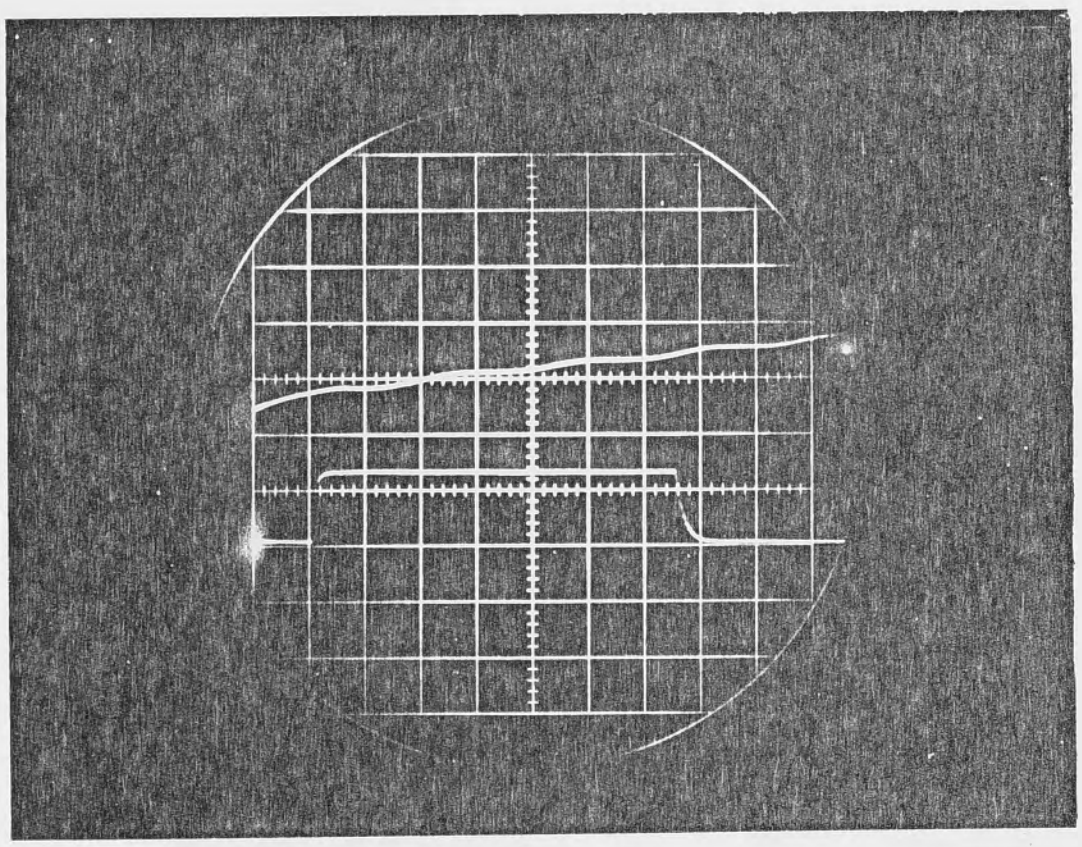

Top trace:
Signal at point C
of Fig. 2.21

Bottom trace:
Output from main
frame

Fig. 2.23: One record of system delay measurement with input slew rate at 155 microvolts/microseconds.

upper vertical = 1 mV/div
lower vertical = 1 V/div
horizontal for top photograph = 10 microseconds/div
horizontal for bottom photograph = 2 microseconds/div

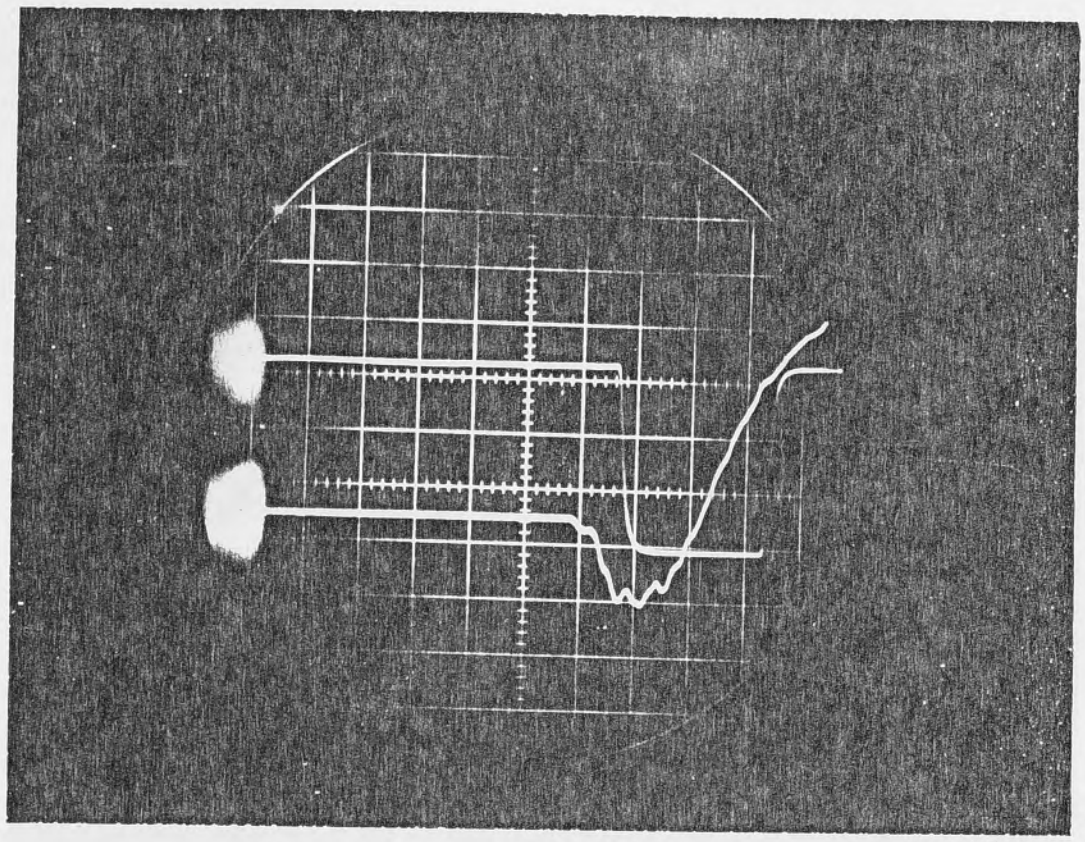

Top trace:
Timing system output

Bottom trace:
Thin-film gauge signal

Fig. 2.24: Photograph showing presence of precursor, causing reversal in signal output at the rising edge.

test gas = air; shock speed = 3.1 km/sec.
initial pressure = 50 torr; upper vert = 1 V/div;
lower vert = 10 mV/div; horizontal = 5 microseconds/div;
delay = 70 microseconds;

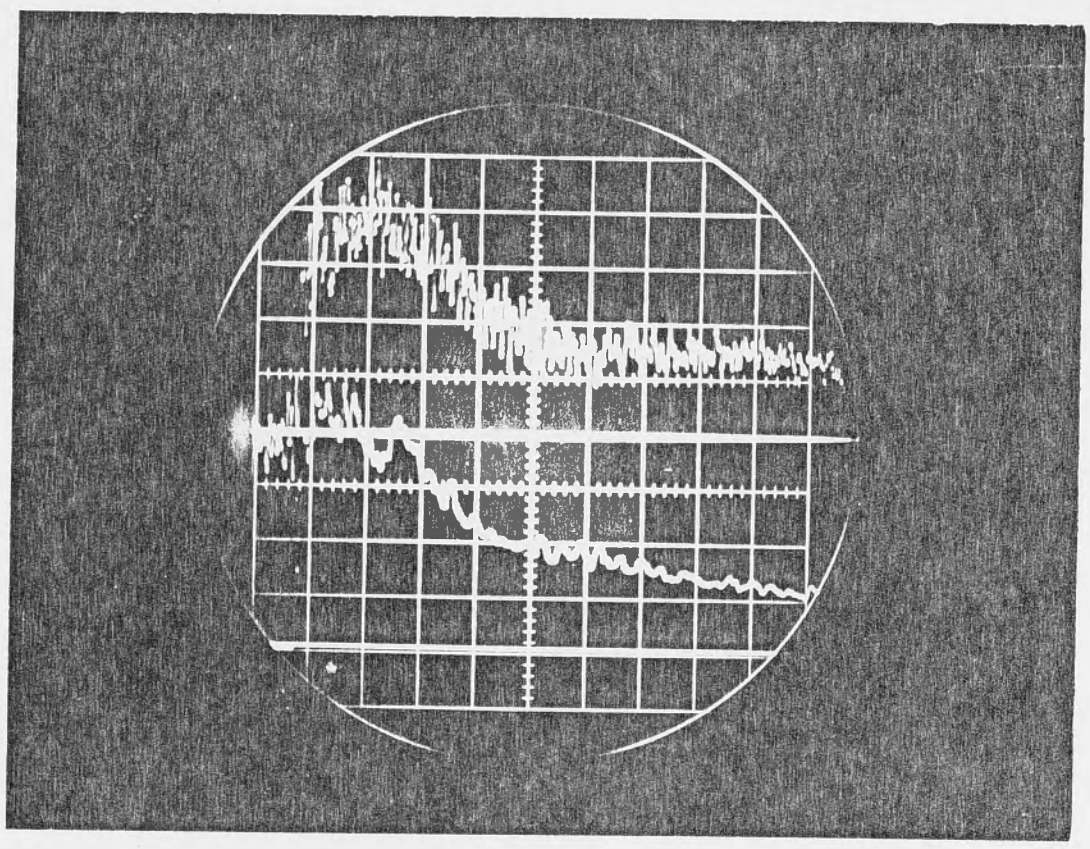

Top trace:
Heat transfer rate from thin-film gauge

Bottom trace:
Heat transfer rate from calorimeter gauges

Fig. 2.25: Photograph showing heat transfer rate to shock tube wall.

test gas = air; shock speed = 2.4 km/sec;
initial pressure = 760 torr; upper vert = 100 mV/div;
lower vert = 200 mV/div; horizontal = 50 microseconds/div;
delay = 100 microseconds.

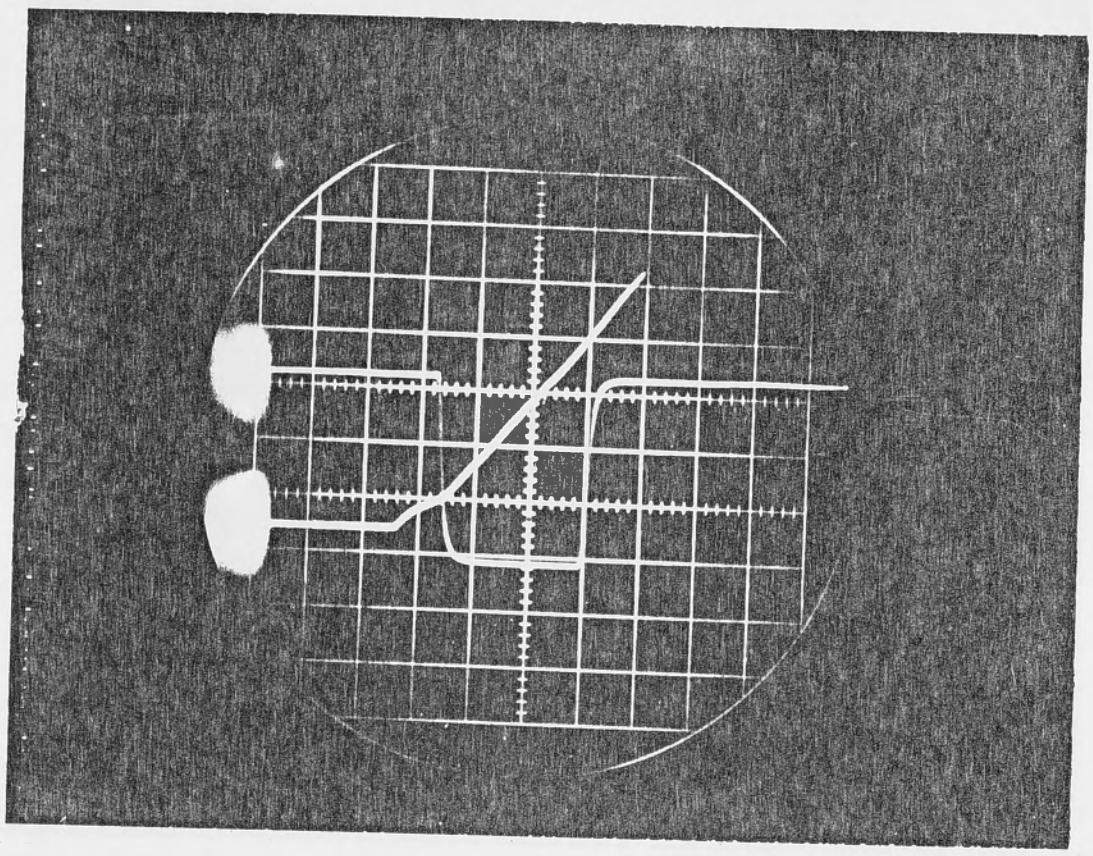

Top trace:
Timing system
output

Bottom trace:
Thin-film gauge
output

Fig. 2.26: Photograph showing case of positive charge pick-up.

upper vert = 1 V/div; lower vert = 10 mV/div;
horizontal = 5 microseconds/div; test gas = air;
shock speed = 2 km/s; initial pressure = 760 torr.

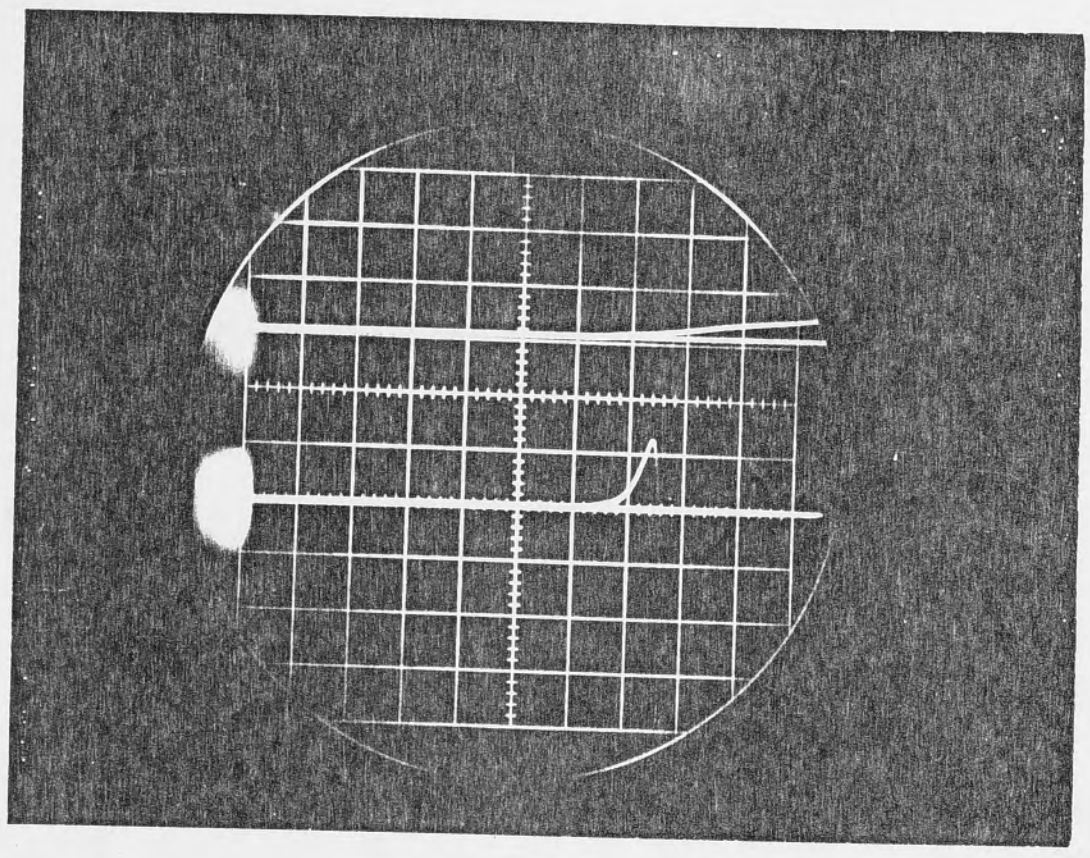

Top trace:
Thin-film gauge signal

Bottom trace:
Ionisation gauge signal

Fig. 2.27a

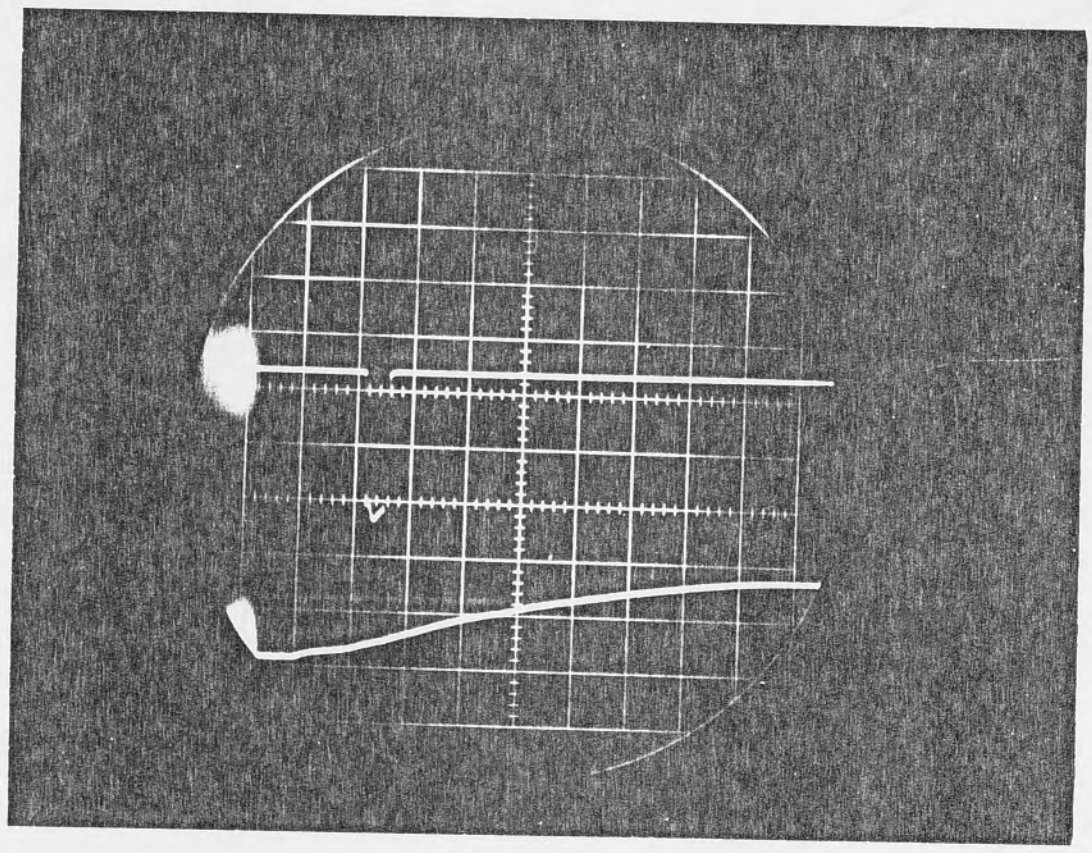

Top trace:
Ionisation gauge signal via trigger unit

Bottom trace:
Thin-film gauge signal

Fig. 2.27b

Photographs showing positive charge pick-up from precursor.

for Fig. 2.27a: upper vert = 20 mV/div; lower vert = 10 mV/div;
for Fig. 2.27b: upper vert = 0.5 V/div; lower vert = 10 mV/div;
horizontal for both = 5 microseconds/div; test gas = nitrogen;
shock speed = 2.8 km/sec; initial pressure = 100 torr.

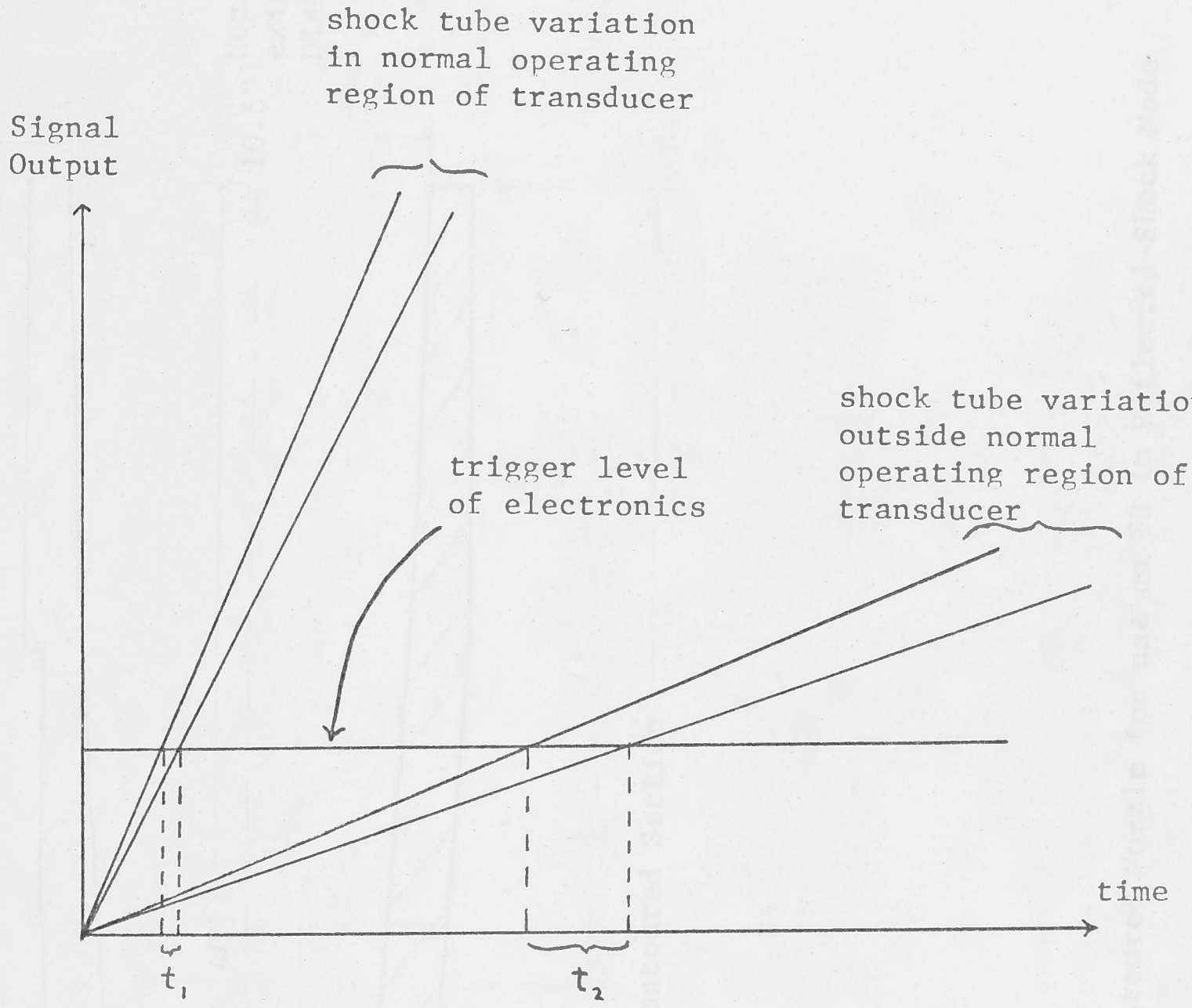

Fig. 2.28: Effect of a timing transducer operating outside its normal region

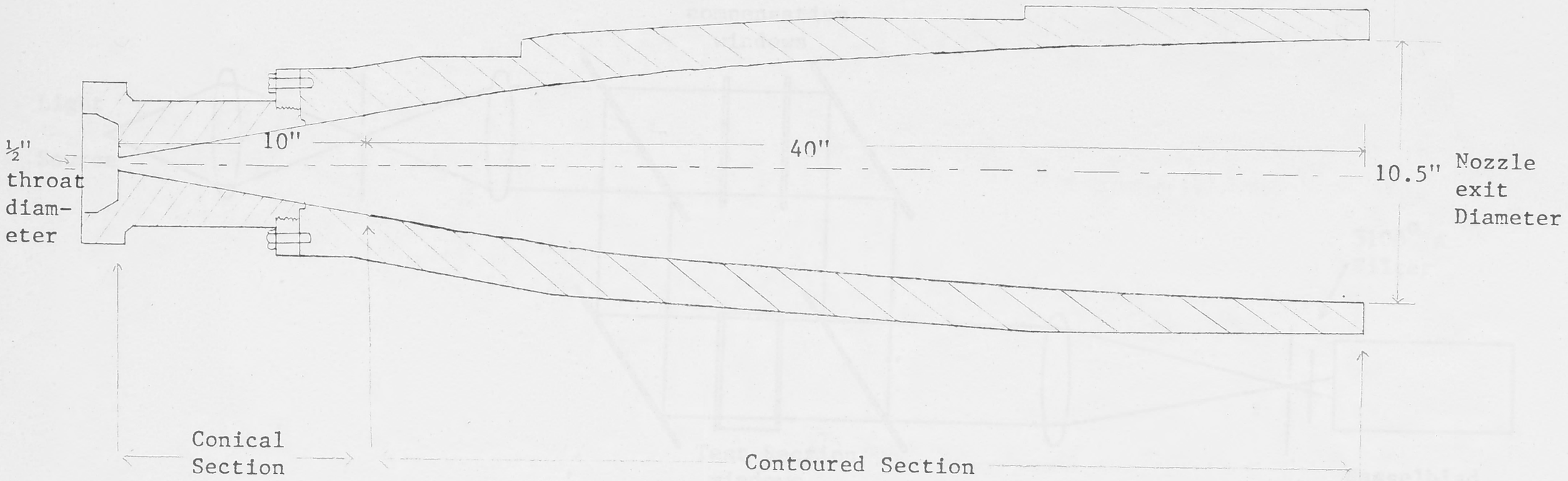

Aluminium

Stainless Steel

Fig. 3.1: Cross-Section of Contoured Nozzle for use on T3 in Reflected-Shock Mode

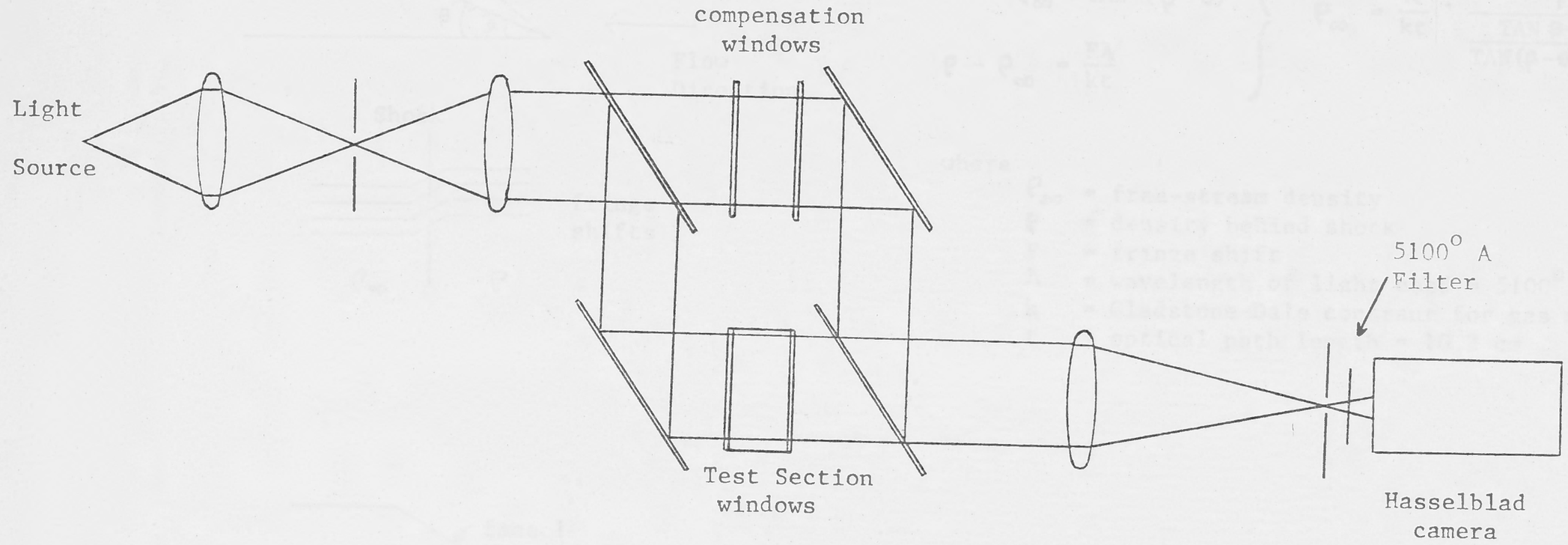

Mach Zender Interferometer

Fig. 3.2: Set-up for the measurement of Free-Stream Density

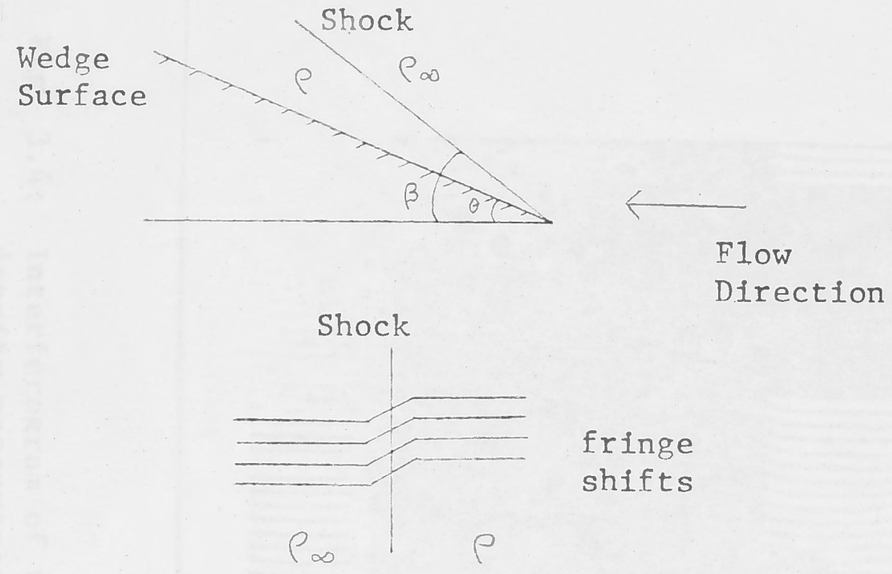

For a straight shock

$$\left.\begin{aligned} \frac{\rho}{\rho_\infty} &= \frac{\text{TAN } \beta}{\text{TAN } (\beta - \theta)} \\ \rho - \rho_\infty &= \frac{F\lambda}{kt} \end{aligned}\right\} \quad \rho_\infty = \frac{\lambda}{kt} \cdot \frac{F}{\frac{\text{TAN } \beta}{\text{TAN}(\beta-\theta)} - 1}$$

where

ρ_∞ = free-stream density
ρ = density behind shock
F = fringe shift
λ = wavelength of light used = 5100° A
k = Gladstone-Dale constant for gas mixture
t = optical path length = 10.2 cm

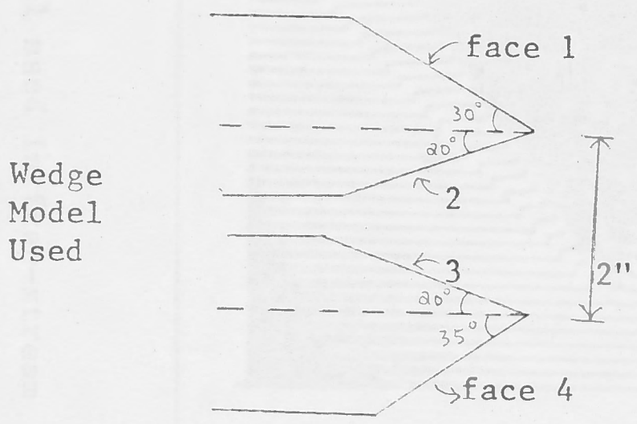

Fig. 3.3: Principle of Free-Stream Density Measurement.

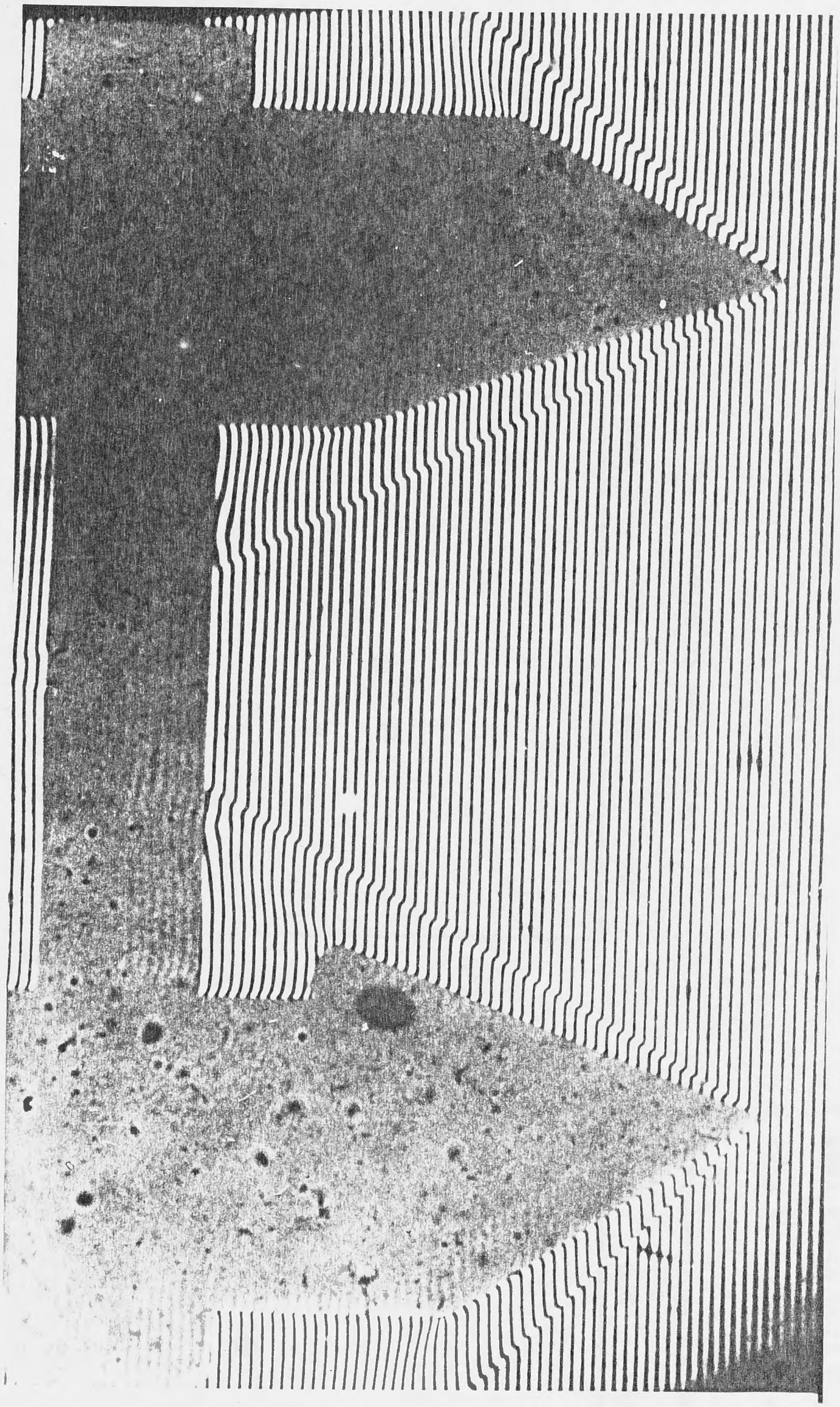

Fig. 3.4: Interferogram of the wedge model used in free-stream density measurements

Free-Stream Density

$\rho_\infty \times 10^{-6}$ $\frac{GM}{CC}$

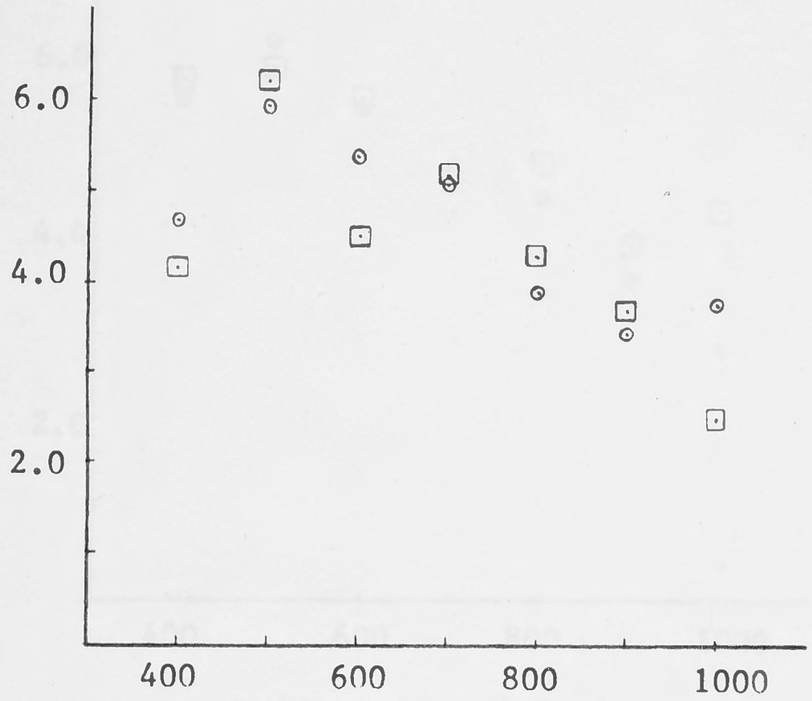

Normalised Density

$\frac{\rho_\infty P_o}{U_s} \times 10^{-9}$ $\frac{GM\text{-}ATM\text{-}SEC}{CM^4}$

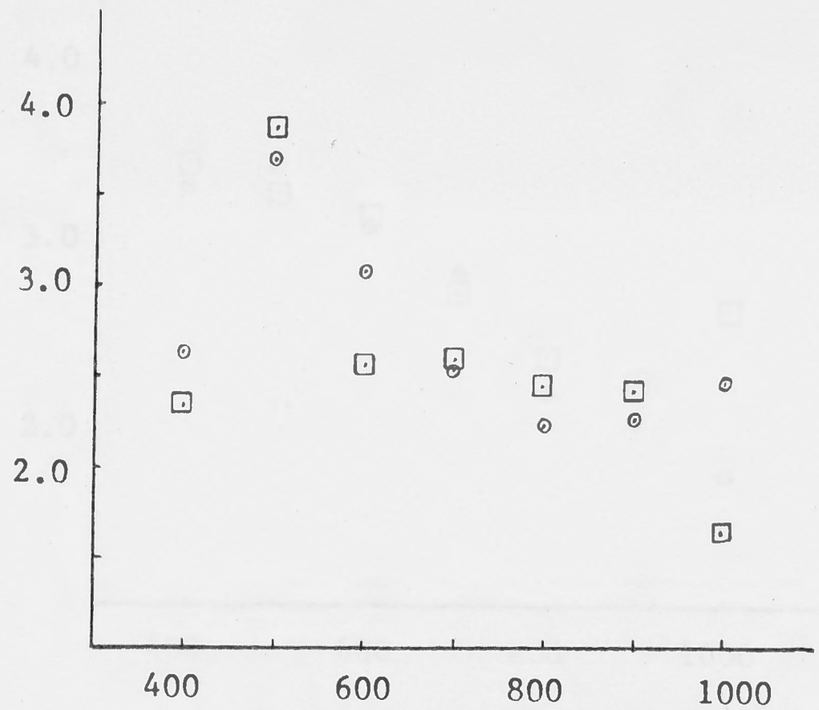

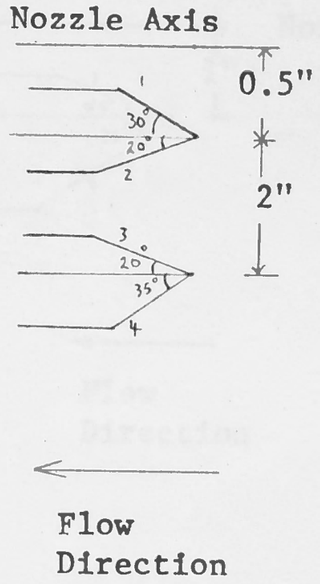

⊙ Measurements from wedge face 2

⊡ Measurements from wedge face 3

Fig. 3.5: Contoured Nozzle Free-Stream Density for Air.

Initial Shock Tube Pressure = 6" Hg; Compression Ratio = 60;
Stagnation Enthalpy = 18 MJ/KGM.

Free-Stream Density

$\rho_\infty \times 10^{-6} \frac{GM}{CC}$

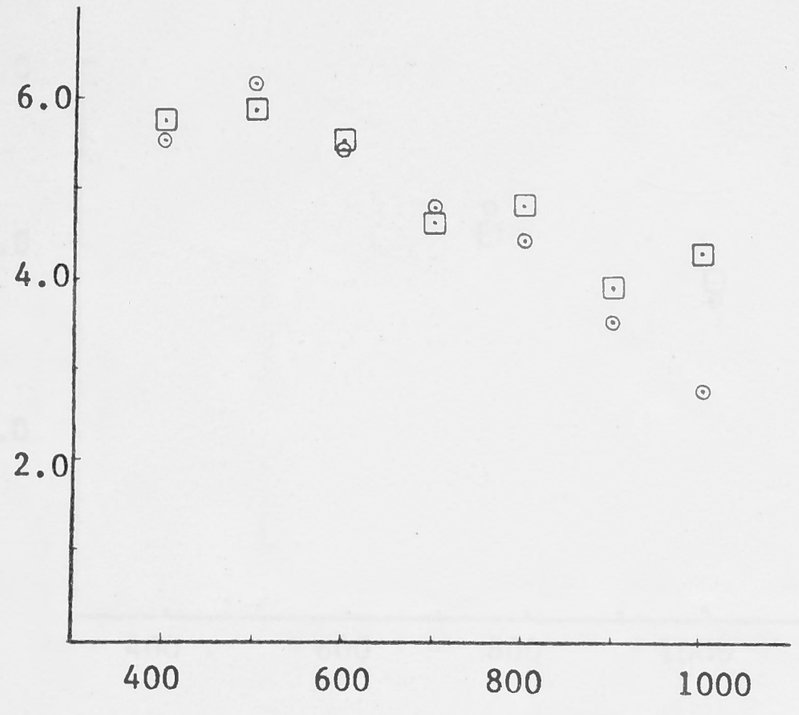

Normalised Free-Stream Density

$\frac{\rho_\infty P_o}{U_s} \times 10^{-9} \frac{GM\text{-}ATM\text{-}SEC}{CM^4}$

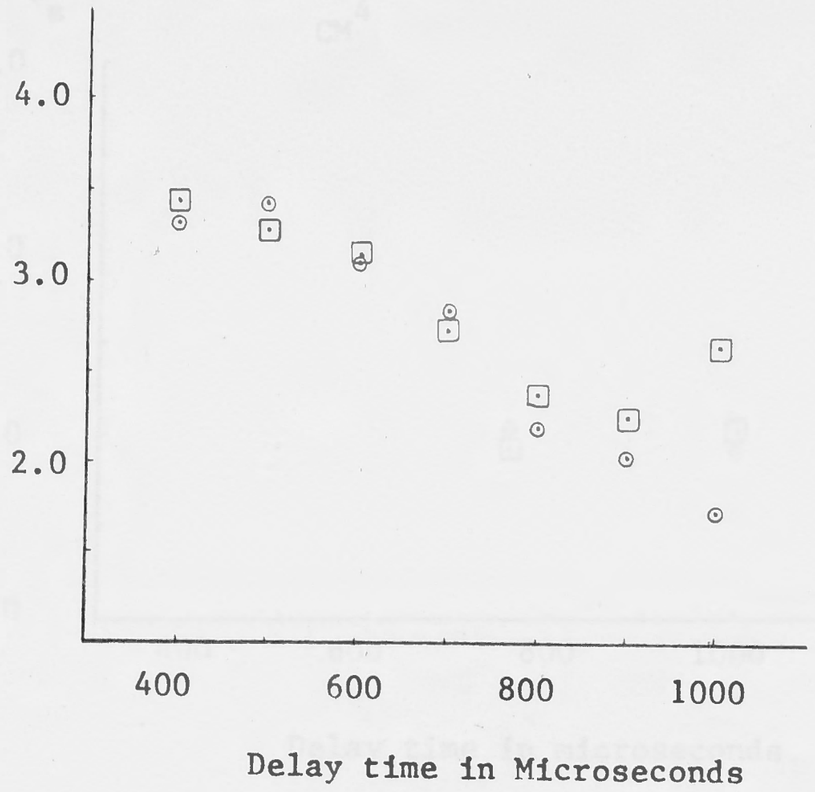

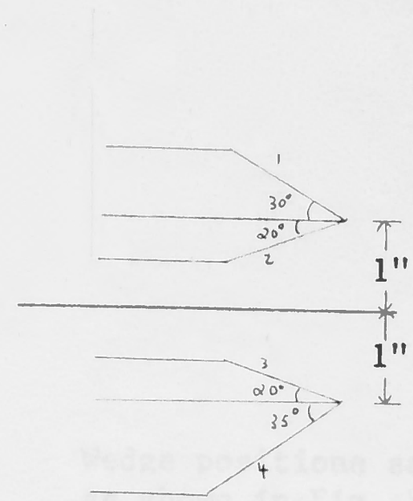

⊙ Measurements from wedge face 2

⊡ Measurements from wedge face 3

Fig. 3.6: Contoured Nozzle Free-Stream Density for Air.
Same condition as Fig. 3.5.

Free-Stream Density

$\rho_\infty \times 10^{-6} \frac{GM}{CC}$

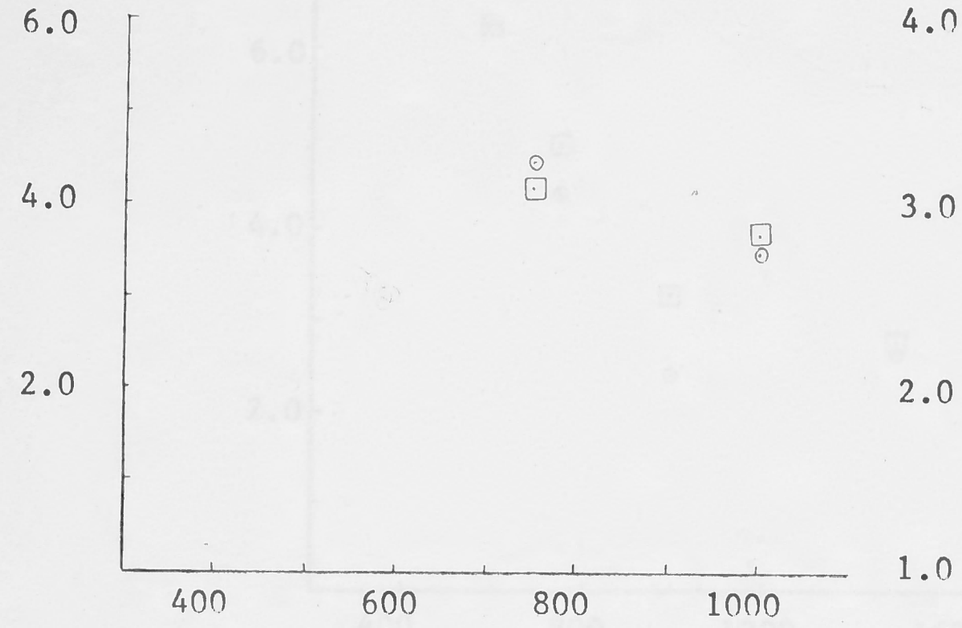

Delay time in microseconds

Normalised Density

$\frac{\rho_\infty P_o}{U_s} \times 10^{-9} \frac{GM\text{-}ATM\text{-}SEC}{CM^4}$

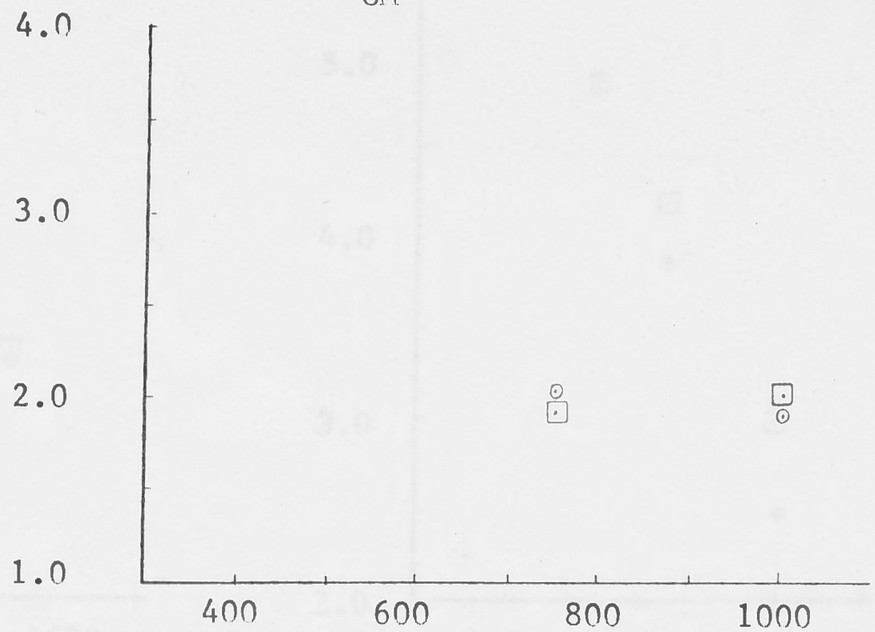

Delay time in microseconds

Wedge positions same as shown in Fig. 3.5

⊙ Measurements from wedge face 2

⊡ Measurements from wedge face 3

Fig. 3.7: Contoured Nozzle Free-Stream Density for Air.

Initial Shock Tube Pressure = 4" Hg; Compression ratio = 30;
Stagnation Enthalpy = 20 MJ/KGM.

Free-Stream Density

$\rho_\infty \times 10^{-6} \frac{GM}{CC}$

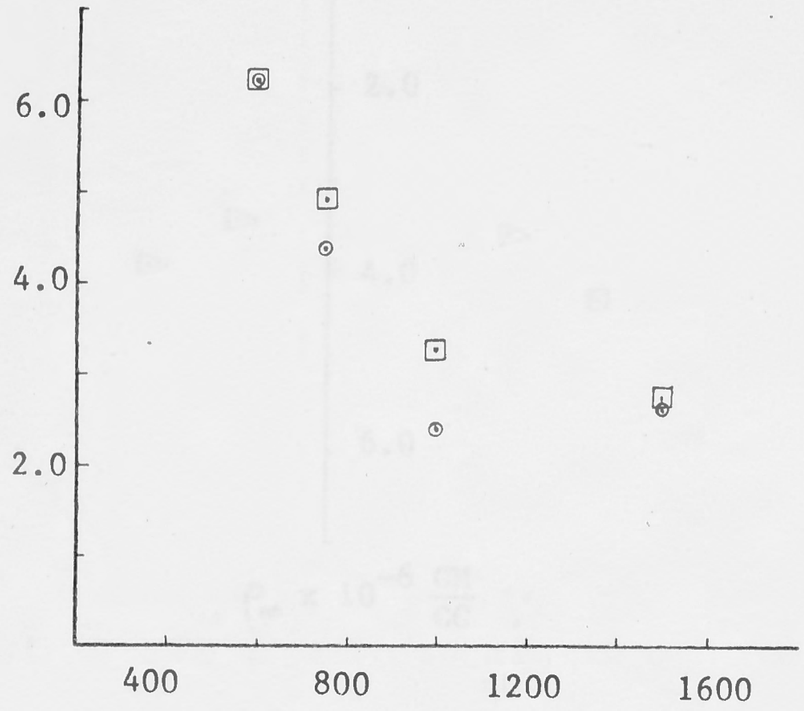

Delay time in Microseconds

Normalised Density

$\frac{\rho_\infty P_o}{U_s} \times 10^{-9} \frac{GM\text{-}ATM\text{-}SEC}{CM^4}$

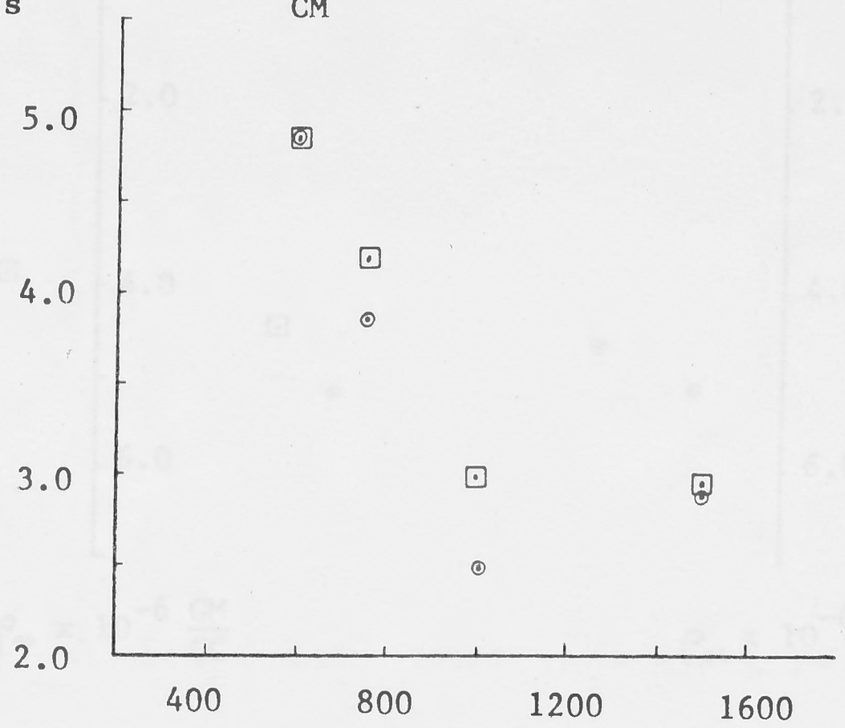

Delay time in Microseconds

⊙ Measurements from wedge face 2

⊡ Measurements from wedge face 3

Fig. 3.8: Contoured Nozzle Free-Stream Density for CO_2

Initial Shock Tube Pressure = 4" Hg;
Compression ratio = 30;
Stagnation Enthalpy = 7 MJ/KGM.

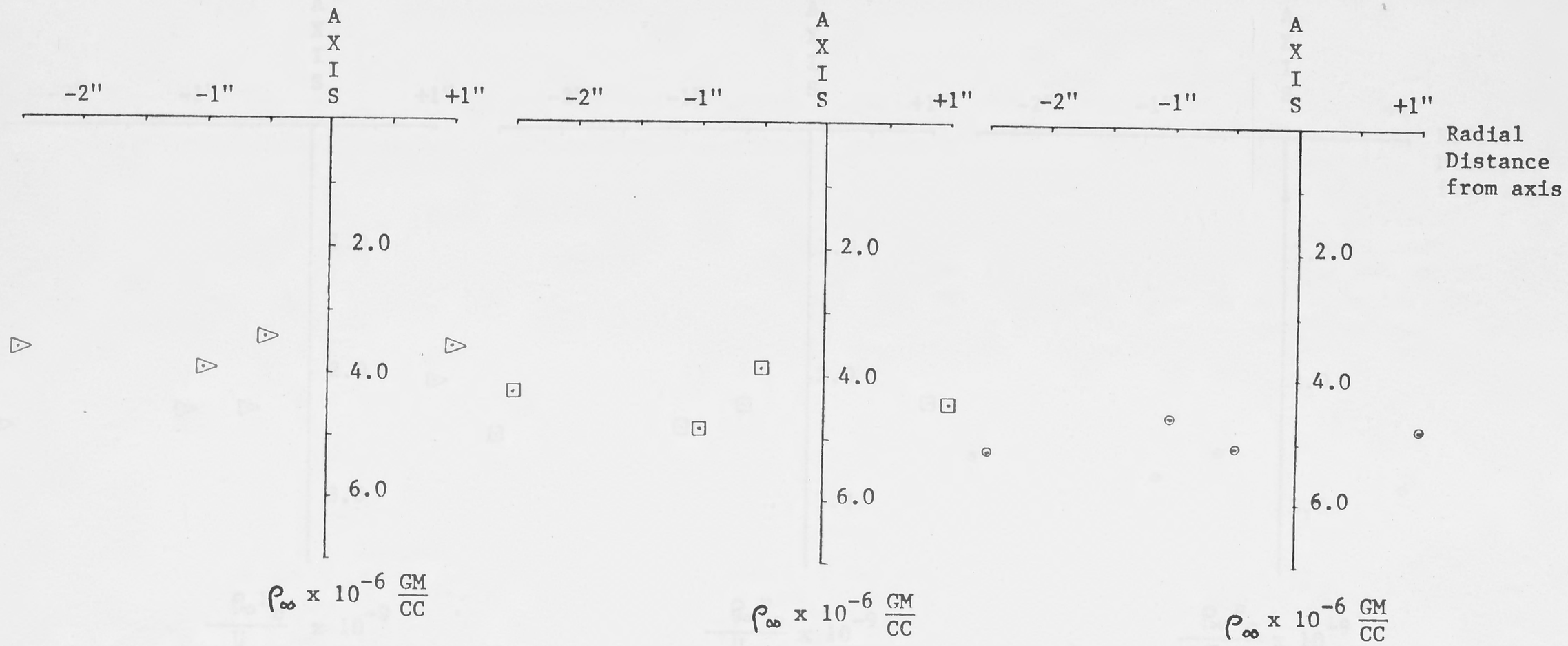

⊙ Measurements taken at 700 microseconds delay

⊡ Measurements taken at 800 microseconds delay

△ Measurements taken at 900 microseconds delay

Fig. 3.9: Radial Profile of Contoured Nozzle Free-Stream Density for Air. Condition same as in Fig. 3.5.

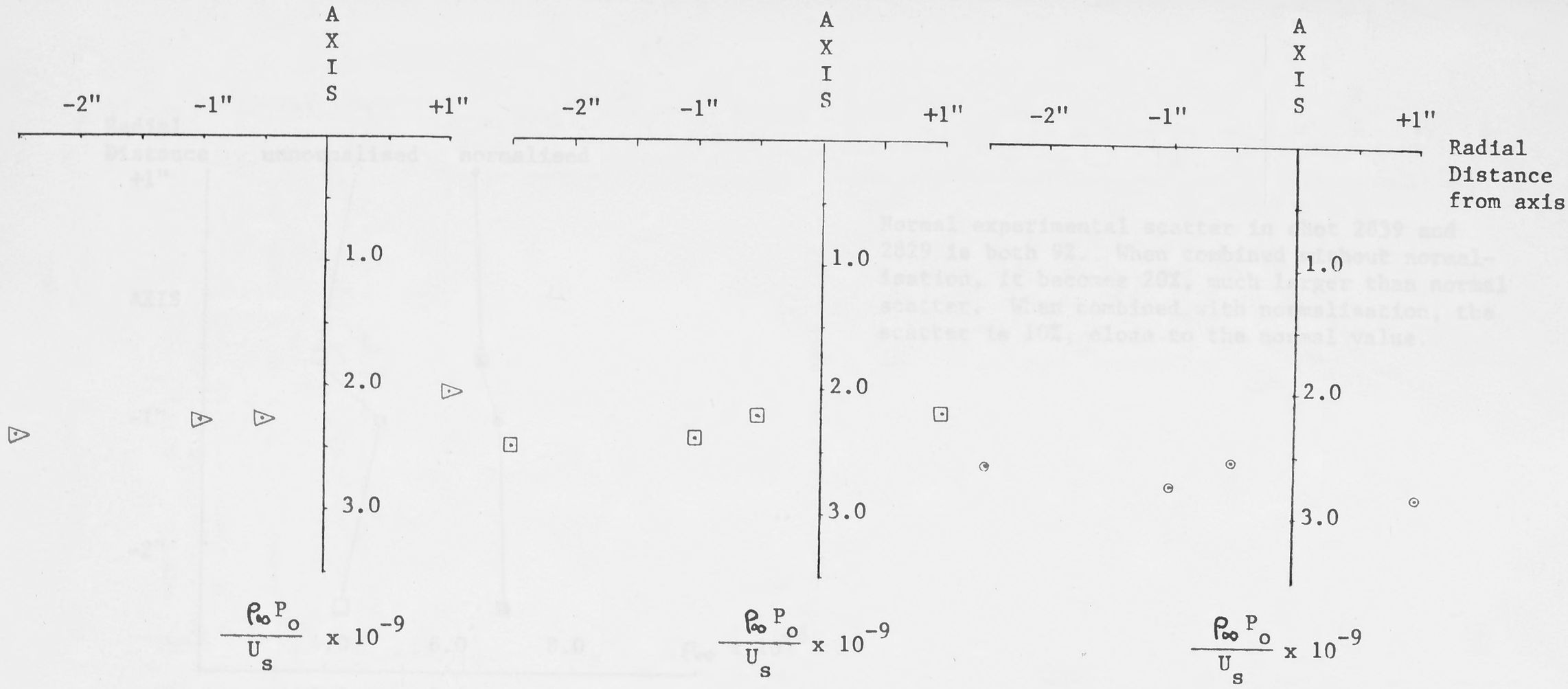

⊙ Measurements taken at 700 microseconds delay

⊡ Measurements taken at 800 microseconds delay

△ Measurements taken at 900 microseconds delay

Fig. 3.10: Radial Profile of Contoured Nozzle Normalised Free-Stream Density for Air. Conditions same as in Fig. 3.5.

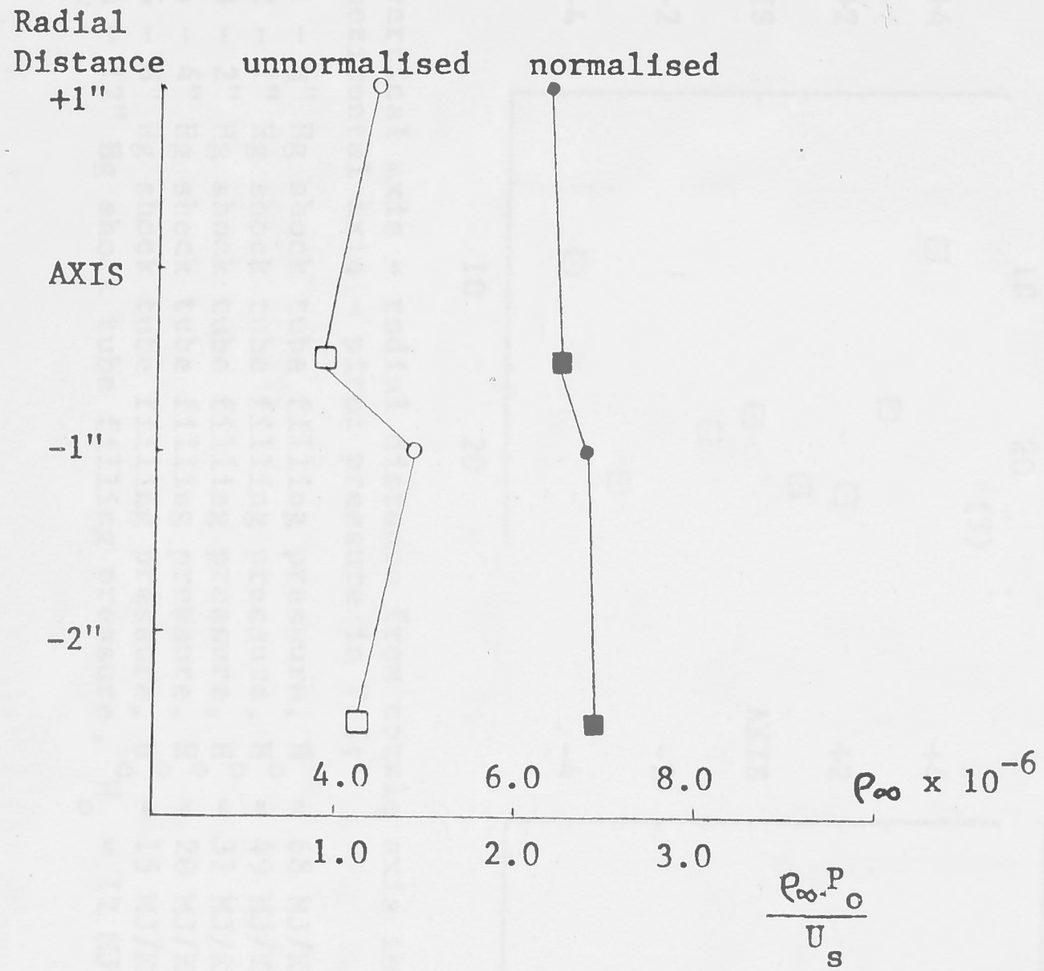

Normal experimental scatter in shot 2839 and 2829 is both 9%. When combined without normalisation, it becomes 20%, much larger than normal scatter. When combined with normalisation, the scatter is 10%, close to the normal value.

Fig. 3.11: Effect of normalisation on the scatter of free-stream density measurement data points. Data derived from Fig. 3.5 and 3.6.

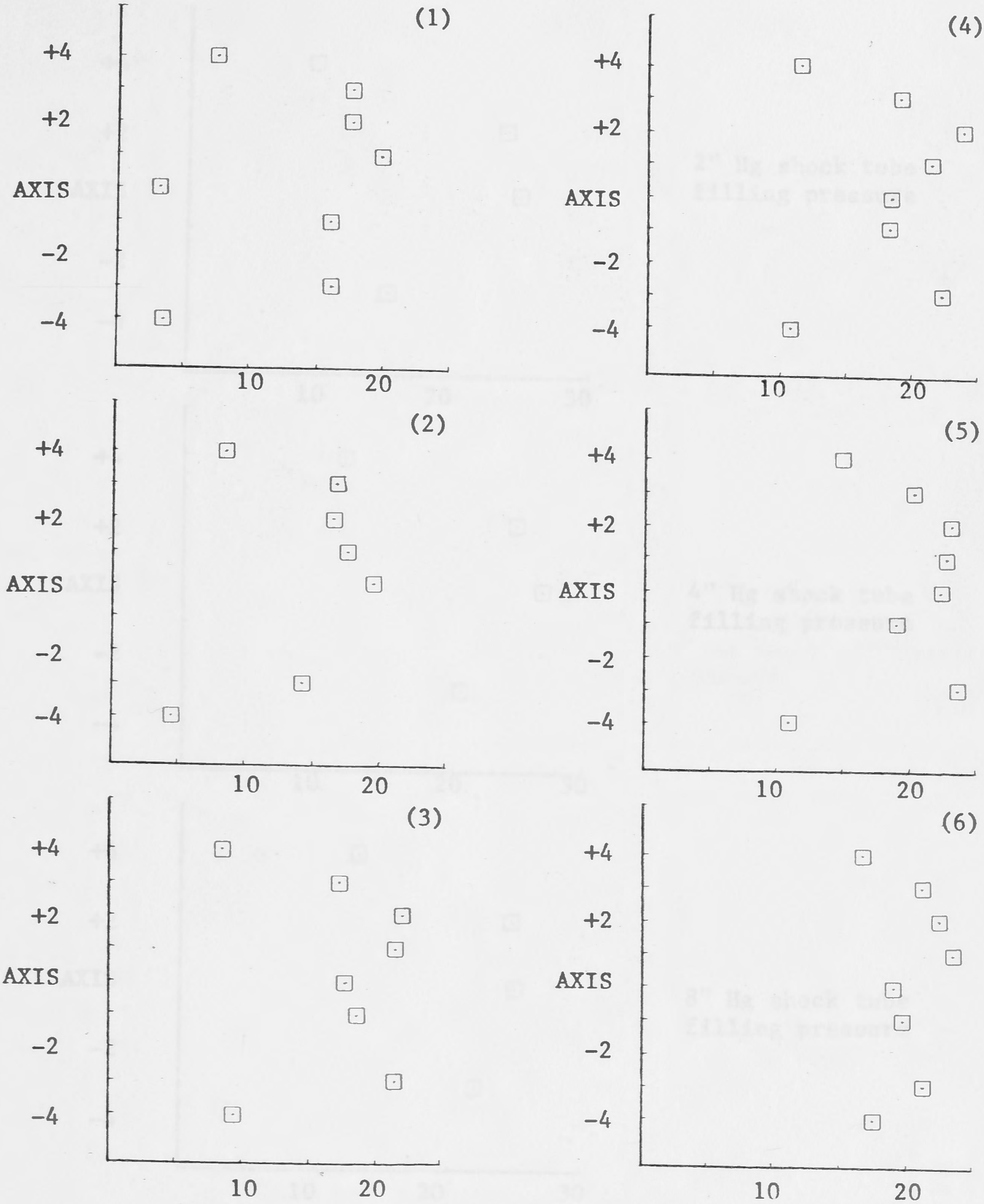

vertical axis - radial distance from nozzle axis in inches;
horizontal axis - pitot pressure in PSI;

1 - ½" Hg shock tube filling pressure, H_o = 68 MJ/KGM;
2 - 1" Hg shock tube filling pressure, H_o = 49 MJ/KGM;
3 - 2" Hg shock tube filling pressure, H_o = 31 MJ/KGM;
4 - 4" Hg shock tube filling pressure, H_o = 20 MJ/KGM;
5 - 8" Hg shock tube filling pressure, H_o = 15 MJ/KGM;
6 - 12" Hg shock tube filling pressure, $^{o}H_{o}$ = 12 MJ/KGM

Fig. 3.12: Contoured Nozzle Radial Pitot Pressure Profile for Air, taken at 2" inside Nozzle Exit Plane

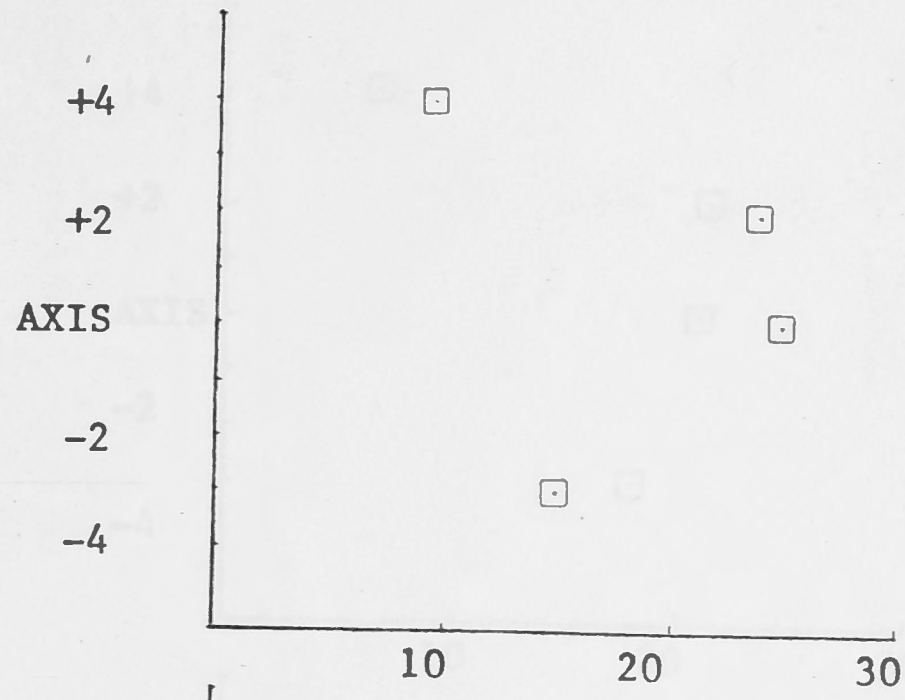

2" Hg shock tube filling pressure

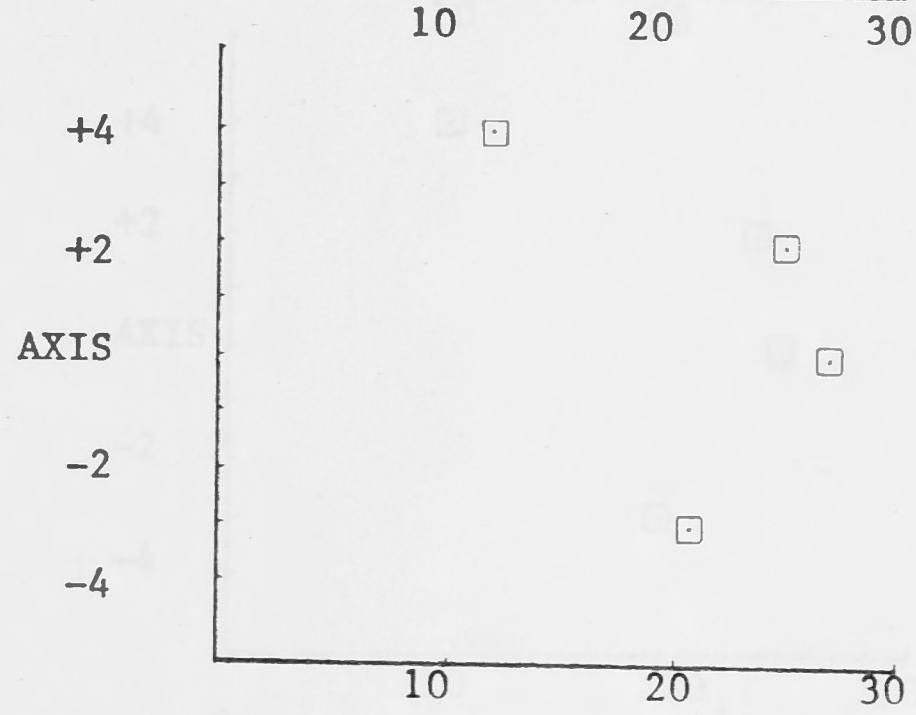

4" Hg shock tube filling pressure

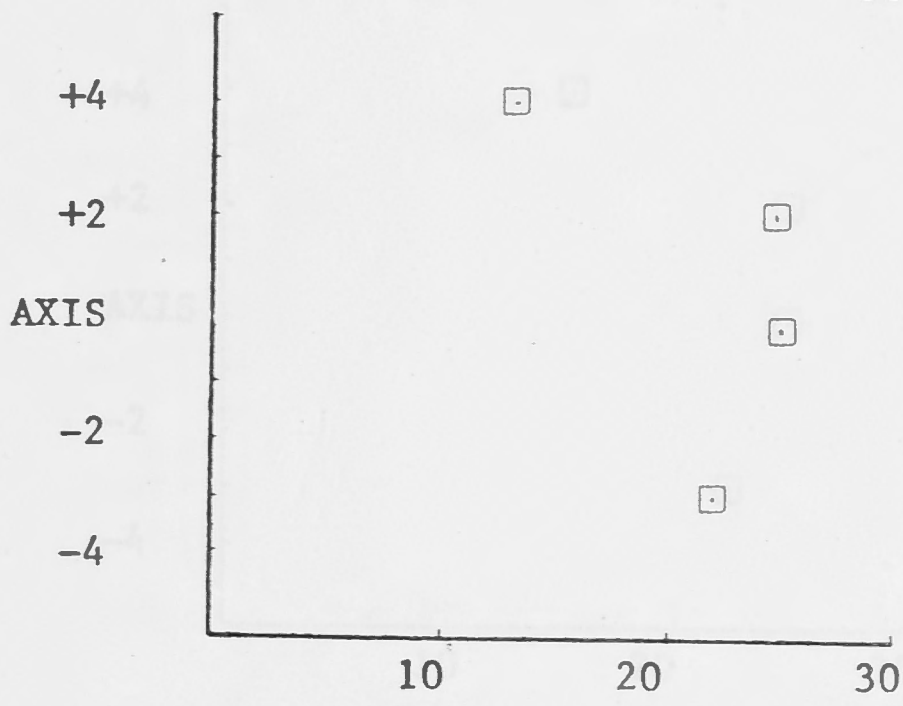

8" Hg shock tube filling pressure

vertical axis - radial distance from nozzle axis in inches;
horizontal axis - pitot pressures in PSI;
H_o as given in Fig. 3.12.

Fig. 3.13: Contoured Nozzle Radial Pitot Pressure Profile for Air, taken at Nozzle Exit Plane.

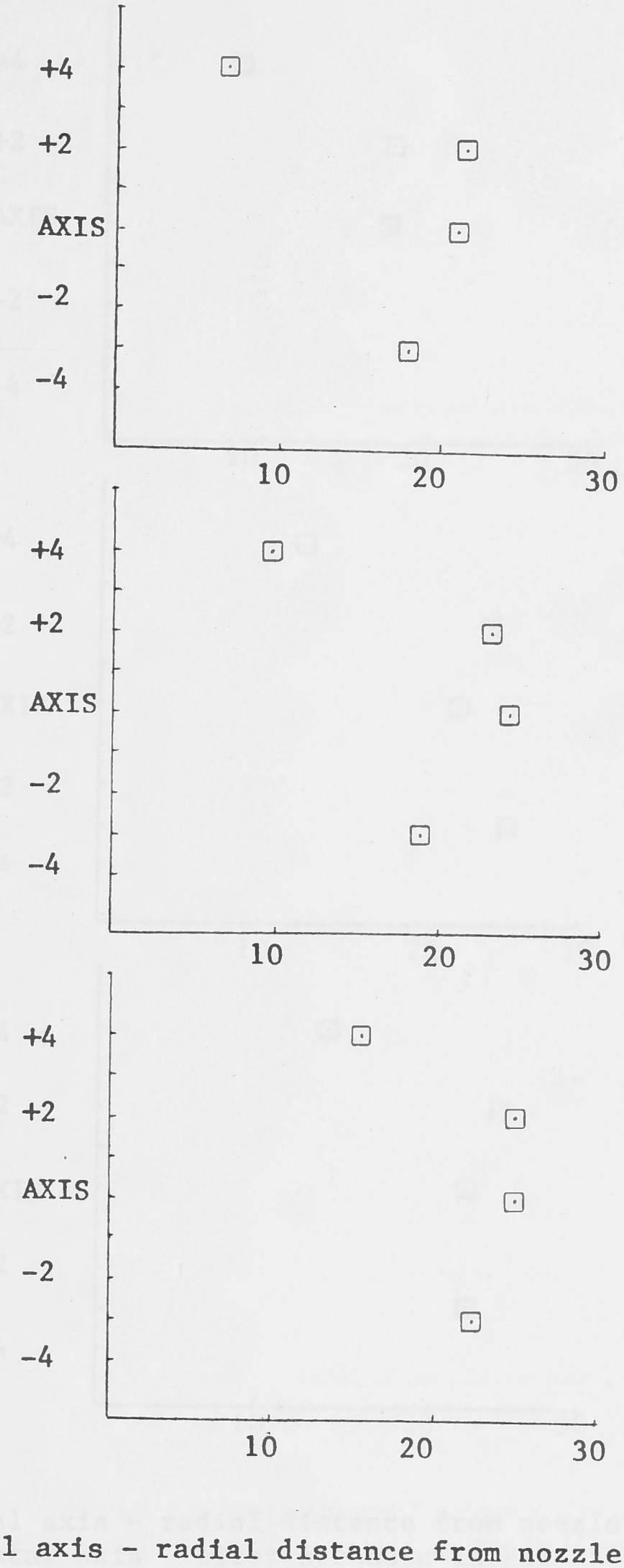

2" Hg shock tube filling pressure

4" Hg shock tube filling pressure

8" Hg shock tube filling pressure

vertical axis - radial distance from nozzle axis in inches;
horizontal axis - pitot pressures in PSI;
H_o as given in Fig. 3.12.

Fig. 3.14: Contoured nozzle Radial Pitot Pressure Profile for Air, taken at 2" outside nozzle exit plane

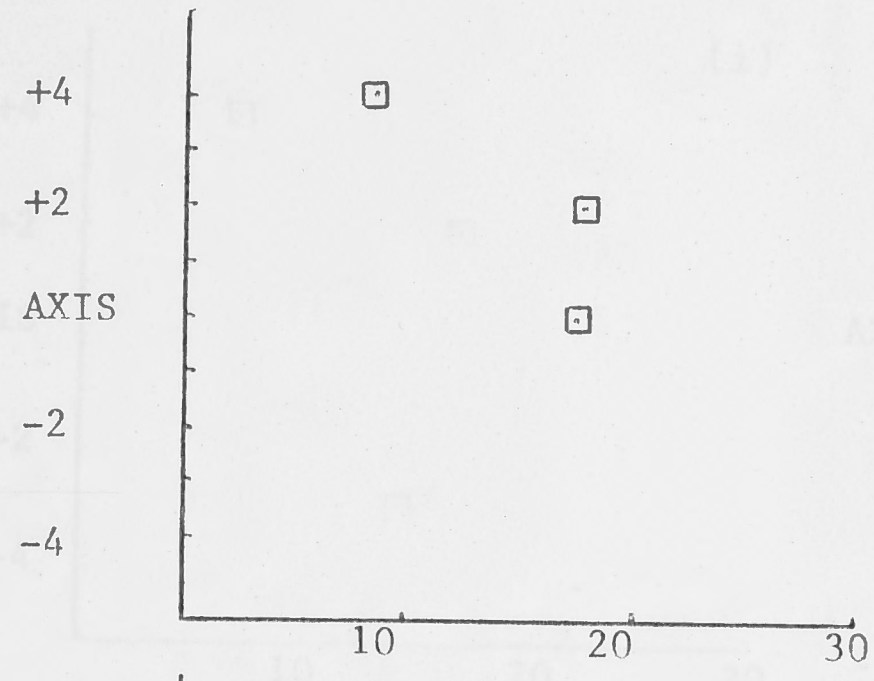

2" Hg shock tube filling pressure

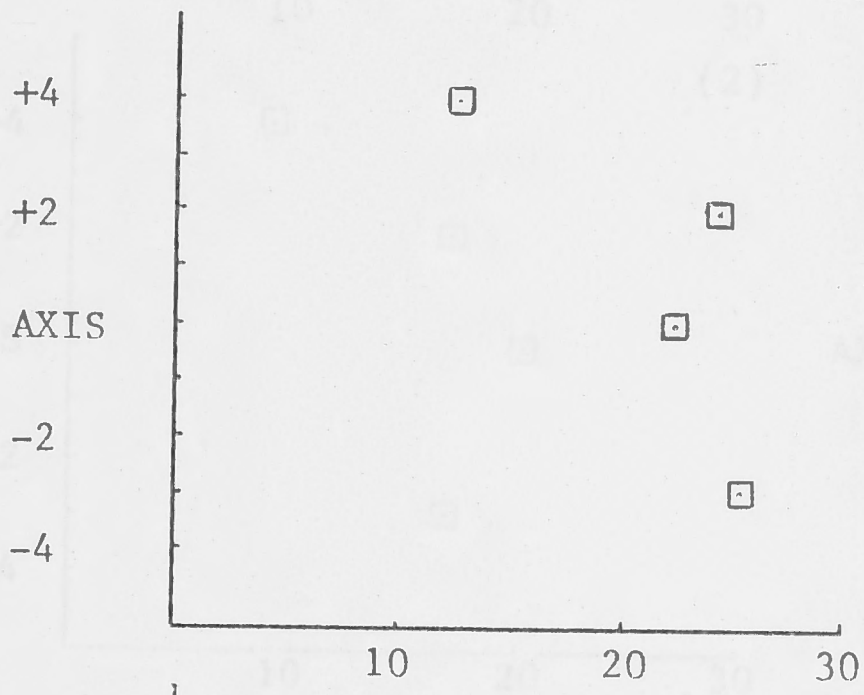

4" Hg shock tube filling pressure

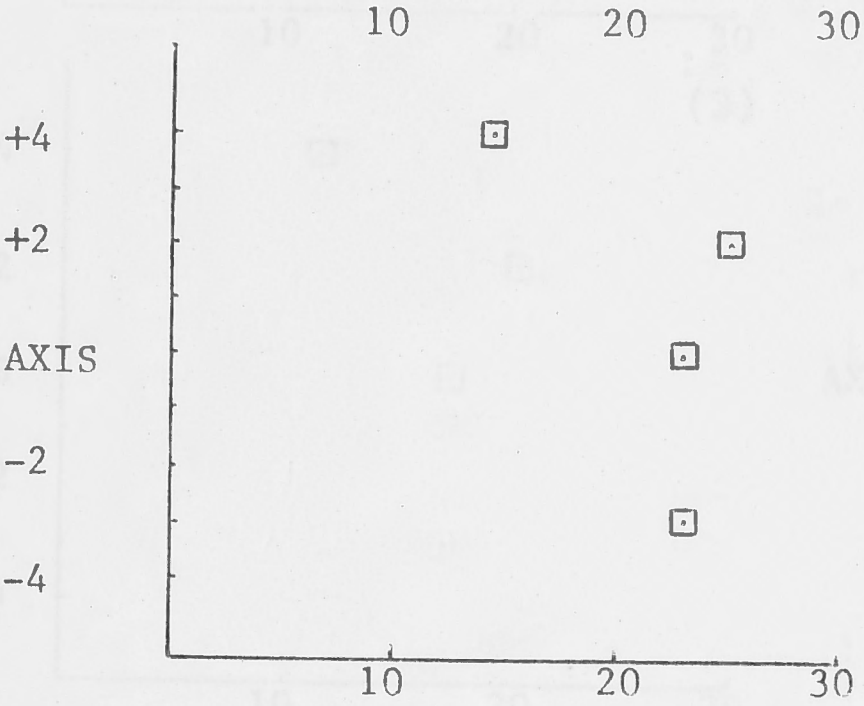

8" Hg shock tube filling pressure

vertical axis - radial distance from nozzle axis in inches;
horizontal axis - pitot pressure in PSI;
H_o as given in Fig. 3.12

Fig. 3.15: Contoured Nozzle Radial Pitot Pressure Profile for Air, taken at 4" outside nozzle exit plane

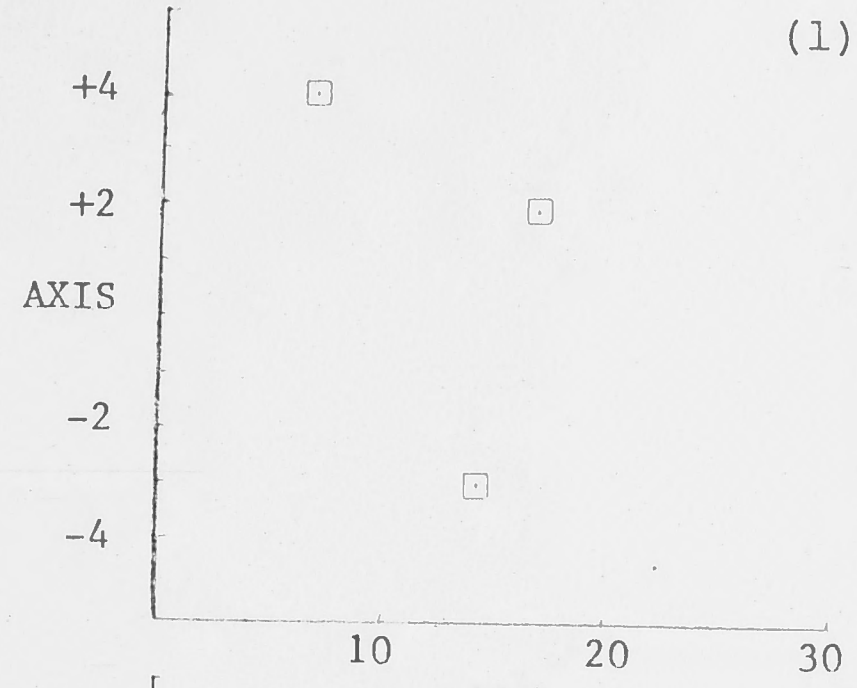

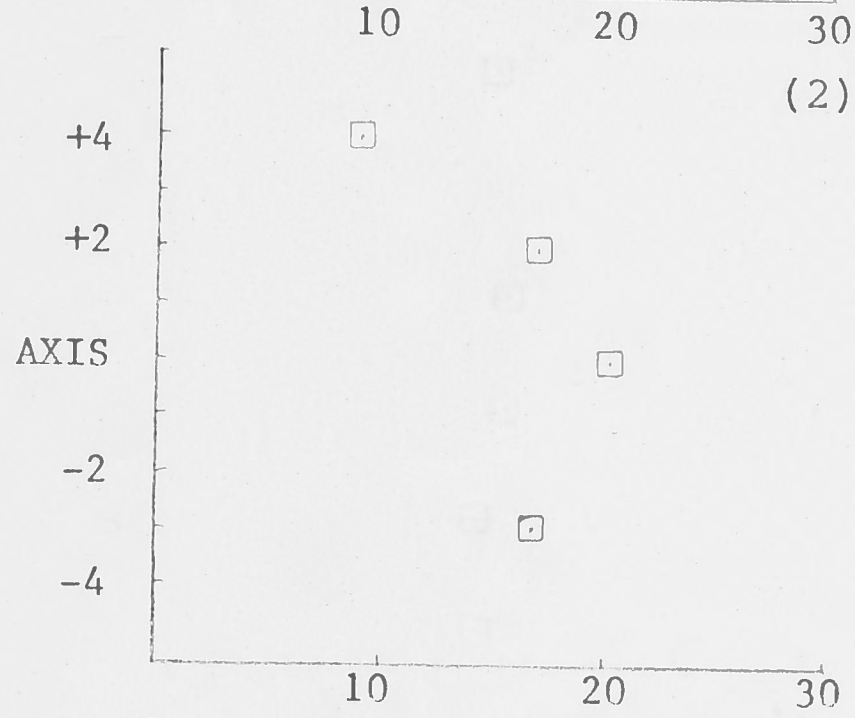

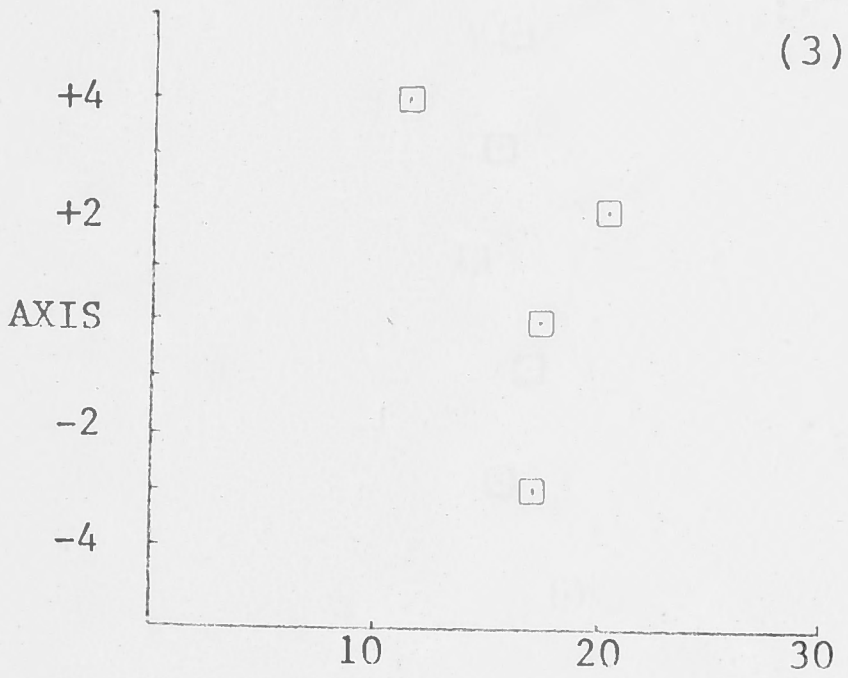

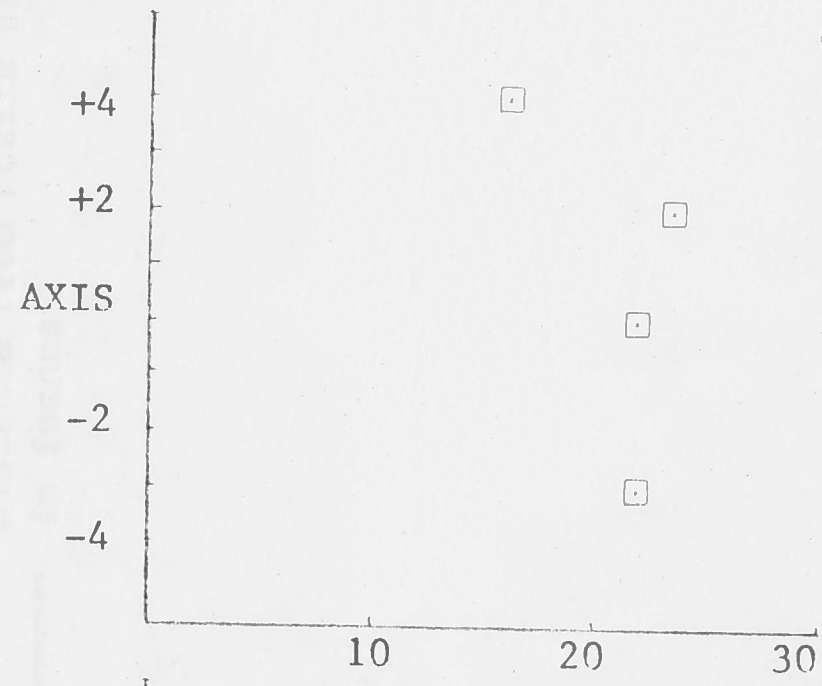

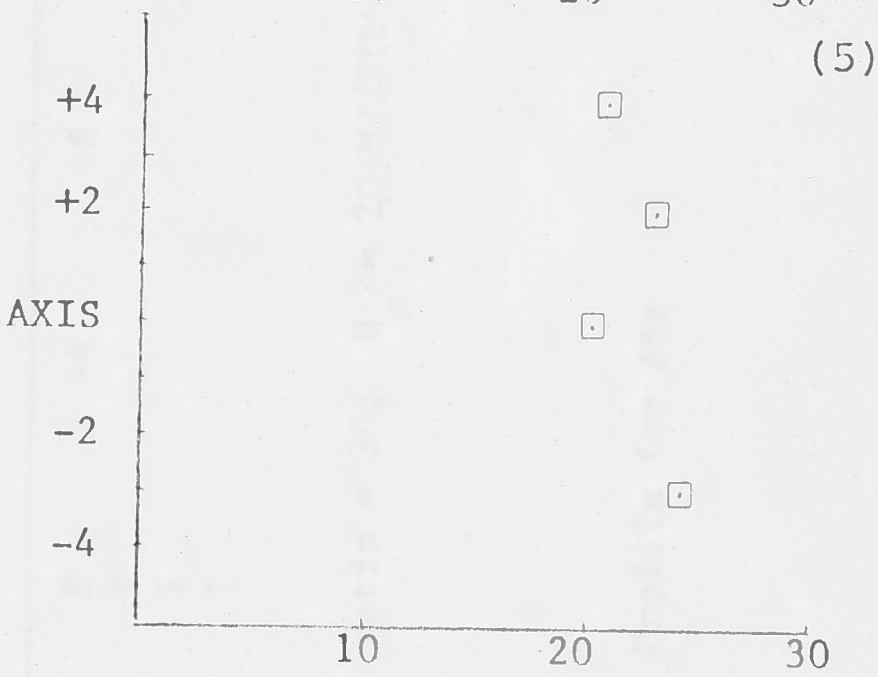

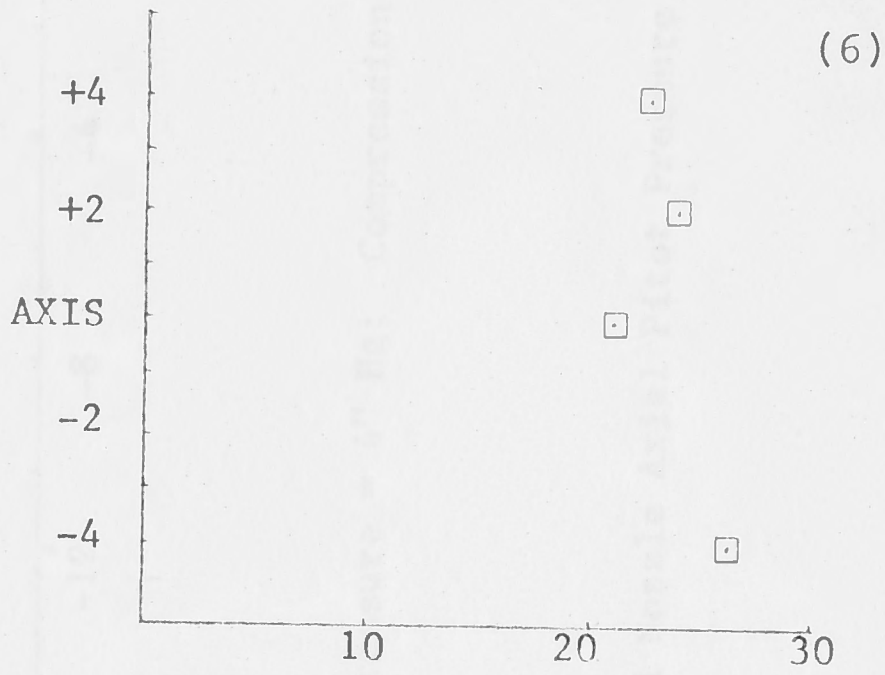

vertical axis - radial distance from nozzle axis in inches;
horizontal axis - Pitot Pressures in PSI;
1 - ½" Hg shock tube filling pressure, Hs = 40 MJ/KGM;
2 - 1" Hg shock tube filling pressure, Hs = 31 MJ/KGM;
3 - 2" Hg shock tube filling pressure, Hs = 13 MJ/KGM;
4 - 4" Hg shock tube filling pressure, Hs = 7 MJ/KGM;
5 - 8" Hg shock tube filling pressure, Hs = 5 MJ/KGM;
6 - 12" Hg shock tube filling pressure, Hs = 3 MJ/KGM;

Fig. 3.16: Contoured Nozzle Radial Pitot Pressure Profile for CO_2, taken at 2" outside nozzle exit plane

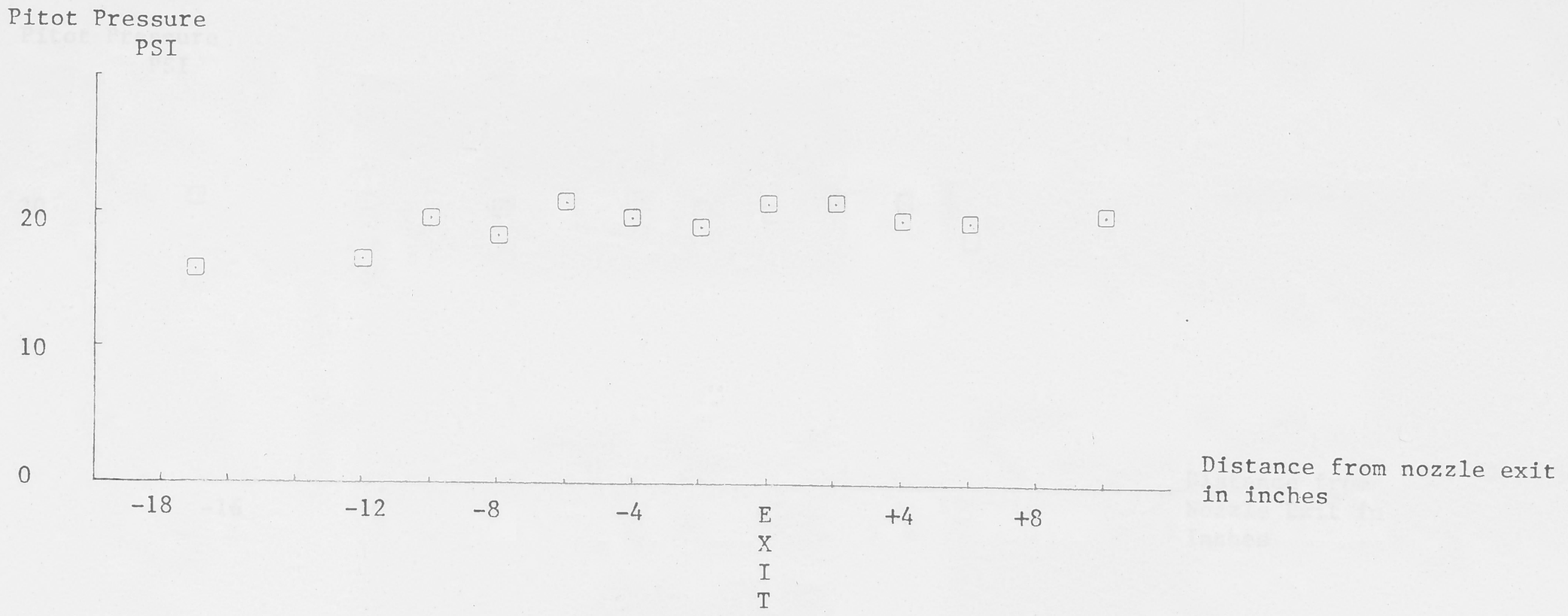

shock tube filling pressure = 4" Hg; Compression ratio = 30; H_o = 20 MJ/KGM;

Fig. 3.17: Contoured Nozzle Axial Pitot Pressure Profile for Air

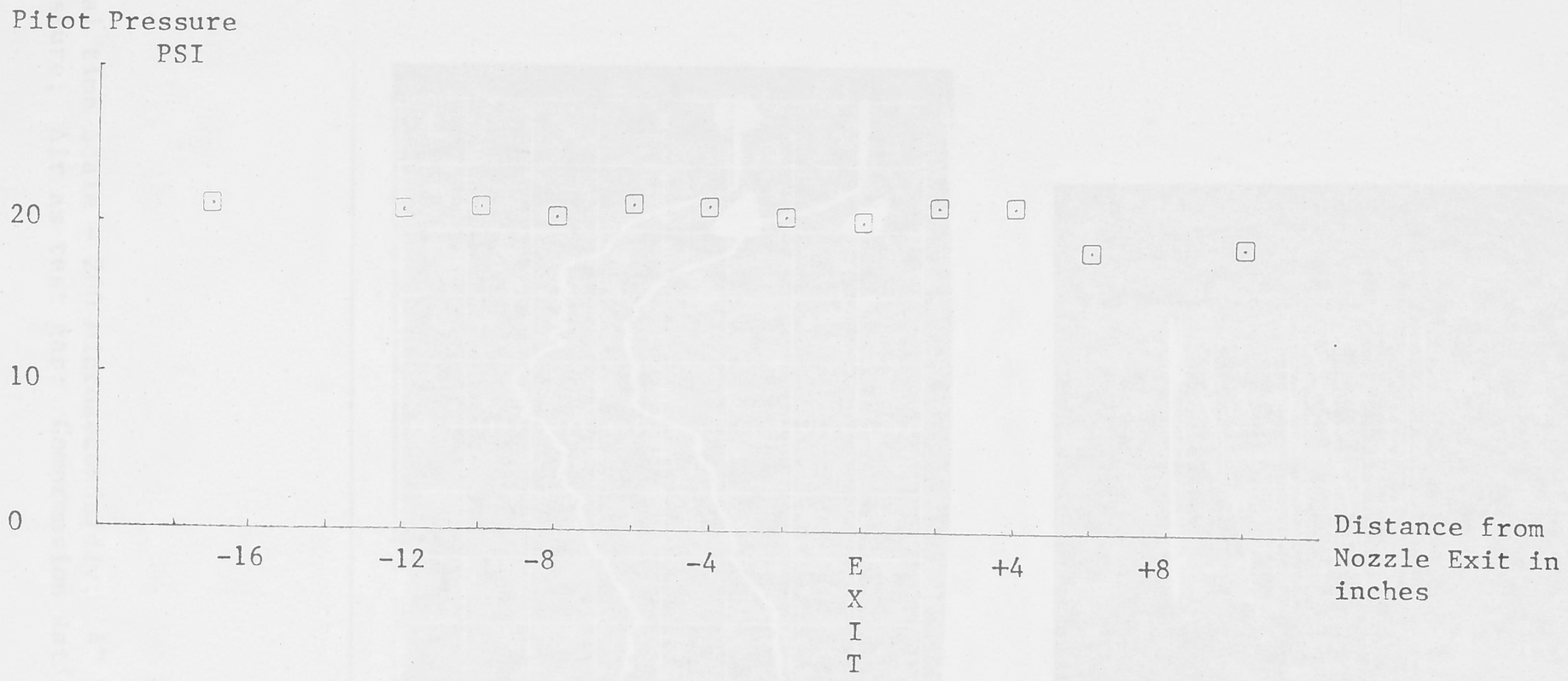

shock tube filling pressure = 4" Hg; compression ratio = 30; H_o = 7 MJ/KGM.

Fig. 3.18: Contoured Nozzle Axial Pitot Pressure Profile for CO_2

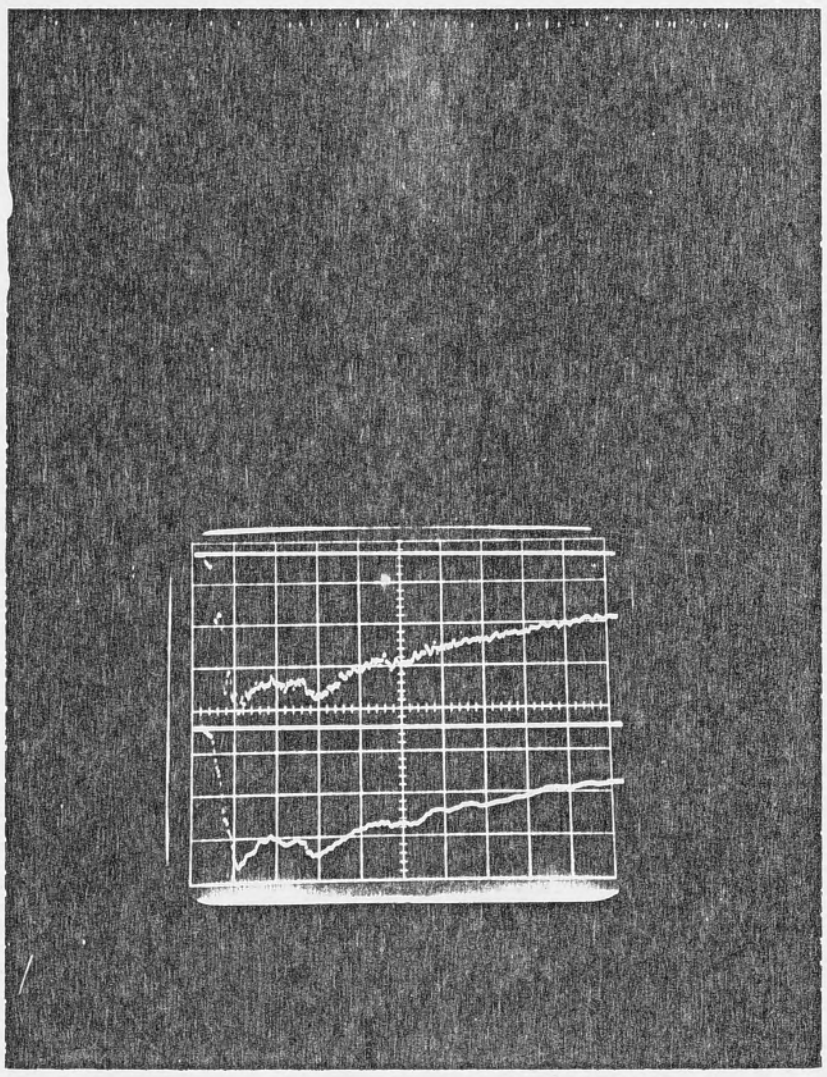

Stagnation
Traces

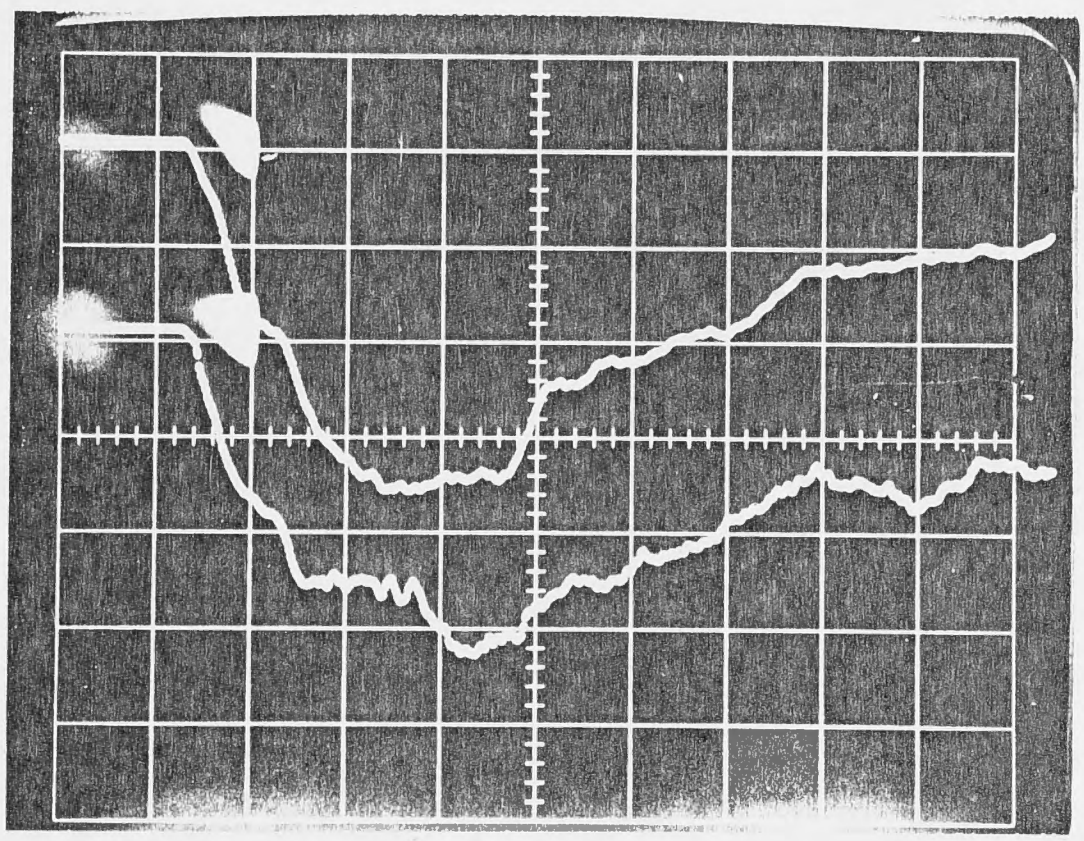

Pitot
Pressure
Traces

Horizontal time scale - 200 microseconds/div; 4" Hg initial shock tube pressure; Air as test gas: Compression Ratio = 30

Fig. 3.19: Pitot Pressure and Stagnation Pressure Traces.

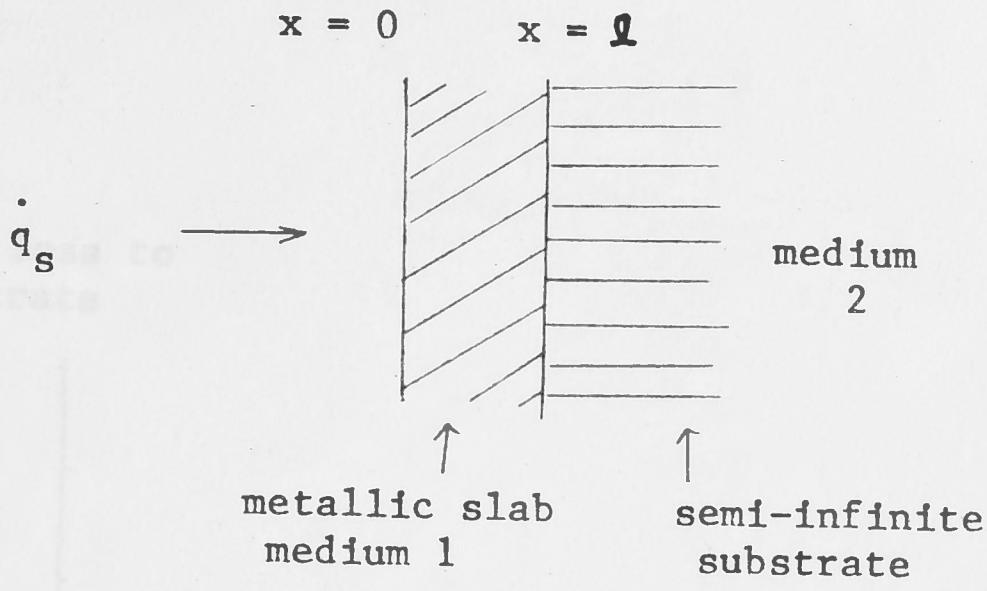

Thin-Film Gauges:

$\ell \sim 500$ Å

Calorimeter Gauges:

$\ell \sim 0.2$ MM

Fig. 4.1: Heat Transfer Gauges

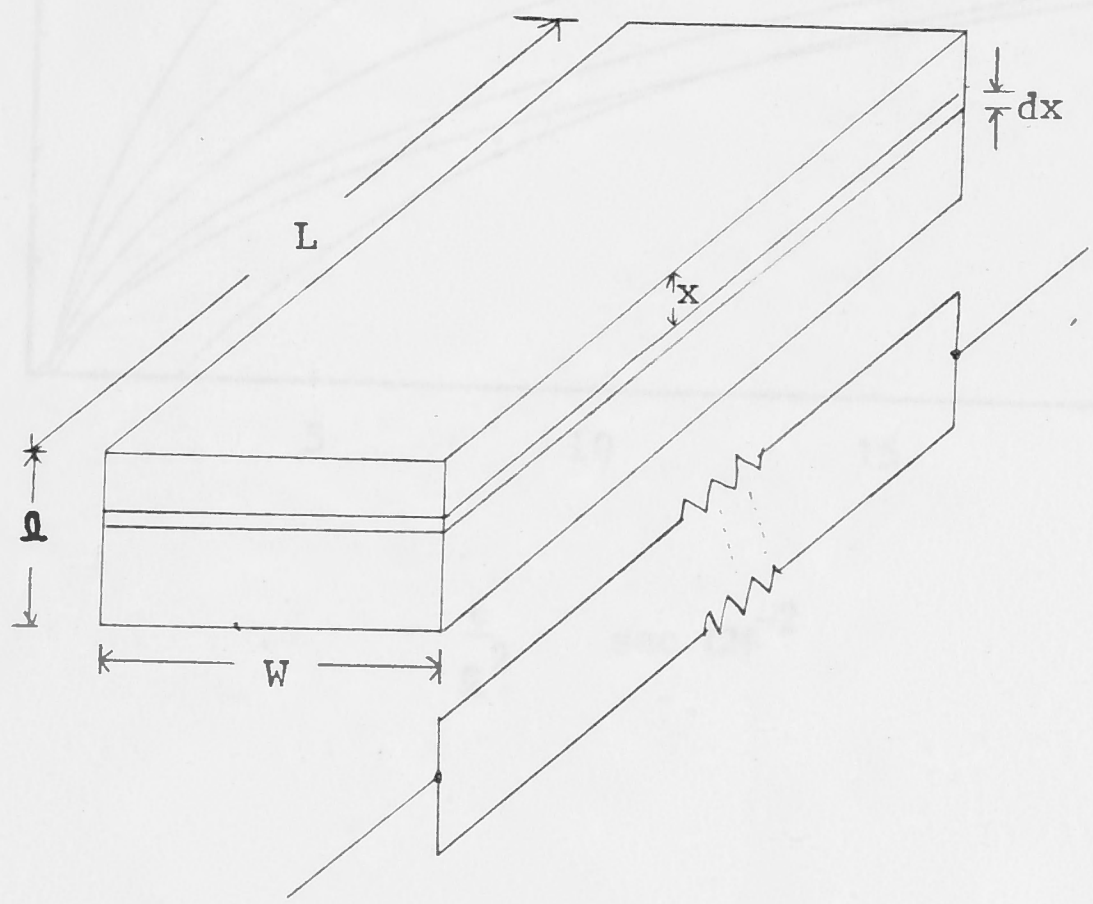

Fig. 4.2: Equivalent resistance of metallic slab

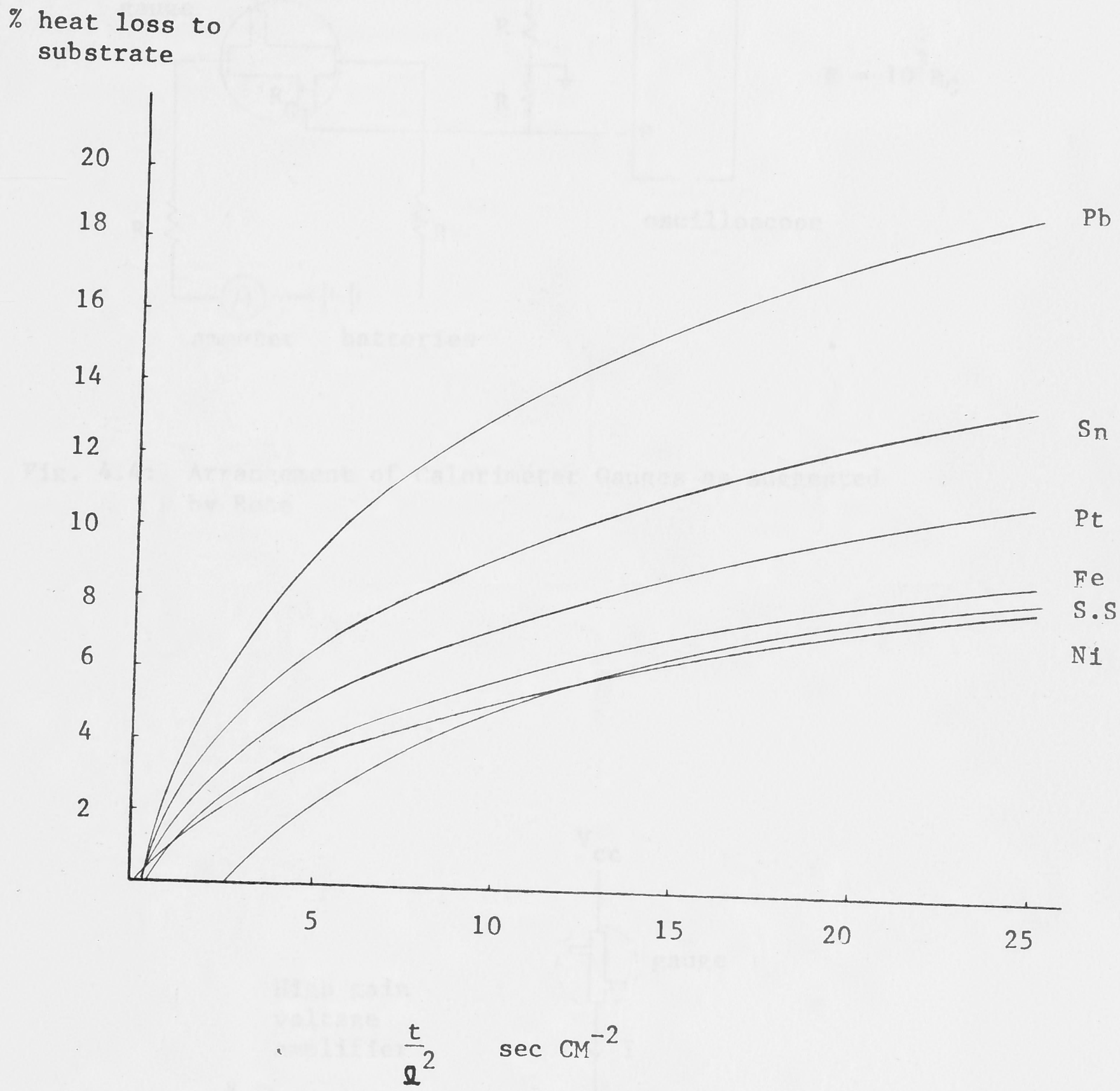

Fig. 4.3: Heat loss to substrate of various metals on epoxy substrate, calculated using Eq. 4.13.

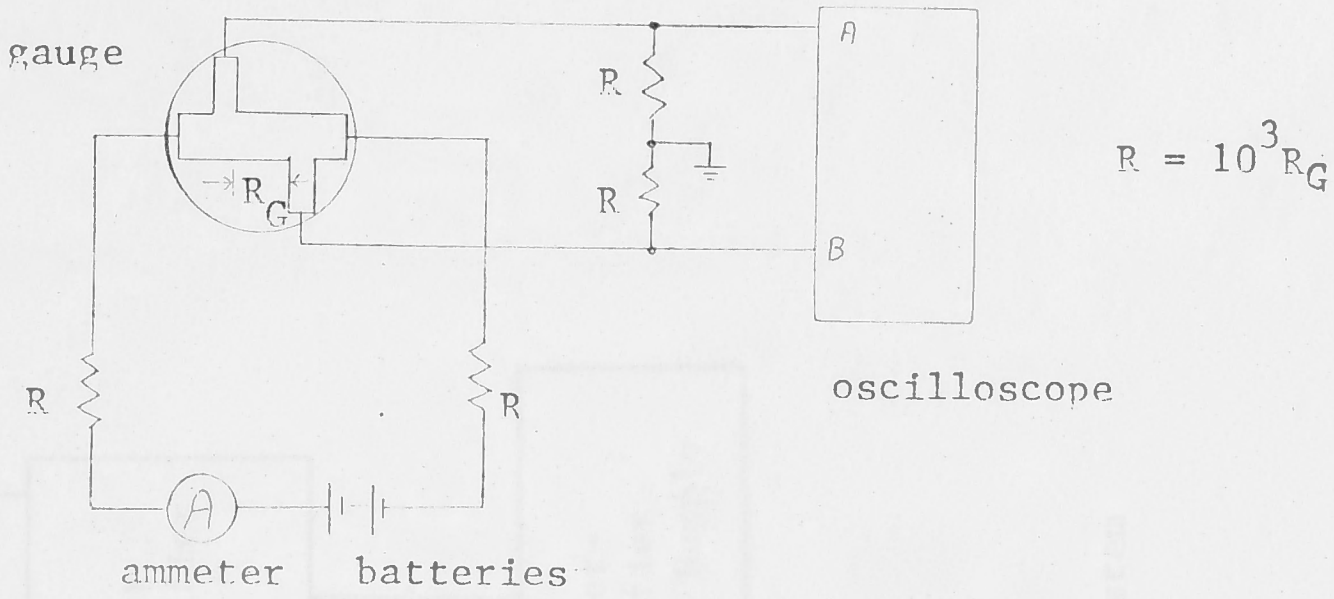

$R = 10^3 R_G$

Fig. 4.4: Arrangement of Calorimeter Gauges as suggested by Rose

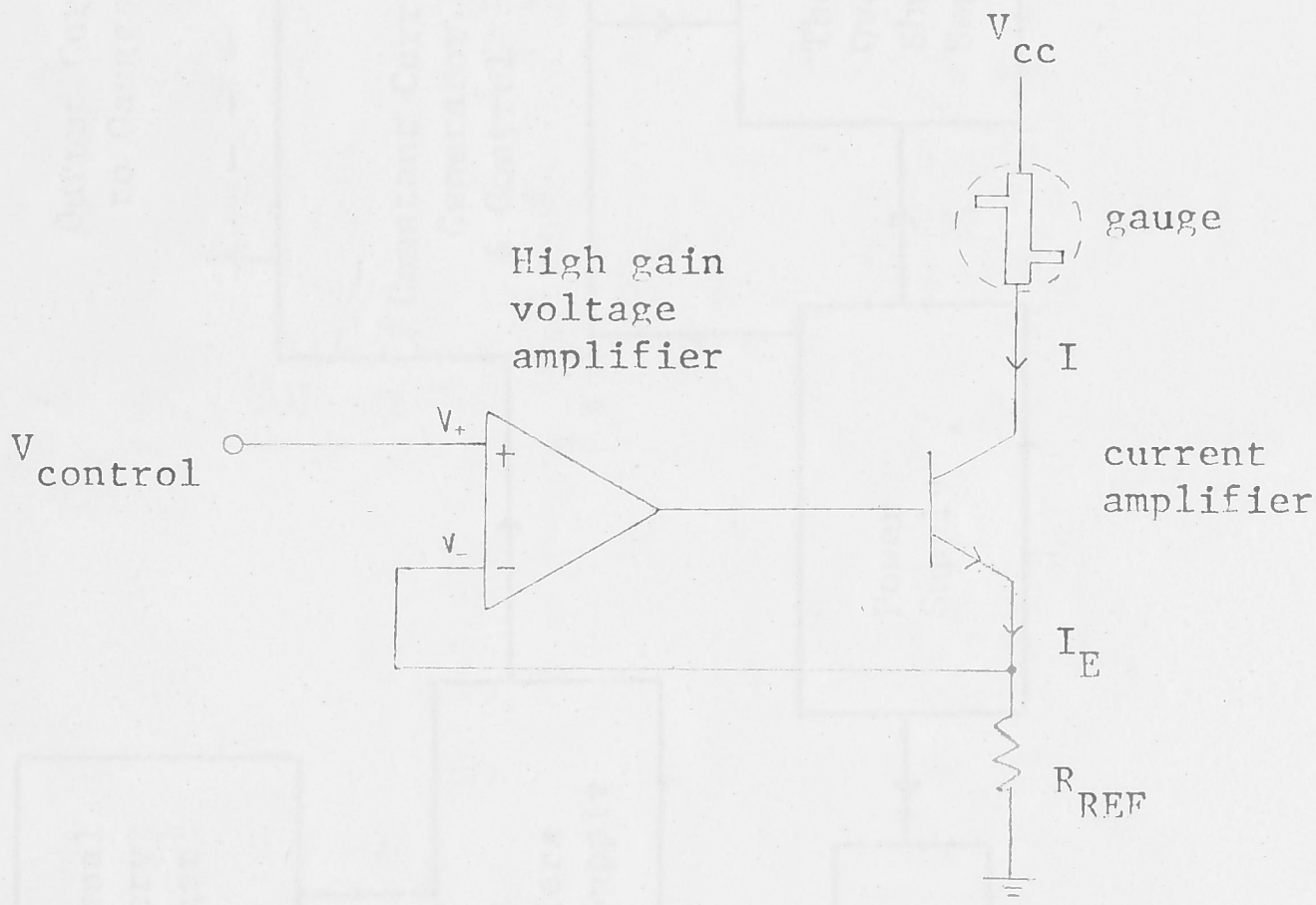

Fig. 4.5: Basic Principle of Constant Current Supply used in this project.

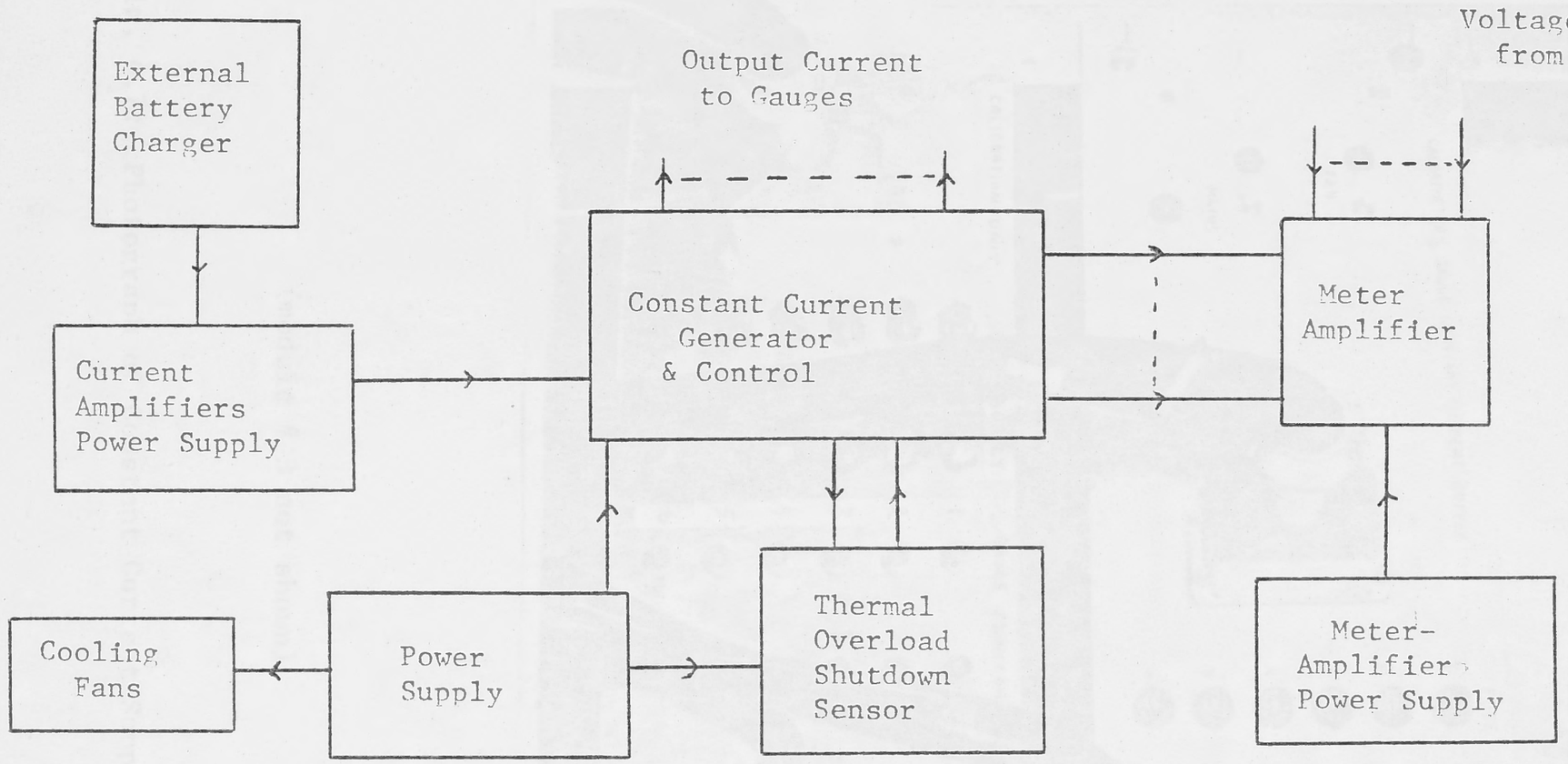

Fig. 4.6: Functional Block Diagram of Constant Current Generator System

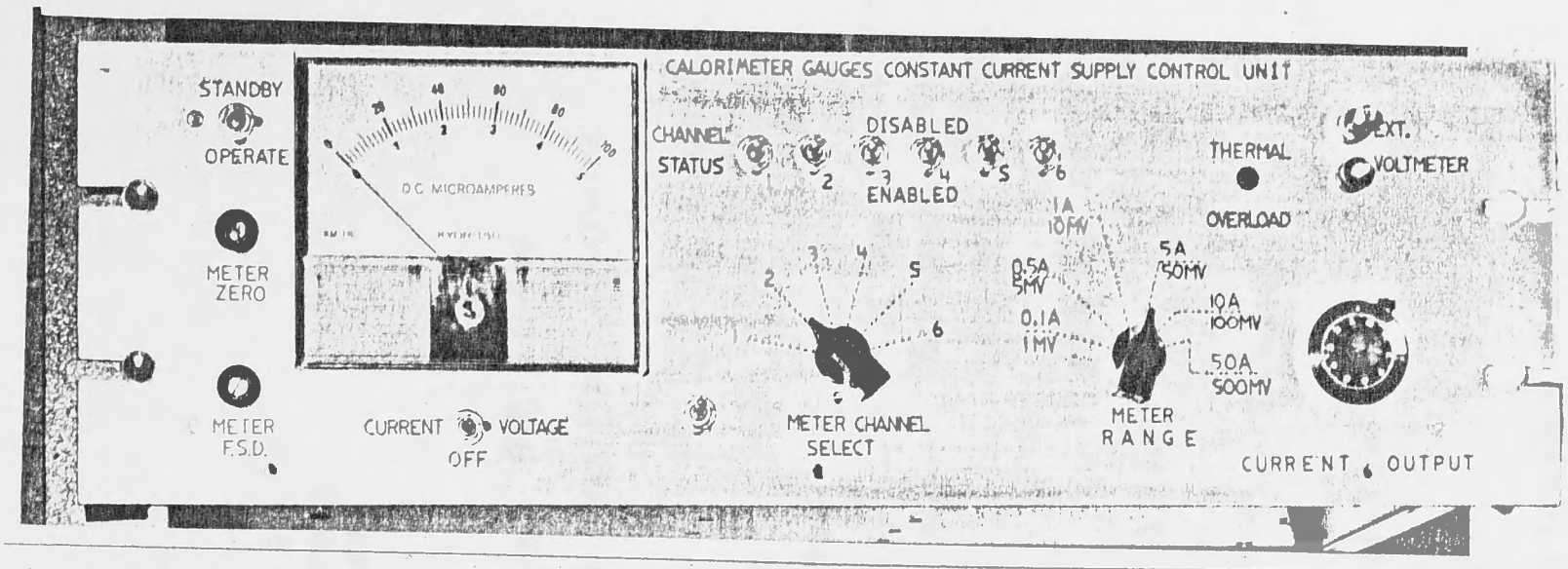

Module # 1

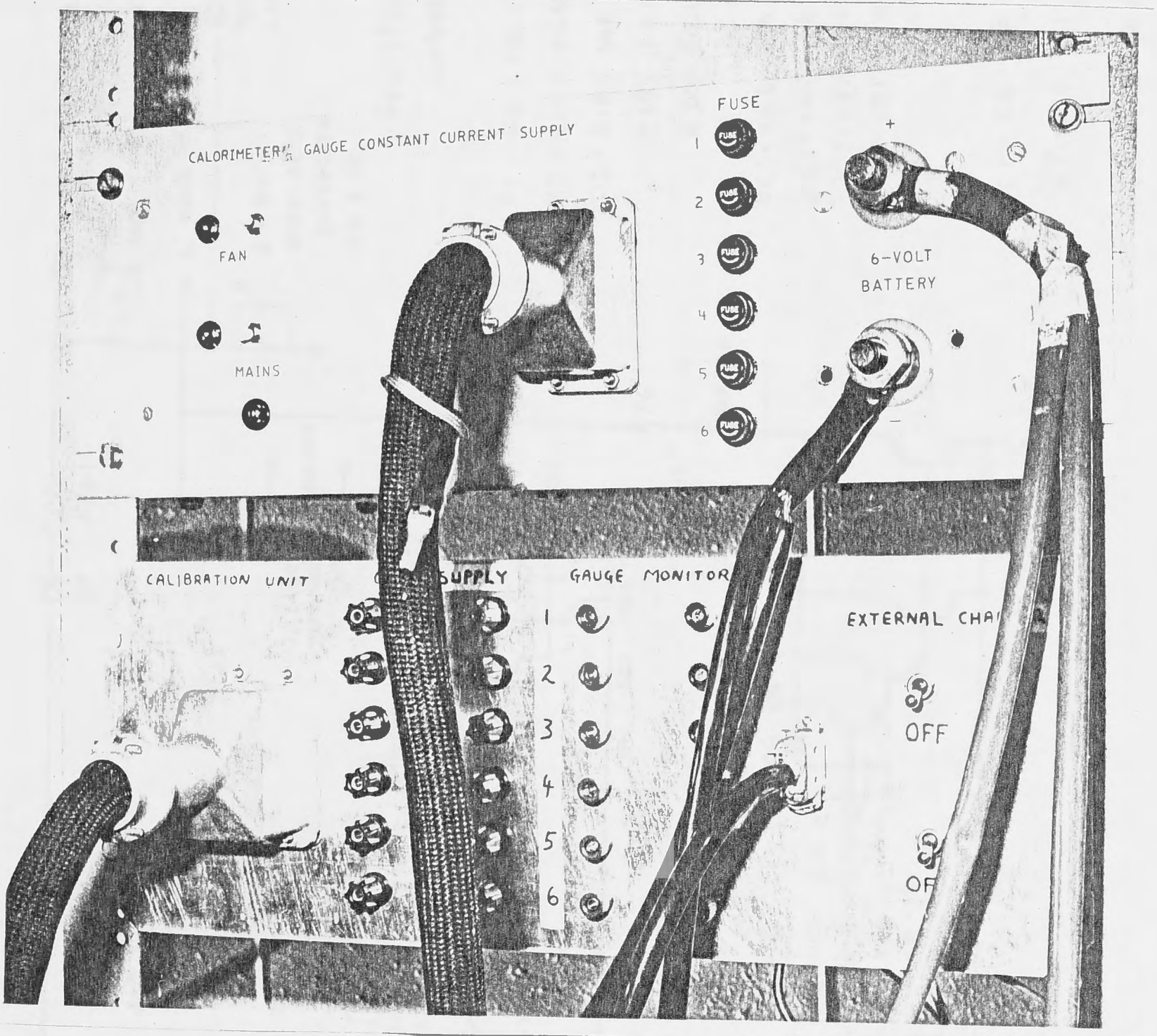

Module # 2

Module # 4

(module # 3 not shown)

Fig. 4.7: Photograph of Constant Current Supply.

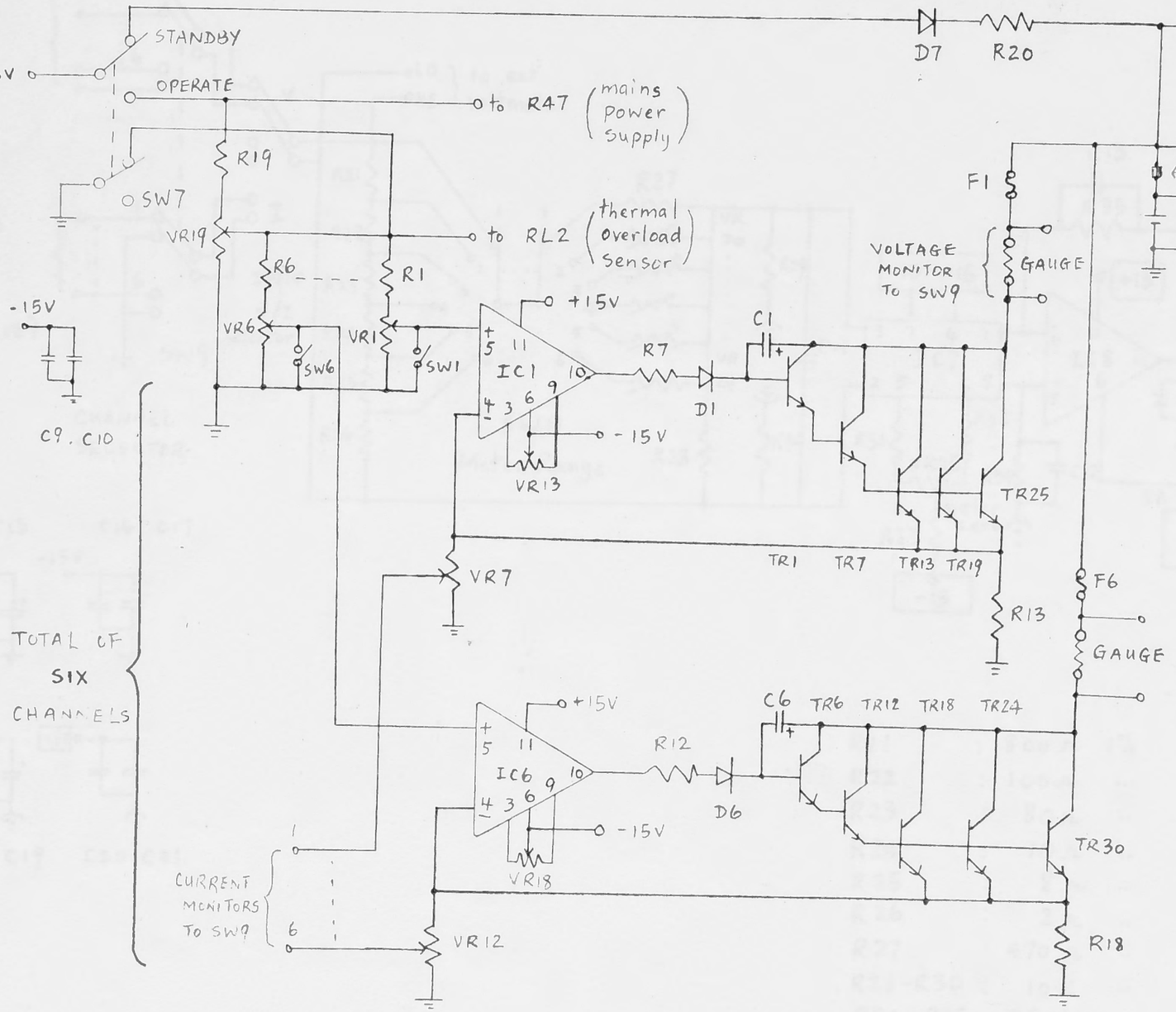

Fig. 4.8: Circuit of Constant Current Output Control
(2 channels shown)

Resistors : 5% 0.5W
unless specified otherwise

R1 - R6 : 150K
R7 - R12 : 56K
R13 - R18 : see text
R19 : 1 KΩ
R20 : 50Ω 7W

VR1 - VR6 : 10k
VR7 - VR12 : 1k
VR13 - VR18 : 10K
VR19 : 1 KΩ 10 turn

D1 - D6 : IN914
D7 : EM401

TR1 - TR6 : BC108
TR7 - TR12 : 2N3054
TR13 - TR30 : 2N3055

F1 - F6 : 10A

SW1 - SW6 : spst
SW7 : dpdt
SW8 : dpst 20A CONTACTS

C1 - C6 : 3.3 μf tantalum
C7 - C10 : 0.1 μf

IC1 - IC6 : μA741CD

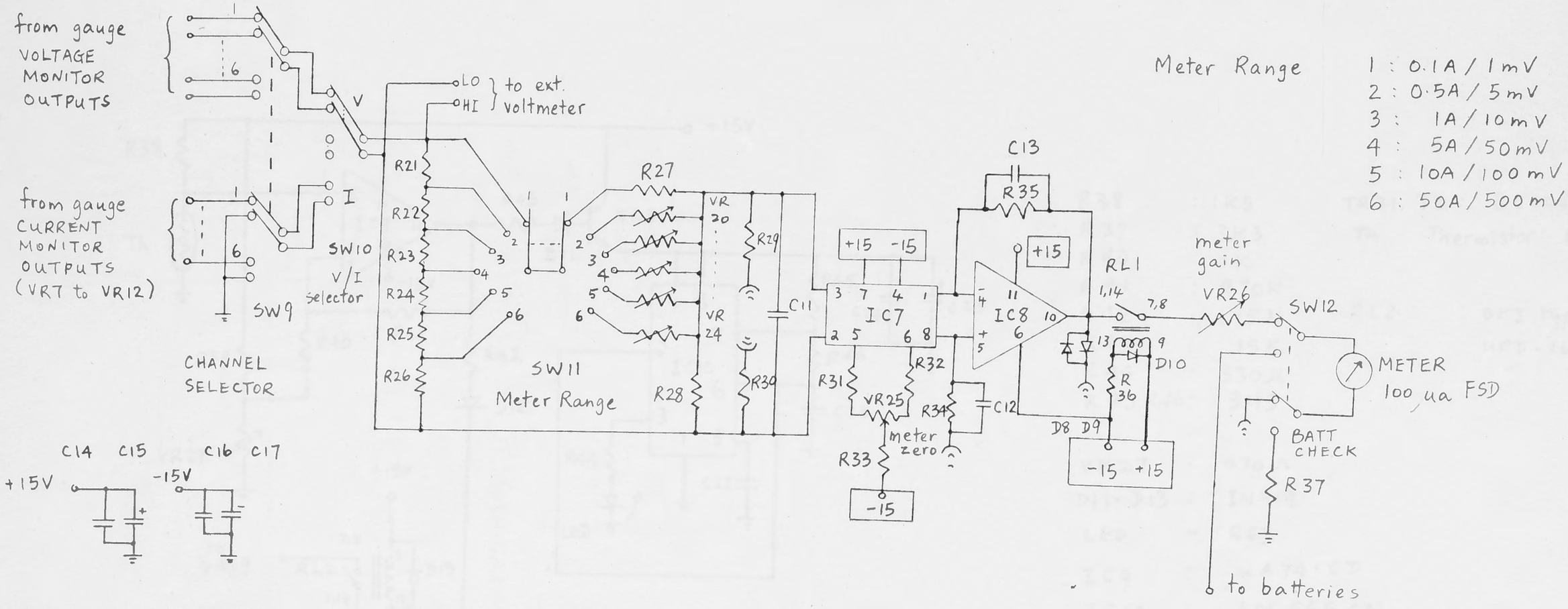

Meter Range

1 : 0.1A / 1mV
2 : 0.5A / 5mV
3 : 1A / 10mV
4 : 5A / 50mV
5 : 10A / 100mV
6 : 50A / 500mV

R21	: 800 Ω	1%
R22	: 100 Ω	"
R23	: 80 Ω	"
R24	: 10 Ω	"
R25	: 8 Ω	"
R26	: 2 Ω	"
R27	: 470 Ω	"
R28-R30	: 10K	"
R34-R35	: 680K	"

R31-R32	: 47K	2%
R33	: 10K	"
R36	: 2K7	5%
R37	: 66K	"
C11	: 0.1μf	
C12-C13	: 0.1μf	5%
C14,16,18,20	:	"
C15,17,19,21	: 100μf	25V

D8-D10	: IN914
VR20-VR24	: 1K
VR25	: 500Ω WIRE
VR26	: 1KΩ WOUND
IC7	: LM321H
IC8	: μA741CD
RL1	: OKI type URD-1620

SW9: 2 pole 6 position 2 section
SW11: " " 1 "
SW10: dpdt centre off
SW12: dpdt momentary contact

Fig. 4.9: Circuit of Meter Amplifier.

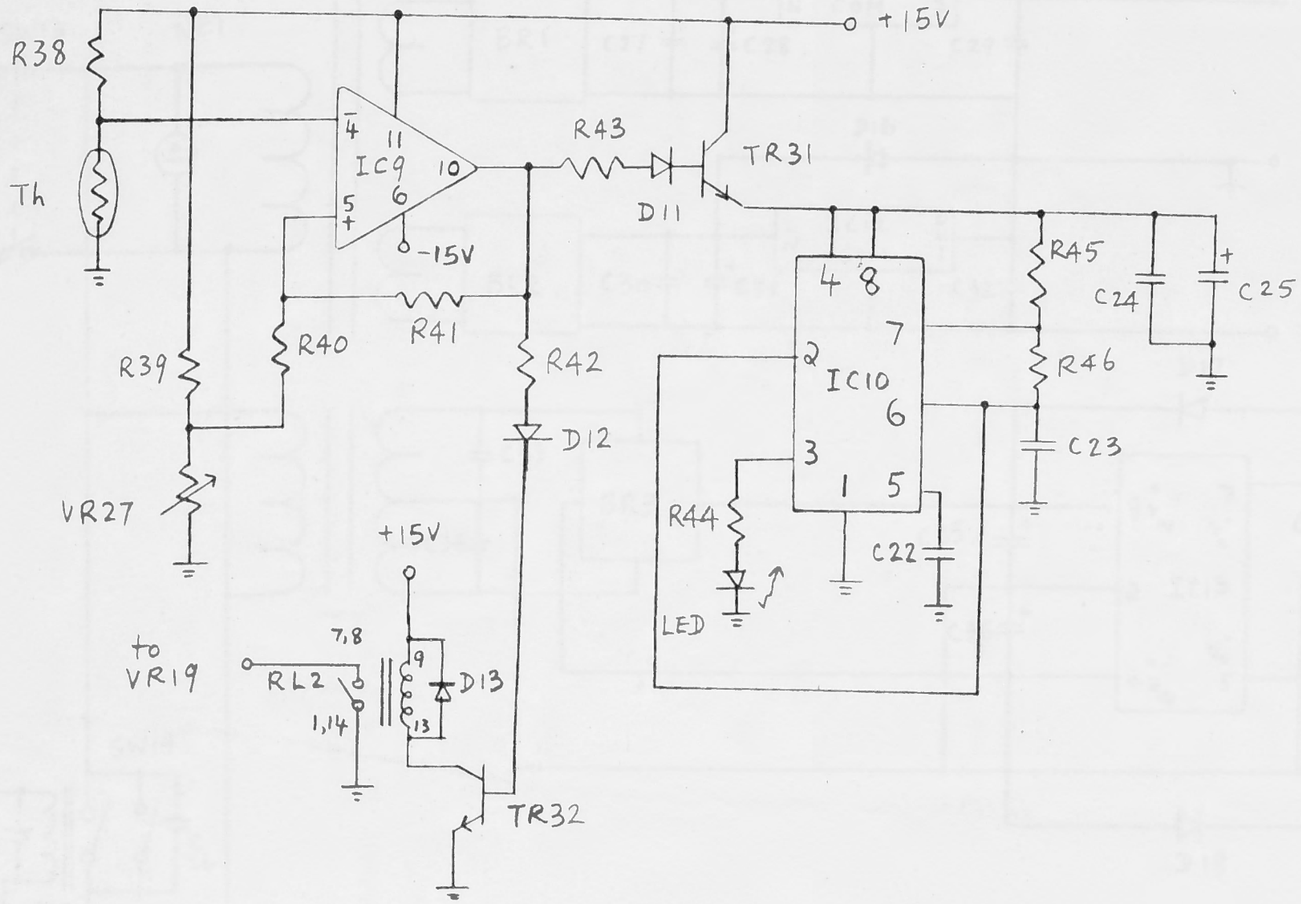

R38	: 1K5	TR31, 32	: BC108
R39	: 3K3	Th	– Thermistor CZ 11
R40	: 1K		
R41	: 470K		
R42	: 15K	RL2	: OKI type URD-1620
R43	: 15K		
R44	: 330Ω		
R45, R46	: 3M3		
VR27	: 470Ω		
D11-D13	: IN914		
LED	– RED		
IC9	: μA741CD		
IC10	: LM555CN		
C22-24	: 0.1 μf		
C25	: 1000 μf 25V		

Fig. 4.10: Circuit of Thermal Overload Shutdown Sensor

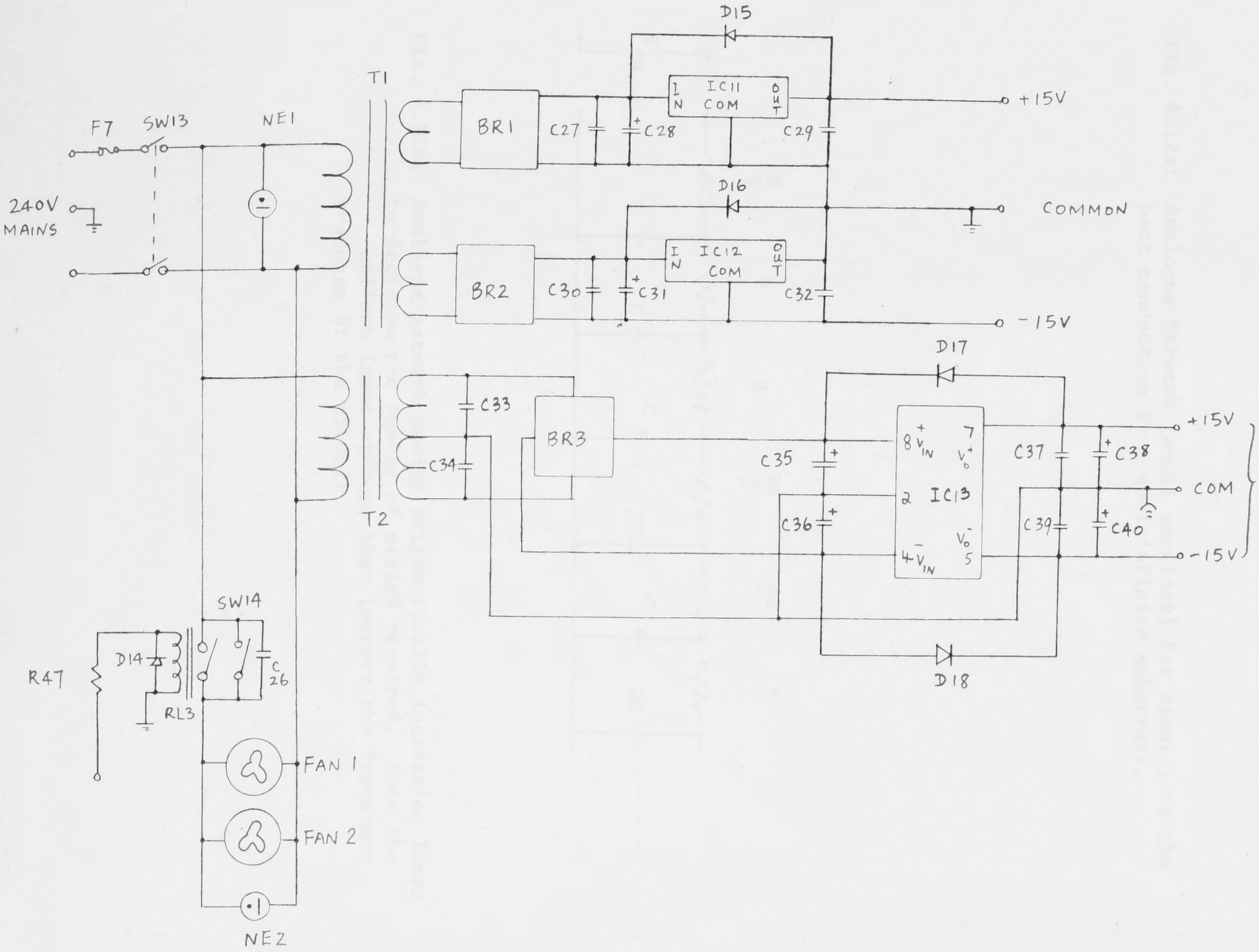

C26 : 0.1 μf 600V paper
C27, 29, 30, 32, 33, 34, 37, 39 - 0.1 μf
C28, 31 - 2500 μf 25V
C35, 36 - 500 μf 25V
C38 40 - 100 μf 25V

BR1 - BR3 : VM68
IC11 - IC12 : LM340T-15
IC13 : RC4195
D14 : IN914
D15 - D18 : EM401

for meter circuit only

R47 : 100 Ω
T1, T2 : A&R 6672

SW13 : dpst
SW14 : spst
NE1 : RED NEON
NE2 : GREEN NEON
F7 : 1A
FAN 1, 2 : 10HP188 PITO ETRI AXIAL FAN

Fig. 4.11: Power Supply for Constant Current Generator System

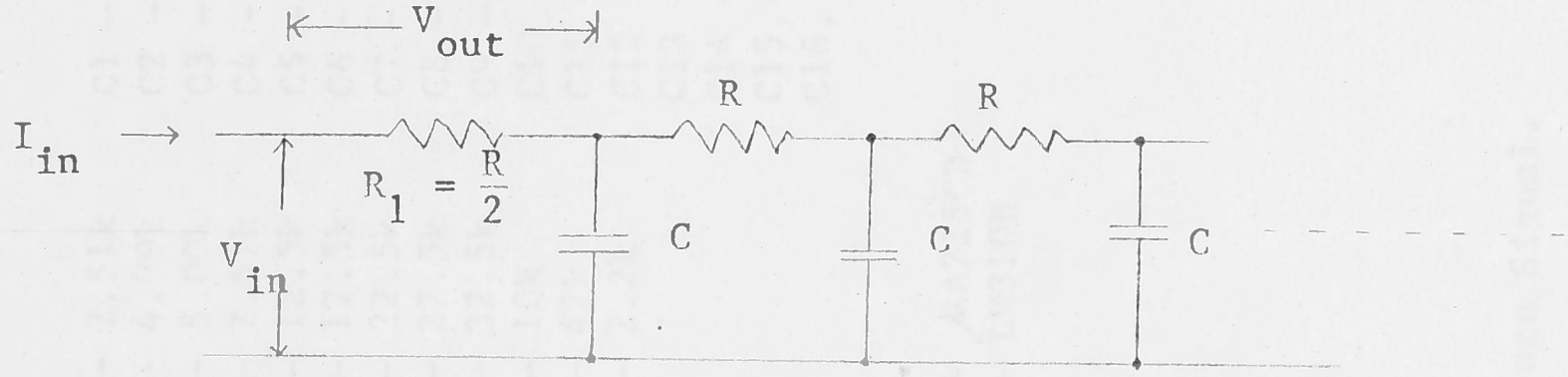

Fig. 4.12a: Analogue Network (equal sections) for simulating the heat conduction in a semi-infinite substrate.

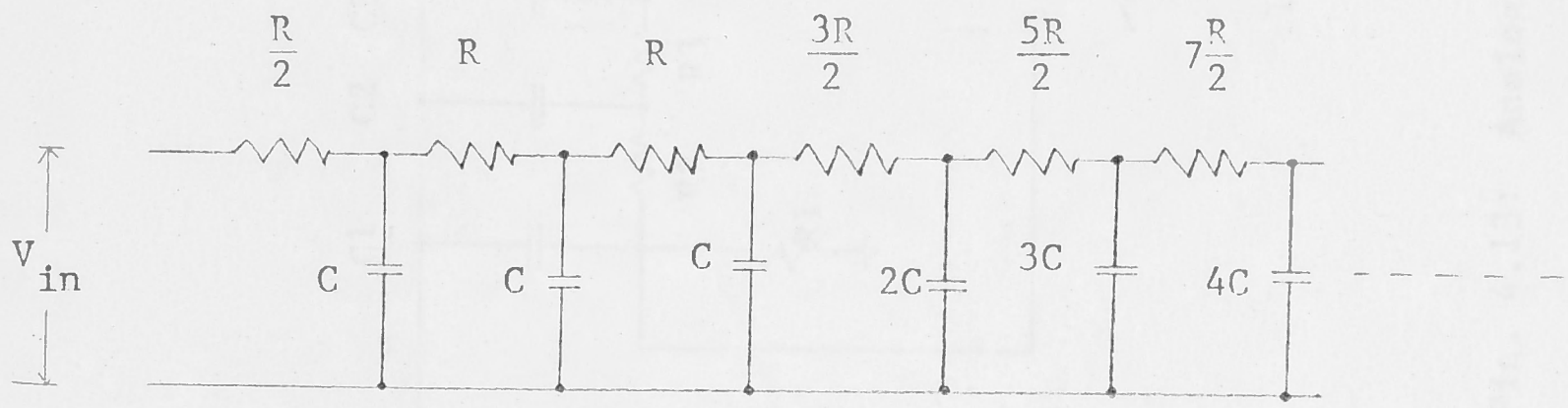

Fig. 4.12b: Analogue network having arithmetically increasing lumps to decrease the number of stages required. Note the uniform input stages, they improve the frequency response of the circuit.

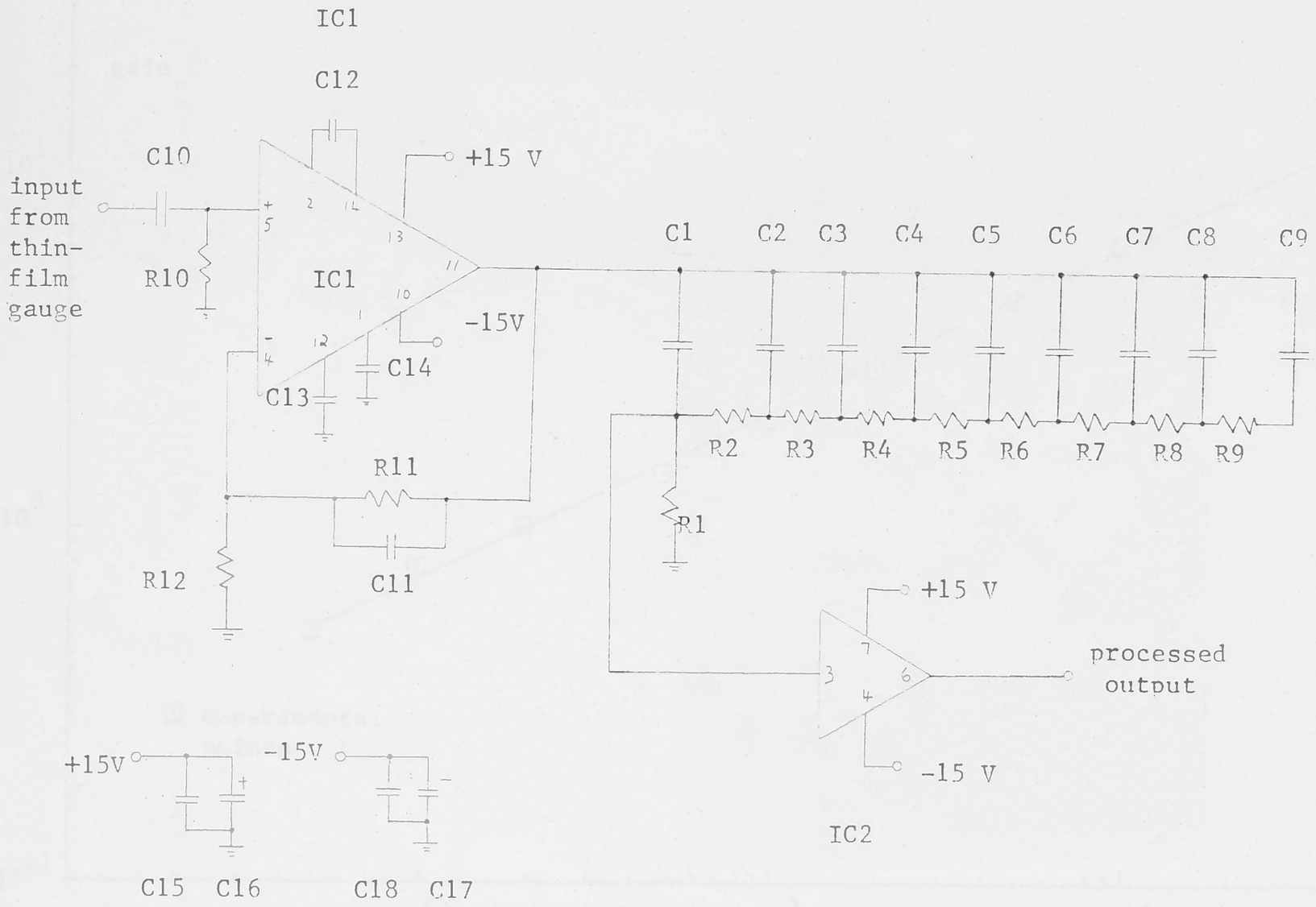

R1 - 2.51k
R2 - 4.99k
R3 - 5.00k
R4 - 7.51k
R5 - 12.5k
R6 - 17.5k
R7 - 22.5k
R8 - 27.5k
R9 - 32.5k
R10 - 10k
R11 - 47k
R12 - 2.2k

C1 - 1kpf
C2 - 1kpf
C3 - 1kpf
C4 - 2kpf
C5 - 3kpf
C6 - 4kpf
C7 - 5kpf
C8 - 6kpf
C9 - 7kpf
C10 - 2200 μf 35V
C11 - 3pf
C12 - 470pf
C13 - 2.2kpf
C14 - 1kpf
C15, C18 - 0.1 μf
C16, C17 - 100 μf 25V

IC1 - μA715CD
IC2 - LM310H

Fig. 4.13: Analogue Circuit for Processing Thin-Film Gauge Signal.

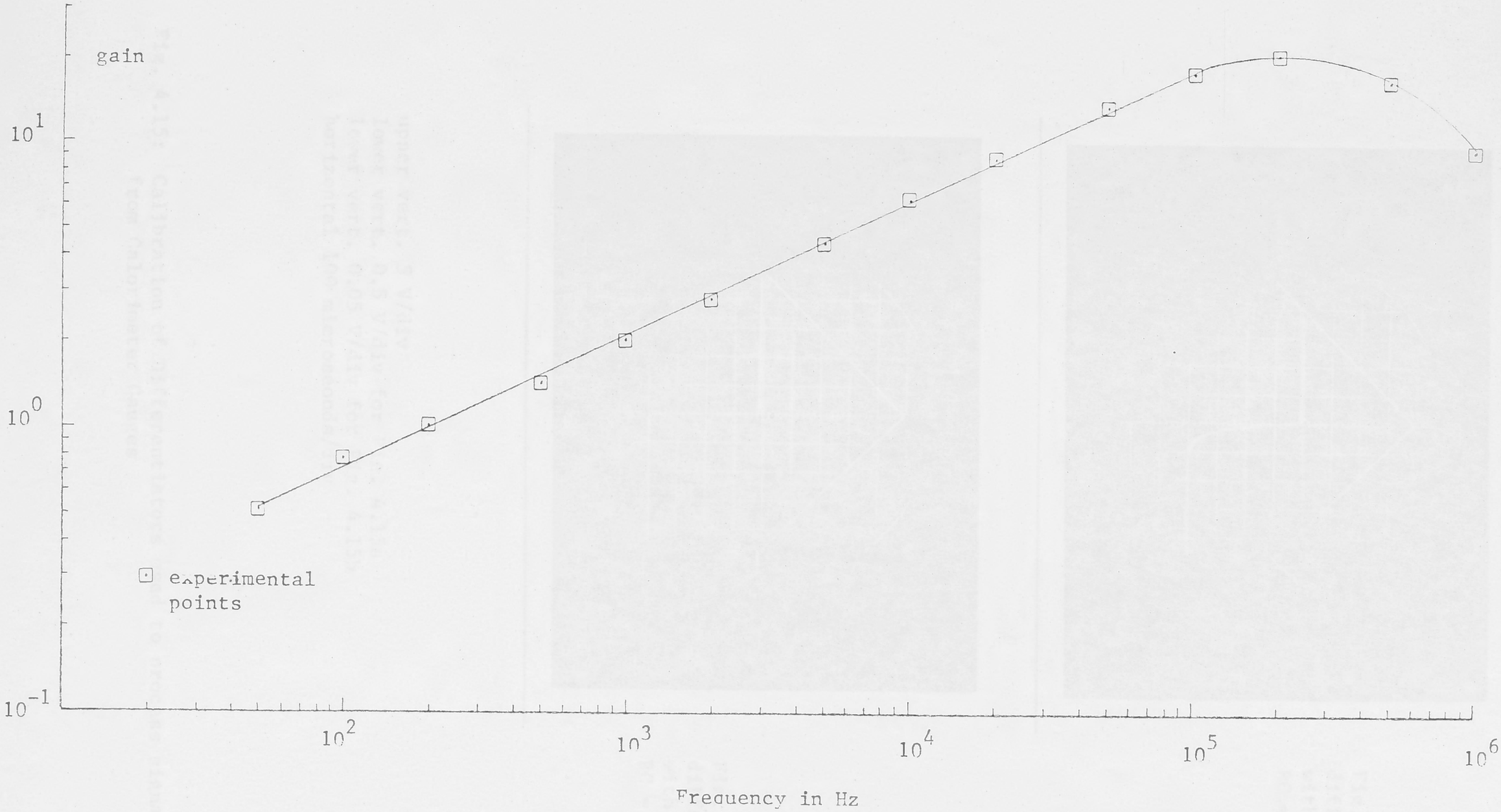

Fig. 4.14: Gain versus Frequency plot for Analogue Network.

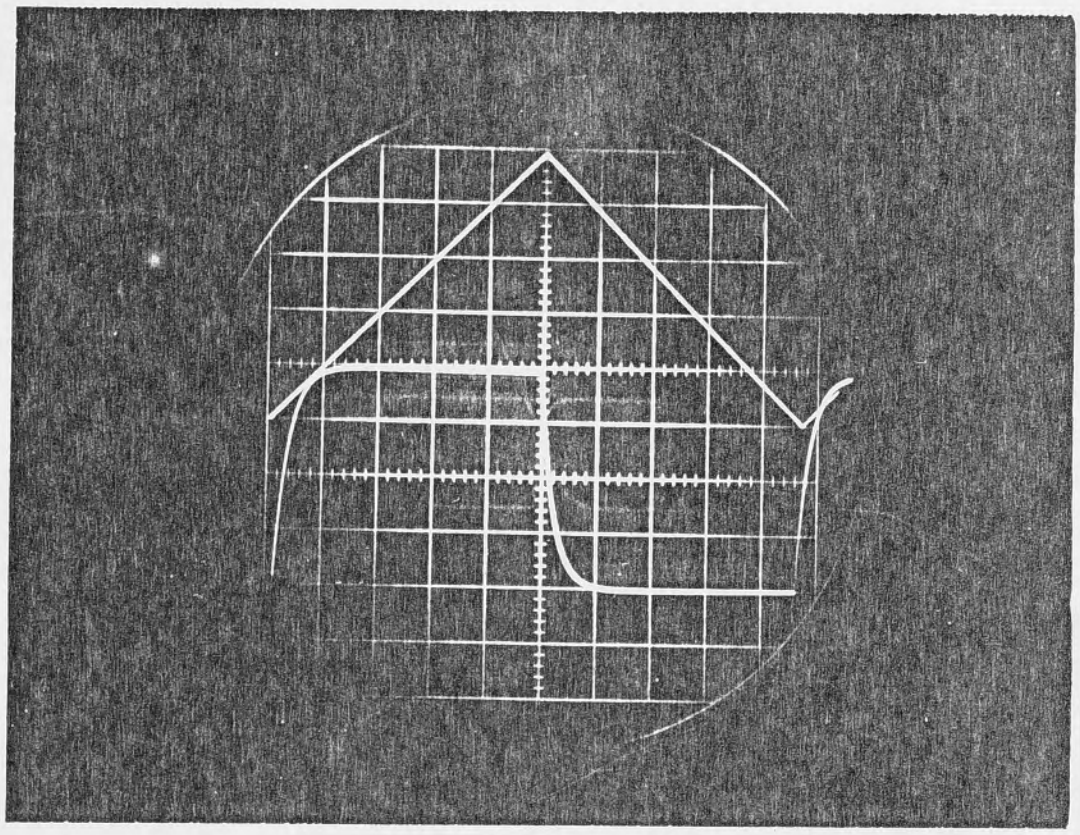

Fig. 4.15a: differentiator with RC = 19.8 ± 0.2 microseonds

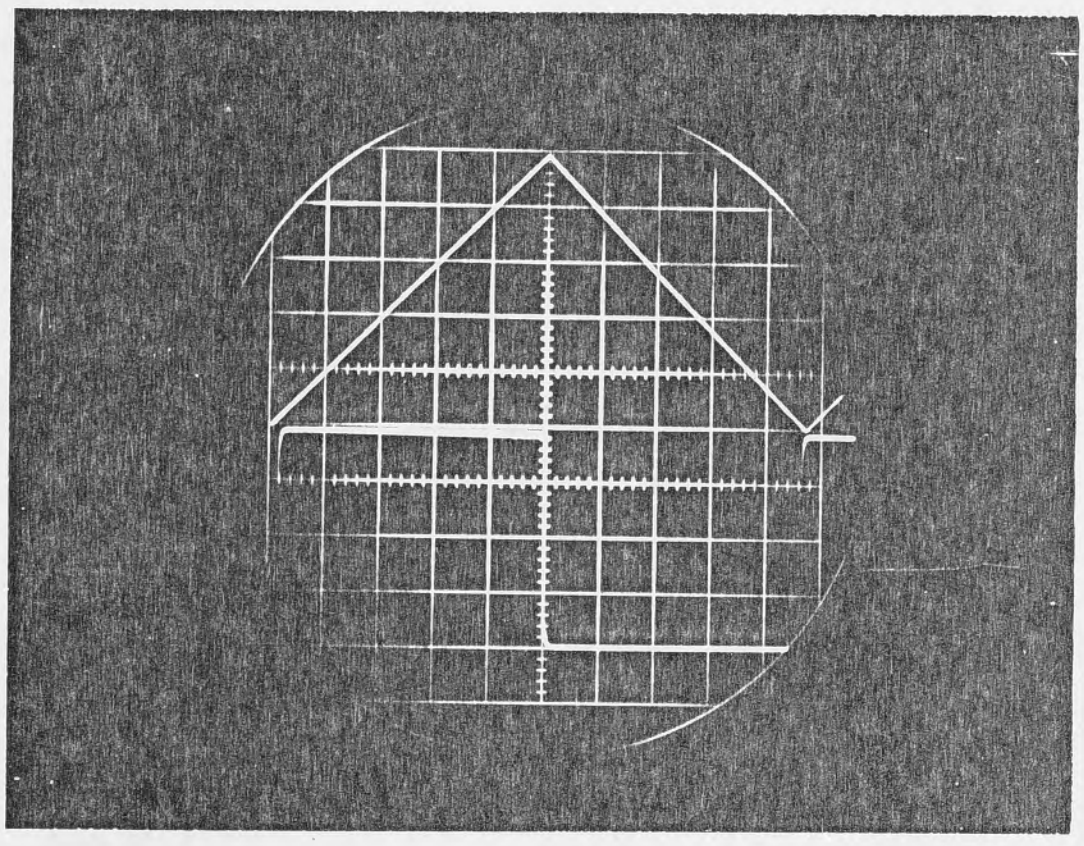

Fig. 4.15b: differentiator with RC = 1.91 ± 0.03 microseonds

upper vert. 5 V/div
lower vert. 0.5 V/div for Fig. 4.15a
lower vert. 0.05 V/div for Fig. 4.15b
horizontal 100 microseonds/div

Fig. 4.15: Calibration of Differentiators used to process signal from Calorimeter Gauges

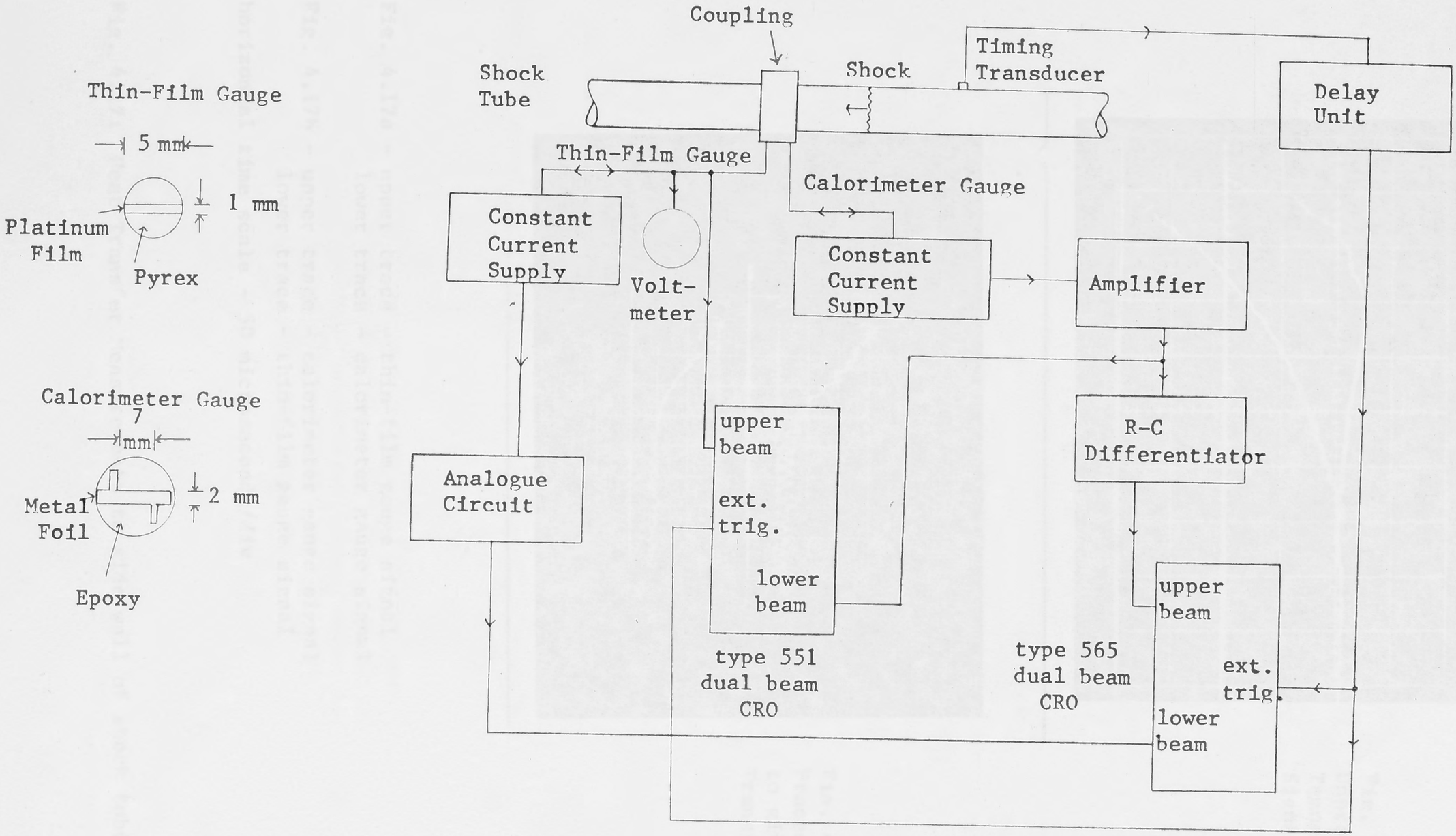

Fig. 4.16: Set-up for comparison of Thin-Film Gauge with Calorimeter Gauge on T1.

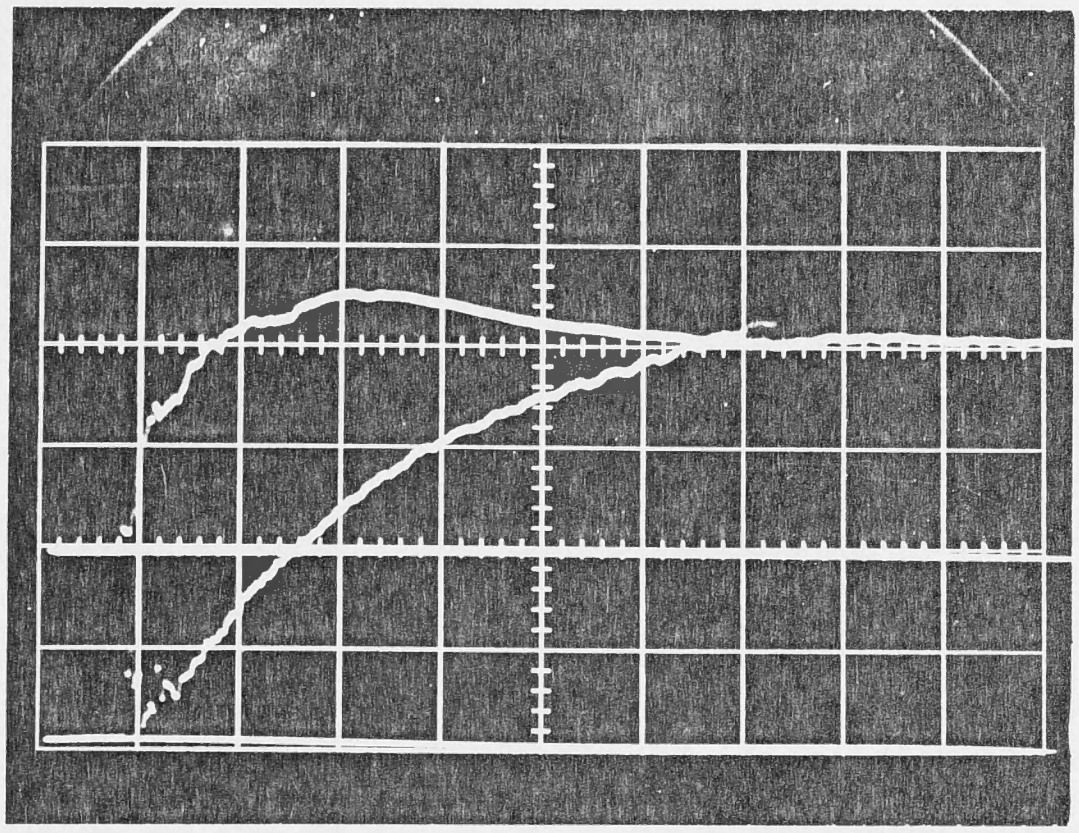

Fig. 4.17a: Unprocessed Temperature Signals

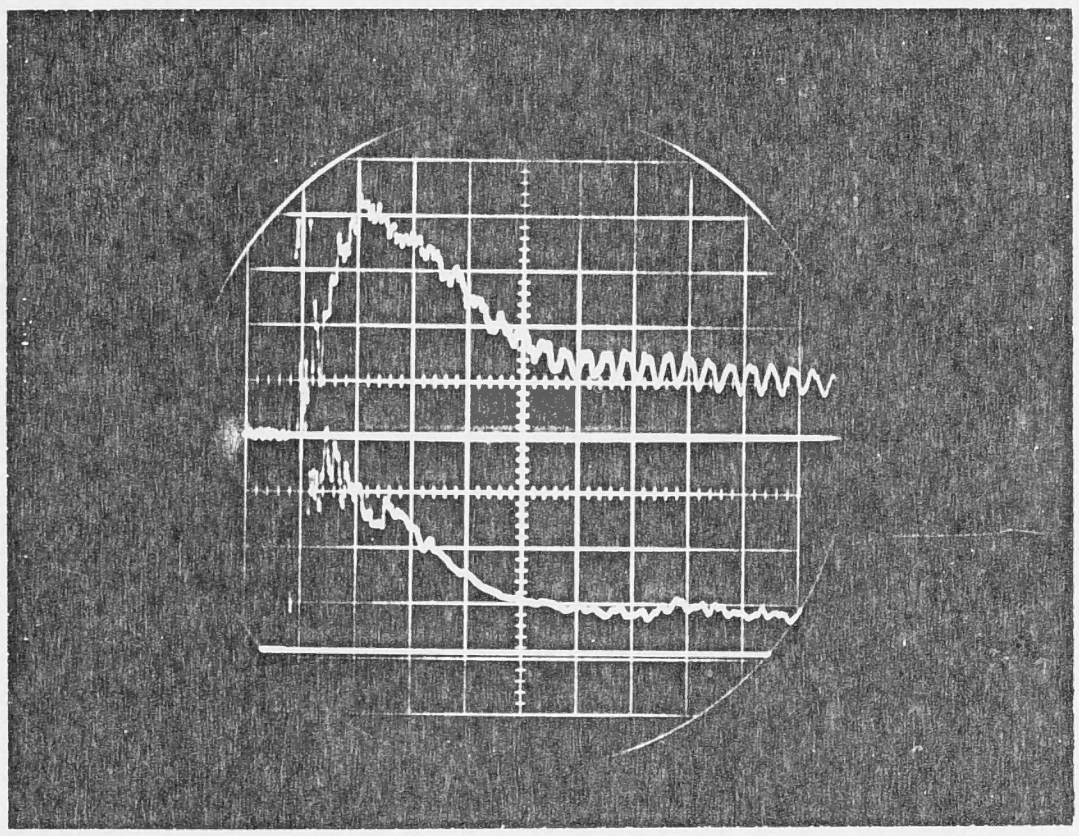

Fig. 4.17b: Processed Signals to give Heat Transfer Rates

Fig. 4.17a - upper trace - thin-film gauge signal
lower trace - calorimeter gauge signal

Fig. 4.17b - upper trace - calorimeter gauge signal
lower trace - thin-film gauge signal

horizontal time scale - 50 microseconds/div

Fig. 4.17: Heat Transfer Measurements to side wall of shock tube (T1).

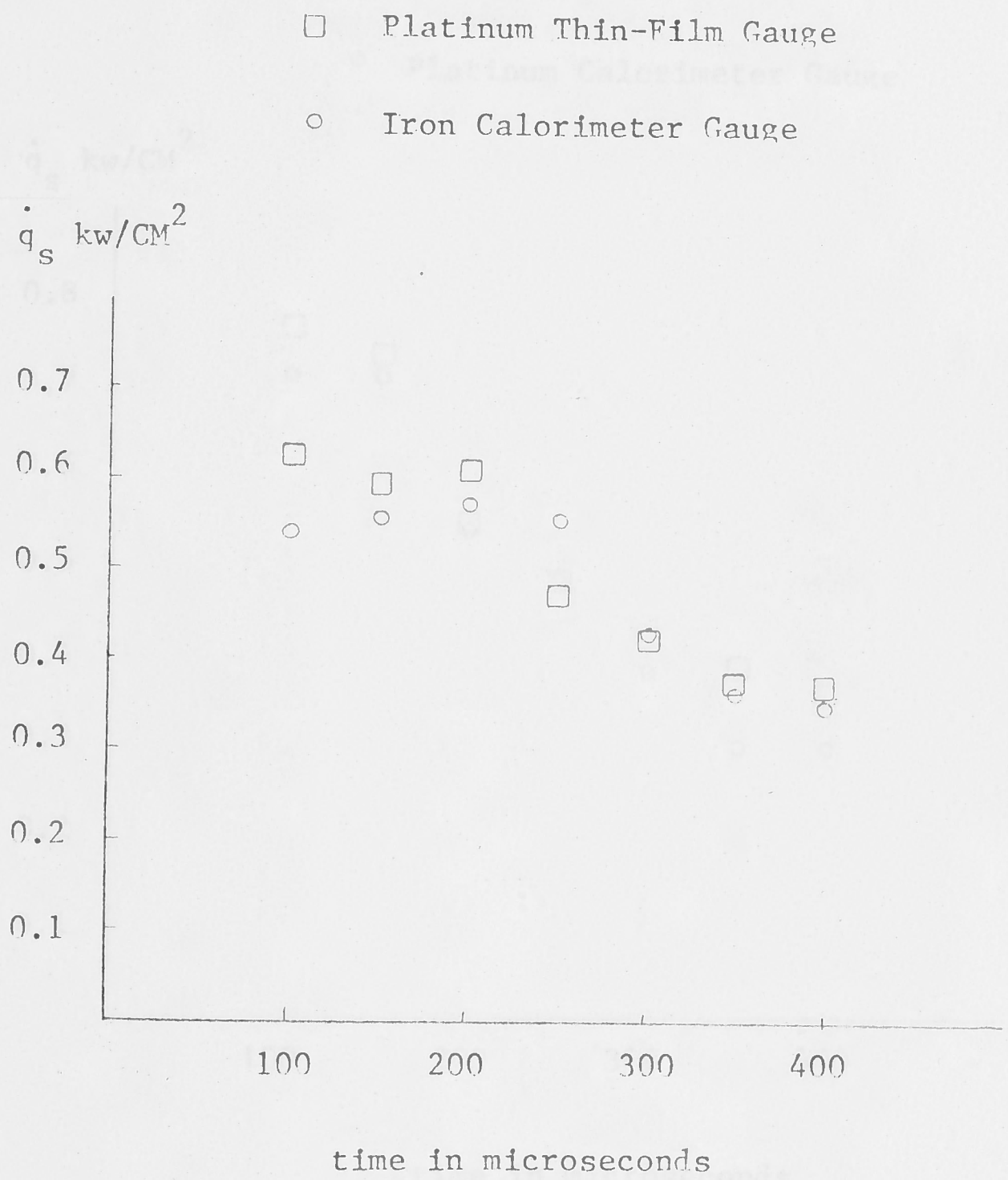

Fig. 4.18: Comparison of heat transfer to side wall of a shock tube deduced from platinum thin-film gauge and iron calorimeter gauge, at low heat transfer condition.

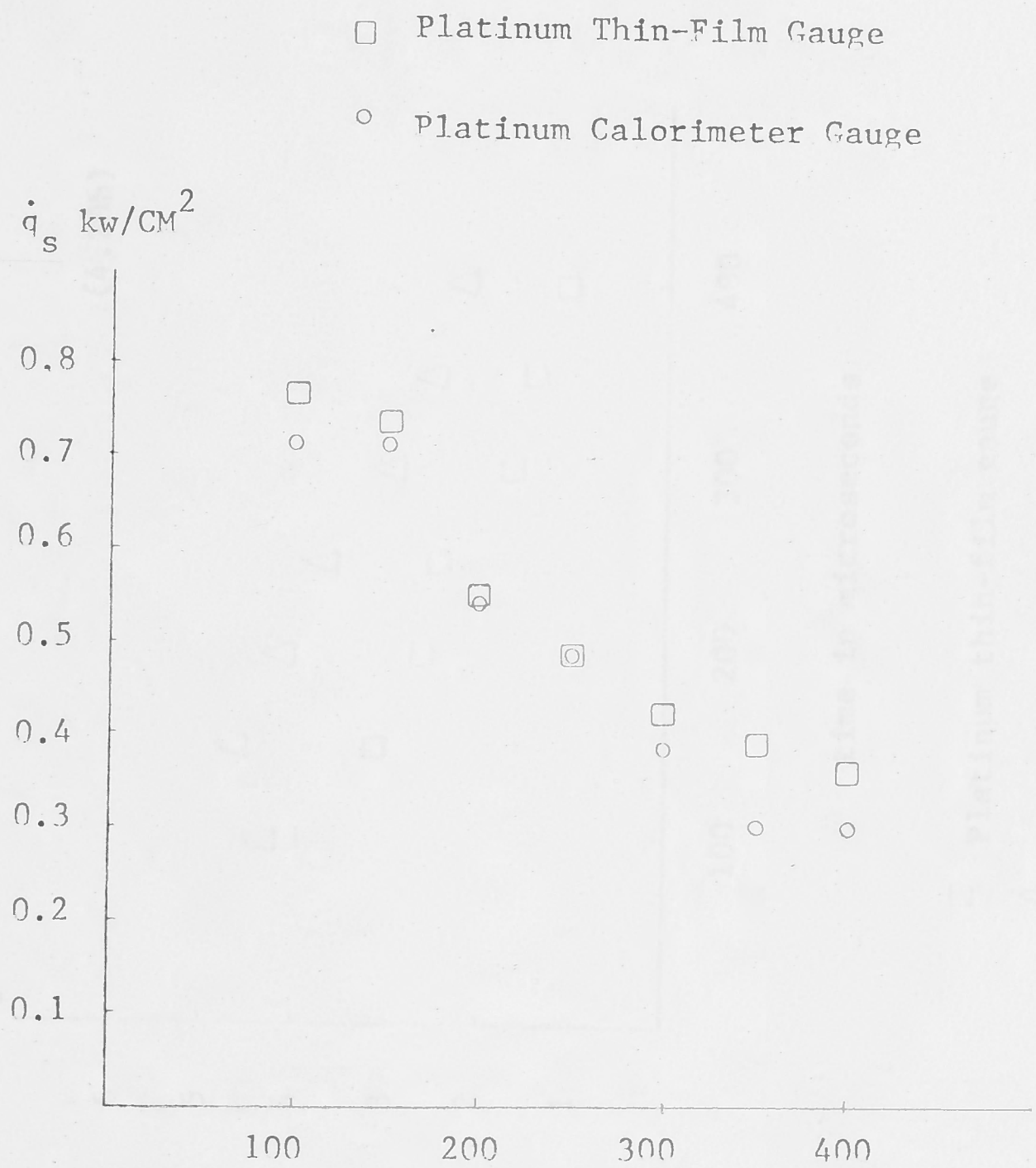

Fig. 4.19: Comparison of Platinum Thin-Film Gauge and Platinum Calorimeter Gauge, showing the effect of heat loss to substrate.

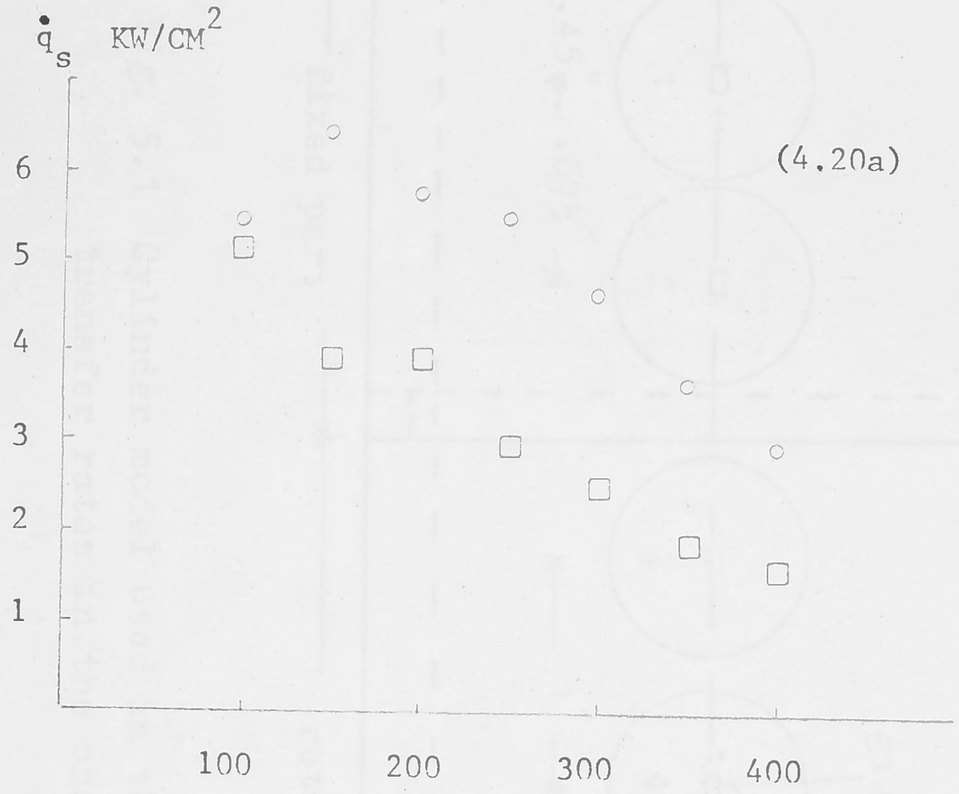

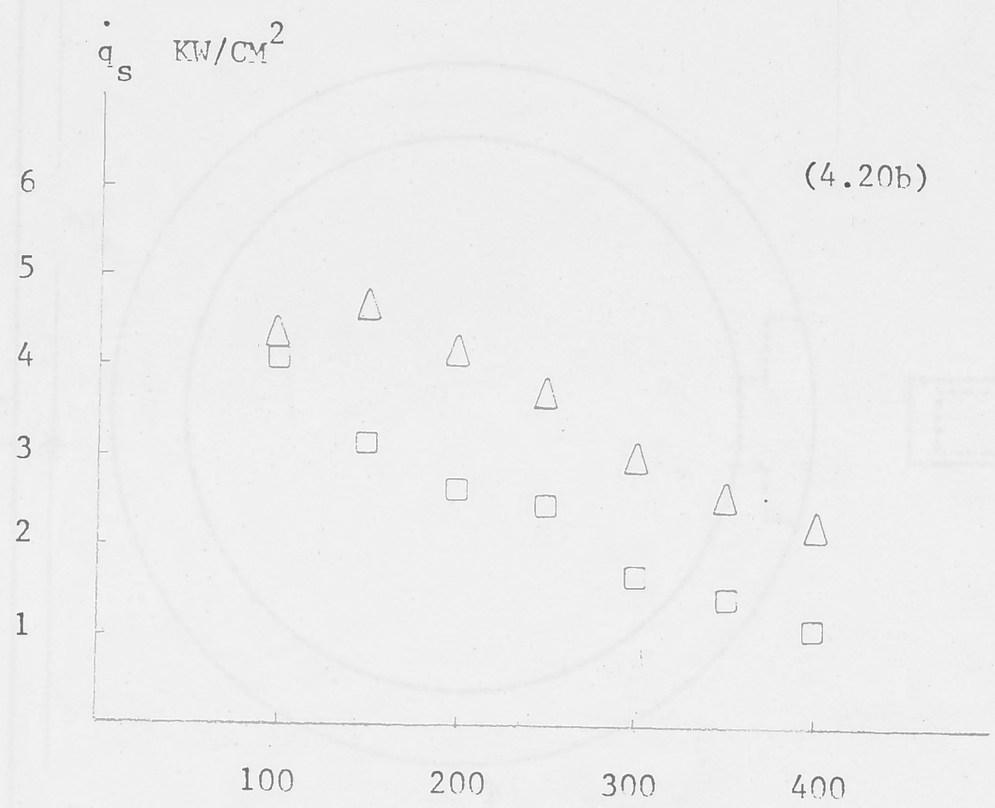

Fig. 4.20: Comparison of Thin-Film Gauge and Calorimeter Gauges at High Heat-Transfer Rates.

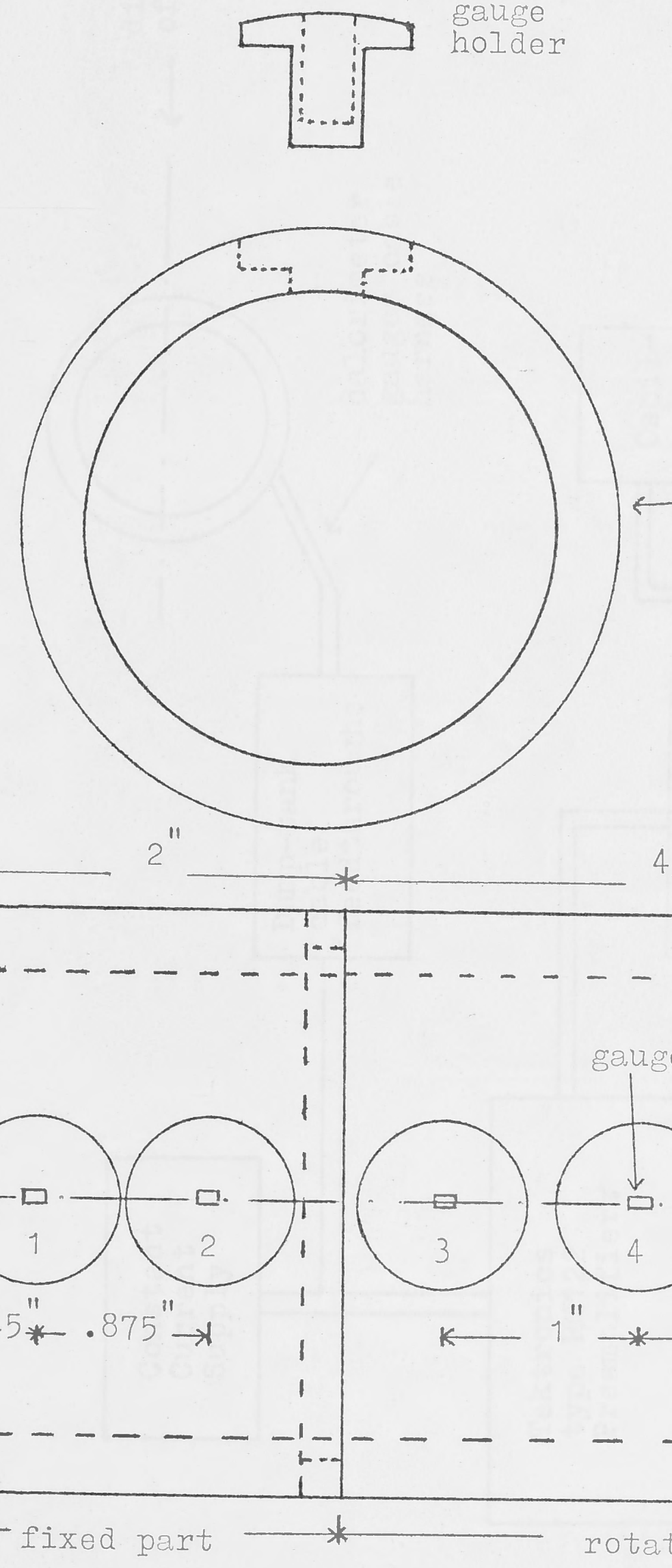

Fig. 5.1 Cylinder model used in the measurement of heat transfer rates in the shock tunnel T3.

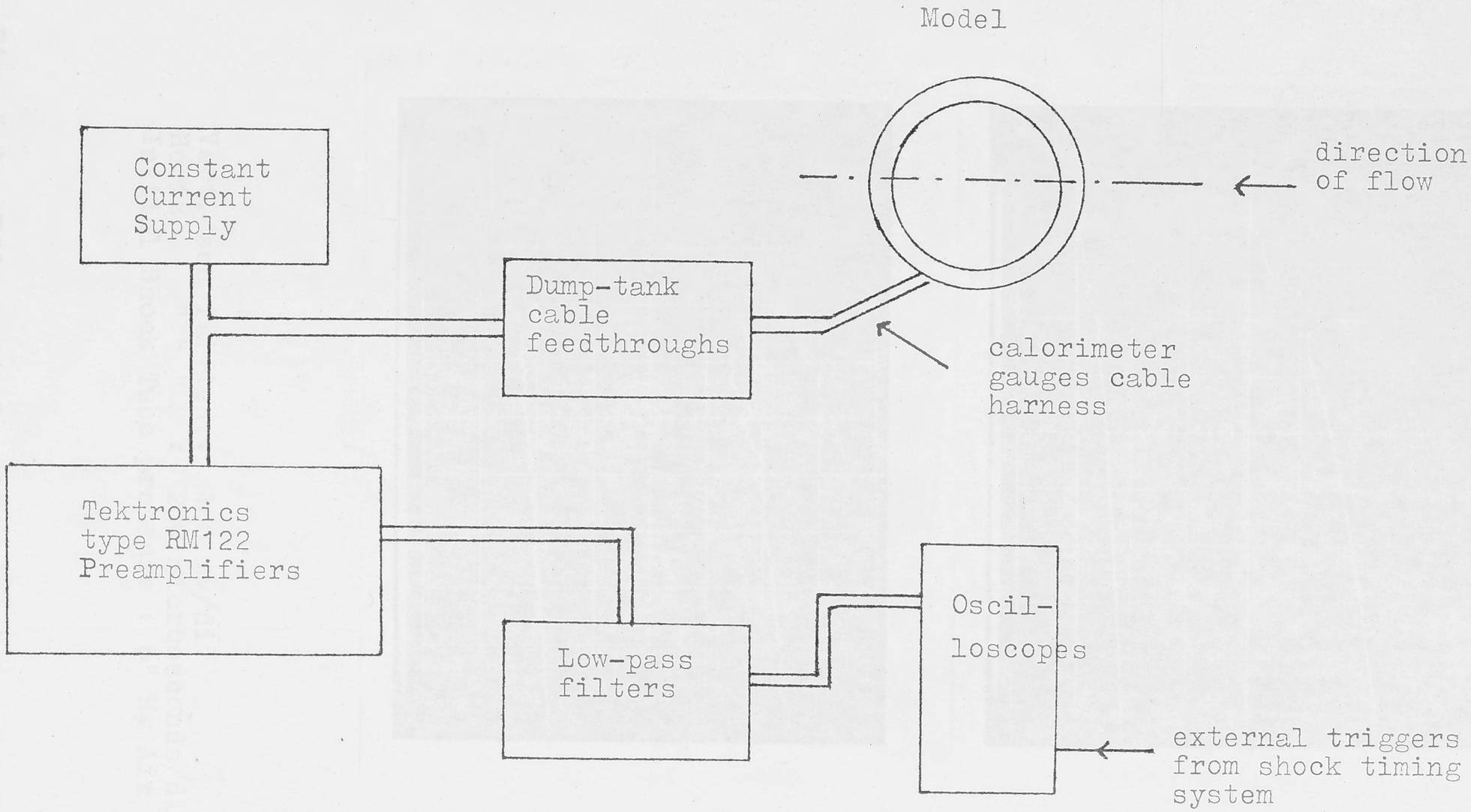

Fig. 5.2: Experimental set-up on T3 for measurement of heat transfer rates

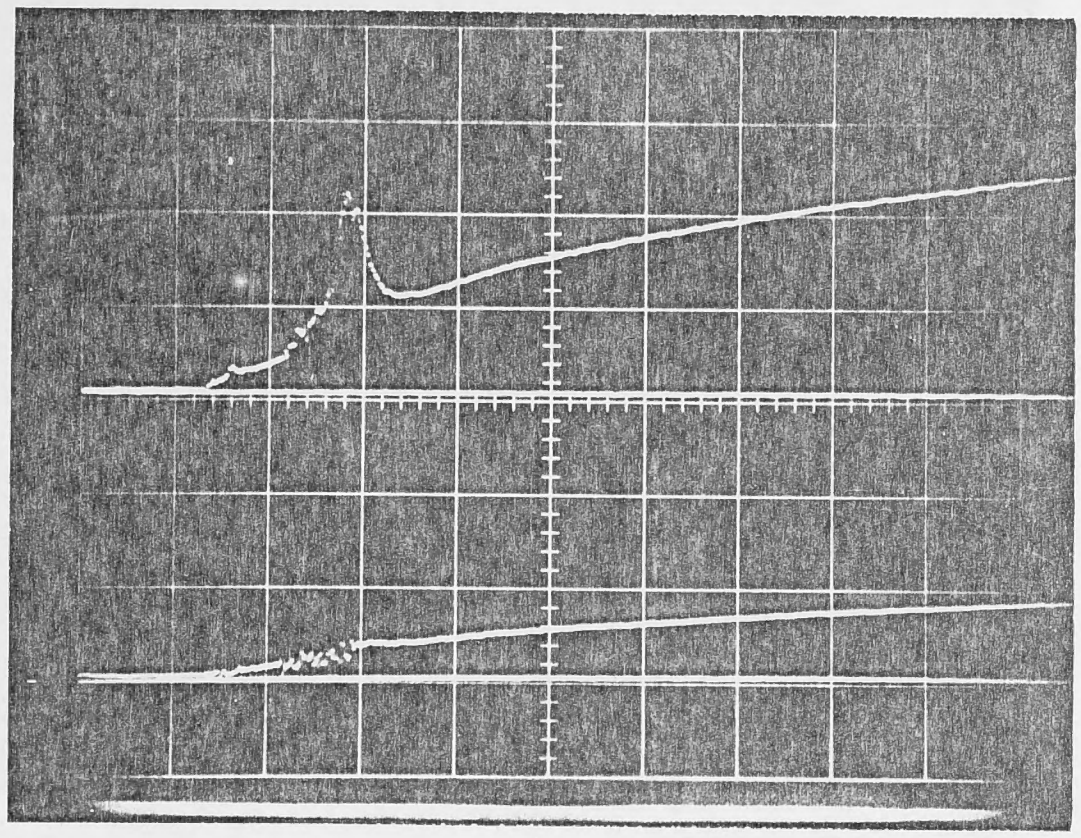

Model and gauges cleaned before shot

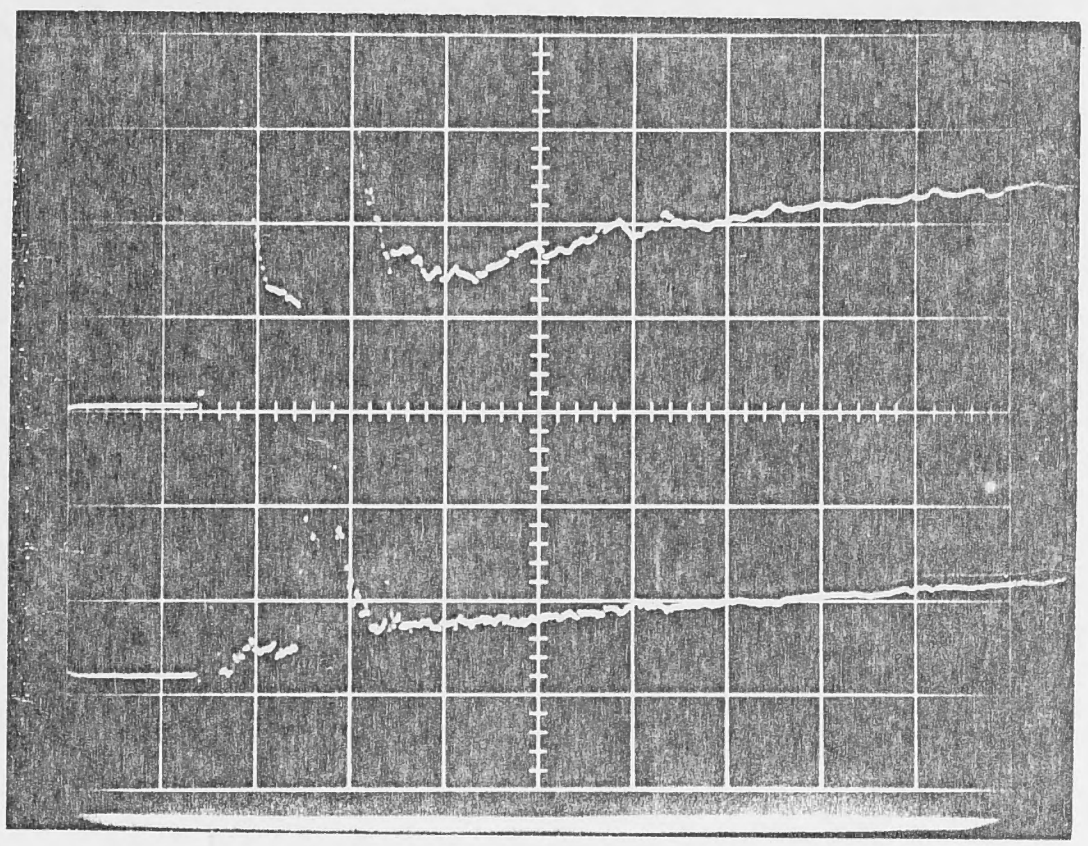

Model and gauges not cleaned for two shots

Vert. sensitivies : 100 mv/div
Horiz. " " : 200 microseconds/div
Initial Shock Tube pressure : 6" Hg Air

Fig. 5.3: Effect of cleaning of model and gauges on noise level of signal

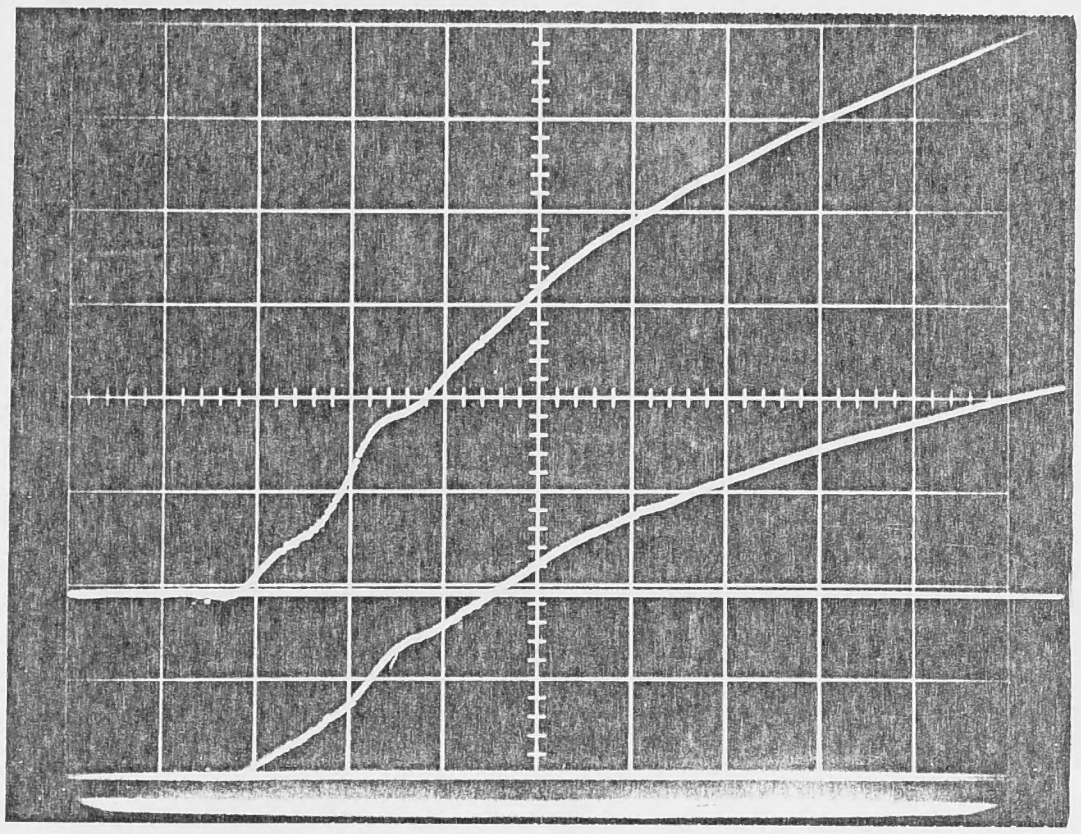

Undifferentiated heat transfer signals

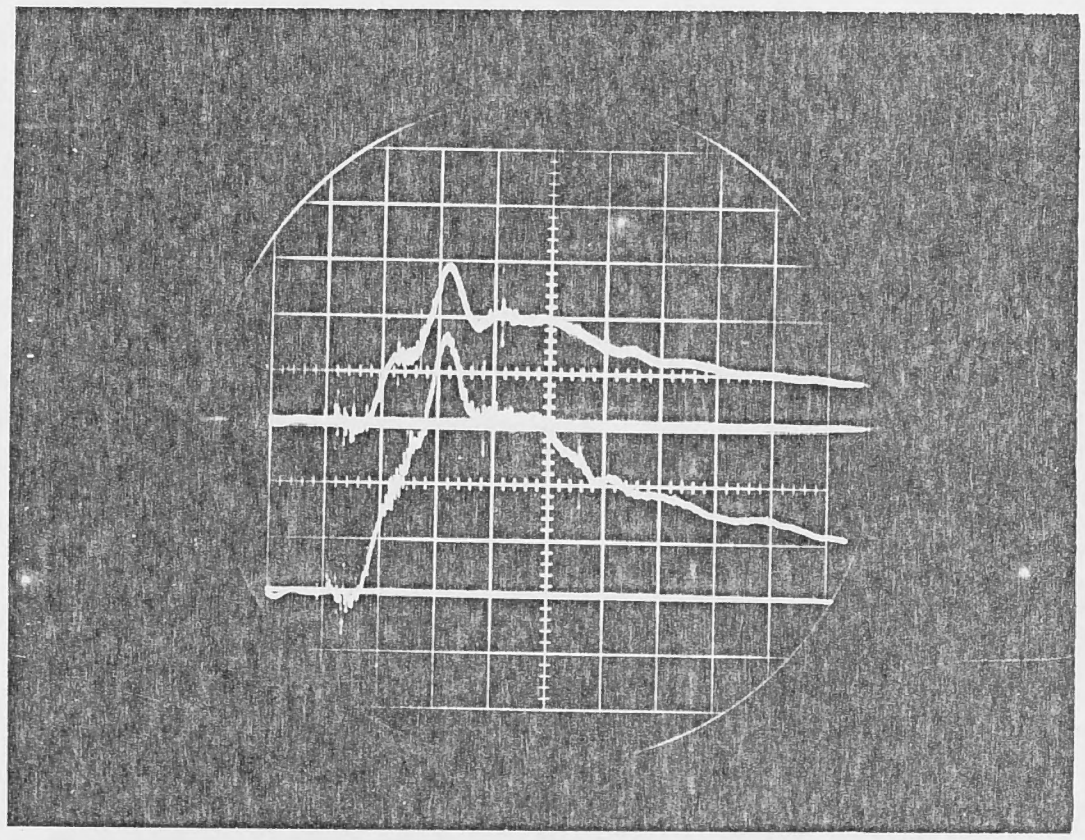

RC differentiated heat transfer signals

Upper picture vert. sensitivities: 0.2V/div
Lower " " " : top trace- 20mv/div
bot. " 10 "
Horiz. scale : 200 microseconds/div
Initial shock tube filling pressure : 6" Hg Air

Fig. 5.4: A relatively good heat transfer record in which differentiation of signal is possible

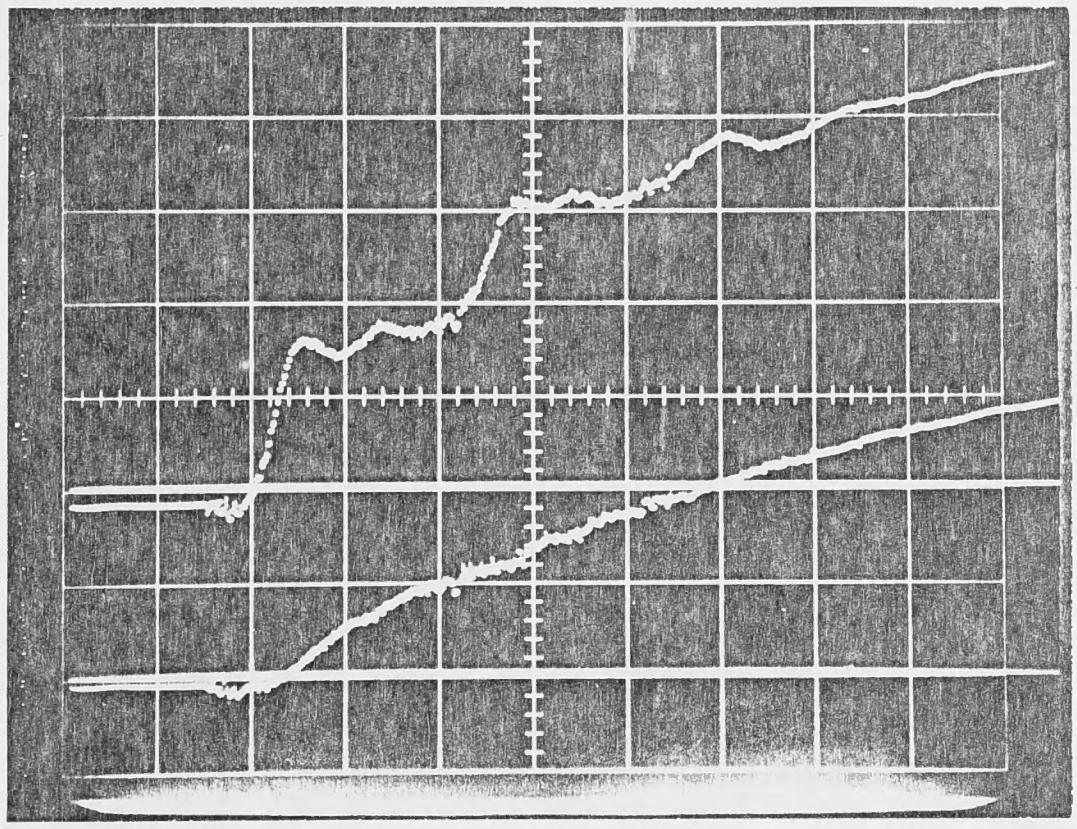

Undifferent-
iated heat
transfer
signals

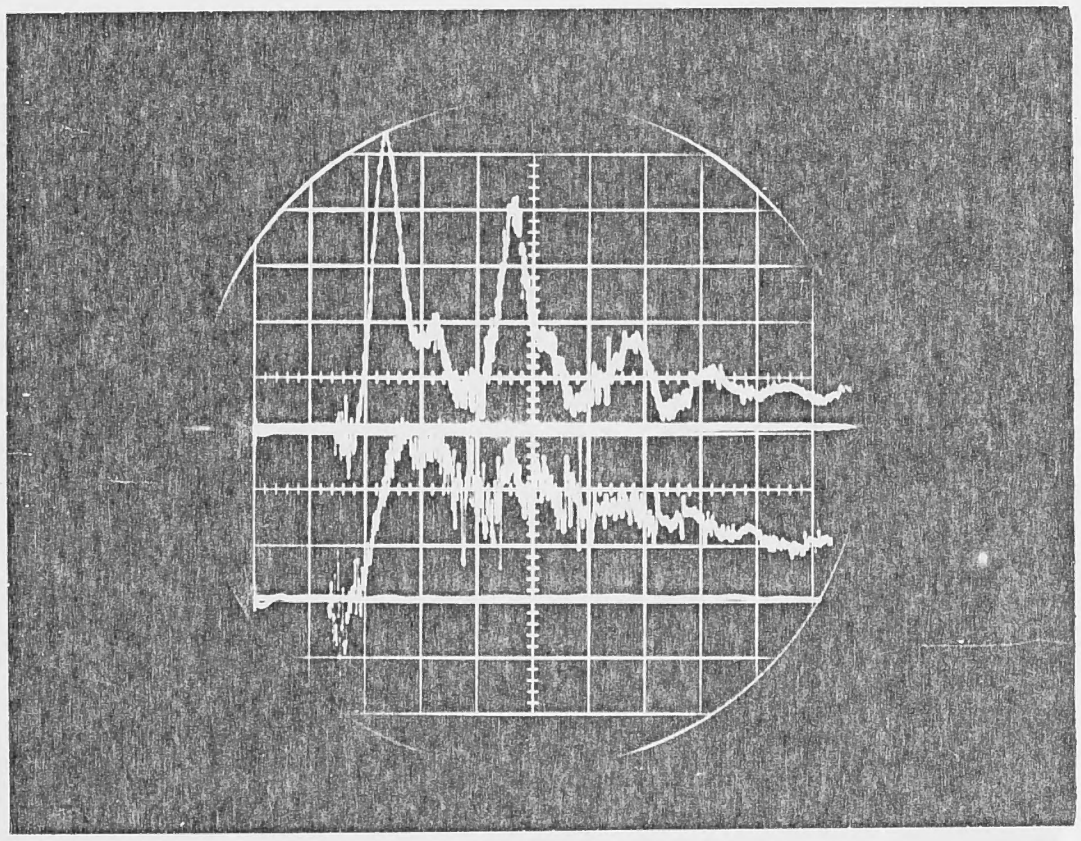

RC differen-
iated heat
transfer
signals

Upper picture vert. scale : 100 mv/div
Lower " " " :top trace- 50 mv/div
bot. " 20 "
Horiz. scale : 200 microseconds/div

Initial shock tube filling pressure : 6" Hg Air

Fig. 5.5: An example of a noisy shot in which differentiation of signal is not possible

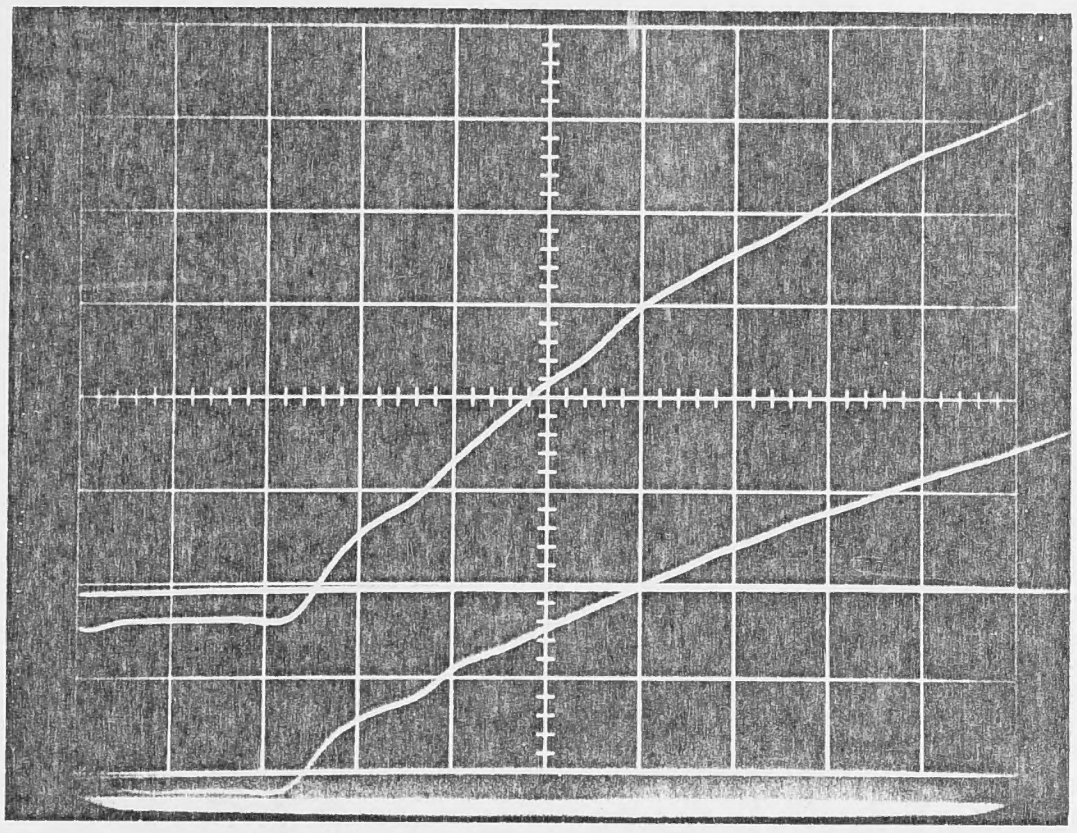

Undifferentiated heat transfer signals

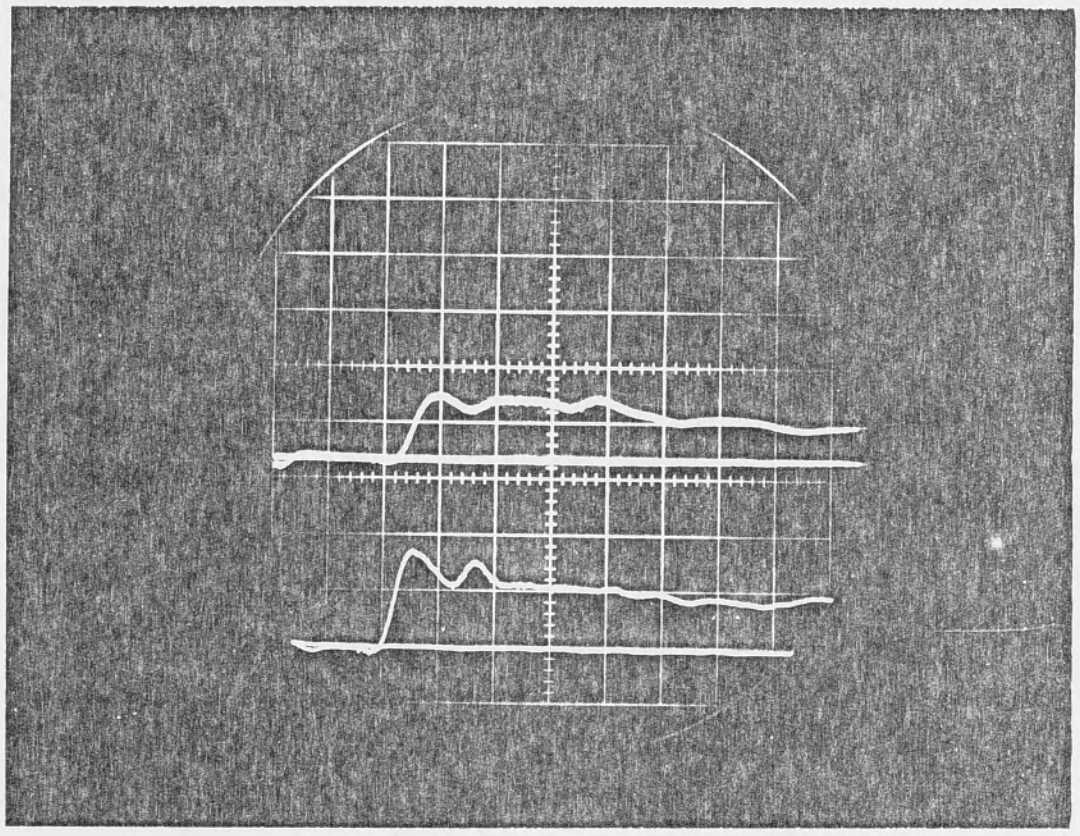

RC differentiated heat transfer signals

Upper picture vert. scale : 50 mv/div
Lower " " " : top trace- 20 mv/div
bot. " 10 "
Horiz. scale : 200 microseconds/div
Initial shock tube filling pressure : 6" Hg CO_2

Fig. 5.6: Heat transfer signals for situation when tunnel flow quality is good

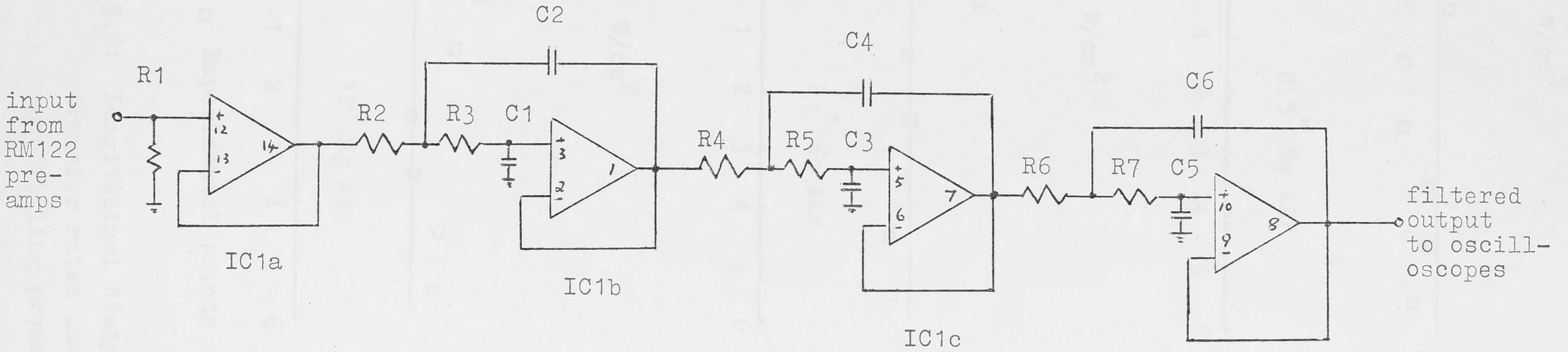

R1	:	100 K
R2-R7	:	22 K
C1,C2	:	1 NF
C3	:	680 PF
C4	:	1.5 NF
C5	:	330 PF
C6	:	3.3 NF
C7,C9	:	100 μF 25V
C8,C10	:	0.1 μF

IC1 : LM324N
(pin 4 - +12V)
(pin 11 - -12V)

Fig. 5.7: Circuit of 6-th order low-pass filter

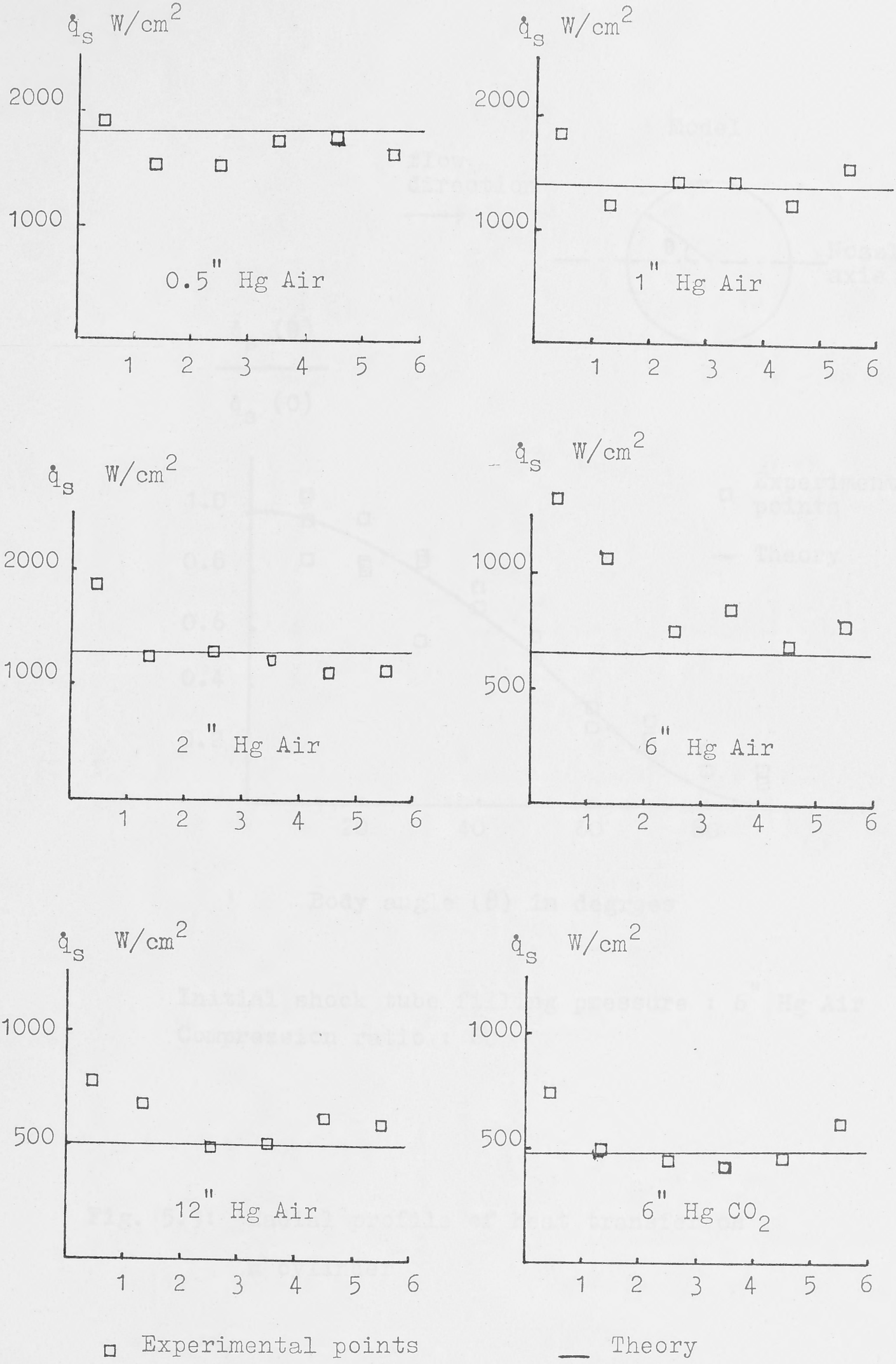

Fig. 5.8: Longitudinal distribution of stagnation heat transfer rates under various initial shock tube filling pressures for T3.

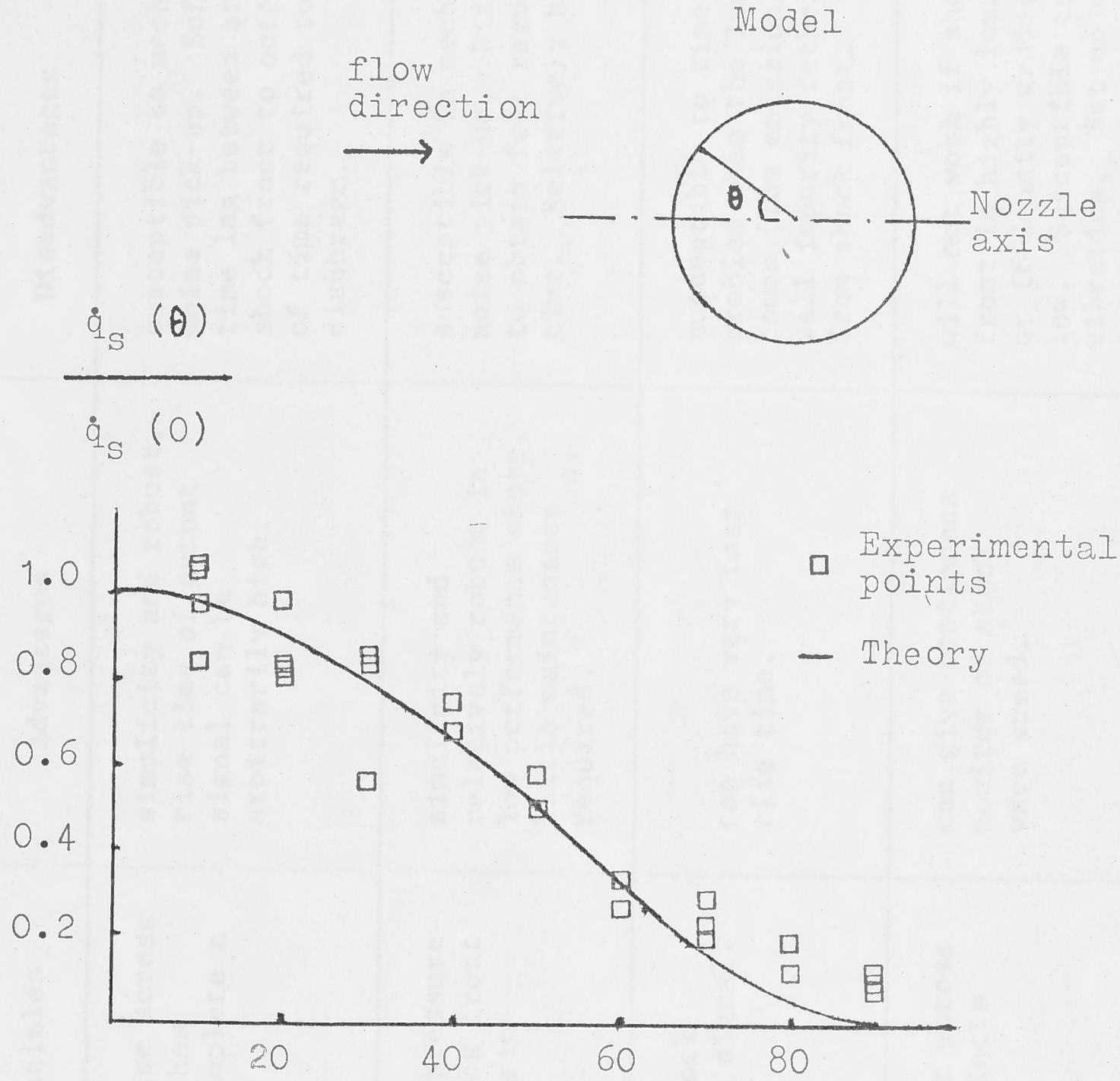

Initial shock tube filling pressure : 6" Hg Air
Compression ratio : 60

Fig. 5.9: Radial profile of heat transfer on a cylinder

Table 2.1: Characteristics of various timing transducers

Category	Detector	Operating Principles	Advantages	Disadvantages
I. Pressure Sensor	(a) Contact Shock Wave Detector (Mulac et al)	the pressure rise across shock front pushes diaphragm to complete a circuit.	simplicity and robust, rise time of output signal can be arbitrarily high.	susceptible to mechanical noise pick-up. Suffer from time lag between arrival of shock front to output becaus of time required to deform diaphragm.
	(b) Piezoelectric Pressure Transducer (Bradley, Gaydon et al)	compression by pressure rise across shock front generates electric charge.	simplicity and relatively robust in low performance shots, little maintenance required.	susceptible to mechanical noise pick-up. Difficult to obtain fast response time. Relatively high cost.
II. Optical Sensor	(a) Photodiodes and photomultipliers (Bradley, Gaydon et al)	the luminous shock front generates signal.	can have very fast rise time.	susceptible to time lag problem when the luminosity comes from emission by wall impurity rather than from shock front.
	(b) Schlieren Photography (Bradley, Gaydon et al)	Density gradient across shock front deflects light beam.	can give continuous monitor of shock wave speed.	will not work if shock front is highly luminous or if density gradient is low. Susceptible to vibration. Set up can be involved.

TABLE 2.1 Continued

Category	Detector	Operating Principles	Advantages	Disadvantages
	(c) Image Converter Camera photography.	the image of the shock front (luminous or visualised using interferometer) is time-resolved by camera in sweeping mode.	continuous monitor of shock speed.	complicated set-up. Very expensive. Not suitable if more than one location is to be monitored.
	(d) Microwave technique (Bradley)	reflection of microwave from shock front.	continuous monitor of shock speed.	too complicated set-up for routine use.
III. Ionisation Sensor	(a) Ionisation gauges (Bradley, Gaydon et al, Stalker, McClenahan)	change of electrical conductivity of gas behind shock front generates signal.	extremely simple and robust, no maintenance problem, can have a very fast response time under right condition.	limited operating conditions though can be extended by suitable techniques (McClenahan, Knight et al). Suffers from premature triggering from precursor effects. Possibility of time lag problem if ionisati comes from wall impurities and not from test gas.
	(b) Glow-Discharge detector (Bradley, Gaydon et al)	ionisation behind shock front causes discharge, generating signal.	similar to ionisation gauges, but works to lower pressure.	longer response time than ionisation gauges, similar possibility of time lag problem, and limited operatir conditions.

TABLE 2.1 Continued

Category	Detector	Operating Principles	Advantages	Disadvantages
	(c) Positive ion beam detector (Bradley, Gaydon et al)	shock front causes defocussing of positive ion, generating signal.	works to low pressure.	interference to gas flow, similar problem as ionisation gauges.
	(d) Gas conductivity probe (Dannenberg et al)	change in gas impedance behind shock front generates signal.	can provide identification of various regimes in shock tube flow.	limited to conditions when gas impedance is reasonably low. Also can suffer possibility of time lag problem.
IV. Thermal Sensor	(a) Thin-film gauges (Ch 4, Bradley, Gaydon et al, Schultz et al)	temperature rise after shock front causes resistance change of a thin metallic film on insulator.	works down to low enthalpy conditions, fast response time, freedom from mechanical noise pick up.	too fragile to operate in even moderate heat transfer rate environment (a few hundred watts/sq cm)
	(b) Calorimeter Gauges (Ch 4, Schultz et al, Rose)	temperature rise after shock front causes resistance change of a metallic foil of suitable thickness.	same advantage as IVa but more robust.	not as sensitive as IVa. Suitable current supply a problem if a number of gauges are employed and isolated from each other.

TABLE 2.1 Continued

Category	Detector	Operating Principles	Advantages	Disadvantages
	(c) Hot-wire anemometer (Gaydon et al)	temperature rise after shock front causes resistance change of a thin wire.	same advantage as IVa, but more robust.	more complicated set-up, less sensitivity.
	(d) Thermocouples	temperature rise after shock front causes heating of junction, generating voltage due to Seebeck effect.	extremely simple, robust, inexpensive in addition to the advantages as in IVa.	no reported literature on its systematic use as a shock timing transducer except preliminary work reported by Furler.

Test Gas	Diaphragm used	Initial Pressure Torr	Shock Speed km/sec	Estimated Output per thermocouple microvolt/microsecond
Air	mylar*	760	1.2	12
Air	mylar	100	2.1	21
Air	mylar	20	2.7	28
Air	mylar	1.0	7.5	10
Air	26 G Al	760	2.1	80
Air	26 G Al	100	3.0	67
Air	22 G Al	20	4.3	92
CO_2	mylar	760	0.86	21
CO_2	mylar	10	2.7	25
Ar	mylar	760	1.2	28
Ar	mylar	10	2.8	25
N_2	mylar	760	1.2	20
N_2	mylar	200	1.7	18
He	mylar	760	2.1	8
He	mylar	100	3.0	11
He	26 G Al	760	3.0	29
He	26 G Al	100	4.2	27
He	22 G Al	760	3.6	81
He	22 G Al	20	5.7	28

* All mylar 0.1 mm thick

Table 2.2: Estimated output per thermocouple element for various shock tube operating conditions in T1.

Channel #	System Delay in Microseconds				
	Input signal slew rate microvolt/microsecond				
	160	80	40	20	3
1	2.0	2.4	2.8	3.5	6.1 $\pm$ 0.1
2	1.9	2.4	2.8	3.4	
3	1.7	2.1	2.5	3.0	
4	1.6	2.0	2.5	3.1	
Average	1.8 $\pm$ 0.2	2.2 $\pm$ 0.2	2.7 $\pm$ 0.2	3.2 $\pm$ 0.2	

Table 2.3: Measured System Delay for various input signal slew rates for four different timing channels.

Test Gas	Initial gas pressure Torr	Shock Speed KM/s	Estimated System Delay μs
Air	1.0	7.50	2.2
Air	760	1.17	2.5
Air	20	4.26	1.4
Carbon Dioxide	760	0.86	2.0
Argon	760	1.23	2.0
Nitrogen	760	1.18	2.2
Helium	760	2.13	3.0
Helium	760	3.01	2.0
Helium	100	3.00	2.8
Helium	20	5.69	2.0

Table 2.4: Estimated System Delay for various Shock Tube (T1) Operating Conditions, for a 5-element thermocouple transducer.

Test Gas	Initial filling pressure Torr	Shock Speed km/sec	Estimated delay microseconds	Measured delay microseconds
Air	100	1.8	2.2	2
Air	100	2.8	1.6	1
Helium	760	2.1	3.0	3
Helium	100	4.2	2.0	2

Table 2.5: Comparision between thermocouples and thin-film gauges on T1.

Test Gas	Series	Mean Shock Timings in microseconds			$\frac{\text{Standard Deviation}}{\text{Mean Shock Timings}} \times 100\%$			Normalised Standard Deviation		
		Stations			Stations			Stations		
		1 - 2	2 - 3	4 - 5	1 - 2	2 - 3	4 - 5	1 - 2	2 - 3	4 - 5
Air	A	192.7	196.2	208.5	2.7	2.1	1.5	1.8	1.4	1
Air	B	185.3	189.8	201.5	2.3	2.1	1.7	1.4	1.2	1
CO_2	A	231.8	237.6	228.8	3.1	2.5	0.8	3.9	3.1	1
CO_2	B	216.6	220.6	224.0	3.8	1.4	1.3	2.9	1.1	1

Table 2.6: Comparision of performance of thermocouples and ionisation gauges for 4" Hg initial test gas pressure.

Series A - Stations 1, 2, 3, 4, 5 are all ionisation gauges.

Series B - Stations 1, 2, 3 are thermocouples,
Stations 4, 5 are ionisation gauges.

Case #	Differences between the two repeat shots expressed as percentage				
	Shock Speed	Stag. Pressure Upper	Stag. Pressure Lower	Stag. Pressure Average	Pitot Pressure
1	-0.2	-10	-13	-12	-3
2	-0.3	0	-2	-1	+3
3	-1	-5	-1	-3	-3
4	+0.9	+14	-2	+6	-2
5	-2	+20	0	+11	0

Table 3.1: Stagnation Pressure Variations and Pitot Pressure Variations for Shots Repeated Under the Same Conditions.

Sensitivity PSI/mV	Stagnation Pressure Transducers		Pitot Pressure Transducers			
	Upper	Lower	04	05	06	07
	63.7± 1.3	69.7± 1.4	5.02×10^{-2}	5.66×10^{-2}	5.93×10^{-2}	5.93×10^{-2}

Table 3.2: Sensitivities of the Pressure Transducers used in Measurements of Stagnation Pressure and Pitot Pressure.

Stagnation Enthalpy MJ/KGM		Normalised Free-Stream Density $\frac{\rho_\infty P_o}{U_s}$ $(\frac{GM.ATM.SEC}{CM^4}) \times 10^{-9}$		Pitot Pressure in PSI	
		Averaged Experimental Values	Nenzf Values	Averaged Experimental Values	Nenzf Values
AIR	21	2.0 ± 0.1	2.1		
	18	2.4 ± 0.3	2.3		
	17			22 ± 2	22
	35			20 ± 2	22
	67			17 ± 2	18
CO_2	7	4.0 ± 0.2	3.8		
	38			19 ± 2	21

Table 3.3: Comparision Between Measured Experimental Values of Free-Stream Density and Pitot Pressures with Nenzf Calculated Values.

Material	Density gm/cc	Specific Heat J/(°K·gm)	Thickness (ℓ) x 10^{-2} cm	Resistivity $\mu\Omega$ - CM	Resistance mΩ	Temp. Coeff. of Resist. x 10^{-3}	$\frac{dT}{dt} \times 10^{3}$ °K/sec	$\frac{dV_{out}}{dt}$ mv/sec
Stainless Steel AISI 430	7.9	0.46	2.0	70	18	1.13	14	280
Lead	11.3	0.13	3.6	20.6	2.9	4.3	19	220
Iron	8.0	0.45	2.3	13.9	3.1	6.21	12	200
Tin	7.3	0.23	4.1	11.5	1.4	5.0	15	92
Nickel	8.9	0.46	2.4	6.8	1.4	6.0	10	73
Platinum	21.5	0.14	2.8	10.5	1.9	3.5	12	72
Silver	10.5	0.24	4.7	1.6	0.17	4.0	8.4	53
Aluminium	2.7	0.91	4.6	2.65	0.29	4.3	8.9	10
Gold	19.3	0.13	4.5	2.42	0.27	3.4	8.9	7.7
Copper	8.9	0.37	3.5	1.7	0.24	3.9	8.5	7.5

Table 4.1: Comparison of Sensitivities of Various Metals, figures based on 1 millisecond run time, 4% heat loss to substrate, 1 KW/CM^2 heat transfer rate, 1 ampere current through gauge, pyrex substrate, dimensions: 1 cm long x 0.2 cm wide x ℓ cm thick.

The values for density, specific heat, resistivity, and temperature coefficients of resistance are either measured or taken from Clark, Schultz et al (p 83), Chapman, or Touloukian.

Material	Melting Point °C	Density, ρ gm/cc	Specific Heat, c J/gm-k	Thermal Conductivity, k J/cm K sec	$\sqrt{\rho ck}$ J/cm^2 K sec$^{\frac{1}{2}}$
Air (NTP)		0.00129	1.005	0.000253	0.000473
Polystyrene	80	1.06	1.26	1.0013	0.040
PVC	80	1.4	1.05	0.0017	0.05
Silicone	288	1.3	1.2	0.0016	0.05
Perspex	100	1.2	1.47	0.0021	0.061
Terylene	256	1.38	1.34	0.0021	0.062
Araldite	80	1.2	1.7	0.002	0.063
Bakelite		1.3	1.68	0.0021	0.068
Teflon	400	2.18	1.05	0.0025	0.076
Delrin	175	1.42	1.47	0.0028	0.076
Nylon	210	1.14	2.1	0.0025	0.077
Polythene	110	0.93	2.31	0.0034	0.086
Pyrex	1100	2.22	0.775	0.0136	0.153
Quartz	1100	2.20	0.75	0.0143	0.154

Table 4.2: Comparison of Thermal Products $\sqrt{\rho_2 c_2 k_2}$ for various substrate materials. Values taken from Schultz et al, Clark and Kaye et al.

Input mV	100	90.0	80.0	70	60.0	50.0	40.0	30.0	20.0	10
Output mV (meter)	100	90.7	81.0	70	60.5	50.0	40.2	29.7	19.6	10
Output mV (DMM)	100	90.0	79.9	70	59.9	49.9	39.9	30.0	19.9	

1. The input is applied at the HI-LO terminals and measured using a 3½ digit Fluke digital multimeter having an accuracy of 0.1% $\pm$ 1 digit.

2. The output (meter) is read from the analog meter movement installed on the panel of the control unit. Three ranges are used to take the readings, the 100 mV, the 50 mV and the 10 mV ranges. Note that the meter amplifier has been calibrated before this test.

3. The output (DMM) is a normalised reading. The original reading is taken from the meter amplifier output measured using the 3½ digit Fluke DMM (at the meter end of VR 26), with an amplifier gain up to this point of 1.63 $\pm$ 0.02.

Table 4.3: Linearity Measurement of Meter Amplifier Circuit, using the installed meter movement and also an external digital voltmeter.